Syntheses, Crystal Structures, and Magnetic Properties of Paramagnetic Assemblies Consisting of Trans-bridged Heterometallic Multinuclear Complexes

（常磁性トランス架橋異種金属多核錯体の集積化と
その結晶構造および磁気物性）

Atsushi Takamori

March　2023

Syntheses, Crystal Structures, and Magnetic Properties of Paramagnetic Assemblies Consisting of Trans-bridged Heterometallic Multinuclear Complexes

（常磁性トランス架橋異種金属多核錯体の集積化と
その結晶構造および磁気物性）

Atsushi Takamori

March　2023

Preface

This study presented in this thesis has been performed by the author under the direction of Associate Professor Kazuhiro Uemura at the Department of Chemistry and Biomolecular Science, Faculty of Engineering, Gifu University, from April 2020 to March 2023. In this thesis the author described the relationship between the structure and magnetic properties of *trans* bridged paramagnetic multinuclear assembles.

The author would like to express his deepest gratitude to Associate Professor Kazuhiro Uemura for his kindest guidance, helpful suggestions and discussions, and warm encouragement in the laboratory.

The author is also grateful to Professor Masahiro Ebihara for his advice and kind encouragement.

The author is thankful to Professor Osamu Sakurada and Assistant Professor Michiyuki Yoshida for their kind technical supports of XRPD. The author is thankful to Technical Stuff Dr. Motoyasu Hujiwara, Mrs. Shinako Iki, and Dr. Mizuki Miyajima (National Institutes of Natural Sciences, Institute for Molecular Science) for their kind technical supports of Magnetic Measurement and EPR. The author is thankful to Technical Stuff Dr. Yoshinori Okano (National Institutes of Natural Sciences, Institute for Molecular Science) for his kind technical supports of X-ray diffraction measurements.

The author is thankful to Associate Professor Yuji Naruse and Assistant Professor Taro Udagawa for their valuable suggestions on theoretical analysis.

The author is thankful to Mr. Yusuke Aoki, Mr. Yuya Ikeda, Mr. Itsuki Nagasawa, Ms. Haruka Hasegawa, Mr. Tomonori Adachi, Ms. Momoka Oshika, Mr. Shota Kanamori, Mr. Yuma Ito, Mr. Kou Shinyama, and Mr. Ryunosuke Tomita for their valuable suggestions and kind technical supports.

Acknowledgement is made to all members of the group of Associate Professor Uemura for their kind supports, encouragement, and friendship.

Finally, the author expresses his deep appreciation to his parents and brother, Mr. Takeaki Takamori, Mrs. Mari Takamori, and Mr. Naohisa Takamori for personal support and affectionate encouragement.

March 2023

Atsushi Takamori

Department of Engineering Science

Graduate School of Engineering

Gifu University

Contents

General Introduction

1. Paramagnetic one-dimensional complexes with metal–metal bonds

To date, much research has been conducted on molecular-based magnetic materials in which paramagnetic metal species are bridged with organic molecules or halide ions to reveal various characteristics of magnetism such as phase transition, spin-crossover, and single-chain magnets.[1-5] The treated paramagnetic species in these compounds are primarily first-row transition metals with high-spin configurations including cleverly overlapped five anisotropic d-orbitals via the p-orbitals in the bridging ligands designed to control the coordinated directions and to desired expected magnetic interactions.[1-5] In contrast, several compounds have been recently reported in which the first row of transition metals is bridged by metal–metal bonds with significant magnetic interactions.[6] They are one-dimensional (1D) complexes in which the five d-orbitals overlap and connect with another d-orbital, forming a d–d system (Figure 1). These paramagnetic 1D complexes with metal–metal bonds are categorized into several types: finite or infinite and homometallic or heterometallic.

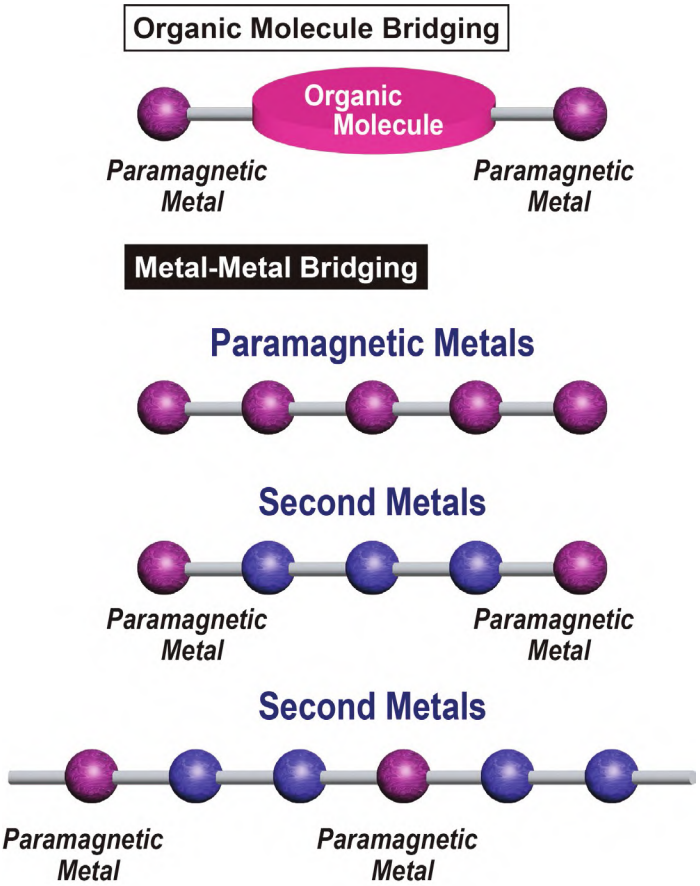

Figure 1. Conceptual scheme for the magnetic interaction between two paramagnetic species through organic molecules or second metals.

2. Finite one-dimensional complexes aligning homometals with metal–metal bonds

One of the principal strategies to obtain finite one-dimensional complexes with aligned homometals through metal–metal bonds is a template method utilizing multidentate ligands (Figure 2), such as oligopyridylamidate,[7] oligophosphines,[8] and polyenes of conjugated ligands.[9] These finite 1-D metal complexes consisted of homometals are called extended metal atom chains (EMACs). In 1968, the trinuclear nickel complex $[Ni_3(dpa)_4Cl_2]$ (dpa = bis(2-pyridyl)amide)[10,11] was discovered, then various metal centers such as Cr,[12] Co,[13] Cu,[14] and Ru[15] have been reported.[16] Until now, various nuclear numbers of Ni^{II} string complexes have been synthesized and characterized.[11,16-21] Although the series of these Ni string complexes including Ni^{II} atoms with the spin state S = 1 in the outer positions, the spin state of the inner Ni^{II} atoms is S = 0, which is attributed to the coordination environment; the low-spin state of the inner Ni^{II} atoms is in a square coordination, while the high-spin state of the outer Ni^{II} atoms is in a square pyramidal coordination. Although the template method utilizing multidentate ligands is effective for one-dimensionally aligned several metals, the control for the spin state of metals is difficult due to degenerated molecular orbitals with the same metal species in similar coordination environments. In the series of Ni^{II} string complexes, the magnetic interaction between the outermost Ni^{II} atoms of high-spin state becomes weaker as the number of Ni atoms increases. In recent research, trinuclear nickel complex $[Ni_3(dpa)_4Cl_2]$ connected by halide ions one-dimensionally aligned in Ni–Ni–Ni–Cl–Ni–Ni–Ni–Cl was reported, in which intra- and interdimer antiferromagnetic interactions were observed.[22]

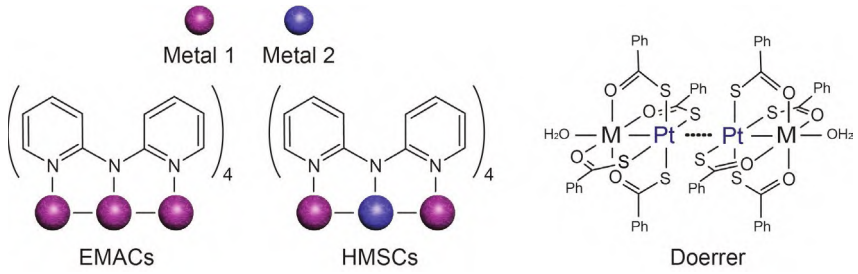

Figure 2. One-dimensional metal complexes containing paramagnetic species bridged by metal–metal bonds found in EMACs and HMSCs with bis(2-pyridyl)amide.

3. Finite one-dimensional complexes aligning heterometals with metal–metal bonds

One of the principal strategies to obtain finite one-dimensional complexes aligning several kinds of metal with metal–metal bonds is a template method similar to EMACs utilizing multidentate

ligands, which compound is called heteronuclear metal string complexes (HMACs). Although the syntheses of HMACs are more difficult than EMACs due to various combinations of metal atom, several synthetic methods to obtain the design of specific HMSCs have been reported, such as the metal backbones of M_A–M_B–M_A, M_A–M_A–M_B, and M_A–M_B–M_C.[6,16] M_A–M_B–M_A type with one metal atom sandwiched between two other atoms mainly consists of paramagnetic metal species and diamagnetic metal species such as M_A = Mn, Fe, Co, Ni, and Cu and M_B = Pd and Pt.[23-26] For example, Co–Pd–Co exhibits strong antiferromagnetic interaction via –Pd– bonds.[25] M_A–M_A–M_B type with the heterometal at the end of the chain mainly consists of various species pairs of M_A and M_B such as M_A = Cr, Mo, Cu and W and M_B = Mn, Fe, Co, Ni, Cr, Pd and Pt.[27-33] For example, Mo–Mo–Ni exhibits extraordinarily large ferromagnetic coupling thorough metal–metal bonds due to the orthogonality of Mo and Ni orbitals.[34] M_A–M_B–M_C type with three different metals has a few reports such as Mo–W–Co and Ni–Co–Rh.[35,36] In addition to these, pentanuclear Ni–Ru–Ru–Ni–Ni and Mo–Mo–Ni–Mo–Mo have been reported.[37,38] Considering unpaired electrons in a d-orbital connected through metal–metal bonds, stronger and more diverse magnetic properties are expected than conventional materials, however, a few reports exploring rational synthetic methods for such compounds exist. Doerrer et al. recently published pioneering research on magnetic interactions of first-row transition metals via –Pt···Pt– bonds using paddlewheel Pt–M dinuclear complexes (Figure 2).[39-43] Using the fact that planar Pd and Pt complexes tend to dimerize by themselves due to the d^8 configurations, it is possible to connect metal species that are difficult to align one-dimensionally on their own. For example, the Ni–Pt---Pt–Ni tetranuclear complexes created by dimerizing a paddlewheel dinuclear complex $[PtNi(tba)_4(OH_2)]$ (tba = thiobenzoate) bridged by four tba ligands show a strong antiferromagnetic interaction via –Pt···Pt– bonds. As a result of the gluing effect of d^8 metals, designed paramagnetic heterometallic 1D chains and HMACs incorporating various metal species are expected.

4. Infinite one-dimensional complexes aligning heterometals with metal–metal bonds

In general, synthetic methods of infinite one-dimensional chain are obtained by the oxidation of d^8 square-planar metals connected to other metals at the dz^2 orbital, as result of partially oxidized dz^2 bands showing metal–metal chains. The metal species in infinite one-dimensional metal complexes are very restricted to d^7 or d^8 metal species, such as Ir, Pt, Rh, and Pd.[44-53] Nevertheless, to explore magnetic properties, Uemura et al. have synthesized heterometallic one-dimensional

chains in which paramagnetic metal species are connected by direct metal–metal bonds with a second metal species instead of an organic ligand (Figure 3).[54-56] The synthetic method for the paramagnetic heterometallic one-dimensional chains uses the HOMO–LUMO interaction at the dz^2 orbital (σ*) between two kinds of complex, where mixing *cis*-$[Pt_2M(piam)_4(NH_3)_4]X_2$ (piam = pivalamidate, M = Mn, Co, and Cu, X = anion) and $[Rh_2(O_2CCH_3)_4]$ that have filled and vacant σ*, respectively, afforded –Pt–M–Pt–Rh–Rh– alignments, showing antiferromagnetic interactions through –Pt–Rh–Rh–Pt– bonds.

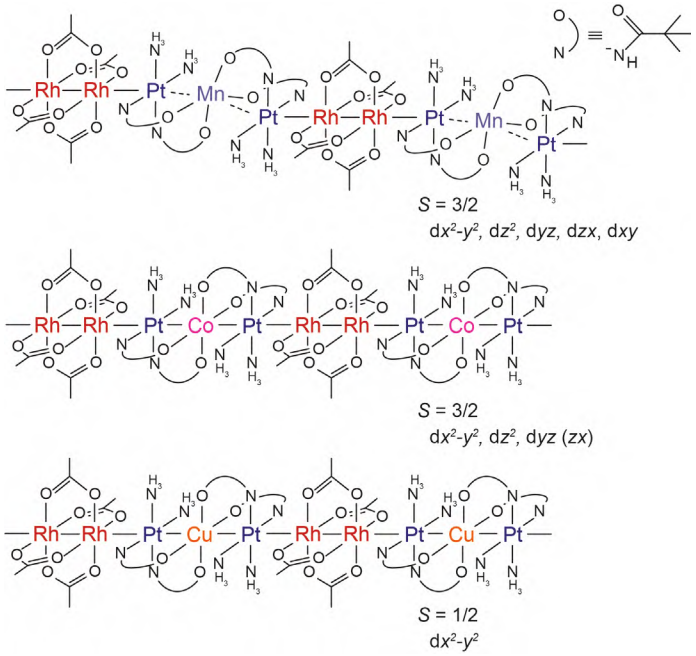

Figure 3. Structures of paramagnetic one-dimensional complexes with metal–metal bonds by HOMO–LUMO interaction.

5. Survey of this thesis

The purpose of this thesis research is to find a new construction strategy for paramagnetic multinuclear assembles with heterometallic bonds and to elucidate the crystal structure, spin state, and magnetic properties of paramagnetic multinuclear assemblies. Particularly, this thesis mainly describes several paramagnetic *trans* bridged multinuclear assembles, where high-spin first-row transition metals are bridged by the diamagnetic second- or third-row metals, such as Pt or Rh atoms. Among paramagnetic multinuclear assemblies few examples of infinite one-dimensional chain complexes with metal–metal bonds have been reported. Thus, a new construction strategy is useful to conduct the research in this field.

Chapter 1 describes paramagnetic trinuclear complexes, *trans*-$[Pt_2M(piam)_4(NH_3)_4](ClO_4)_x$ (***t*-M**; piam = pivalamidate, M = Mn, Fe, Co, Ni, and Cu, x = 2 or 3), aligned as Pt–M–Pt, which comprised of *trans*-$[Pt(piam)_2(NH_3)_2]$. Except for ***t*-Fe**, the trinuclear complexes are dimerized with close contact (3.9 Å) between the end Pt atoms to form Pt–M–Pt···Pt–M–Pt alignments with high-spin M(+2) containing five (***t*-Mn**), three (***t*-Co**), two (***t*-Ni**), and one (***t*-Cu**) unpaired electrons localized on M atoms. Several physical measurements and calculations revealed that the dimerized structures were maintained in MeCN, where cyclic voltammograms for ***t*-M** exhibited two-step oxidation and reduction attributed to Pt–M(+2)–Pt···Pt–M(+2)–Pt ↔ Pt–M(+3)–Pt···Pt–M(+2)–Pt ↔ Pt–M(+3)–Pt···Pt–M(+3)–Pt, via mixed-valent states. Magnetic susceptibility measurements for ***t*-M** showed antiferromagnetic interaction, ***t*-Mn**: J = –0.9 cm^{-1}, ***t*-Co**: J = –3.5 cm^{-1}, ***t*-Ni**: J = –7.3 cm^{-1}, and ***t*-Cu**: J = 0.0 cm^{-1}, between the two M centers with distances of 9.0 Å through Pt···Pt bonds.

Chapter 2 describes paramagnetic trinuclear complexes, *trans*-$[Pt_2M(acam)_4(NH_3)_4](ClO_4)_2$ (**1-M**; acam = acetamidate, M = Co, Ni, and Cu), aligned as Pt–M–Pt were successfully synthesized and characterized by single-crystal X-ray structure analyses and physical measurements. The trinuclear complexes extend infinitely one-dimensional chains formed ···Pt–M–Pt···Pt–M–Pt··· alignments with Pt···Pt interactions between the adjacent end Pt atoms in close contact with each other (3.5 Å). Several physical measurements revealed all three first-row transition metals in **1-M** have high-spin states, where unpaired electrons are localized on M atoms, which three (**1-Co**), two (**1-Ni**), and one (**1-Cu**) respectively. Magnetic susceptibility measurements for **1-Co** and **1-Ni** showed relatively strong antiferromagnetic interaction (**1-Co**: $2J$ = –17.9 cm^{-1}, **1-Ni**: $2J$ = –27.9 cm^{-1}) between the high-spin M centers through Pt···Pt bonds. In contrast, **1-Cu** showed ferromagnetic interaction (**1-Cu**: $2J$ = 0.28 cm^{-1}) between the Cu centers through Pt···Pt bonds.

Chapter 3 describes paramagnetic one-dimensional chain complexes $[PtCu(piam)_2(NH_3)_2Cl_2]\cdot H_2O$ (**2-Cu**) with aligned –Pt–Cu–Pt–Cu– were successfully synthesized and characterized by single-crystal X-ray structure analyses and physical measurements. The one-dimensional chain extends infinitely, where all the metals are bridged by amidate ligands, and by piam ligands the coordinated platinum atoms are hanged to the opposite direction to bind the copper

atoms. Several physical measurements revealed that unpaired electrons in the one-dimensional chains are localized on the copper atoms, $dx^2–y^2$ orbital. Magnetic susceptibility measurements showed the presence of antiferromagnetic interaction (J = –0.91 cm^{-1}) between the copper atoms with distances of 5.7 Å through –Pt– bonds.

Chapter 4 describes paramagnetic one-dimensional chain complexes with direct metal–metal bond containing three types of metal species aligned with ⋯Pt–Cu–Pt–Rh–Rh–Pt–Cu–Pt⋯ (**4-Cu**) and –Rh–Rh–Pt–Cu–Pt– (**5-Cu**) were successfully synthesized and characterized by single-crystal X-ray structure analyses and physical measurements. Several physical measurements revealed the oxidation states of the one-dimensional complexes are Rh(+2), Pt(+2), and Cu(+2), where the unpaired electrons lie on the Cu $dx^2–y^2$ orbitals. Magnetic susceptibility measurements in **4-Cu** showed an antiferromagnetic interaction (J = –0.28 cm^{-1}) between the copper atoms centers through –Pt⋯Pt– bonds. In contrast, **5-Cu** showed a weak ferromagnetic interaction (J = 0.01 cm^{-1}) between the copper centers through –Pt–Rh–Rh–Pt– bonds.

Chapter 5 describes the paramagnetic trinuclear complex *trans*-$[Pt_2Fe(piam)_4(NH_3)_4](ClO_4)_3·H_2O$ (***t*-Fe**) has a half-filled σ-type orbital over Pt–Fe–Pt, making it an excellent option for magnetic assemblies. It was successfully used in synthesizing $[\{Rh_2(O_2CCH_3)_4Cl_2\}\{Pt_2Fe(piam)_4(NH_3)_4\}_2]_n(ClO_4)_{4n}$ (**6**) from ***t*-Fe** and $[Rh_2(O_2CCH_3)_4Cl_2]$, where each trinuclear complex was bridged by Cl^- ions aligned as –Pt–Fe–Pt–Cl–Pt–Fe–Pt– with Fe⋯Fe distance of 10.1 Å. The zigzag chains were further linked by –Rh–Rh– to form a two-dimensional honeycomb sheet. The X-ray photoelectron spectroscopy, electron paramagnetic resonance, and magnetic susceptibilities measurements revealed that the formal metal oxidation states in **6** were Pt(+2), Fe(+3), and Rh(+2), where five unpaired electrons were located on the Fe(+3) atoms. A significant decrease in χT below 40 K was observed, where the theoretical fitting affords the axial zero-field splitting parameter D = 5.23 cm^{-1} and zJ = −0.12 cm^{-1}.

References

1. Miller, J. S.; Epstein, A. J., Organic and Organometallic Molecular Magnetic Materials—Designer Magnets. *Angew. Chem., Int. Ed.* **1994,** *33*, 385–415.
2. Coronado, E.; Day, P., Magnetic Molecular Conductors. *Chem. Rev.* **2004,** *104*, 5419–5448.
3. Miyasaka, H.; Clérac, R., Synthetic Strategy for Rational Design of Single-Chain Magnets. *Bull. Chem. Soc. Jpn.* **2005,** *78*, 1725–1748.
4. Oshio, H.; Nihei, M., Rational Syntheses of Multinuclear High-Spin Complexes. *Bull. Chem. Soc. Jpn.* **2007,** *80*, 608–620.
5. Ferrando-Soria, J.; Vallejo, J.; Castellano, M.; Martínez-Lillo, J.; Pardo, E.; Cano, J.; Castro, I.; Lloret, F.; Ruiz-García, R.; Julve, M., Molecular magnetism, *quo vadis*? A historical perspective from a coordination chemist viewpoint. *Coord. Chem. Rev.* **2017,** *339*, 17–103.
6. Chipman, J. A.; Berry, J. F., Paramagnetic Metal−Metal Bonded Heterometallic Complexes. *Chem. Rev.* **2020,** *120*, 2409–2447.
7. Liu, I. P.-C.; Wang, W.-Z.; Peng, S.-M., New generation of metal string complexes: strengthening metal–metal interaction *via* naphthyridyl group modulated oligo-α-pyridylamido ligands. *Chem. Commun.* **2009**, 4323–4331.
8. Goto, E.; Begum, R. A.; Zhan, S.; Tanase, T.; Tanigaki, K.; Sakai, K., Linear, Redox-Active Pt_6 and $Pt_2Pd_2Pt_2$ Clusters. *Angew. Chem., Int. Ed.* **2004,** *43*, 5029–5032.
9. Murahashi, T.; Mochizuki, E.; Kai, Y.; Kurosawa, H., Organometallic Sandwich Chains Made of Conjugated Polyenes and Metal−Metal Chains. *J. Am. Chem. Soc.* **1999,** *121*, 10660–10661.
10. Hurley, T. J.; Robinson, M. A., Nickel(II)-2,2'-dipyridylamine system. I. Synthesis and stereochemistry of the complexes. *Inorg. Chem.* **1968,** *7*, 33–38.
11. Clérac, R.; Cotton, F. A.; Dunbar, K. R.; Murillo, C. A.; Pascual, I.; Wang, X., Further Study of the Linear Trinickel(II) Complex of Dipyridylamide. *Inorg. Chem.* **1999,** *38*, 2655–2657.
12. Cotton, F. A.; Daniels, L. M.; Murillo, C. A.; Pascual, I., Compounds with Linear, Bonded Trichromium Chains. *J. Am. Chem. Soc.* **1997,** *119*, 10223–10224.
13. Yang, E.-C.; Cheng, M.-C.; Tsai, M.-S.; Peng, S.-M., Structure of a linear unsymmetrical trinuclear cobalt(II) complex with a localized CO^{II}–CO^{II} bond: dichlorotetrakis[μ_3-bis(2-pyridyl)amido]tricobalt(II). *J. Chem. Soc., Chem. Commun.* **1994**, 2377–2378.
14. Berry, J. F.; Cotton, F. A.; Lei, P.; Murillo, C. A., Further Structural and Magnetic Studies of Tricopper Dipyridylamido Complexes. *Inorg. Chem.* **2003,** *42*, 377–382.
15. Sheu, J.-T.; Lin, C.-C.; Chao, I.; Wang, C.-C.; Peng, S.-M., Linear trinuclear three-centred metal–metal multiple bonds: synthesis and crystal structure of $[M_3(dpa)_4Cl_2]$[M = Ru^{II} or Rh^{II}, dpa = bis(2-pyridyl)amidoanion]. *Chem. Commun.* **1996**, 315–316.

16. Hua, S.-A.; Cheng, M.-C.; Chen, C.-h.; Peng, S.-M., From Homonuclear Metal String Complexes to Heteronuclear Metal String Complexes. *Eur. J. Inorg. Chem.* **2015**, 2510–2523.
17. López, X.; Huang, M.-Y.; Huang, G.-C.; Peng, S.-M.; Li, F.-Y.; Bénard, M.; Rohmer, M.-M., Even-Numbered Metal Chain Complexes: Synthesis, Characterization, and DFT Analysis of $[Ni_4(\mu_4\text{-}Tsdpda)_4(H_2O)_2]$ ($Tsdpda^{2-}$ = *N*-(*p*-toluenesulfonyl)dipyridyldiamido), $[Ni_4(\mu_4\text{-}Tsdpda)_4]^+$, and Related Ni_4 String Complexes. *Inorg. Chem.* **2006,** *45*, 9075–9084.
18. Berry, J. F.; Cotton, F. A.; Lei, P.; Lu, T.; Murillo, C. A., Additional Steps toward Molecular Scale Wires: Further Study of $Ni_5^{10/11+}$ Chains Embraced by Polypyridylamide Ligands. *Inorg. Chem.* **2003,** *42*, 3534–3539.
19. Lai, S.-Y.; Lin, T.-W.; Chen, Y.-H.; Wang, C.-C.; Lee, G.-H.; Yang, M.-h.; Leung, M.-k.; Peng, S.-M., Metal String Complexes: Synthesis and Crystal Structure of $[Ni_4(\mu_4\text{-}phdpda)_4]$ and $[Ni_7(\mu_7\text{-}teptra)_4Cl_2]$($H_2$phdpda = *N*-Phenyldipyridyldiamine and H_3teptra = Tetrapyridyltriamine). *J. Am. Chem. Soc.* **1999,** *121*, 250–251.
20. Peng, S.-M.; Wang, C.-C.; Jang, Y.-L.; Chen, Y.-H.; Li, F.-Y.; Mou, C.-Y.; Leung, M.-K., One-dimensional metal string complexes. *J. Magn. Magn. Mater.* **2000,** *209*, 80–83.
21. Chen, P.-J.; Sigrist, M.; Horng, E.-C.; Lin, G.-M.; Lee, G.-H.; Chen, C.-h.; Peng, S.-M., A ligand design with a modified naphthyridylamide for achieving the longest EMACs: the 1st single-molecule conductance of an undeca-nickel metal string. *Chem. Commun.* **2017,** *53*, 4673–4676.
22. Aoki, K.; Otsubo, K.; Yoshida, Y.; Kimura, Y.; Sugimoto, K.; Kitagawa, H., Synthesis and Magnetic Properties of a Dimerized Trinuclear Ni String Complex, $[Ni_6Cl_2(dpa)_8](I_5)_2\cdot 0.25I_2$ (dpa^- = 2,2′-Dipyridylamide Anion). *Inorg. Chem.* **2021,** *60*, 16029–16034.
23. Yu, L.-C.; Lee, G.-H.; Sigrist, M.; Lin, T.-S.; Peng, S.-M., Structure and Antiferromagnetism of Trinuclear Heterometallic Strings Containing Mn^{II}–M^{II}–Mn^{II} Frameworks (M = Ni, Pd, Pt). *Eur. J. Inorg. Chem.* **2016**, 4250–4256.
24. Liu, Y.-C.; Hua, S.-A.; Cheng, M.-C.; Yu, L.-C.; Demeshko, S.; Dechert, S.; Meyer, F.; Lee, G.-H.; Chiang, M.-H.; Peng, S.-M., Electron Delocalization of Mixed-Valence Diiron Sites Mediated by Group 10 Metal Ions in Heterotrimetallic Fe–M–Fe (M=Ni, Pd, and Pt) Chain Complexes. *Chem. −Eur. J.* **2018,** *24*, 11649–11666.
25. Rohmer, M.-M.; Liu, I. P.-C.; Lin, J.-C.; Chiu, M.-J.; Lee, C.-H.; Lee, G.-H.; Bénard, M.; López, X.; Peng, S.-M., Structural, Magnetic, and Theoretical Characterization of a Heterometallic Polypyridylamide Complex. *Angew. Chem., Int. Ed.* **2007,** *46*, 3533–3536.
26. Liu, I. P.; Lee, G.-H.; Peng, S.-M.; Bénard, M.; Rohmer, M.-M., Cu−Pd−Cu and Cu−Pt−Cu Linear Frameworks: Synthesis, Magnetic Properties, and Theoretical Analysis of Two Mixed-Metal Complexes of Dipyridylamide (dpa), Isostructural, and Isoelectronic with $[Cu_3(dpa)_4Cl_2]^+$. *Inorg. Chem.* **2007,** *46*, 9602–9608.
27. Nippe, M.; Wang, J.; Bill, E.; Hope, H.; Dalal, N. S.; Berry, J. F., Crystals in Which Some Metal Atoms are More Equal Than Others: Inequalities From Crystal Packing and Their

Spectroscopic/Magnetic Consequences. *J. Am. Chem. Soc.* **2010,** *132*, 14261–14272.

28. Nippe, M.; Bill, E.; Berry, J. F., Group 6 Complexes with Iron and Zinc Heterometals: Understanding the Structural, Spectroscopic, and Electrochemical Properties of a Complete Series of M≡M···M′ Compounds. *Inorg. Chem.* **2011,** *50*, 7650–7661.
29. Nippe, M.; Turov, Y.; Berry, J. F., Remote Effects of Axial Ligand Substitution in Heterometallic Cr≡Cr···M Chains. *Inorg. Chem.* **2011,** *50*, 10592–10599.
30. Chang, W.-C.; Chang, C.-W.; Sigrist, M.; Hua, S.-A.; Liu, T.-J.; Lee, G.-H.; Jin, B.-Y.; Chen, C.-h.; Peng, S.-M., Nonhelical heterometallic $[Mo_2M(npo)_4(NCS)_2]$ string complexes (M = Fe, Co, Ni) with high single-molecule conductance. *Chem. Commun.* **2017,** *53*, 8886–8889.
31. Nippe, M.; Victor, E.; Berry, J. F., Do Metal–Metal Multiply-Bonded "Ligands" Have a *trans* Influence? Structural and Magnetic Comparisons of Heterometallic Cr≡Cr···Co and Mo≡Mo···Co Interactions. *Eur. J. Inorg. Chem.* **2008,** *2008*, 5569−5572.
32. Chipman, J. A.; Berry, J. F., Facile Axial Ligand Substitution in Linear Mo≡Mo–Ni Complexes. *Inorg. Chem.* **2018,** *57*, 9354–9363.
33. Liu, I. P.; Chen, C.-H.; Chen, C.-F.; Lee, G.-H.; Peng, S.-M., Asymmetric heterometal string complexes: stereochemical control of the unique isomer of (4,0)$[CuCuPd(npa)_4Cl][PF_6]$ and (4,0)$[CuCuPt(npa)_4Cl][PF_6]$. *Chem. Commun.* **2009**, 577–579.
34. Chipman, J. A.; Berry, J. F., Extraordinarily Large Ferromagnetic Coupling ($J \geq 150$ cm^{-1}) by Electron Delocalization in a Heterometallic Mo−Mo−Ni Chain Complex. *Chem. −Eur. J.* **2018,** *24*, 1494–1499.
35. Nippe, M.; Timmer, G. H.; Berry, J. F., Remarkable regioselectivity in the preparation of the first heterotrimetallic Mo≡W···Cr chain. *Chem. Commun.* **2009**, 4357–4359.
36. Cheng, M.-C.; Mai, C.-L.; Yeh, C.-Y.; Lee, G.-H.; Peng, S.-M., Facile synthesis of heterotrimetallic metal–string complex $[NiCoRh(dpa)_4Cl_2]$ through direct metal replacement. *Chem. Commun.* **2013,** *49*, 7938–7940.
37. Huang, M.-J.; Hua, S.-A.; Fu, M.-D.; Huang, G.-C.; Yin, C.; Ko, C.-H.; Kuo, C.-K.; Hsu, C.-H.; Lee, G.-H.; Ho, K.-Y.; Wang, C.-H.; Yang, Y.-W.; Chen, I.-C.; Peng, S.-M.; Chen, C.-h., The First Heteropentanuclear Extended Metal-Atom Chain: $[Ni^{+}–Ru_2^{5+}–Ni^{2+}–Ni^{2+}(tripyridyldiamido)_4(NCS)_2]$. *Chem. −Eur. J.* **2014,** *20*, 4526–4531.
38. Hung, W.-C.; Sigrist, M.; Hua, S.-A.; Wu, L.-C.; Liu, T.-J.; Jin, B.-Y.; Lee, G.-H.; Peng, S.-M., A heteropentanuclear metal string complex $[Mo_2NiMo_2(tpda)_4(NCS)_2]$ with two linearly aligned quadruply bonded Mo_2 units connected by a Ni ion and a meso configuration of the complex. *Chem. Commun.* **2016,** *52*, 12380–12382.
39. Dahl, E. W.; Baddour, F. G.; Fiedler, S. R.; Hoffert, W. A.; Shores, M. P.; Yee, G. T.; Djukic, J.-P.; Bacon, J. W.; Rheingold, A. L.; Doerrer, L. H., Antiferromagnetic coupling across a tetrametallic unit through noncovalent interactions. *Chem. Sci.* **2012,** *3*, 602–609.
40. Baddour, F. G.; Fiedler, S. R.; Shores, M. P.; Bacon, J. W.; Golen, J. A.; Rheingold, A. L.; Doerrer, L. H., Pt···Pt vs Pt···S Contacts Between Pt-Containing Heterobimetallic

Lantern Complexes. *Inorg. Chem.* **2013,** *52*, 13562–13575.

41. Baddour, F. G.; Fiedler, S. R.; Shores, M. P.; Golen, J. A.; Rheingold, A. L.; Doerrer, L. H., Heterobimetallic Lantern Complexes That Couple Antiferromagnetically through Noncovalent Pt···Pt Interactions. *Inorg. Chem.* **2013,** *52*, 4926–4933.
42. Guillet, J. L.; Bhowmick, I.; Shores, M. P.; Daley, C. J. A.; Gembicky, M.; Golen, J. A.; Rheingold, A. L.; Doerrer, L. H., Thiocyanate-Ligated Heterobimetallic {PtM} Lantern Complexes Including a Ferromagnetically Coupled 1D Coordination Polymer. *Inorg. Chem.* **2016,** *55*, 8099–8109.
43. Beach, S. A.; Doerrer, L. H., Heterobimetallic Lantern Complexes and Their Novel Structural and Magnetic Properties. *Acc. Chem. Res.* **2018,** *51*, 1063–1072.
44. Atoji, M.; Richardson, J. W.; Rundle, R. E., On the Crystal Structures of the Magnus Salts, $Pt(NH_3)_4PtCl_4$. *J. Am. Chem. Soc.* **1957,** *79*, 3017–3020.
45. Krogmann, K.; Hausen, H. D. Z., Pt-Chain Structures. 1. Potassium Tetracyanoplatinate Violets $K_2[Pt(CN)_4]X_{0.3}\cdot 2.5H_2O$ (X = Cl, Br). *Z. Anorg. Allg. Chem.* **1968,** *358*, 67.
46. Krogmann, K.; Binder, W.; Hausen, H. D., Crystal Structure of "$Ir(CO)_3Cl$" = $Ir(CO)_{2.93}CI_{1.07}$. *Angew. Chem., Int. Ed.* **1968,** *7*, 812.
47. Finniss, G. M.; Canadell, E.; Campana, C.; Dunbar, K. R., Unprecedented Conversion of a Compound with Metal-Metal Bonding into a Solvated Molecular Wire. *Angew. Chem., Int. Ed.* **1996,** *35*, 2772–2774.
48. Prater, M. E.; Pence, L. E.; Clerac, R.; Finniss, G. M.; Campana, C.; Auban-Senzier, P.; Jerome, D.; Canadell, E.; Dunbar, K. R., A Remarkable Family of Rhodium Acetonitrile Compounds Spanning Three Oxidation States and with Nuclearities Ranging from Mononuclear and Dinuclear to One-Dimensional Chains. *J. Am. Chem. Soc.* **1999,** *121*, 8005–8016.
49. Sakai, K.; Ishigami, E.; Konno, Y.; Kajiwara, T.; Ito, T., New Partially Oxidized 1-D Platinum Chain Complexes Consisting of Carboxylate-Bridged *cis*-Diammineplatinum Dimer Cations. *J. Am. Chem. Soc.* **2002,** *124*, 12088–12089.
50. Mitsumi, M.; Ueda, H.; Furukawa, K.; Ozawa, Y.; Toriumi, K.; Kurmoo, M., Constructing Highly Conducting Metal–Metal Bonded Solids by Electrocrystallization of $[Pt^{II2}(RCS_2)_4]$ (RCS_2^-) Dithiocarboxylato, R = Methyl or Ethyl). *J. Am. Chem. Soc.* **2008,** *130*, 14102–14104.
51. Cotton, F. A.; Dikarev, E. V.; Petrukhina, M. A., *cis*-Di(μ-trifluoroacetate)dirhodium tetracarbonyl: structure and chemistry. *J. Chem. Soc., Dalton Trans.* **2000**, 4241–4243.
52. Pruchnik, F. P.; Jakimowicz, P.; Ciunik, Z.; Stanislawek, K.; Oro, L. A.; Tejel, C.; Ciriano, M. A., Rhodium wires based on binuclear acetate-bridged complexes. *Inorg. Chem. Commun.* **2001,** *4*, 19–22.
53. Campbell, M. G.; Powers, D. C.; Raynaud, J.; Graham, M. J.; Xie, P.; Lee, E.; Ritter, T., Synthesis and structure of solution-stable one-dimensional palladium wires. *Nature Chem.* **2011,** *3*, 949–953.

54. Uemura, K.; Ebihara, M., Paramagnetic One-Dimensional Chains Comprised of Trinuclear Pt−Cu−Pt and Paddlewheel Dirhodium Complexes with Metal−Metal Bonds. *Inorg. Chem.* **2013,** *52*, 5535–5550.
55. Uemura, K.; Miyake, R., Paramagnetic One-Dimensional Chain Complex Consisting of Three Kinds of Metallic Species Showing Magnetic Interaction through Metal–Metal Bonds. *Inorg. Chem.* **2020,** *59*, 1692–1701.
56. Uemura, K.; Aoki, Y.; Takamori, A., Paramagnetic One-dimensional Chain Containing High-spin Manganese Atoms Showing Weak Antiferromagnetic Interaction Through –Pt–Rh–Rh–Pt– Bonds. *Dalton Trans.* **2022,** *51*, 946–957.

Chapter 1

Dimerization of Paramagnetic Trinuclear Complexes by Coordination Geometry Changes Showing Mixed Valency and Significant Antiferromagnetic Coupling through –Pt···Pt– Bonds

Abstract

Paramagnetic trinuclear complexes, *trans*-$[Pt_2M(piam)_4(NH_3)_4](ClO_4)_x$ (***t*-M**; piam = pivalamidate, M = Mn, Fe, Co, Ni, and Cu, x = 2 or 3), aligned with Pt–M–Pt were successfully synthesized and characterized. The dihedral angles between the Pt and M coordination planes in ***t*-M** are approximately parallel, showing straight metal–metal bonds with distances of approximately 2.6 Å. Except for ***t*-Fe**, the trinuclear complexes are dimerized with close contact (approximately 3.9 Å) between the end Pt atoms to form Pt–M–Pt···Pt–M–Pt alignments with high-spin M(+2) containing five (***t*-Mn**), three (***t*-Co**), two (***t*-Ni**), and one (***t*-Cu**) unpaired electrons localized on M atoms. Several physical measurements and calculations revealed that the dimerized structures were maintained in MeCN, where cyclic voltammograms for ***t*-M** exhibited two-step oxidation and reduction attributed to Pt–M(+2)–Pt···Pt–M(+2)–Pt ↔ Pt–M(+3)–Pt···Pt–M(+2)–Pt ↔ Pt–M(+3)–Pt···Pt–M(+3)–Pt, via mixed-valent states. Magnetic susceptibility measurements for ***t*-M** showed antiferromagnetic interaction, ***t*-Mn**: J = –0.9 cm^{-1}, ***t*-Co**: J = –3.5 cm^{-1}, ***t*-Ni**: J = –7.3 cm^{-1}, and ***t*-Cu**: J = 0.0 cm^{-1}, between the two M centers with distances of 9.0 Å through Pt···Pt bonds.

Introduction

Metal–metal bonds are powerful pathways for electronic communication between two active metal sites providing cooperative catalysis,[1] as well as physical properties such as conductivity[2,3] and magnetism.[4] Compared to halogen- or organic-molecule-bridged metals, that is, the d-π-d system, second metal-mediated ones, presented as d-d-d systems, would afford significant d orbital overlapping, with potential for good communication despite the long range of distances. Taking advantage of five types of anisotropic d orbitals, the characteristic magnetic behavior has been designed with metal–metal wires by specific combinations of metal species.[4] For example, an asymmetric trinuclear complex arranged as Mo–Mo–Ni shows an extraordinarily large ferromagnetic coupling through metal–metal bonds,[5] whereas Cu–Pt–Cu shows strong antiferromagnetic interactions,[6] which are attributed to abnormal electronic structures induced by connecting multiple metals. These one-dimensionally aligned wires are called extended metal atom chains (EMACs)[7,8] and heteronuclear metal string complexes (HMSCs).[9,10] Although extensive synthetic and physical research has been accomplished to date, the length of wire required to obtain the characteristic magnetic behavior and desired metal position in the wire remains to be investigated.

The well-known synthetic approach to obtain these EMACs or HMSCs is a template method utilizing multidentate ligands, such as oligopyridylamidate,[7] oligophosphines,[11] and polyenes of conjugated ligands.[12] Although the template method is useful for constructing metal–metal bonds and achieves specific length of wire by pre-organized ligands, it is still difficult to achieve the placement of metal species in desired positions. In contrast, Pt-assisted extension of wires has been the focus of attention[13] because the combination of Pt and desired metals (= M) afforded thioacetate-bridged paddlewheel heterometallic Pt–M complexes, which are dimerized as M–Pt···Pt–M (Scheme 1), showing strong magnetic interactions through metal–metal bonds.[14-16] Such metalophilic gluing by two Pt atoms is found in one-dimensional (1D) chains by d^8 configuration metals, classical Pt chains such as KCP and magnus salts,[17,18] Ir and Rh chains,[19-21] and dinuclear (Pt_2,[22,23] Rh_2,[24,25] and Pd_2[26])-based chains. Furthermore, metalophilic dz^2 interactions between two kinds of complexes also afforded 1D chains,[27-29] where there are few examples of dimerized EMACs by these interactions,[11,30] meaning that $d^8\cdots d^8$ interactions are effective for extending structures; thus, further systematic investigations are required to explore this research field.

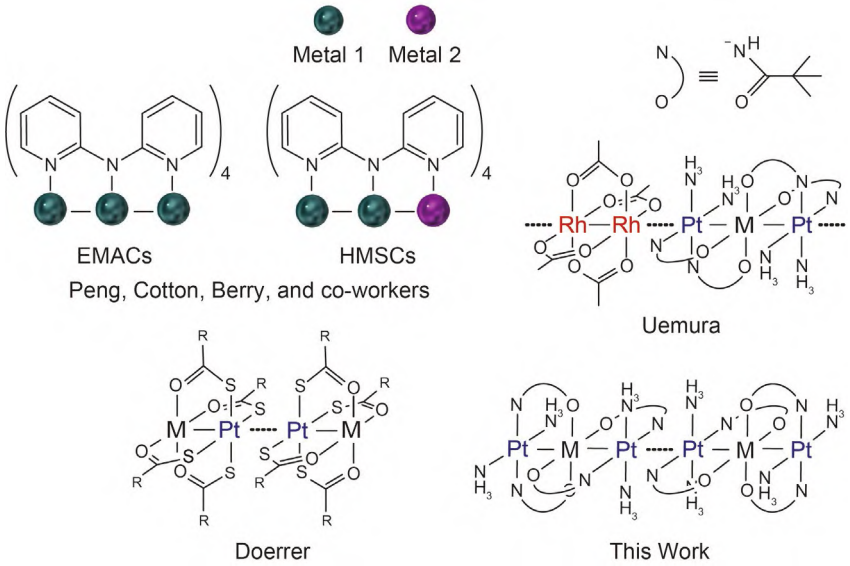

Scheme 1. Several one-dimensional complexes containing paramagnetic species (M) bridged by metal–metal bonds found in EMACs and HMSCs.

To date, several trinuclear Pt–M–Pt complexes, in which two Pt atoms sandwich an M atom, have been synthesized and characterized.[31-33] The crystal structures of rigid aromatic bridging ligands, *cis*-$[Pt_2M(NH_3)_4(1\text{-MeU})_2(1\text{-MeC})_2]^{x+}$ (1-MeU = 1-methyluracil, 1-MeC = 1-methylcytosine),[34] and *trans*-$[Pt_2M(NH_3)_4(C_5H_4NO)_4]^{x+}$,[33] and flexible bridging ligands *cis*-$[Pt_2M(NH_3)_4(piam)_4]^{x+}$ (piam = pivalamidate) revealed discrete Pt–M–Pt alignments without further extension, which are probably due to the repulsion of bulky ligands and charge valencies. In particular, in *cis*-$[Pt_2M(NH_3)_4(piam)_4]^{x+}$, trinuclear Pt–M–Pt complexes have significant bite angles among each coordination plane, resulting in relatively weaker heterometallic bonds, because the two piam bridging ligands are connected in the *cis* fashion. However, further extension was realized with other linkers, such as $[Rh_2(O_2CCH_3)_4]$, which resulted in –Rh–Rh–Pt–M–Pt– chains.[35-38] The crystal structure of *trans*-$[Pt_2Cu(NH_3)_4(piam)_4](NO_3)_2$ inspired synthetic research because these trinuclear complexes spontaneously dimerize to align with Pt–Cu–Pt···Pt–Cu–Pt.[39] Here, we will present the synthesis and characterization of *trans*-bridged trinuclear Pt–M–Pt complexes with M = Mn, Fe, Co, Ni, and Cu, compared with previous *cis*-bridged complexes. We were successful in obtaining *trans*-$[Pt(piam)_2(NH_3)_2]$ with amidate-hanging in a *trans* fashion, as expected for binding M with non-coordinated oxygen atoms. Interestingly, the obtained trinuclear Pt–M–Pt complexes were further extended, showing characteristic mixed-valence and magnetic interactions through –Pt···Pt– bonds.

Results and Discussion

Synthetic Procedure.

The amidate-hanging Pt mononuclear complex, *cis*-$[Pt(piam)_2(NH_3)_2]\cdot 2H_2O$, is a useful precursor for heterometal multinuclear complexes, where non-coordinated oxygen atoms are easily bound to second metals (M) in solution (Scheme 2).[40] The previous amidate-hanging Pt mononuclear complex, *cis*-$[Pt(piam)_2(NH_3)_2]\cdot 2H_2O$ (***c***), was obtained by the hydrolysis of nitrile in *cis*-$[Pt(NC^tBu)_2(NH_3)_2](ClO_4)_2$ under the basic conditions. Such direct ligand conversion of coordinated nitrile to amidate prevents the dimerization of platinum atoms bridged by amidate ligands, only giving mononuclear complexes as the precursor for further multinuclear complexes. As mentioned in the Experimental Section, using *trans*-$[PtCl_2(NH_3)_2]$ as the starting material instead of *cis*-$[PtCl_2(NH_3)_2]$, *trans*-$[Pt(piam)_2(NH_3)_2]$ (***t***) was successfully obtained by a similar synthetic procedure to ***c***. Thereafter, mixing ***t*** and $M(ClO_4)_2$ (M = Mn, Fe, Co, Ni, and Cu) in MeOH afforded single-crystals of *trans*-$[Pt_2M(piam)_4(NH_3)_4](ClO_4)_x$ (***t*-M**, $x = 2$ or 3). The crystal dates and structure refinement results are summarized in Table 1. As shown in the crystal structures (Figure 1), all ***t*-M** have Pt–M–Pt trinuclear structures where each metal is bridged by two piam ligands in a *trans* fashion.

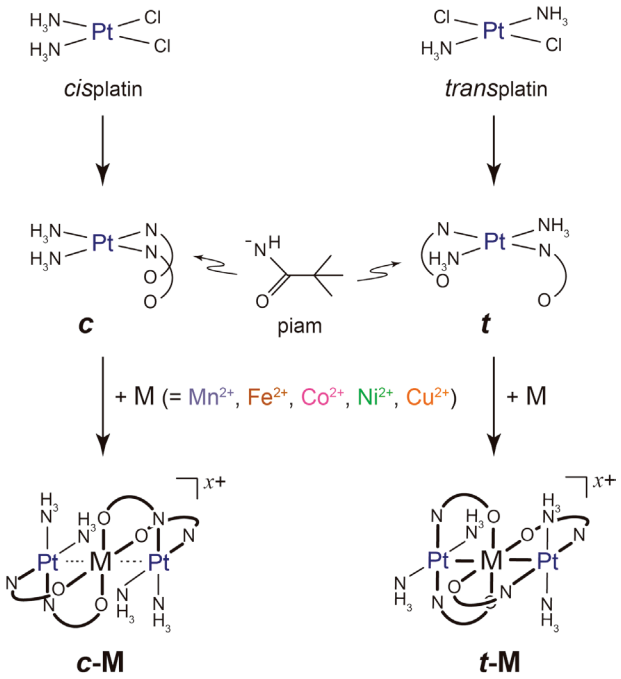

Scheme 2. Synthetic routes for ***c*-M** or ***t*-M** from cisplatin or transplatin, respectively.

Table 1. Crystallographic Data and Structure Refinements for *trans*-$[Pt_2Mn(piam)_4(NH_3)_4](ClO_4)_2$ (***t*-Mn**), *trans*-$[Pt_2Fe(piam)_4(NH_3)_4](ClO_4)_3$ (***t*-Fe**), *trans*-$[Pt_2Co(piam)_4(NH_3)_4](ClO_4)_2$ (***t*-Co**), *trans*-$[Pt_2Ni(piam)_4(NH_3)_4](ClO_4)_2$ (***t*-Ni**), and *trans*-$[Pt_2Cu(piam)_4(NH_3)_4](ClO_4)_2$ (***t*-Cu**).

	***t*-Mn**	***t*-Fe**
Empirical formula	$C_{20}H_{52}Cl_2MnN_8O_{12}Pt_2$	$C_{20}H_{52}Cl_3FeN_8O_{17}Pt_2$
Formula weight	1112.71	1229.07
Crystal system	Monoclinic	Monoclinic
Space group	$P2_1/n$	$P2_1/n$
a (Å)	13.2360(2)	14.7233(5)
b (Å)	13.5100(2)	18.3508(4)
c (Å)	21.3811(4)	16.5226(6)
α (°)	90	90
β (°)	97.383(2)	96.804(4)
γ (°)	90	90
V (Å^3)	3791.63(11)	4432.7(2)
Z	4	4
Temperature (K)	293	293
Dc (Mgm^{-3})	1.949	1.842
absorption coefficient (mm^{-1})	7.889	6.867
F(000)	2156	2388
crystal size (mm^3)	0.35 × 0.35 × 0.45	0.30 × 0.45 × 0.65
measured reflections	49880	58270
Independent reflections	8651 [R_{int} = 0.0395]	9990 [R_{int} = 0.0512]
Goodness-of fit on F^2	0.789	1.091
R [$I > 2\sigma(I)$]	R_1 = 0.0259, wR_2 = 0.0873	R_1 = 0.0474, wR_2 = 0.1346
R (all data)	R_1 = 0.0306, wR_2 = 0.0941	R_1 = 0.0729, wR_2 = 0.1601

***t*-Co**	***t*-Ni**	***t*-Cu**
$C_{20}H_{52}Cl_2CoN_8O_{12}Pt_2$	$C_{20}H_{52}Cl_2NiN_8O_{12}Pt_2$	$C_{20}H_{52}Cl_2CuN_8O_{12}Pt_2$
1116.70	1116.48	1121.31
Monoclinic	Monoclinic	Monoclinic
$P2_1/n$	$P2_1/n$	$P2_1/n$
13.1881(3)	13.1777(3)	13.1426(3)
13.4219(2)	13.3873(2)	13.4285(2)
21.3054(4)	21.2913(4)	21.3925(4)
90	90	90
96.842(2)	96.824(2)	97.106(2)
90	90	90
3744.40(12)	3729.47(12)	3746.46(12)
4	4	4
293	293	293
1.981	1.988	1.988
8.095	8.187	8.215
2164	2168	2172
0.30 × 0.40 × 0.40	0.15 × 0.30 × 0.40	0.15 × 0.23 × 0.30
49695	49317	50244
8560 [R_{int} = 0.0345]	8575 [R_{int} = 0.0337]	8612 [R_{int} = 0.0378]
0.831	0.836	0.817
R_1 = 0.0267, wR_2 = 0.0929	R_1 = 0.0248, wR_2 = 0.0935	R_1 = 0.0274, wR_2 = 0.0904
R_1 = 0.0313, wR_2 = 0.0988	R_1 = 0.0308, wR_2 = 0.1015	R_1 = 0.0342, wR_2 = 0.1016

Crystal Structures of *trans*-[$Pt_2M(piam)_4(NH_3)_4$]$(ClO_4)_x$.

Figure 1 shows the crystal structure of *trans*-[$Pt_2Mn(piam)_4(NH_3)_4$]$(ClO_4)_2$ (***t*-Mn**). The Mn ions are sandwiched between two Pt atoms, where four piam ligands are bridged in a *trans* fashion, resulting in linear Pt–Mn–Pt alignment (Figure 1a). The Pt–Mn distances are Pt(1)–Mn(1) = 2.6799(5) Å and Mn(1)–Pt(2) = 2.6801(5) Å. The coordination environments for both sides of the Pt atoms are planar and stacked on the Mn coordination plane in a face-to-face manner (Figure 1b). The NH_3 ligands coordinated to Pt atoms are hydrogen bonded to the oxygen atoms of the piam ligands with a distance of 3.0 Å between the atoms. A significant feature of ***t*-Mn** is that each trinuclear complex is dimerized to Pt(1)–Mn(1)–Pt(2)···Pt(2′)–Mn(1′)–Pt(1′) with Pt(2)···Pt(2′) at a distance of 3.8118(5) Å, where ClO_4^- anions are bridged with hydrogen bonds to NH_3 and nitrogen atoms of piam. The outer Pt(1) atoms do not interact with other metals, but are in close contact with the carbon atoms of the piam ligand in the neighboring Pt–Mn–Pt···Pt–Mn–Pt hexamer with perpendicular relationships (Figure 1d).

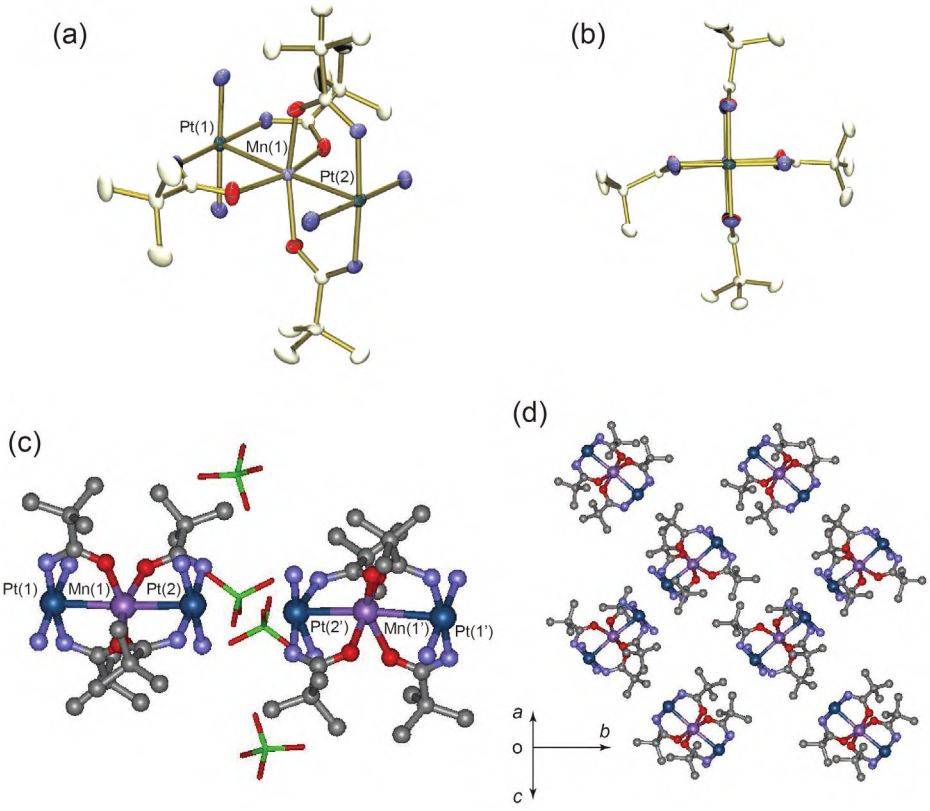

Figure 1. Molecular structure of (a) *trans*-[$Pt_2Mn(piam)_4(NH_3)_4$]$(ClO_4)_2$ (***t*-Mn**). (b) View along the metal–metal bonds. (c) Packing view of two trinuclear complexes with ClO_4^- anions. (d) Packing structure. The hydrogen atoms are omitted for clarity.

As shown in Figure 2, *trans*-$[Pt_2Fe(piam)_4(NH_3)_4](ClO_4)_3 \cdot H_2O$ (***t*-Fe**), *trans*-$[Pt_2Co(piam)_4(NH_3)_4](ClO_4)_2$ (***t*-Co**), *trans*-$[Pt_2Ni(piam)_4(NH_3)_4](ClO_4)_2$ (***t*-Ni**), and *trans*-$[Pt_2Cu(piam)_4(NH_3)_4](ClO_4)_2$ (***t*-Cu**) also formed trinuclear structures aligned with Pt–M–Pt. In all five compounds, there were two crystallographically independent Pt atoms. The Pt–M distances are ***t*-Fe**: Pt(1)–Fe(1) = 2.5909(9) Å and Fe(1)–Pt(2) = 2.5983(9) Å, ***t*-Co**: Pt(1)–Co(1) = 2.6193(5) Å and Co(1)– Pt(2) = 2.6236(5) Å, ***t*-Ni**: Pt(1)–Ni(1) = 2.5850(5) Å and Ni(1)–Pt(2) = 2.5892(5) Å, and ***t*-Cu**: Pt(1)–Cu(1) = 2.6575(5) Å and Cu(1)–Pt(2) = 2.6495(5) Å. In addition to ***t*-Mn**, each trinuclear complex is dimerized to Pt(1)–M(1)–Pt(2)···Pt(2′)–M(1′)–Pt(1′), with Pt(2)···Pt(2′) distances of 3.8688(5) Å (***t*-Co**), 3.9584(5) Å (***t*-Ni**), and 3.8475(5) Å (***t*-Cu**). In ***t*-Fe**, Pt atoms do not interact with each other in the crystal (Figure 2a), where the Pt(2)···Pt(1′) distances are 6.0154(5) Å. Considering the chemical formula ***t*-Fe**, the sum of the metal oxidation states of Pt–Fe–Pt is +7, which is probably because the additional surrounding anions present as a result of the higher cationic charge in the trinuclear complex hinders the dimerization. Because Pt(+3) complexes favor axial coordination with anions,[41-47] the formal oxidation states are Pt(+2)–Fe(+3)–Pt(+2). Although Fe(+2) was used as the starting material, iron atoms were easily oxidized to Fe(+3) during the reaction to trinuclear complexes, which are similar to *cis*-$[Pt_2Fe(piam)_4(NH_3)_4]^{3+}$.[48,49] In contrast, in ***t*-Mn**, ***t*-Co**, ***t*-Ni**, and ***t*-Cu**, the formal oxidation states are Pt(+2)–M(+2)–Pt(+2), which are unchanged from the original compounds during the reaction. Even if trinuclear Pt–M–Pt complexes are cationic +2, and four hydrogen bond donor ligands, NH (piam) and NH_3, are coordinated at the end, Pt atoms tend to obstruct the Pt···Pt interaction and dimerization is realized in the crystal (Figures 1c and 2b–d).

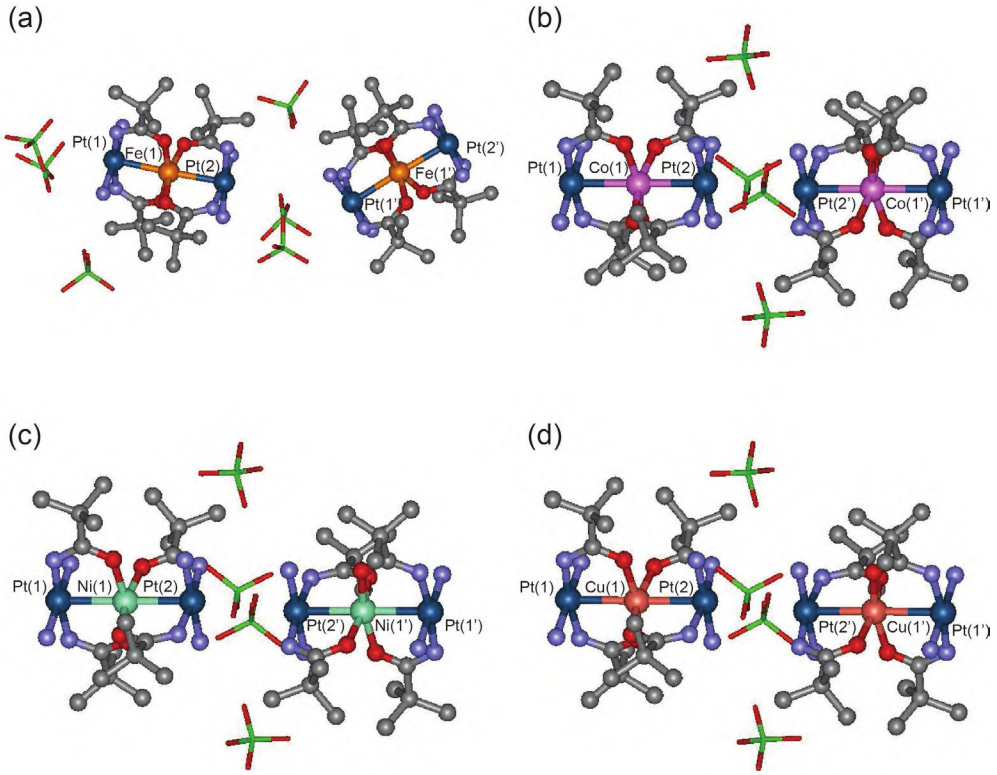

Figure 2. Packing view of two trinuclear complexes with ClO_4^- anions for (a) *trans*-$[Pt_2Fe(piam)_4(NH_3)_4](ClO_4)_3 \cdot H_2O$ (***t*-Fe**), (b) *trans*-$[Pt_2Co(piam)_4(NH_3)_4](ClO_4)_2$ (***t*-Co**), (c) *trans*-$[Pt_2Ni(piam)_4(NH_3)_4](ClO_4)_2$ (***t*-Ni**), and (d) *trans*-$[Pt_2Cu(piam)_4(NH_3)_4](ClO_4)_2$ (***t*-Cu**). The hydrogen atoms and water molecules are omitted for clarity.

Table 2 summarizes the metal–metal distances and angles between *cis*-$[Pt_2M(piam)_4(NH_3)_4](X)_x$ (***c*-M**, x = 2 or 3, X = ClO_4^- or PF_6^-)[35,37,38,48,49] and ***t*-M**. In *cis*-$[Pt_2Mn(piam)_4(NH_3)_4](PF_6)_2$ (***c*-Mn**), the asymmetric unit consists of two Pt–Mn–Pt molecules, where one Mn atom is tetrahedrally coordinated by four oxygen atoms in the piam ligands, and the other is planarly coordinated.[38,48] However, in ***t*-Mn**, only one crystallographically independent Mn atom is planarly coordinated by four oxygen atoms, showing an octahedral coordination geometry with two axial Pt atoms. Among the 10 compounds, the Pt−M distances were found to be of the order ***c*-Cu** > ***c*-Co** > ***c*-Mn** > ***c*-Ni** ≈ ***c*-Fe** and ***t*-Mn** > ***t*-Cu** > ***t*-Co** > ***t*-Ni** ≈ ***t*-Fe**. In ***t*-M**, owing to the bridging in the *trans* fashion, the dihedral angles between the Pt and M coordination planes are approximately parallel, although those in ***c*-M** are 12–17°.[35,37,38,48,49] Although the angles of Pt–M–Pt for ***c*-Mn**, ***c*-Co**, ***c*-Ni**, and ***c*-Cu**, are 180°, those for other compounds are approximately 177°, showing a slight bending from the 1D axis. This is attributed to the asymmetry of the trinuclear structure due to the two crystallographically

independent Pt atoms. Microcrystals of ***t*-M** synthesized under similar reaction conditions were used for physical measurements, in which X-ray powder diffraction coincided well with those calculated from single-crystal X-ray analyses (Figure S1).

Table 2. Comparison of Selected Distances and Angles between *cis*-$[Pt_2Mn(piam)_4(NH_3)_4](PF_6)_2$ (***c*-Mn**), *cis*-$[Pt_2Fe(piam)_4(NH_3)_4](ClO_4)_3$ (***c*-Fe**), *cis*-$[Pt_2Co(piam)_4(NH_3)_4](PF_6)_2$ (***c*-Co**), *cis*-$[Pt_2Ni(piam)_4(NH_3)_4](ClO_4)_2$ (***c*-Ni**), *cis*-$[Pt_2Cu(piam)_4(NH_3)_4](PF_6)_2$ (***c*-Cu**), and *trans*-$[Pt_2M(piam)_4(NH_3)_4](ClO_4)_x$ (***t*-M**).

	Pt–M (Å)	Pt···Pt (Å)	Pt–M–Pt (°)	dihedral angles[a] (°)	ref
***c*-Mn**[b]	2.62666(18)	-	180.0	14.6	38
***c*-Fe**	2.5566(15), 2.5718(15)	-	176.40(7)	14.3, 14.6	49
***c*-Co**	2.6339(8)	-	180.0	15.0	37
***c*-Ni**	2.5870(4)	-	180.0	12.7	48
***c*-Cu**	2.6870(6)	-	180.0	16.6	35
***t*-Mn**	2.6799(5), 2.6801(5)	3.8118(5)	176.23(2)	1.5, 2.9	this work
***t*-Fe**	2.5909(9), 2.5983(9)	6.0154(5)	177.51(4)	0.1, 0.5	this work
***t*-Co**	2.6193(5), 2.6236(5)	3.8688(5)	177.66(2)	0.6, 2.1	this work
***t*-Ni**	2.5850(5), 2.5892(5)	3.9584(5)	177.84(2)	0.3, 1.6	this work
***t*-Cu**	2.6495(5), 2.6575(5)	3.8475(5)	177.72(2)	0.6, 1.7	this work

[a]Dihedral angles between Pt and M coordination planes. [b]Trinuclear complex with octahedrally coordinated Mn atoms is shown. In ***c*-Mn**, there are two kinds of trinuclear complex.

Oxidation and Spin States of *trans*-$[Pt_2M(piam)_4(NH_3)_4](ClO_4)_x$.

XPS measurements were performed to determine the metal oxidation states in ***t*-M** (Figure 3). The Pt $4f_{7/2}$ binding energy for ***t*** is 72.6 eV, which is closer to the previous compounds of $[Pt_2^{II,II}(en)_2(\alpha\text{-pyridonato})_2](NO_3)_2$ (73.1 eV; en = ethylenediamine) than $[Pt_2^{III,III}(NH_3)_4(\alpha\text{-pyrrolidonato})_2(NO_3)_2](NO_3)_2$ (74.6 eV).[50] As summarized in Table 3, both the Pt $4f_{7/2}$ and $4f_{5/2}$ binding energies for ***t*-Mn**, ***t*-Co**, ***t*-Ni**, and ***t*-Cu** are characteristic values for Pt(+2). By contrast, the Pt $4f_{7/2}$ binding energy for ***t*-Fe** is higher than 74.2 eV, which is closer to the value for Pt(+3). The Fe $2p_{1/2}$ and $2p_{3/2}$ binding energies are 725.2 and 711.6 eV, respectively, which are characteristic values for Fe(+3) as found in $Fe^{III}Cl_3$ ($2p_{3/2}$: 711.3 eV).[51] Considering the crystal structure, the oxidation state of ***t*-Fe** is Pt(+2)–Fe(+3)–Pt(+2), where the higher energy shift of Pt binding energies of ***t*-Fe** might be caused by charge fluctuation in the

Pt atoms originating from the close Pt–Fe(+3) contact. The M $2p_{3/2}$ binding energies for ***t*-M** are 641.8 eV (***t*-Mn**), 781.0 eV (***t*-Co**), 855.4 eV (***t*-Ni**), and 933.8 eV (***t*-Cu**), whereas the values of M $2p_{3/2}$ binding energies for ***t*-Mn**, ***t*-Co**, ***t*-Ni**, and ***t*-Cu** are closer to that of M(+2) than M(+1) or M(+3).[51-54] Consequently, based on the crystal structure and XPS results, the formal oxidation states are Pt(+2)–M(+2)–Pt(+2)···Pt(+2)–M(+2)–Pt(+2) for ***t*-M** (M = Mn, Co, Ni, and Cu), and is Pt(+2)–Fe(+3)–Pt(+2) for ***t*-Fe**.

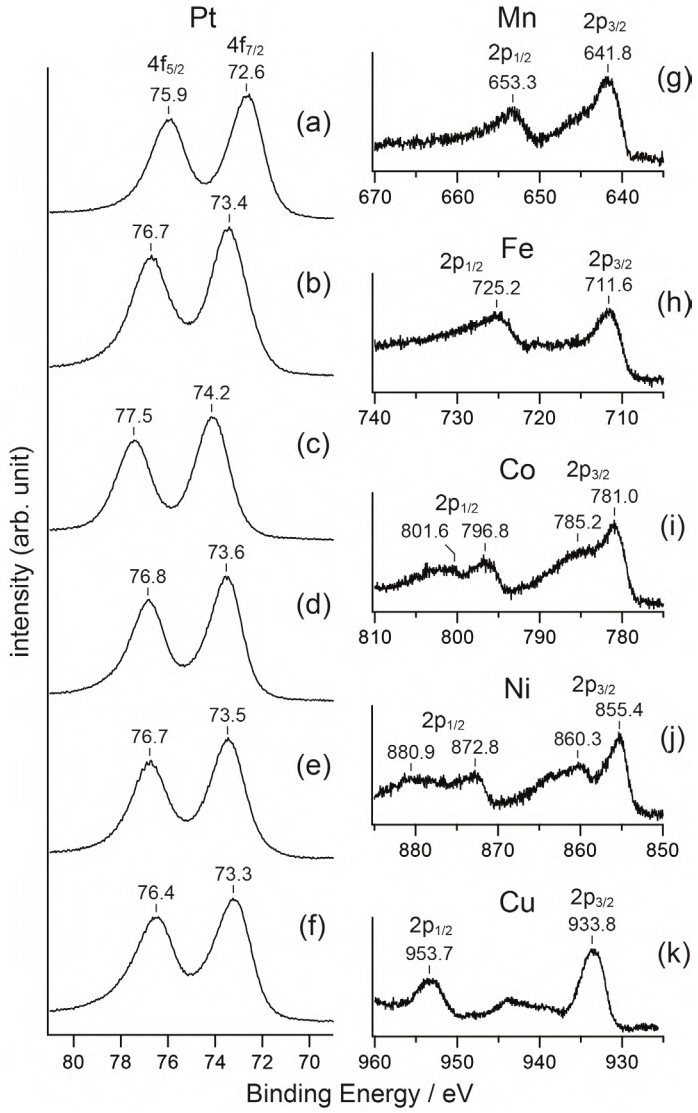

Figure 3. Pt $4f_{5/2}$ and $4f_{7/2}$ and M $2p_{1/2}$ and $2p_{3/2}$ core levels of XPS for (a) ***t***, (b) ***t*-Mn**, (c) ***t*-Fe**, (d) ***t*-Co**, (e) ***t*-Ni**, (f) ***t*-Cu**, (g) ***t*-Mn**, (h) ***t*-Fe**, (i) ***t*-Co**, (j) ***t*-Ni**, and (k) ***t*-Cu**.

Table 3. The Binding Energies (eV) for 4f of Pt and 2p of M in ***t*** and ***t*-M**.

	Pt $4f_{5/2}$	Pt $4f_{7/2}$	M $2p_{1/2}$	M $2p_{3/2}$
t	75.9	72.6	-	-
***t*-Mn**	76.7	73.4	653.3	641.8
***t*-Fe**	77.5	74.2	725.2	711.6
***t*-Co**	76.8	73.6	801.6, 796.8	785.2, 781.0
***t*-Ni**	76.7	73.5	880.9, 872.8	860.3, 855.4
***t*-Cu**	76.4	73.3	953.7	933.8

Although Pt(+2) atoms in ***t*-M** have a d^8 configuration being diamagnetic, Mn(+2), Fe(+3), Co(+2), Ni(+2), and Cu(+2) have d^5, d^5, d^7, d^8, and d^9 configurations, respectively, which have high-spin states that are paramagnetic. As mentioned in the section on magnetic susceptibilities, all five first-row transition metals in ***t*-M** have high-spin states, where unpaired electrons are localized on M atoms. To confirm these configurations, EPR measurements of powdered ***t*-Mn**, ***t*-Fe**, and ***t*-Cu** at 77 K or room temperature were conducted (Figure 4). The EPR spectrum for ***t*-Mn** at 77 K shows an overlapping profile of two axial-type signals with g_1 = 8.07, g_2 = 4.83, g_3 = 2.80, and g_4 = 1.89 (Figure 4b). A large apparent g is observed when the zero-field splitting at the Mn atom is larger than the Zeeman effect,[55-57] which evidently indicates the Mn(+2) high-spin state. The observation of two kinds of signals is probably due to the dimerization of the trinuclear complex. In ***t*-Fe** at 77 K with a d^5 configuration at Fe(+3), the spectrum shows an axial-type signal with $g_\perp$ = 5.51 and $g_{//}$ = 1.96 (Figure 4d), which are also characteristic of high-spin Fe(+3).[58-61] Although it is difficult to observe the EPR signal for both ***t*-Co** and ***t*-Ni** at 77 K because the spin-lattice relaxation time is very short, it is possible to determine the spin-state by XPS profiles: high-spin Co(+2) or Ni(+2) normally exhibits a rather strong satellite at approximately 5 eV higher binding energy from the main peak.[54,62] As shown in Figure 3i, the Co $2p_{1/2}$ and $2p_{3/2}$ binding energies in ***t*-Co** are 796.8 and 781.0 eV with broad satellite peaks at 801.6 and 785.2 eV, indicating high-spin Co(+2).[62] Moreover, as shown in Figure 3j, Ni $2p_{1/2}$ and $2p_{3/2}$ binding energies in ***t*-Ni** are 872.8 and 855.4 eV with broad satellite peaks at 880.9 and 860.3 eV, indicating high-spin Ni(+2).[54] In ***t*-Cu** at room temperature, one electron is on the Cu(+2) atom. As shown in Figure 4f, the EPR spectrum is an axial-type signal with $g_{//}$ = 2.35 and $g_\perp$ = 2.07, without hyperfine splitting. The observed profile at $g_{//} > g_\perp$ is characteristic of the Cu $dx^2–y^2$ spin.[32-34, 63-66] Consequently, hexanuclear ***t*-Mn**, ***t*-Co**, ***t*-Ni**,

and ***t*-Cu** have high-spin M in Pt–M–Pt···Pt–M–Pt, where five, three, two, and one unpaired electrons lie on M, respectively.

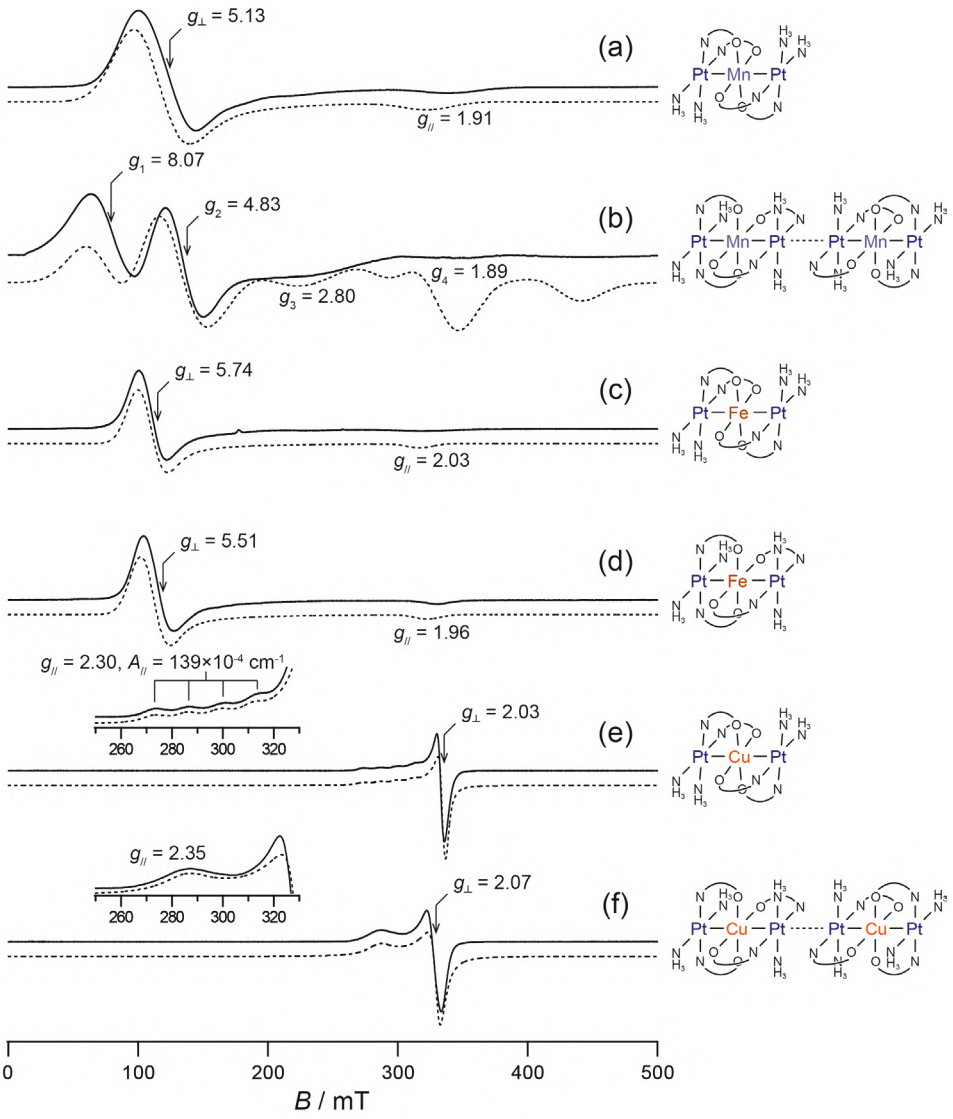

Figure 4. Continuous wave EPR spectra for powder samples of (a) ***c*-Mn**, (b) ***t*-Mn**, (c) ***c*-Fe**, and (d) ***t*-Fe** at 77 K and (e) ***c*-Cu** and (f) ***t*-Cu** at room temperature. Experimental settings: microwave frequency, (a) 9.0661, (b) 9.0577, (c) 9.0706, (d) 9.0573, (e) 9.4471, and (f) 9.4473 GHz; microwave power, 6 mW; and field modulation, 0.2 mT. Dotted lines are simulation calculated using the EasySpin software.

Electronic Structures of *trans*-[$Pt_2M(piam)_4(NH_3)_4$](ClO_4)$_x$.

The model structures *trans*-[$Pt_2M(NHCOCH_3)_4(NH_3)_4$]$^{x+}$ (**M**, x = 2, M = Mn, Co, Ni, and Cu; x = 3, M = Fe) were calculated to obtain the electronic structures (Figure S2). The metal–metal distances and related angles between the crystal structures and optimized results coincide well, where Highest Occupied Molecular Orbital (HOMO), Lowest Unoccupied

Molecular Orbital (LUMO), and neighboring molecular orbitals are around metals, especially in M. The σ-type orbitals overlapped with the three dz^2 orbitals of Pt–M–Pt with two nodes observed in **Mn**: α-HOMO–1 and β-LUMO (Figure S2a), **Fe**: α-HOMO–3 and β-LUMO (Figure S2b), **Co**: α-HOMO–3 and β-LUMO (Figure S2c), **Ni**: α-HOMO–3 and β-LUMO+1 (Figure S2d), and **Cu**: α-HOMO–3 and β-LUMO (Figure 5), which indicates that the dz^2 orbital of the first-row transition metal is electronically coordinated to both sides of the filled dz^2 orbitals on Pt atoms for each M. Figure 5 shows the energy diagrams for the molecular orbitals of **Cu** with schematic σ-type orbitals. When three dz^2 orbitals of two Pt atoms and one Cu atom overlapped along the z axis, three molecular orbitals with bonding–bonding, bonding–antibonding, and antibonding–antibonding relationships were expected, where those with many nodes become energetically higher. As shown in Figure 5 (left panel), the energetically higher σ-type orbitals with two nodes are found in α-HOMO–3 and β-LUMO, whereas Cu dx^2–y^2 orbitals are mainly occupied in both α- and β-HOMO. Considering that the σ-type orbitals with two nodes are found in both α-filled and β-vacant orbitals, those in **Cu** are half-filled orbitals, with results that were similar to those observed in other models such as **Mn**, **Fe**, **Co**, and **Ni** (Figure S2).

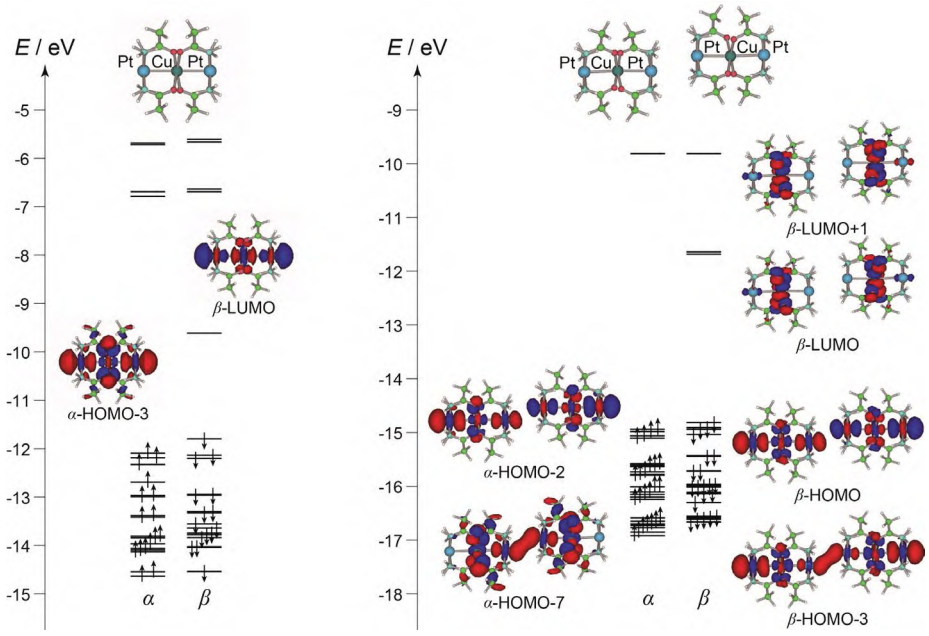

Figure 5. Results of DFT calculation of *trans*-$[Pt_2Cu(NHCOCH_3)_4(NH_3)_4]^{2+}$ (**Cu**) and $\{$*trans*-$[Pt_2Cu(NHCOCH_3)_4(NH_3)_4]\}_2^{4+}$ (**Cu$_2$**).

As shown in Figures 1 and 2, trinuclear complexes dimerize in ***t*-Mn**, ***t*-Co**, ***t*-Ni**, and ***t*-Cu**. Therefore, the dimerized $\{trans\text{-}[Pt_2M(NHCOCH_3)_4(NH_3)_4]\}_2^{4+}$ (**M_2**, M = Mn, Co, Ni, and Cu) based on the crystal structures of ***t*-M** were also calculated under frozen conditions of metals and coordinated atoms to obtain optimized structures (Figures S3). In the four models, σ-type orbitals over the six metals constructed with antibonding–antibonding and antibonding–antibonding are observed in **Mn_2**: *α*-HOMO–2, *α*-HOMO–3, *β*-LUMO, and *β*-LUMO+1 (Figure S3a); **Co_2**: *α*-HOMO, *α*-HOMO–5, *β*-LUMO, and *β*-LUMO+3 (Figure S3b); **Ni_2**: *α*-HOMO–4, *α*-HOMO–7, *β*-LUMO, and *β*-LUMO+1 (Figure S3c); and **Cu_2**: *α*-HOMO–2, *α*-HOMO–3, *β*-HOMO, and *β*-HOMO–3 (Figure S3d), where half-filled σ-type orbitals found in monomer M are further connected with metal–metal bonds to afford two stabilized and destabilized σ-type orbitals. Consequently, the dimerization is attributed to the half-filled σ-type orbitals over Pt–M–Pt, in which electronic coordination between Pt and M is realized in a face-to-face manner with bridging in the *trans* fashion. Figure 5 (right panel) shows the energy diagrams for molecular orbitals of **Cu_2** with schematic σ-type orbitals. Interestingly, the σ-type orbital of *β*-LUMO found in **Cu** is stabilized as *β*-HOMO and *β*-HOMO–3 in **Cu_2**, due to admixing of the Cu $dx^2–y^2$ orbitals.

Comparison of EPR spectra between ***c*-M** and ***t*-M** would provide information on the difference in electronic structures caused by dimerization. As mentioned previously, ***t*-Fe** and ***c*-Fe** trinuclear complexes do not dimerize; both EPR spectra were similar and characteristic for high-spin Fe(+3) (Figure 4c and 4d). Conversely, although the spectrum for ***c*-Mn** shows a single axial-type signal influenced by the ZFS effect, the spectrum for ***t*-Mn** contained two types of axial signals, the splitting of which is caused by dimerization. By contrast, the spectra for both ***c*-Cu** and ***t*-Cu** show axial-type signals, which are characteristic of Cu $dx^2–y^2$ spins. Although the *g* values are similar, ***c*-Cu**: $g_{//} = 2.30$ and $g_{\perp} = 2.03$, ***t*-Cu**: $g_{//} = 2.35$, and $g_{\perp} = 2.07$, the degree of hyperfine coupling is different between ***c*-Cu** and ***t*-Cu**. As shown in Figure 4e, the spectrum of powdered ***c*-Cu** showed $A_{//} = 139 \times 10^{-4}$ cm^{-1}. By contrast, in ***t*-Cu**, there is no obvious splitting in the region of parallel absorption, with $A_{//} \approx 0$ cm^{-1} (Figure 4f). Based on the EPR parameters, it is possible to estimate the α^2-value, which evaluates the unpaired electron density on the d-orbital of Cu(+2) ions, using the following equation:[67]

$$\alpha^2 = A_{//}/P + (g_{//} - 2) + (3/7)(g_{\perp} - 2) + 0.04$$

where P is 0.036 cm^{-1} and A is a hyperfine term. The bonding parameter α is a measure of the covalency of the in-plane σ bonding, where a value of $\alpha^2 = 1$ denotes a complete ionic character.[67] According to the aforementioned equation, α^2 values are 0.74 (***c*-Cu**) and 0.42 (***t*-Cu**), which indicate that the electron density of Cu(+2) in ***t*-Cu** is lower than that of ***c*-Cu**. These results revealed that the spin density of Cu dx^2–y^2 decreased and was influenced by both sides of the Pt atoms. This trend was also found in the results of the DFT calculations, where the β-HOMO in **Cu2** is formed by the admixture of Cu dx^2–y^2 and both sides of the Pt dz^2 orbitals.

Stabilities of Dimerized Structures {*trans*-[$Pt_2M(piam)_4(NH_3)_4]_2$}$^{4+}$ in the Solvent.

Compounds ***t*-M** were soluble in polar organic solvents. Figure 6 shows the UV–vis spectra of the 3.0 mM MeCN solution containing ***t*-M** and the diffuse reflectance spectra of ***t*-M** with the results of TD-DFT calculations. As shown in Figure 6a, the MeCN solution of ***t*-Mn** shows intense absorption around 200 nm with the shoulder at 250 and 293 nm. The spectrum of solid ***t*-Mn** showed a similar adsorption profile, where the shoulder was clearly observed at 302 nm. The results of the TD-DFT calculations for **Mn** show that the adsorption at 250 nm is caused by the transition from α-HOMO−1 to α-LUMO+4, indicating the transition from σ-type orbitals over the Pt−Mn−Pt to dz^2 orbitals on both sides of the Pt atoms. However, the result of **Mn2** shows that the adsorption around 300 nm is caused by the transition from α-HOMO–2 to α-LUMO and α-LUMO+3, which are involved with σ-type bonds along the z axis, attributed to the formation of the hexanuclear structure of Pt–Mn–Pt···Pt–Mn–Pt. In the spectra of the MeCN solution containing ***t*-Co**, ***t*-Ni**, and ***t*-Cu**, absorption peaks, which do not appear in the corresponding ***c*-M**, are observed at ***t*-Co**: 484 and 637 nm, ***t*-Ni**: 459 and 815 nm, and ***t*-Cu**: 845 and 1466 nm. These adsorption peaks also appeared in the diffuse reflectance spectra. In particular, in ***t*-Cu**, the intense peaks at 845 and 1466 nm coincide well with those of the powdered sample, which are assigned to β-HOMO–1/–2 to β-LUMO/+1 and β-HOMO/–3 to β-LUMO/+1, respectively. Considering that β-HOMO and β-HOMO–3 are σ-type orbitals over Pt–Cu–Pt···Pt–Cu–Pt (Figure 5), which are characteristic of hexanuclear structures, the obvious adsorption at 1466 nm proves the maintenance of dimerization in MeCN. Figure 7 shows ESI–MS spectra of the MeOH solution containing ***t*-Mn**, ***t*-Co**, ***t*-Ni**, or ***t*-Cu**. In all four compounds, the peaks attributed to dimerized structures were observed at m/z = 2126 for $\{[Pt_2Mn(piam)_4(NH_3)_4]_2(ClO_4)_3\}^+$ (Figure 7a), 2133 for $\{[Pt_2Co(piam)_4(NH_3)_4]_2(ClO_4)_3\}^+$

(Figure 7b), 2133 for $\{[Pt_2Ni(piam)_4(NH_3)_4]_2(ClO_4)_3\}^+$ (Figure 7c), and 2143 for $\{[Pt_2Cu(piam)_4(NH_3)_4]_2(ClO_4)_3\}^+$ (Figure 7d), which also supports dimerization in solvents.

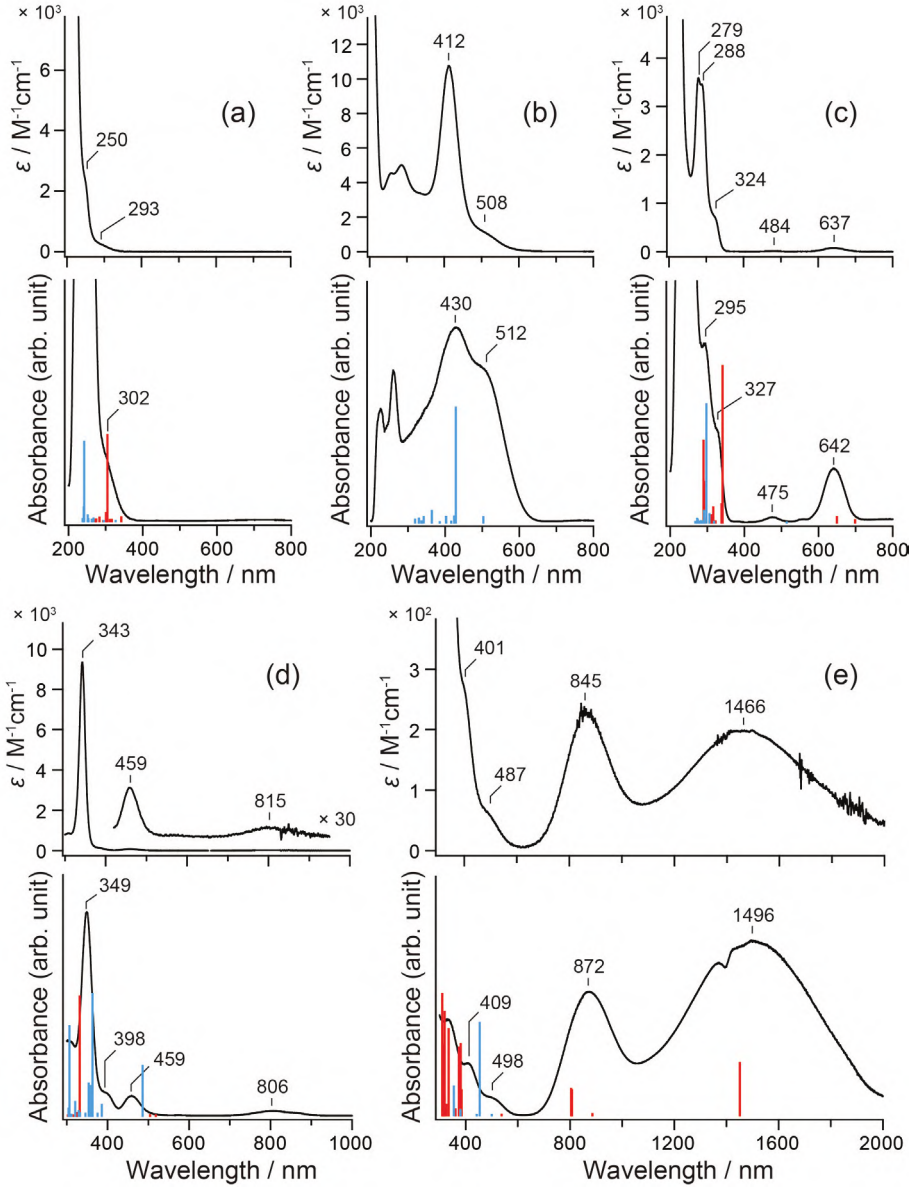

Figure 6. UV−vis spectra (upper) of 3.0 mM MeCN solution and diffuse reflectance spectra (bottom) with MgO for (a) ***t*-Mn**, (b) ***t*-Fe**, (c) ***t*-Co**, (d) ***t*-Ni**, and (e) ***t*-Cu** at room temperature. Blue and red bars show the result of TD-DFT calculations based on **M** and **M2** structures, respectively.

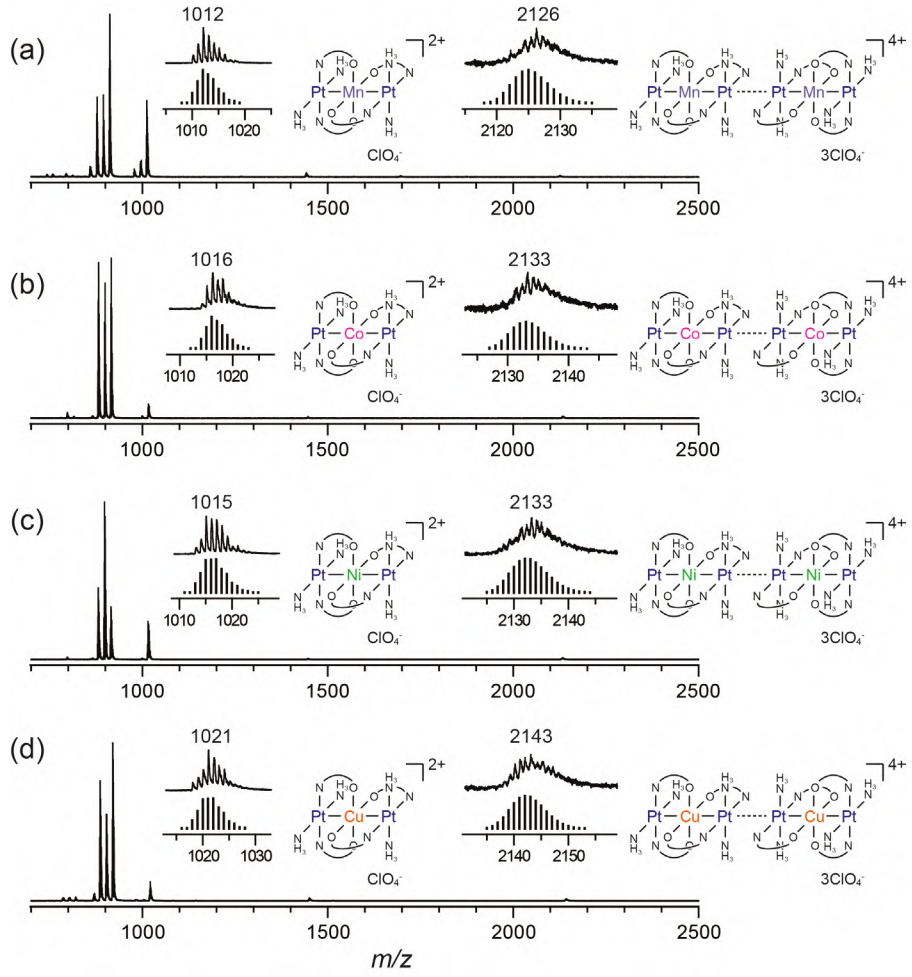

Figure 7. ESI-MS (positive) spectra for (a) ***t*-Mn**, (b) ***t*-Co**, (c) ***t*-Ni**, and (d) ***t*-Cu** measured by dilution in MeOH. Selected peaks are simulated with isotope patterns as bars.

A brief summary of the difference between ***c*-M** and ***t*-M** in solvents shows whether the trinuclear complex is dimerized or not, where ***t*-Mn**, ***t*-Co**, ***t*-Ni**, and ***t*-Cu** formed hexanuclear structures aligned as Pt–M–Pt···Pt–M–Pt. Figure 8 shows the cyclic voltammetry for ***c*-M** and ***t*-M** recorded in MeCN solutions containing 0.1 M Bu_4NPF_6 or Bu_4NClO_4 as a supporting electrolyte. The voltammograms for both ***c*-Cu** and ***t*-Cu** showed no oxidation waves, indicating the difficulties in oxidizing under these conditions. Meanwhile, the voltammograms for other ***c*-M** showed one oxidation wave at $E = 0.13$ V (***c*-Mn**), –0.14 V (***c*-Fe**), 0.54 V (***c*-Co**), and 0.74 V (***c*-Ni**), which was attributed to one-electron oxidation as follows, Pt–M(+2)–Pt → Pt–M(+3)–Pt.

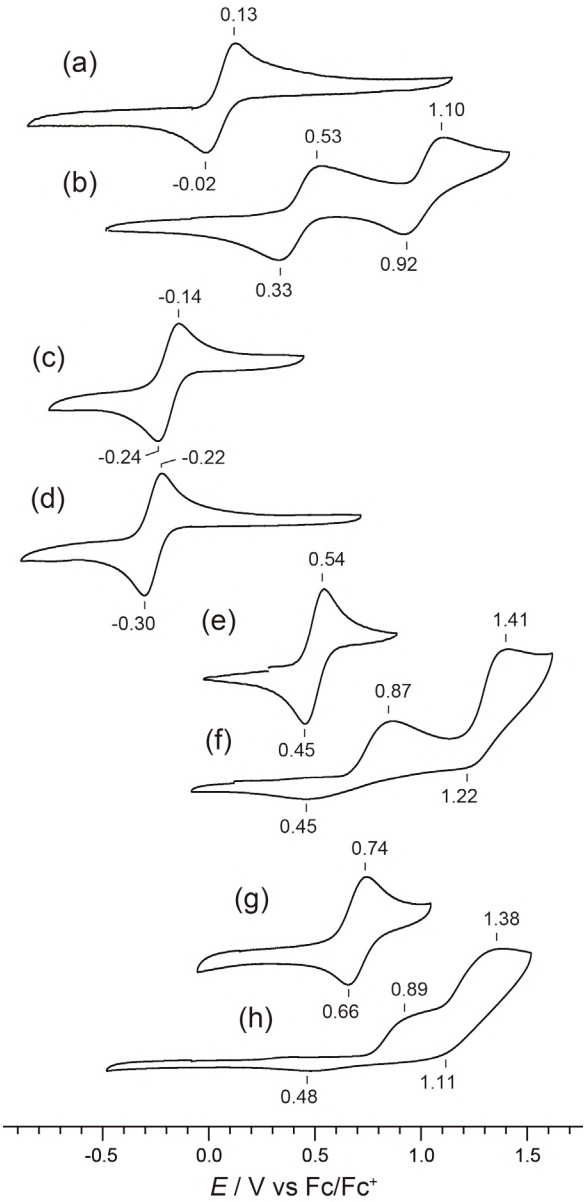

Figure 8. Cyclic voltammograms of 1 mM (a) ***c*-Mn**, (b) ***t*-Mn**, (c) ***c*-Fe**, (d) ***t*-Fe**, (e) ***c*-Co**, (f) ***t*-Co**, (g) ***c*-Ni**, and (h) ***t*-Ni** in MeCN with 0.1 M supporting electrolyte (scan rate 100 mV/s). Electrode potentials were converted to those relative to Fc/Fc^+.

By contrast, in ***t*-Mn**, ***t*-Co**, and ***t*-Ni**, two oxidation waves were observed, which are undoubtedly due to dimerization. In ***t*-Mn**, ***t*-Co**, and ***t*-Ni**, two oxidation waves were observed at $E = 0.53$ and 1.10 V, $E = 0.87$ and 1.41 V, and $E = 0.89$ and 1.38 V, respectively. Thus, ***t*-Mn**, ***t*-Co**, and ***t*-Ni** showed a two-step oxidation process, Pt–M(+2)–Pt···Pt–M(+2)–Pt → Pt–M(+3)–Pt···Pt–M(+2)–Pt → Pt–M(+3)–Pt···Pt–M(+3)–Pt, involving mixed valencies. Compared to the oxidation potential of 0.13 (***c*-Mn**), 0.54 (***c*-Co**), and 0.74 V (***c*-Ni**), those of corresponding ***t*-M** are 0.1–0.4 V higher, indicating that the energy levels of HOMO in ***t*-M** are

more stable than those in ***c*-M**. As mentioned earlier, only ***t*-Fe** does not dimerize, and the redox wave shows a single step at $E_{1/2}$ = –0.26 V. Although two reversible oxidation and reduction waves were observed in ***t*-Mn** (Figure 8b), the reduction wave in both ***t*-Co** (Figure 8f) and ***t*-Ni** (Figure 8h) was ambiguous indicating irreversibility, which is probably due to the dissociation of dimerized structures. In both ***c*-M** and ***t*-M**, the Mn(+2), Fe(+3), Co(+2), and Ni(+2) have high-spin d^5, d^5, d^7, and d^8 configurations, respectively. The oxidation potentials found in ***c*-M** and ***t*-M** tend to increase as follows: $d^5 < d^7 < d^8$, indicating that HOMOs are energetically stabilized, which is due to spin-pairing effects.[68] Furthermore, the oxidation potentials of ***t*-Mn**, ***t*-Co**, and ***t*-Ni** are higher than those of the corresponding ***c*-M**, revealing that HOMOs for ***t*-M** are energetically more stable than ***c*-M**, which are probably due to the coordination environments of M being closer to the octahedral structure.

Magnetic Behaviors of *trans*-[$Pt_2M(piam)_4(NH_3)_4$](ClO_4)$_x$.

The temperature-dependent magnetic susceptibilities of powdered samples of ***t*-M** measured from 2 to 300 K are shown in Figure 9, with the previous results for ***c*-M**.[37,38,49,69] The χT values in ***t*-M** at 300 K are 3.90 (***t*-Mn**), 4.34 (***t*-Fe**), 2.51 (***t*-Co**), 1.05 (***t*-Ni**), and 0.43 (***t*-Cu**) cm^3 K mol^{-1} (Figure 9f–j), which are close to the theoretical values for high-spin Mn(+2) and Fe(+3) (S = 5/2, 4.37 cm^3 K mol^{-1}), Co(+2) (S = 3/2, 1.87 cm^3 K mol^{-1}), Ni(+2) (S = 1, 1.00 cm^3 K mol^{-1}), and Cu(+2) (S = 1/2, 0.37 cm^3 K mol^{-1}), respectively. The larger χT value of ***t*-Co** than the theoretical value is consistent with a significant orbital contribution to susceptibility, which is common for Co(+2) complexes.[70,71] As shown in Figure 9, the χT values at 300 K for ***t*-M** are similar to those for ***c*-M**. The χT values in ***t*-Mn**, ***t*-Co**, and ***t*-Ni** gradually decreased significantly below 50, 80, and 95 K, reaching 0.29, 0.03, and 0.01 cm^3 K mol^{-1} at 2 K, respectively. However, the χT values in ***t*-Fe** plateaued until 20 K and decreased to 2.40 cm^3 K mol^{-1} at 2 K, whereas those of ***t*-Cu** plateaued over the temperature range investigated. The data for ***t*-Mn**, ***t*-Co**, and ***t*-Ni** follow the Curie−Weiss law (Figure S4), with Weiss constants of θ = −8.00, −24.8, and −19.3 K, respectively (Table 4), where negative θ values indicate antiferromagnetic coupling between the M(+2) ions. Furthermore, the plots of χ versus T for ***t*-Mn**, ***t*-Co**, and ***t*-Ni** show maxima at 9, 13, and 24 K, respectively (Figure 10), supporting the antiferromagnetic coupling, although those of ***c*-M**, ***t*-Fe**, and ***t*-Cu** were inversely proportional to temperature (Figure S4). Considering the crystal structures, the antiferromagnetic

interactions found in ***t*-Mn**, ***t*-Co**, and ***t*-Ni** are attributed to dimerized structures of Pt–M–Pt···Pt–M–Pt, where electronic coordination is expected through –Pt···Pt– bonds.

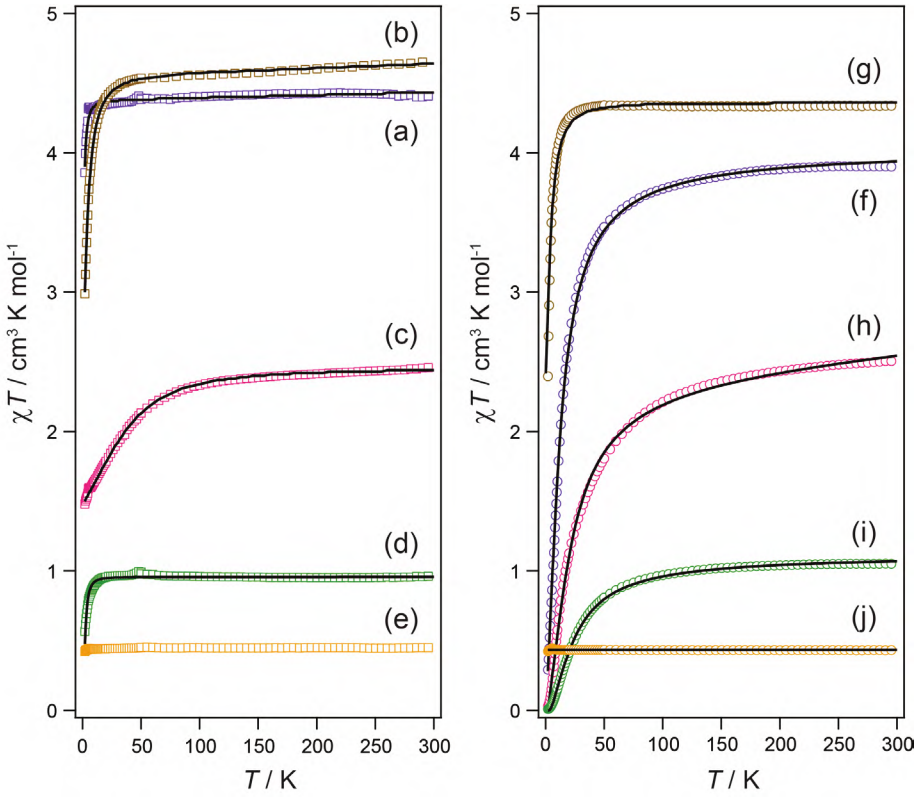

Figure 9. Temperature dependence of χT in (a) ***c*-Mn**, (b) ***c*-Fe**, (c) ***c*-Co**, (d) ***c*-Ni**, (e) ***c*-Cu**, (f) ***t*-Mn**, (g) ***t*-Fe**, (h) ***t*-Co**, (i) ***t*-Ni**, and (j) ***t*-Cu** per M ion. The solid line represents the theoretical fitting for (f, h–j) the molar susceptibility derived from $H = -2JS_1 \cdot S_2$ and (a–d, g) the axial ZFS model.

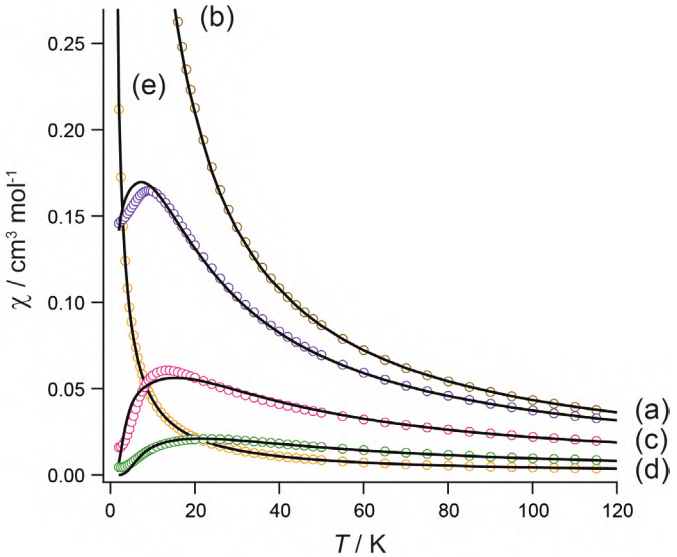

Figure 10. Temperature dependence of χ in (a) ***t*-Mn**, (b) ***t*-Fe**, (c) ***t*-Co**, (d) ***t*-Ni**, and (e) ***t*-Cu** per M ion. The solid line represents the theoretical fitting for (a, c–e) the molar susceptibility derived from $H = -2JS_1 \cdot S_2$ and (b) the axial ZFS model.

Table 4. Magnetic Parameters Estimated by Theoretical Fittings in ***c*-M** and ***t*-M**.

	C (cm^3 K mol^{-1})[a]	θ (K)[a]	D (cm^{-1})	zJ (cm^{-1})	$2J$ (cm^{-1})
***c*-Mn**	4.42	−0.40	1.21	-	-
***c*-Fe**	4.66	−1.73	5.43	-	-
***c*-Co**	2.53	−9.07	44.21	-	-
***c*-Ni**	0.95	0.89	5.54	-	-
***c*-Cu**	0.45	0.01	-	-	-
***t*-Mn**	4.02	−8.00	0.22	−1.7	−1.8
***t*-Fe**	4.34	−0.05	5.45	0.0	-
***t*-Co**	2.73	−24.8	0.40	−9.1	−7.0
***t*-Ni**	1.13	−19.3	0.38	−19.6	−14.6
***t*-Cu**	0.43	0.15	-	-	0.0

[a]Estimated from the Curie–Weiss law $\chi = C/(T - \theta)$.

As shown in Figure 9a−d, the χT values for ***c*-Mn**, ***c*-Fe**, ***c*-Co**, and ***c*-Ni** also decreased at lower temperatures, which are due to the ZFS for high-spin Mn(+2), Fe(+3), Co(+2), and Ni(+2). The experimental data were fitted to the expression for molar susceptibility with the axial ZFS parameter (D), and the best fit to the χT versus T curve gave ***c*-Mn**: g = 2.00 and D = 1.21 cm^{-1} (Figure S5a),[38] ***c*-Fe**: g = 2.04 and D = 5.43 cm^{-1} (Figure S6a),[49] ***c*-Co**: g = 2.29 and D = 44.2 cm^{-1} (Figure S7a),[37] and ***c*-Ni**: g = 1.96 and D = 5.54 cm^{-1} (Figure S8a), which are within the typical values for Mn(+2) S = 5/2, Fe(+3) S = 5/2, Co(+2) S = 3/2, and Ni(+2) S = 1. As shown in Figure 2a, the distances of Pt between Pt−Fe−Pt trinuclear complexes in ***t*-Fe** are 6.02 Å. Therefore, the assumption that the decrease of χT values for ***t*-Fe** in lower temperature regions is due to ZFS is valid. The best fit to the χT versus T curve gave g = 2.00 and D = 5.45 cm^{-1} (Figure S6b), which are similar to those of ***c*-Fe**.

To extract an approximate value for the antiferromagnetic intrachain exchange strength, J, in ***t*-Mn**, ***t*-Co**, and ***t*-Ni**, the data were fitted to the predictions for the model of a molecular field-corrected susceptibility equation to obtain an estimate of J. Based on the g and D simulated from the EPR results, the susceptibility data were fit to the theoretical prediction(Figure S5b, 7b, and 8b). The best fits were obtained for the values zJ = −1.6 (***t*-Mn**), −7.2 (***t*-Co**), and −19.3 cm^{-1} (***t*-Ni**), where z represents the number of the nearest paramagnetic atoms. These results indicated that the decreased χT values in lower-temperature regions are attributed not only to ZFS but also to antiferromagnetic couplings. However, as shown in Figures S5b, 7b, and 8b,

these theoretical predictions were slightly different from the experimental plots. Consequently, applying the susceptibility expression derived from the spin pair 5/2–5/2 for ***t*-Mn**, 3/2–3/2 for ***t*-Co**, 1–1 for ***t*-Ni**, and 1/2–1/2 for ***t*-Cu**, to the magnetic data coupled through an isotropic exchange interaction J (the Hamiltonian is written as: $H = -2JS_1 \cdot S_2$, Figures 9f, h–j) gave the exchange parameter $J = -0.9$ cm^{-1} (***t*-Mn**), −3.5 (***t*-Co**), and −7.3 cm^{-1} (***t*-Ni**), and 0.0 cm^{-1} (***t*-Cu**). In the case of ***t*-Cu**, the exchange interaction involved only one single occupied dx^2–y^2 orbital, which was dominated by the antiferromagnetic contribution to the J value, where the small overlapping of the d-orbitals resulted in a lower coordination. Conversely, in ***t*-Ni** as well as the dx^2–y^2 orbital, a single occupied dz^2 orbital contributed to the antiferromagnetic interaction, which resulted in a higher coordination (Scheme 3). The trend of magnitude, ***t*-Mn** < ***t*-Co** < ***t*-Ni**, is probably due to the ratio of single occupied d-orbitals, because the direction along the z axis is electronically coordinated, where the degree of overlap is as follows: dz^2 > dyz ≈ dzx > dxy ≈ dx^2–y^2.

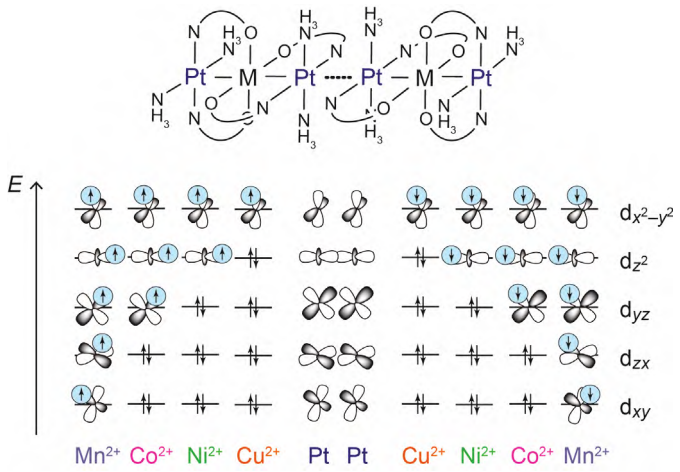

Scheme 3. Schematic d-orbital shapes for Pt and first transition metals found in ***t*-M**.

Figure 11 shows the plots of the 2J values against the M---M distances found in several 1D compounds in which high-spin Mn(+2) ions (Table S1),[38,72-94] Co(+2) ions (Table S2),[14,16,37,95-108] and Ni(+2) ions (Table S3)[14,16,109-117] are bridged by organic molecules or second metals. As a general trend, the strength of the interaction becomes weaker as the M---M distance becomes longer. Among the three groups, 1D compounds containing Ni(+2) tend to have relatively larger 2J values. There are many reports of azide bridged compounds showing a relatively strong antiferromagnetic interaction for the distance.[115-117] Conversely, there is no significant difference between the three groups with organic ligand molecules or halide ions.

Meanwhile, 1D compounds bridged by the second metals with metal–metal bonds appear to have stronger interactions, especially in Ni(+2) compounds, which are due to high populations of dz^2 spins as found in our system, ***t*-M**. The strongest compound in Figure 11 is $[PtNi(tba)_4(OH_2)]_2$ (tba = thiobenzoate) showing $2J = -120$ cm^{-1} in Ni---Ni = 8.2 Å,[14] where the dinuclear complex is dimerized and the distances of Ni–Pt and Pt···Pt are 2.570(1) and 3.0823(4) Å, respectively. Compared with this compound, the $2J$ value of ***t*-Ni** is small (−14.6 cm^{-1}), which may be attributed to the relatively longer Pt···Pt distance (3.9584(5) Å). However, it is a surprising result that the magnetic interaction was observed at a distance of 3.9584(5) Å. It is proposed therefore that a stronger interaction could be realized by removing the steric hindrance of the terminal ligands in ***t*-Ni**.

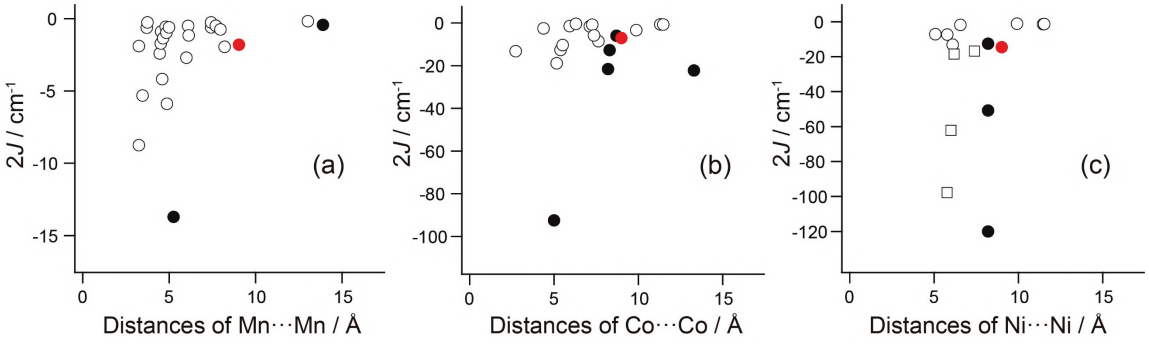

Figure 11. The comparison of $2J$ values (cm^{-1}) against distances (Å) of (a) Mn---Mn, (b) Co---Co, and (c) Ni---Ni in reported 1-D compounds, where each metal is bridged by organic molecules or halide ions (open circles), azide (open squares), or second metals (filled circles). Red filled circles indicate ***t*-M**. The J values were calculated from $H = -2JS_1S_2$.

Conclusions

In this study, trinuclear Pt–M–Pt (M = Mn, Fe, Co, Ni, and Cu) complexes bridged in a trans fashion were successfully synthesized from the amidate-hanging Pt mononuclear complex, *trans*-$[Pt(piam)_2(NH_3)_2]$, and characterized. Each trinuclear complex is dimerized in both solvents and solid with Pt···Pt interactions aligned as hexanuclear Pt–M–Pt···Pt–M–Pt with high-spin M. Thereby, the spin density was modified, which allowed for mixed valencies. Although relatively longer distances of unbridged Pt···Pt (3.9 Å) were observed, significant antiferromagnetic interactions with lengths of approximately 9.0 Å were observed, which are caused by electronic coupling through –Pt···Pt– bonds, revealing fundamental insights for

magnetic interactions through metal–metal bonds. The *trans*-$[Pt_2M(piam)_4(NH_3)_4](ClO_4)_x$ does not infinitely extend with Pt···Pt interactions, probably because of the repulsion between the cationic charge and hydrogen atoms. Because it is possible to change and tune the ligands that are coordinated to metals, there is potential to align ligands along the *z* axis; hence, further synthesis of paramagnetic 1D chains is in progress.

Experimental Section

Materials. Potassium tetrachloroplatinate(II) was obtained from Tanaka Kikinzoku Co. Pivalonitrile was obtained from the Tokyo Chemical Industry Co. $Mn(ClO_4)_2 \cdot 6H_2O$, $Co(ClO_4)_2 \cdot 6H_2O$, and $NaClO_4$ were obtained from Wako Co. $Fe(ClO_4)_2 \cdot 6H_2O$ and $CuCl_2 \cdot 2H_2O$ were obtained from Nacalai Tesque Co. $Ni(ClO_4)_2 \cdot 6H_2O$ was obtained from Aldrich Chemical Co. *trans*-$[PtCl_2(NH_3)_2]$ was synthesized according to a previously reported procedure.[118] *cis*-$[Pt_2Mn(piam)_4(NH_3)_4](PF_6)_2$ (***c*-Mn**),[38] *cis*-$[Pt_2Fe(piam)_4(NH_3)_4](ClO_4)_3$ (***c*-Fe**),[48,49] *cis*-$[Pt_2Co(piam)_4(NH_3)_4](PF_6)_2$ (***c*-Co**),[37] *cis*-$[Pt_2Ni(piam)_4(NH_3)_4](ClO_4)_2$ (***c*-Ni**),[48] and *cis*-$[Pt_2Cu(piam)_4(NH_3)_4](PF_6)_2$ (***c*-Cu**)[35] were synthesized according to a previously reported procedure.

Synthesis of *trans*-$[Pt(piam)_2(NH_3)_2]$ (*t*)

An aqueous solution (75 mL) containing *trans*-$[PtCl_2(NH_3)_2]$ (2.4 g, 8.0 mmol) and $AgClO_4$ (3.3 g, 16.0 mmol) was stirred for 16 h at room temperature under dark conditions, and the resulting AgCl was removed by filtration. The filtrate was mixed with pivalonitrile (3.5 mL, 32 mmol) and stirred for 24 h at room temperature. The resulting gray powder was collected by filtration, washed with water, and dried (4.3 g). The gray powder was treated with a 1 M aqueous NaOH solution (15 mL), and stirred for 2 days at room temperature. The resulting gray powder of *trans*-$[Pt(piam)_2(NH_3)_2]$ was collected by filtration, washed with water, and dried at room temperature for 24 h (3.1 g, 7.2 mmol). Yield: 90%. Elemental analysis calculated for $C_{10}H_{26}N_4O_2Pt$: C, 27.97; H, 6.10; N, 13.05%. Found: C, 26.01; H, 5.52; N, 12.50%.

Synthesis of *trans*-$[Pt_2Mn(piam)_4(NH_3)_4](ClO_4)_2$ (*t*-Mn)

The suspension of *trans*-$[Pt(piam)_2(NH_3)_2]$ (432 mg, 1.0 mmol) in MeOH (12 mL) was mixed with $Mn(ClO_4)_2 \cdot 6H_2O$ (362 mg, 1.0 mmol) and stirred for 9 h at room temperature. After removing the unreacted *trans*-$[Pt(piam)_2(NH_3)_2]$ by filtration, the solution was gently evaporated to obtain crystals of *trans*-$[Pt_2Mn(piam)_4(NH_3)_4](ClO_4)_2$ (486 mg). Yield: 87%. Elemental analysis calculated for $C_{20}H_{52}Cl_2MnN_8O_{12}Pt_2$: C, 21.59; H, 4.71; N, 10.07%. Found: C, 21.60; H, 4.90; N, 10.15%.

Synthesis of *trans*-$[Pt_2Fe(piam)_4(NH_3)_4](ClO_4)_3 \cdot H_2O$ (*t*-Fe)

The suspension of *trans*-[Pt(piam)$_2$(NH$_3$)$_2$] (346 mg, 0.8 mmol) in MeOH (10 mL) was mixed with Fe(ClO$_4$)$_2$·6H$_2$O (290 mg, 0.8 mmol) and stirred for 10 h at room temperature. After removing the unreacted *trans*-[Pt(piam)$_2$(NH$_3$)$_2$] by filtration, the solution was gently evaporated to obtain crystals of *trans*-[Pt$_2$Fe(piam)$_4$(NH$_3$)$_4$](ClO$_4$)$_3$ (412 mg). Yield: 85%. Elemental analysis calculated for $C_{20}H_{54}Cl_3FeN_8O_{17}Pt_2$: C, 19.51; H, 4.42; N, 9.10%. Found: C, 19.63; H, 4.44; N, 9.06%.

Synthesis of *trans*-[Pt$_2$Co(piam)$_4$(NH$_3$)$_4$](ClO$_4$)$_2$ (*t*-Co)

The suspension of *trans*-[Pt(piam)$_2$(NH$_3$)$_2$] (432 mg, 1.0 mmol) in MeOH (14 mL) was mixed with Co(ClO$_4$)$_2$·6H$_2$O (366 mg, 1.0 mmol) and stirred for 9 h at room temperature. After removing the unreacted *trans*-[Pt(piam)$_2$(NH$_3$)$_2$] by filtration, the solution was gently evaporated to obtain crystals of *trans*-[Pt$_2$Co(piam)$_4$(NH$_3$)$_4$](ClO$_4$)$_2$ (502 mg). Yield: 90%. Elemental analysis calculated for $C_{20}H_{52}Cl_2CoN_8O_{12}Pt_2$: C, 21.51; H, 4.69; N, 10.03%. Found: C, 21.63; H, 4.69; N, 10.22%.

Synthesis of *trans*-[Pt$_2$Ni(piam)$_4$(NH$_3$)$_4$](ClO$_4$)$_2$ (*t*-Ni)

The suspension of *trans*-[Pt(piam)$_2$(NH$_3$)$_2$] (432 mg, 1.0 mmol) in MeOH (12 mL) was mixed with Ni(ClO$_4$)$_2$·6H$_2$O (367 mg, 1.0 mmol), and stirred for 6 h at room temperature. After removing the unreacted *trans*-[Pt(piam)$_2$(NH$_3$)$_2$] by filtration, the solution was gently evaporated to obtain crystals of *trans*-[Pt$_2$Ni(piam)$_4$(NH$_3$)$_4$](ClO$_4$)$_2$ (498 mg). Yield: 89%. Elemental analysis calculated for $C_{20}H_{52}Cl_2NiN_8O_{12}Pt_2$: C, 21.52; H, 4.69; N, 10.04%. Found: C, 21.75; H, 4.69; N, 10.28%.

Synthesis of *trans*-[Pt$_2$Cu(piam)$_4$(NH$_3$)$_4$](ClO$_4$)$_2$ (*t*-Cu)

The suspension of *trans*-[Pt(piam)$_2$(NH$_3$)$_2$] (432 mg, 1.0 mmol) in a mixed solution of water and MeOH (90 mL, v/v = 2:1) was mixed with CuCl$_2$·2H$_2$O (170 mg, 1.0 mmol), and stirred for 3 h at room temperature. After removing the unreacted *trans*-[Pt(piam)$_2$(NH$_3$)$_2$] by filtration, NaClO$_4$ (490 mg, 4.0 mmol) was added into the solution and stirred for 3 h at room temperature. The solution was filtered to obtain the orange powdered product of *trans*-[Pt$_2$Cu(piam)$_4$(NH$_3$)$_4$](ClO$_4$)$_2$ (423 mg). Yield: 76%. Elemental analysis calculated for $C_{20}H_{52}Cl_2CuN_8O_{12}Pt_2$: C, 21.42; H, 4.67; N, 9.99%. Found: C, 21.40; H, 4.78; N, 10.04%.

Physical Measurements. Infrared (IR) spectra were recorded using a PerkinElmer Spectrum 400 (in the range of 400–4000 cm^{-1}) at room temperature. X-ray photoelectron spectroscopy (XPS) measurements were performed using a Quantera-SXM spectrometer at room temperature. The binding energies were measured relative to the C 1s peak (284.8 eV) of the internal hydrocarbons. Electron paramagnetic resonance (EPR) spectra were recorded using a JEOL TE-200 spectrometer. Diffuse reflectance spectra were recorded using a Jasco V-770 spectrophotometer (in the range of 200–2500 nm) at room temperature. The obtained reflectance spectra were converted to absorption spectra using the Kubelka–Munk function $F(R_\infty)$. Cyclic voltammetry (CV) measurements were carried out at room temperature using a BAS 617E electrochemical analyzer. CVs were recorded in MeCN solutions containing 0.1 M Bu_4NPF_6 for ***c*-M** or 0.1 M Bu_4NClO_4 for ***t*-M** as the supporting electrolyte. A conventional three-electrode arrangement was used, consisting of a glassy carbon working electrode, a saturated calomel electrode (SCE) for ***c*-M** or Ag/Ag^+ for the ***t*-M** reference electrode, and a Pt wire as the counter electrode. Magnetic data were obtained in the 2–300 K range using a Quantum Design MPMS-7 SQUID susceptometer working at a 1.0 T field strength. Data were corrected for the sample holder, and the diamagnetism of the content was estimated from the Pascal constants.

Density Functional Theory (DFT) Calculations. The electronic structures of model compounds, *trans*-$[Pt_2M(NHCOCH_3)_4(NH_3)_4]^{x+}$ (**M**, M = Mn, Fe, Co, Ni, and Cu, x = 2 or 3) and $\{$*trans*-$[Pt_2M(NHCOCH_3)_4(NH_3)_4]\}_2^{4+}$ (**M2**, M = Mn, Co, Ni, and Cu), were determined using the DFT method with the UB3LYP function[119-121] and Gaussian 16 program package.[122] For Pt, the LANL2DZ basis set was used together with the effective core potential of Hay and Wadt.[123] For the other elements, the 6-31G(d,p) basis sets were selected.[124] The initial model of *trans*-$[Pt_2M(NHCOCH_3)_4(NH_3)_4]^{x+}$ (**M**) and $\{$*trans*-$[Pt_2M(NHCOCH_3)_4(NH_3)_4]\}_2^{4+}$ (**M2**) for optimization was prepared using the geometrical parameters obtained from the crystal structure data of ***t*-M**. For the models, full geometry optimization was conducted. Based on the optimized geometrical structure, 40 excited states were obtained to determine the vertical excitation energy using TD-DFT calculations.[125,126]

X-ray Structure Determination. X-ray diffraction measurements were performed using a Rigaku Mercury diffractometer equipped with a normal-focus Mo-target X-ray tube (λ =

0.71070 Å) operated at 2 kW power (50 kW, 40 mA) and a Rigaku Mercury charge-coupled device (CCD) two-dimensional detector. A total of 1272 frames were collected with a scan width of 0.5º and exposure time of 15 s/frame (***t*-Mn**), 10 s/frame (***t*-Fe**), 15 s/frame (***t*-Co**), 15 s/frame (***t*-Ni**), and 15 s/frame (***t*-Cu**), operated with the CrysAlisPRO software package.[127] Empirical absorption correction using spherical harmonics was implemented in the SCALE3 ABSPACK scaling algorithm.[128] The structure was solved by applying the direct method[129] with subsequent difference Fourier synthesis and refinement using SHELX-2017[130] controlled by the Yadokari-XG software package.[131] Non hydrogen atoms were refined anisotropically, and all the hydrogen atoms were treated as riding atoms. In ***t*-Fe**, the oxygen atoms of the water molecules were refined without hydrogen atoms.

Analyses of magnetic susceptibility measurements data.

The data for ***c*-M** and ***t*-M** were fitted to the Curie–Weiss law $\chi = C/(T - \theta)$. The resulting least-squares fit between 30 K and 300 K yielded ***c*-Mn**: C = 4.42 cm^3 K mol^{-1}, θ = −0.40 K, ***c*-Fe**: C = 4.66 cm^3 K mol^{-1}, θ = −1.73 K, ***c*-Co**: C = 2.53 cm^3 K mol^{-1}, θ = −9.07 K, ***c*-Ni**: C = 0.95 cm^3 K mol^{-1}, θ = 0.89 K, ***c*-Cu**: C = 0.45 cm^3 K mol^{-1}, θ = 0.01 K, ***t*-Mn**: C = 4.02 cm^3 K mol^{-1}, θ = −8.00 K, ***t*-Fe**: C = 4.34 cm^3 K mol^{-1}, θ = −0.05 K, ***t*-Co**: C = 2.73 cm^3 K mol^{-1}, θ = −24.8 K, ***t*-Ni**: C = 1.13 cm^3 K mol^{-1}, θ = −19.3 K, ***t*-Cu**: C = 0.43 cm^3 K mol^{-1}, θ = 0.15 K (Figure S4). $C = N\beta^2g^2S(S + 1)/3k$, where N is Avogadro constant, β is the Bohr magneton, g is the Lande value, k is Boltzmann constant, θ is the Weiss constant, as the combination of constants $3k/N\beta^2$ is 7.991, gives ***c*-Mn**: g = 2.01, ***c*-Fe**: g = 2.06, ***c*-Co**: g = 2.32, ***c*-Ni**: g = 1.95, ***c*-Cu**: g = 2.19, ***t*-Mn**: g = 1.92, ***t*-Fe**: g = 1.99, ***t*-Co**: g = 2.41, ***t*-Ni**: g = 2.13, ***t*-Cu**: g = 2.14.

The equations describing the temperature dependence of the molar magnetic susceptibility of a sextet state undergoing an axial ZFS are

$$\chi_{\parallel} = \frac{Ng^2\beta^2}{4kT}\frac{1 + 9\exp\left(\frac{-2D}{kT}\right) + 25\exp\left(\frac{-6D}{kT}\right)}{1 + \exp\left(\frac{-2D}{kT}\right) + \exp\left(\frac{-6D}{kT}\right)}$$

$$\chi_{\perp} = \frac{Ng^2\beta^2}{8kT}\frac{18 + \frac{kT}{D}\left(16 - 11\exp\left(\frac{-2D}{kT}\right) - 5\exp\left(\frac{-6D}{kT}\right)\right)}{1 + \exp\left(\frac{-2D}{kT}\right) + \exp\left(\frac{-6D}{kT}\right)}$$

where D is axial zero-field splitting parameter, k is Boltzmann constant, T is temperature, N is Avogadro constant, g is g-factor, and β is the Bohr magneton. The average molar magnetic susceptibility of a powdered sample is given by

$$\chi' = \frac{\chi_{\parallel} + 2\chi_{\perp}}{3} + \text{TIP} \qquad (1)$$

where TIP is the temperature independent paramagnetism. In some cases, it was necessary to include the contribution of an impurity present in a proportion P and which was assumed to follow a Curie law with S = 1/2 and a g factor noted as g_{mo} (fixed as 2.00). The complete expression of the magnetic susceptibility used for the refinements was therefore

$$\chi = (1 - P)\chi' + P\frac{Ng_{\text{mo}}^2\beta^2}{4kT} \qquad (2)$$

According to the above equation, the resulting least-squares fit of the data of ***c*-Mn** between 2 K and 300 K yielded g = 2.00, D = 1.21 cm^{-1}, TIP = 0.00 cm^3 mol^{-1}, and P = 1.00 × 10^{-4} (Figure S5a).

For ***t*-Mn**, in order to estimate the intermolecular interaction, the molecular field approximation may be used with the following analytical expression

$$\chi'' = \frac{\chi'}{1 - \left(\frac{2zJ}{Ng^2\beta^2}\right)\chi'} \qquad (3)$$

where zJ is the exchange energy (J multiplied by the number z of interacting neighbors), and χ' is the magnetic susceptibility of an isolated molecules, resulting from previous equation, where D = 0.22 cm^{-1} obtained by the simulation with EPR spectrum for ***t*-Mn**. Similarly, the contribution of a paramagnetic impurity was included to yield the complete expression used for the refinements

$$\chi = (1 - P)\chi'' + P\frac{Ng_{\text{mo}}^2\beta^2}{4kT} \qquad (4)$$

According to the above equation, the resulting least-squares fit of the data of ***t*-Mn** between 2 K and 300 K yielded g = 1.96, zJ = −1.7 cm^{-1}, TIP = 0.00 cm^3 mol^{-1}, and P = 1.02 × 10^{-4} (Figure S5b).

Also for both ***c*-Fe** and ***t*-Fe**, according to the equation (2) with the molar magnetic susceptibility of a sextet state undergoing an axial ZFS, the resulting least-squares fit of the data between 2 K and 300 K yielded ***c*-Fe**: g = 2.04, D = 5.43 cm^{-1}, TIP = 2.92 × 10^{-4} cm^3 mol^{-1}, and P = 1.00 × 10^{-4}, ***t*-Fe**: g = 2.00, D = 5.45 cm^{-1}, TIP = 0.00 cm^3 mol^{-1}, and P = 1.00 × 10^{-4}

(Figure S6).

The equations describing the temperature dependence of the molar magnetic susceptibility of a quartet state undergoing an axial ZFS are following.

$$\chi_{\parallel} = \frac{Ng^2\beta^2}{4kT}\frac{1 + 9\exp\left(\frac{-2D}{kT}\right)}{1 + \exp\left(\frac{-2D}{kT}\right)}$$

$$\chi_{\perp} = \frac{Ng^2\beta^2}{4kT}\frac{4 + \frac{3kT}{D}\left(1 - \exp\left(\frac{-2D}{kT}\right)\right)}{1 + \exp\left(\frac{-2D}{kT}\right)}$$

According to the equation (2) with the above equation, the resulting least-squares fit of the data of ***c*-Co** between 2 K and 300 K yielded $g = 2.29$, $D = 44.2$ cm^{-1}, TIP = 0.00 cm^3 mol^{-1}, and $P = 1.00 \times 10^{-4}$ (Figure S7a). For ***t*-Co**, in order to estimate the intermolecular interaction, the molecular field approximation may be used with the equation (3), where $D = 0.40$ cm^{-1} obtained by the simulation with EPR spectrum for ***t*-Co**. According the above equation (4), the resulting least-squares fit of the data of ***t*-Co** between 2 K and 300 K yielded $g = 2.47$, $zJ = -9.1$ cm^{-1}, TIP = 0.00 cm^3 mol^{-1}, and $P = 1.02 \times 10^{-4}$ (Figure S7b).

The equations describing the temperature dependence of the molar magnetic susceptibility of a triplet state undergoing an axial ZFS are

$$\chi_{\parallel} = \frac{Ng^2\beta^2}{kT}\frac{2\exp\left(\frac{-D}{kT}\right)}{1 + 2\exp\left(\frac{-D}{kT}\right)}$$

$$\chi_{\perp} = \frac{Ng^2\beta^2}{kT}\frac{\frac{2kT}{D}\left(1 - \exp\left(\frac{-D}{kT}\right)\right)}{1 + 2\exp\left(\frac{-D}{kT}\right)}$$

According to the equation (2) with the above equation, the resulting least-squares fit of the data of ***c*-Ni** between 2 K and 300 K yielded $g = 1.96$, $D = 5.54$ cm^{-1}, TIP = 1.50×10^{-6} cm^3 mol^{-1}, and $P = 1.00 \times 10^{-4}$ (Figure S8a). For ***t*-Ni**, in order to estimate the intermolecular interaction, the molecular field approximation may be used with the equation (3), where $D = 0.38$ cm^{-1} obtained by the simulation with EPR spectrum for ***t*-Ni**. According to the above equation (4), the resulting least-squares fit of the data of ***t*-Ni** between 2 K and 300 K yielded $g = 2.24$, $zJ = -19.6$ cm^{-1}, TIP = 0.00 cm^3 mol^{-1}, and $P = 1.02 \times 10^{-4}$ (Figure S8b).

The susceptibility data of ***t*-Mn** was fitted to the following expression for the molar susceptibility derived from $H = -2JS_1 \cdot S_2$.

$$\chi = \frac{Ng^2\beta^2}{kT} \frac{55 + 30x^{10} + 14x^{18} + 5x^{24} + x^{28}}{11 + 9x^{10} + 7x^{18} + 5x^{24} + 3x^{28} + x^{30}} + \text{TIP}$$

$$x = exp\left(\frac{-J}{kT}\right)$$

where J represents the exchange interactions between two adjacent Mn(+2) centers. According to the above equation, the resulting least-squares fit of the data of ***t*-Mn** between 2 K and 300 K yielded $g = 1.92$ and $J = -0.9$ cm^{-1} (Figure 9f).

The susceptibility data of ***t*-Co** was fitted to the following expression for the molar susceptibility derived from $H = -2JS_1 \cdot S_2$.

$$\chi = \frac{Ng^2\beta^2}{kT} \frac{14 + 5x^6 + x^{10}}{7 + 5x^6 + 3x^{10} + x^{12}} + \text{TIP}$$

$$x = exp\left(\frac{-J}{kT}\right)$$

where J represents the exchange interactions between two adjacent Co(+2) centers. According to the above equation, the resulting least-squares fit of the data of ***t*-Co** between 2 K and 300 K yielded $g = 2.28$ and $J = -3.5$ cm^{-1} (Figure 9h).

The susceptibility data of ***t*-Ni** was fitted to the following expression for the molar susceptibility derived from $H = -2JS_1 \cdot S_2$.

$$\chi = \frac{Ng^2\beta^2}{kT} \frac{5 + x^4}{5 + 3x^4 + x^6} + \text{TIP}$$

$$x = exp\left(\frac{-J}{kT}\right)$$

where J represents the exchange interactions between two adjacent Ni(+2) centers. According to the above equation, the resulting least-squares fit of the data of ***t*-Ni** between 2 K and 300 K yielded $g = 2.12$ and $J = -7.3$ cm^{-1} (Figure 9i).

The susceptibility data of ***t*-Cu** was fitted to the following expression for the molar susceptibility derived from $H = -2JS_1 \cdot S_2$.

$$\chi = \frac{Ng^2\beta^2}{kT} \frac{1}{3 + x^2} + \text{TIP}$$

$$x = exp\left(\frac{-J}{kT}\right)$$

where J represents the exchange interactions between two adjacent Cu(+2) centers. According to the above equation, the resulting least-squares fit of the data of ***t*-Cu** between 2 K and 300 K yielded $g = 2.15$ and $J = 0.0$ cm^{-1} (Figure 9j).

Supporting Figures and Tables

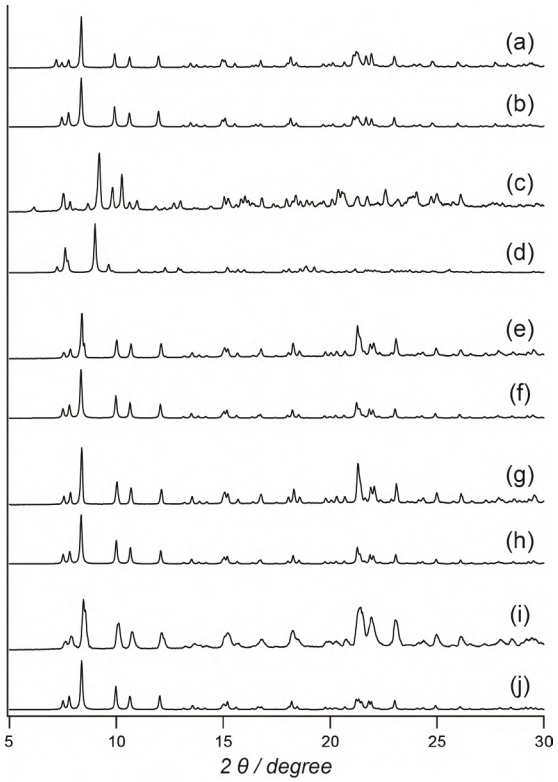

Figure S1. Powder X-ray diffraction for microcrystal samples for (a) ***t*-Mn**, (b) simulation of ***t*-Mn**, (c) ***t*-Fe**, (d) simulation of ***t*-Fe**, (e) ***t*-Co**, (f) simulation of ***t*-Co**, (g) ***t*-Ni**, (h) simulation of ***t*-Ni**, (i) ***t*-Cu**, and (j) simulation of ***t*-Cu**. The simulation data were calculated based on the results of single-crystal X-ray analyses.

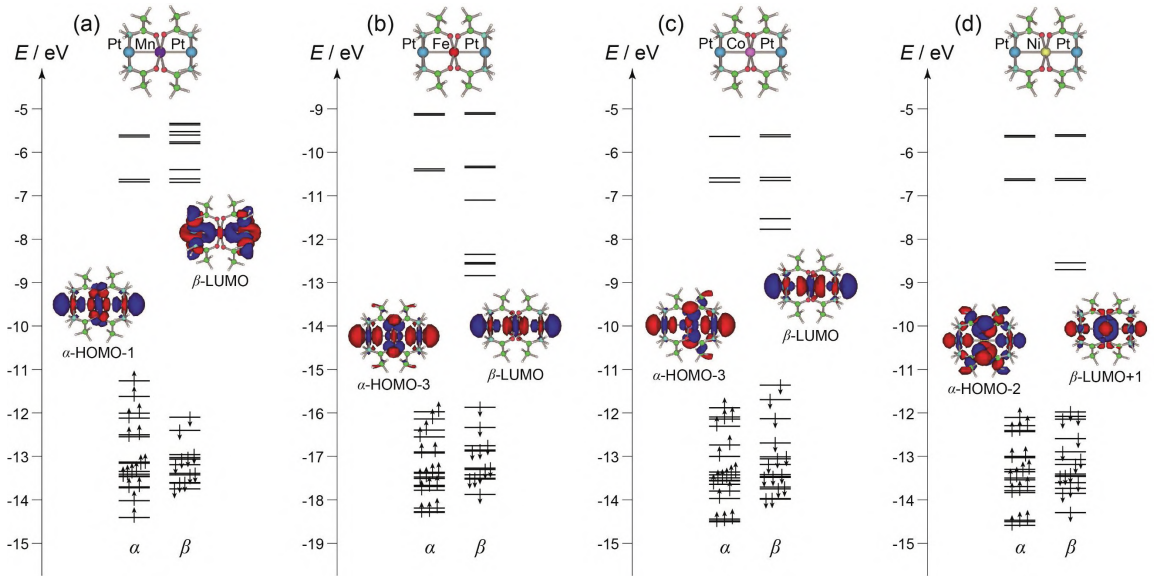

Figure S2. Results of DFT calculation for (a) *trans*-$[Pt_2Mn(NHCOCH_3)_4(NH_3)_4]^{2+}$ (**Mn**), (b) *trans*-$[Pt_2Fe(NHCOCH_3)_4(NH_3)_4]^{3+}$ (**Fe**), (c) *trans*-$[Pt_2Co(NHCOCH_3)_4(NH_3)_4]^{2+}$ (**Co**), and (d) *trans*-$[Pt_2Ni(NHCOCH_3)_4(NH_3)_4]^{2+}$ (**Ni**).

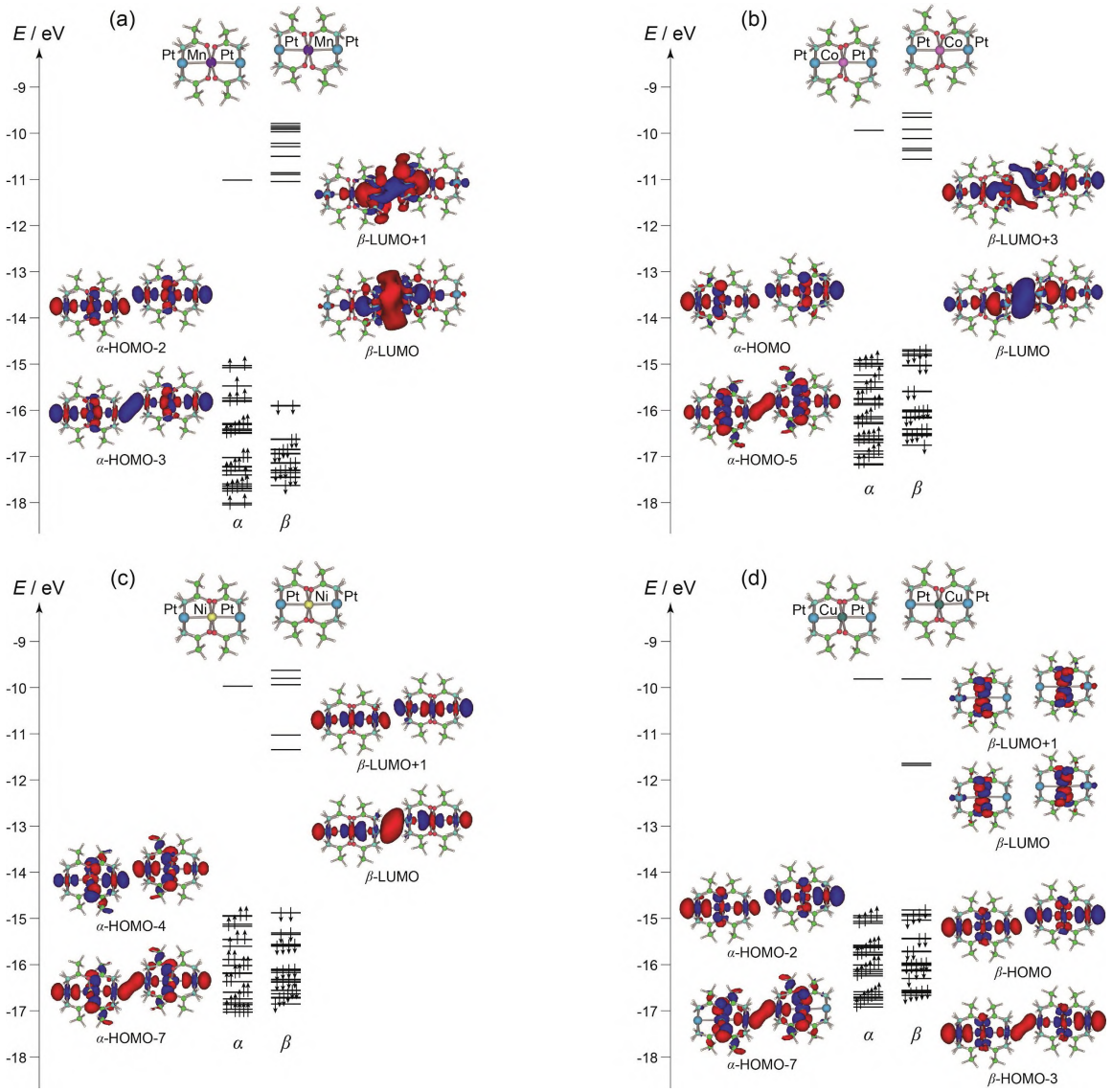

Figure S3. Results of DFT calculation for (a) $\{trans\text{-}[Pt_2Mn(NHCOCH_3)_4(NH_3)_4]\}_2^{4+}$ (**Mn_2**), (b) $\{trans\text{-}[Pt_2Co(NHCOCH_3)_4(NH_3)_4]\}_2^{4+}$ (**Co_2**), (c) $\{trans\text{-}[Pt_2Ni(NHCOCH_3)_4(NH_3)_4]\}_2^{4+}$ (**Ni_2**), and (d) $\{trans\text{-}[Pt_2Mn(NHCOCH_3)_4(NH_3)_4]\}_2^{4+}$ (**Cu_2**).

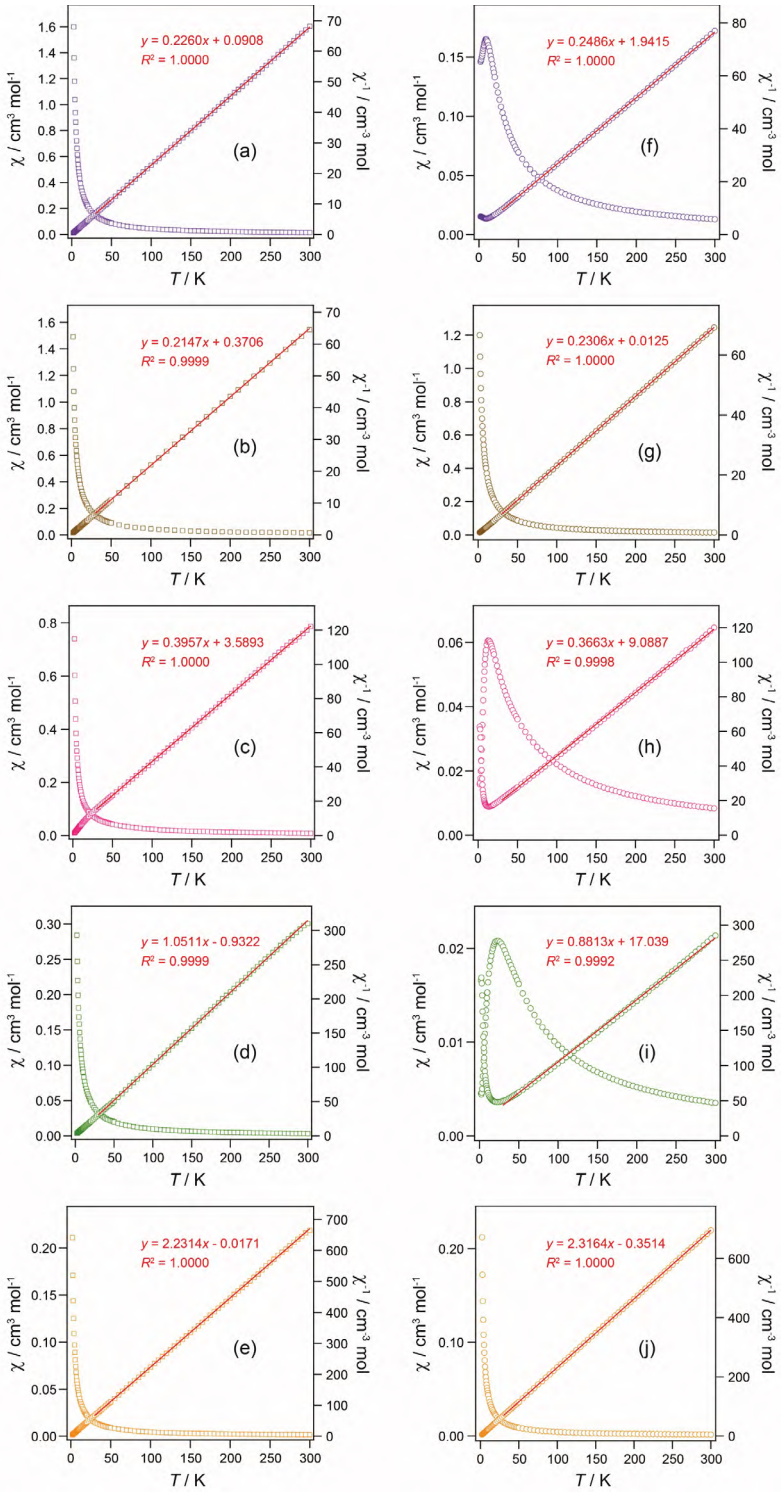

Figure S4. Temperature dependence of χ (square) and χ^{-1} (circle) for (a) *cis*-$[Pt_2Mn(piam)_4(NH_3)_4](PF_6)_2$ (***c*-Mn**), (b) *cis*-$[Pt_2Fe(piam)_4(NH_3)_4](PF_6)_3$ (***c*-Fe**), (c) *cis*-$[Pt_2Co(piam)_4(NH_3)_4](PF_6)_2$ (***c*-Co**), (d) *cis*-$[Pt_2Ni(piam)_4(NH_3)_4](PF_6)_2$ (***c*-Ni**), (e) *cis*-$[Pt_2Cu(piam)_4(NH_3)_4](PF_6)_2$ (***c*-Cu**), (f) *trans*-$[Pt_2Mn(piam)_4(NH_3)_4](ClO_4)_2$ (***t*-Mn**), (g) *trans*-$[Pt_2Fe(piam)_4(NH_3)_4](ClO_4)_3$ (***t*-Fe**), (h) *trans*-$[Pt_2Co(piam)_4(NH_3)_4](ClO_4)_2$ (***t*-Co**), (i) *trans*-$[Pt_2Ni(piam)_4(NH_3)_4](ClO_4)_2$ (***t*-Ni**), and (j) *trans*-$[Pt_2Cu(piam)_4(NH_3)_4](ClO_4)_2$ (***t*-Cu**). The red solid lines represent the results of least square fitting.

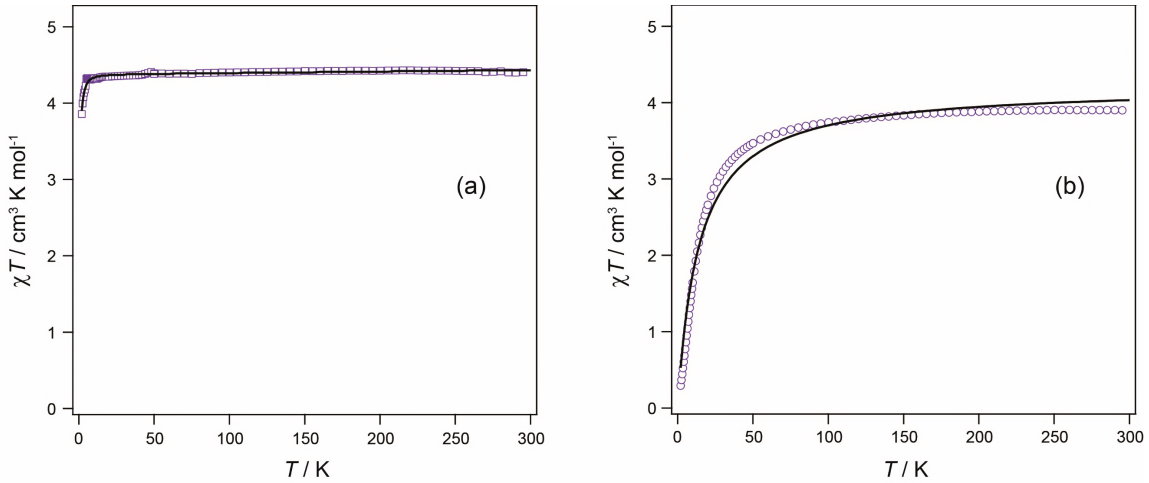

Figure S5. Temperature dependence of χT for (a) *cis*-$[Pt_2Mn(piam)_4(NH_3)_4](PF_6)_2$ (***c*-Mn**) and (b) *trans*-$[Pt_2Mn(piam)_4(NH_3)_4](ClO_4)_2$ (***t*-Mn**) per Mn ion. The solid lines represent the theoretical fitting to (a) the axial ZFS model and (b) the molecular field approximation with D and zJ.

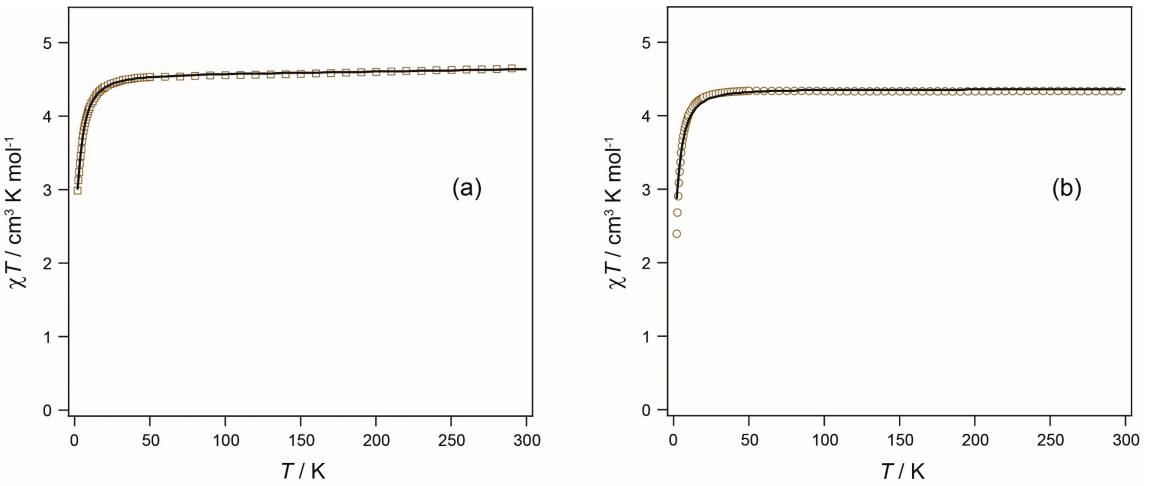

Figure S6. Temperature dependence of χT for (a) *cis*-$[Pt_2Fe(piam)_4(NH_3)_4](PF_6)_3$ (***c*-Fe**) and (b) *trans*-$[Pt_2Fe(piam)_4(NH_3)_4](ClO_4)_3$ (***t*-Fe**) per Fe ion. The solid lines represent the theoretical fitting to the axial ZFS model.

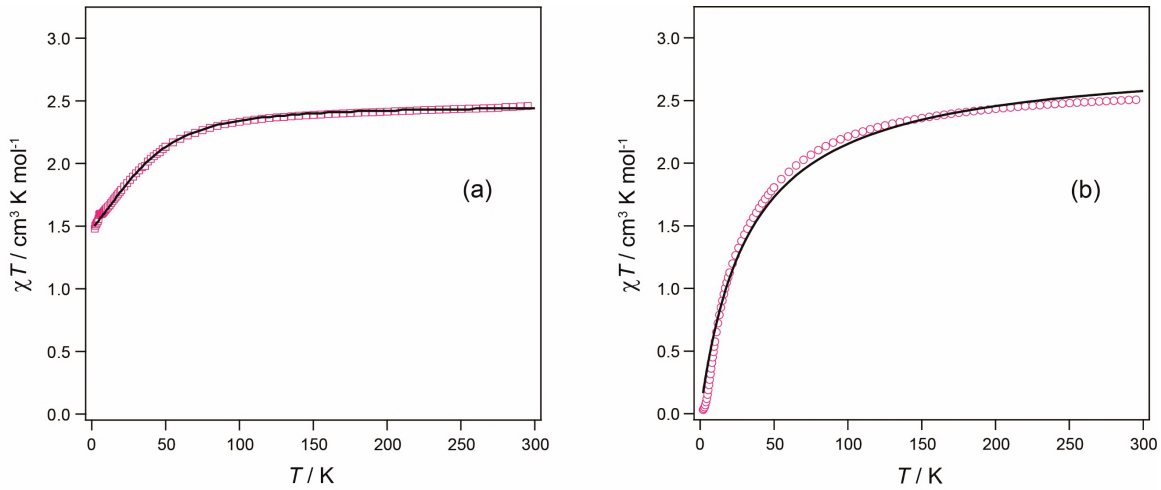

Figure S7. Temperature dependence of χT for (a) *cis*-$[Pt_2Co(piam)_4(NH_3)_4](PF_6)_2$ (***c*-Co**) and (b) *trans*-$[Pt_2Co(piam)_4(NH_3)_4](ClO_4)_2$ (***t*-Co**) per Co ion. The solid lines represent the theoretical fitting to (a) the axial ZFS model and (b) the molecular field approximation with D and zJ.

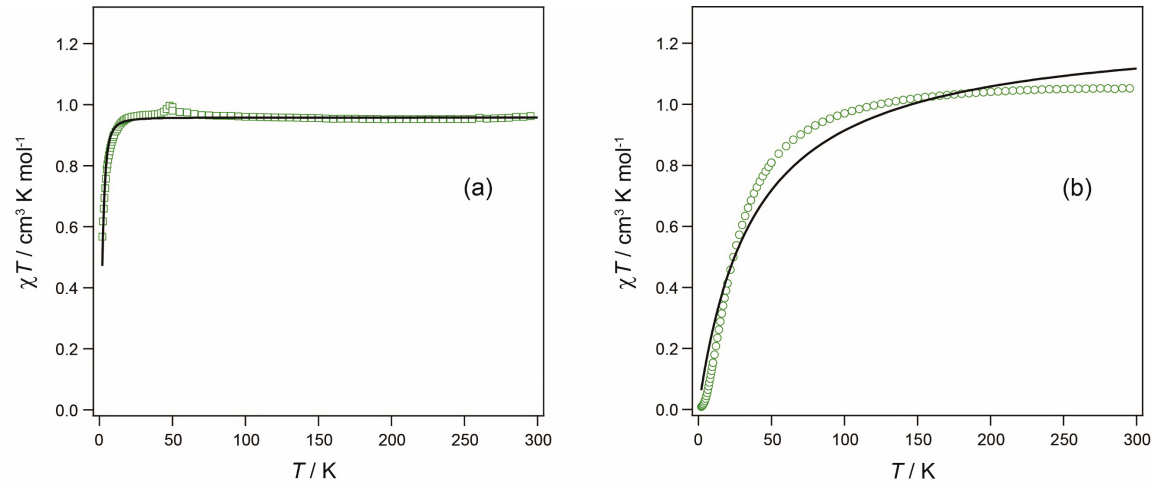

Figure S8. Temperature dependence of χT for (a) *cis*-$[Pt_2Ni(piam)_4(NH_3)_4](PF_6)_2$ (***c*-Ni**) and (b) *trans*-$[Pt_2Ni(piam)_4(NH_3)_4](ClO_4)_2$ (***t*-Ni**) per Ni ion. The solid lines represent the theoretical fitting to (a) the axial ZFS model and (b) the molecular field approximation with D and zJ.

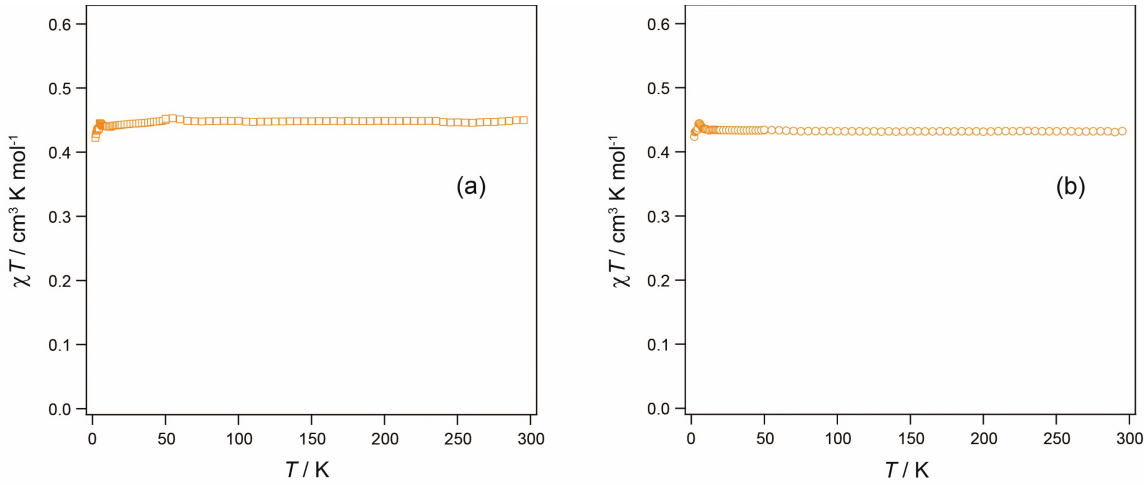

Figure S9. Temperature dependence of χT for (a) *cis*-$[Pt_2Cu(piam)_4(NH_3)_4](PF_6)_2$ (***c*-Cu**) and (b) *trans*-$[Pt_2Cu(piam)_4(NH_3)_4](ClO_4)_2$ (***t*-Cu**) per Cu ion.

Table S1. The distances (Å) of Mn---Mn and J values (cm^{-1}) in reported 1D compounds shown in Figure 11. The J values were calculated on $H = -JS_1S_2$.

Compounds	Mn---Mn (Å)	$2J$ (cm^{-1})	ref
Mn atoms are bridged by organic molecules or halide ions			
$[Mn(L)(pyz)]_n(ClO_4)_n \cdot 2nH_2O$	3.244	−1.9	72
$[(CH_3)_4N]_n[MnCl_3]_n$	3.25	−8.75	73
$[MnL'(N_3)_2]_n$	3.462	−5.31	74
$[MnCl_2]_n \cdot 2nH_2O$	3.7	−0.625	75
$[Mn(\mu\text{-}Cl)_2(mppma)]_n$	3.7398	−0.255	76
$[Mn_2(tpa)_2(o\text{-phth})]_n(ClO_4)_{2n}$	4.452	−2.4	77
$[Mn(\mu\text{-}3\text{-}ClPhCOO)_2(bpy)]_n \cdot nH_2O$	4.515	−1.72	78
$[Mn(\mu\text{-}ClCH_2COO)_2(phen)]_n$	4.53	−0.89	79
$(CH_3NH_3)_n[MnCl_3]_n \cdot 2nH_2O$	4.599	−4.18	80
$[Mn_2(bipy)_4(ta)]_n(ClO_4)_{2n}$	4.643	−0.675	81
$[Mn(PDB)]_n \cdot nH_2O$	4.8	−0.56	82
$[Mn_2(bipy)_4(m\text{-phth})]_n(ClO_4)_{2n} \cdot 4nH_2O$	4.84	−0.98	83
$[Mn\{(CH_3)_2PO_2\}_2]_n$	4.8652	−5.88	84
$[Mn(bic)Cl]_n \cdot nH_2O$	4.987	−0.6	85
$[Mn(bpy)(NCS)_2]_n$	6	−2.7	86
$[Mn_2(EDTA)]_n \cdot 9nH_2O$	6.1	−0.5	87
$[Mn_2(bpym)_3(tcpd)_2(H_2O)_2]_n$	6.13	−1.16	88
$[Mn(CH_3CONH_2)_2(HPhPO_2)_2]_n$	7.43	−0.60	89
$[Mn(HPhPO_2H)_2(HPhPO_2)_2]_n$	7.43	−0.26	89
$[Mn(MAC)\{\mu_{1.5}\text{-}NN(CN)_2\}]_n(PF_6)_n$	7.7	−0.49	90
$[Mn(C_5H_6NO_3)_2]_n$	7.963	−0.75	91
$[Mn(tpa)(TCNQ)(CH_3OH)]_n(TCNQ)_{2n} \cdot nCH_3CN$	8.207	−1.94	92
$[Mn(MAC)(H_2O)_2]_nCl_{2n} \cdot 4nH_2O$	13.03	−0.18	93
Mn atoms are bridged by second metals.			
$[MnNiMn(dpa)_4Cl_2]$	5.25	−13.7	94
$[MnPdMn(dpa)_4Cl_2]$	5.28	−29.7	94
$[MnPtMn(dpa)_4Cl_2]$	5.26	−66.2	94
***t*-Mn**	9.04	−1.8	this work
A	13.9	−0.43	38

Abbreviation: L = Schiff base ligand, pyz = pyrazine, L' = (E)-3-(dimethylamino)-1-(pyridin-

2-yl)prop-2-en-1-one), mppma = *N*-(3-methoxypropyl)-*N*-(pyridin-2-ylmethyl)amine, tpa = tris(2-pyridylmethyl)amine, *o*-phth = terephthalato dianion, phen = phenanthroline, H_2PDB = pyridine-3,4-dicarboxylic acid, *m*-phth = isophthalate, bic = bicinate, bpy = 2,2'-bipyridine, EDTA = ethylenediaminetetraacetic acid, bpym = 2,2'-bipyrimidine, tcpd = 2-dicyanomethylene-1,1,3,3-tetracyanopropanediide anion, MAC = 2,13-dimethyl-3,6,9,12,18-pentaazabicyclo-[12.3.1]octadeca-1(18),2,12,14,16-pentaene, TCNQ = tetracyanoquinodimethane, dpa = bis(2-pyridyl)amide, **A** = $[\{Rh_2(O_2CCH_3)_4\}\{Pt_2Mn(piam)_4(NH_3)_4\}]_n(PF_6)_{2n}\cdot n$EtOH.

Table S2. The distances (Å) of Co---Co and J values (cm^{-1}) in reported 1-D compounds shown in Figure 11. The J values were calculated on $H = -JS_1S_2$.

Compounds	Co---Co (Å)	$2J$ (cm^{-1})	ref
Co atoms are bridged by organic molecules.			
$[Co_2(esp)_2(EtOH)_2]$	2.7245(6), 2.7595(7)	−13.2	95
$[Co_3(Hdcp)_2(phen)_3(H_2O)_2]_n \cdot nH_2O$	4.374	−2.52	96
$[Co_2(N_3)_4(L)]_n \cdot 4nH_2O$	5.158(1)	−18.9	97
$[Co(ox)(Htr)_2]_n \cdot 2nH_2O$	5.39	−12.6	98
$[Co(ox)(en)]_n \cdot 2nH_2O$	5.512	−10.3	99
$[Co(C_{10}H_{20}C_2O_4)(H_2O)_2]_n$	5.93	−1.43	100
$[Co(CH_3(CH_2)_{10}COO)_2(H_2O)_2]_n$	6.3	−0.35	101
$[Co(H_2O)_4(pyz)]_n(NO_3)_{2n} \cdot 2nH_2O$	7.125	−1.53	102
$[Co(acac)_2(pyz)]_n$	7.2667	−0.76	103
$[Co(bipym)Cl_2]_n \cdot 1.5nH_2O$	7.374(1)	−5.8	104
$[Co(bipym)(H_2O)_2]_n(NO_3)_{2n}$	7.632(2)	−8.5	105
$[Co(bnzd)_2(suc)(OH_2)_2]_n \cdot nH_2O$	9.88	−3.31	106
$[Co(H_2btec)(H_2O)_4]_n \cdot n$(4-apy)$\cdot 2nH_2O$	11.302(10)	−0.60	107
$[Co(acac)_2$(4,4′-bipy)$]_n$	11.482(2)	−0.68	103
Co atoms are bridged by second metals.			
$[Co_2PdCl_2(dpa)_4]$	5.0	−92.47	108
$[PtCo(tba)_4(OH_2)]_2$	8.2	−21.6	14
$[PtCo(SAc)_4(OH_2)]_2$	8.3	−25.4	16
$[PtCo(SAc)_4(3\text{-}NO_2py)]_2$	8.7	−12.0	16
***t*-Co**	8.99	−7.0	this work
B	13.3	−22.2	37

Abbreviation: esp = α,α,α′,α′-tetramethyl-1,3-benzenedipropionate, H_3dcp = 3,5-pyrazoledicarboxylic acid, phen = 1,10-phenanthroline, L = tetrakis(3-pyridyloxymethylene)methane, ox = oxalate dianion, Htr = 1,2,4-triazole, en = ethylenediamine, bipym = 2,2′-bipyrimidine, pyz = pyrazine, bnzd = benzidine, suc = succinate dianion, H_2btec = 1,2,4,5-benzenetetracarboxylic acid, 4-apy = 4-aminopyridine, 4,4′-bipy = 4,4′-bipyridine, dpa = bis(2-pyridyl)amide, tba = thiobenzoate, SAc = thioacetate, 3-NO_2py = 3-nitropyridine, **B** = $[\{Rh_2(O_2CCH_3)_4\}\{Pt_2Co(piam)_4(NH_3)_4\}]_n(PF_6)_{2n}$.

Table S3. The distances (Å) of Ni---Ni and J values (cm^{-1}) in reported 1-D compounds shown in Figure 11. The J values were calculated on $H = -JS_1S_2$.

Compounds	Ni---Ni (Å)	$2J$ (cm^{-1})	ref
Ni atoms are bridged by organic molecules.			
$BiM_2BP_2O_{10}$	5.078	–7.15	109
$(NH_4)_2$[Ni(PMIDA)(H_2O)]	5.782	–7.34	110
[Ni(HL)(hfac)]$_n$	6.1	–13.20	111
{[Ni(phen)(H_2O)($H_2P_2O_7$)]·H_2O}$_n$	6.5629	–1.88	112
{[Ni(μ^2-η^2-bp3dc)(H_2O)$_3$]·H_2O}$_n$	9.915	–1.13	113
[Ni(L')(PDC)]·H_2O	11.465	–1.47	114
[Ni(L')(BDC)]·$2H_2O$	11.528	–1.37	114
Ni atoms are bridged by N_3.			
trans-[Ni(333-tet)(μ-N_3)]$_n$(ClO_4)$_n$	6.003	–62.10	115
[Ni(Me_2-1,3-dieneN_4)(μ-N_3)]$_n$(ClO_4)$_n$	5.767	–97.80	116
cis-[Ni(333-tet)(μ-N_3)]$_n$(PF_6)$_n$	6.182	–18.50	115
[NiL''$_2$(μ-N_3)]$_n$(ClO_4)$_n$	7.392	–16.80	117
Ni atoms are bridged by second metals.			
[PtNi(tba)$_4$(OH_2)]$_2$	8.2	–120	14
[PtNi(SAc)$_4$(OH_2)]$_2$	8.2	–50.8	16
[PtNi(SAc)4(3-NO2py)]2	8.2	–12.6	16
***t*-Ni**	9.02	−14.6	this work

Abbreviation: H_4PMIDA = N-(phosphonomethyl)iminodiacetic acid, H_2L = Schiff base, hfac = hexafluoroacetylacetonate anion, bp3dc = 2,2'-bipyridine-3,3'-dicarboxylate, L' = 3,14-dimethyl-2,6,13,17-tetraazatricyclo[14,4,01.18,07.12]docosane, BDC = 1,4-benzenedicarboxylate, PDC = 2,5-pyridinedicarboxylate, 333-tet = tetraamine *N*,*N'*-bis(3-aminopropyl)-1,3-propanediamine, Me_2-l,3-dieneN_4 = 2,3-dimethyl-l,4,8,11-tetraazacyclotetradeca-1,3-diene, 333-tet = tetraamine *N*,*N'*-bis(3-aminopropyl)-1,3-propanediamine, L'' = 1,2-diamino-2-methylpropane, tba = thiobenzoate, SAc = thioacetate, 3-NO_2py = 3-nitropyridine

References

1. Braunstein, P.; Danopoulos, A. A., Transition Metal Chain Complexes Supported by Soft Donor Assembling Ligands. *Chem. Rev.* **2021,** *121*, 7346–7397.
2. Bera, J. K.; Dunbar, K. R., Chain Compounds Based on Transition Metal Backbones: New Life for an Old Topic. *Angew. Chem., Int. Ed.* **2002,** *41*, 4453–4457.
3. Givaja, G.; Amo-Ochoa, P.; Gómez-García, C. J.; Zamora, F., Electrical conductive coordination polymers. *Chem. Soc. Rev.* **2012,** *41*, 115–147.
4. Chipman, J. A.; Berry, J. F., Paramagnetic Metal−Metal Bonded Heterometallic Complexes. *Chem. Rev.* **2020,** *120*, 2409–2447.
5. Chipman, J. A.; Berry, J. F., Extraordinarily Large Ferromagnetic Coupling ($J \geq 150$ cm^{-1}) by Electron Delocalization in a Heterometallic Mo−Mo−Ni Chain Complex. *Chem. −Eur. J.* **2018,** *24*, 1494–1499.
6. Hegmans, A.; Zangrando, E.; Freisinger, E.; Pichierri, F.; Randaccio, L.; Mealli, C.; Gerdan, M.; Trautwein, A. X.; Lippert, B., Pt as Mediator of Strong Antiferromagnetic Coupling between Two Cu^{II} Ions in a Heteronuclear $Cu^{II}Pt^{II}Cu^{II}$ Complex of the Model Nucleobase 1-Methylcytosinate. *Chem. −Eur. J.* **1999,** *5*, 3010–3018.
7. Liu, I. P.-C.; Wang, W.-Z.; Peng, S.-M., New generation of metal string complexes: strengthening metal–metal interaction *via* naphthyridyl group modulated oligo-α-pyridylamido ligands. *Chem. Commun.* **2009**, 4323–4331.
8. Ismayilov, R. H.; Wang, W.-Z.; Lee, G.-H.; Yeh, C.-Y.; Hua, S.-A.; Song, Y.; Rohmer, M.-M.; Bénard, M.; Peng, S.-M., Two Linear Undecanickel Mixed-Valence Complexes: Increasing the Size and the Scope of the Electronic Properties of Nickel Metal Strings. *Angew. Chem., Int. Ed.* **2011,** *50*, 2045–2048.
9. Hua, S.-A.; Cheng, M.-C.; Chen, C.-h.; Peng, S.-M., From Homonuclear Metal String Complexes to Heteronuclear Metal String Complexes. *Eur. J. Inorg. Chem.* **2015**, 2510–2523.
10. Brogden, D. W.; Berry, J. F., Coordination Chemistry of 2,2'-Dipyridylamine: The Gift That Keeps on Giving. *Comments Inorg. Chem.* **2016,** *36*, 17–37.
11. Goto, E.; Begum, R. A.; Zhan, S.; Tanase, T.; Tanigaki, K.; Sakai, K., Linear, Redox-Active Pt_6 and $Pt_2Pd_2Pt_2$ Clusters. *Angew. Chem., Int. Ed.* **2004,** *43*, 5029–5032.
12. Murahashi, T.; Mochizuki, E.; Kai, Y.; Kurosawa, H., Organometallic Sandwich Chains Made of Conjugated Polyenes and Metal−Metal Chains. *J. Am. Chem. Soc.* **1999,** *121*, 10660–10661.
13. Beach, S. A.; Doerrer, L. H., Heterobimetallic Lantern Complexes and Their Novel Structural and Magnetic Properties. *Acc. Chem. Res.* **2018,** *51*, 1063–1072.
14. Dahl, E. W.; Baddour, F. G.; Fiedler, S. R.; Hoffert, W. A.; Shores, M. P.; Yee, G. T.; Djukic, J.-P.; Bacon, J. W.; Rheingold, A. L.; Doerrer, L. H., Antiferromagnetic coupling across a tetrametallic unit through noncovalent interactions.

Chem. Sci. **2012,** *3*, 602–609.

15. Baddour, F. G.; Fiedler, S. R.; Shores, M. P.; Bacon, J. W.; Golen, J. A.; Rheingold, A. L.; Doerrer, L. H., Pt···Pt vs Pt···S Contacts Between Pt-Containing Heterobimetallic Lantern Complexes. *Inorg. Chem.* **2013,** *52*, 13562–13575.
16. Baddour, F. G.; Fiedler, S. R.; Shores, M. P.; Golen, J. A.; Rheingold, A. L.; Doerrer, L. H., Heterobimetallic Lantern Complexes That Couple Antiferromagnetically through Noncovalent Pt···Pt Interactions. *Inorg. Chem.* **2013,** *52*, 4926–4933.
17. Atoji, M.; Richardson, J. W.; Rundle, R. E., On the Crystal Structures of the Magnus Salts, $Pt(NH_3)_4PtCl_4$. *J. Am. Chem. Soc.* **1957,** *79*, 3017–3020.
18. Krogmann, K.; Hausen, H. D. Z., Pt-Chain Structures. 1. Potassium Tetracyanoplatinate Violets $K_2[Pt(CN)_4]X_{0.3}\cdot 2.5H_2O$ (X = Cl, Br). *Z. Anorg. Allg. Chem.* **1968,** *358*, 67.
19. Krogmann, K.; Binder, W.; Hausen, H. D., Crystal Structure of "$Ir(CO)_3Cl$" = $Ir(CO)_{2.93}CI_{1.07}$. *Angew. Chem., Int. Ed.* **1968,** *7*, 812.
20. Finniss, G. M.; Canadell, E.; Campana, C.; Dunbar, K. R., Unprecedented Conversion of a Compound with Metal-Metal Bonding into a Solvated Molecular Wire. *Angew. Chem., Int. Ed.* **1996,** *35*, 2772–2774.
21. Prater, M. E.; Pence, L. E.; Clerac, R.; Finniss, G. M.; Campana, C.; Auban-Senzier, P.; Jerome, D.; Canadell, E.; Dunbar, K. R., A Remarkable Family of Rhodium Acetonitrile Compounds Spanning Three Oxidation States and with Nuclearities Ranging from Mononuclear and Dinuclear to One-Dimensional Chains. *J. Am. Chem. Soc.* **1999,** *121*, 8005–8016.
22. Sakai, K.; Ishigami, E.; Konno, Y.; Kajiwara, T.; Ito, T., New Partially Oxidized 1-D Platinum Chain Complexes Consisting of Carboxylate-Bridged *cis*-Diammineplatinum Dimer Cations. *J. Am. Chem. Soc.* **2002,** *124*, 12088–12089.
23. Mitsumi, M.; Ueda, H.; Furukawa, K.; Ozawa, Y.; Toriumi, K.; Kurmoo, M., Constructing Highly Conducting Metal–Metal Bonded Solids by Electrocrystallization of $[Pt^{II}_2(RCS_2)_4]$ (RCS_2^-) Dithiocarboxylato, R = Methyl or Ethyl). *J. Am. Chem. Soc.* **2008,** *130*, 14102–14104.
24. Cotton, F. A.; Dikarev, E. V.; Petrukhina, M. A., *cis*-Di(μ-trifluoroacetate)dirhodium tetracarbonyl: structure and chemistry. *J. Chem. Soc., Dalton Trans.* **2000**, 4241–4243.
25. Pruchnik, F. P.; Jakimowicz, P.; Ciunik, Z.; Stanislawek, K.; Oro, L. A.; Tejel, C.; Ciriano, M. A., Rhodium wires based on binuclear acetate-bridged complexes. *Inorg. Chem. Commun.* **2001,** *4*, 19–22.
26. Campbell, M. G.; Powers, D. C.; Raynaud, J.; Graham, M. J.; Xie, P.; Lee, E.; Ritter, T., Synthesis and structure of solution-stable one-dimensional palladium wires. *Nature Chem.* **2011,** *3*, 949–953.
27. Hayoun, R.; Zhong, D. K.; Rheingold, A. L.; Doerrer, L. H., Gold(III) and Platinum(II) Polypyridyl Double Salts and a General Metathesis Route to Metallophilic Interactions. *Inorg. Chem.* **2006,** *45*, 6120–6122.
28. Hendon, C. H.; Walsh, A.; Akiyama, N.; Konno, Y.; Kajiwara, T.; Ito, T.;

Kitagawa, H.; Sakai, K., One-dimensional Magnus-type platinum double salts. *Nature Commun.* **2016,** *7*, 11950.

29. Uemura, K., One-dimensional complexes extended by unbridged metal–metal bonds based on a HOMO–LUMO interaction at the dz^2 orbital between platinum and heterometal atoms. *Dalton Trans.* **2017,** *46*, 5474–5492.
30. Nakajima, T.; Tanase, T., Transition Metal Clusters Constrained by Linear Tetradentate Phosphine Ligands. *Chem. Lett.* **2020,** *49*, 386–394.
31. Goodgame, D. M. L.; Hitchman, M. A.; Lippert, B., Ligating Properties of Platinum(II) Ions in Mixed-Metal (Pt_2M) Trimers (M = Cu(II), Ni(II), Co(II), Fe(II)). *Inorg. Chem.* **1986,** *25*, 2191–2194.
32. Erxleben, A.; Albinati, A.; Lippert, B., Heteronuclear Pt−Pd, Pt_2Cu and Pt_2Ni complexes with bridging acetamidate crystal structures and spectroscopic studies. *J. Chem. Soc., Dalton Trans.* **1996**, 1823–1828.
33. Schreiber, A.; Krizanovic, O.; Fusch, E. C.; Lippert, B.; Lianza, F.; Albinati, A.; Hill, S.; Goodgame, D. M. L.; Stratemeier, H.; Hitchman, M. A., Heteronuclear Complexes Derived from *trans*-a_2PtL_2 (a = NH_3 or CH_3NH_2, L = 2-Pyridonate). Distorted Coordination Geometries of All Three Metals in *trans*-$[a_2PtL_2CuL_2Pt(a_2)]^{2+}$ and an Extraordinary Short Hydrogen Bond in *trans*-$[a_2PtL(LH)]^{+}$. *Inorg. Chem.* **1994,** *33*, 6101–6110.
34. Lippert, B.; Thewalt, U.; Schöllhorn, H.; Goodgame, D. M. L.; Rollins, R. W., Formation, Crystal Structure, and EPR Spectroscopic Properties of a Heteronuclear (Pt_2, Cu) Mixed-Nucleobase (1-Methylcytosine, 1-Methyluracil) Complex: Bis[(μ-1-methyluracilato-N^3,O^4)(μ-1-methylcytosine-N^3,O^2)-*cis*-diammineplatinum(II)]-copper(II) Tetranitrate-6-Water. *Inorg. Chem.* **1984,** *23*, 2807–2813.
35. Uemura, K.; Ebihara, M., Paramagnetic One-Dimensional Chains Comprised of Trinuclear Pt−Cu−Pt and Paddlewheel Dirhodium Complexes with Metal−Metal Bonds. *Inorg. Chem.* **2013,** *52*, 5535–5550.
36. Uemura, K.; Ito, D.; Pirillo, J.; Hijikata, Y.; Saeki, A., Modulation of Band Gaps toward Varying Conductivities in Heterometallic One-Dimensional Chains by Ligand Alteration and Third Metal Insertion. *ACS Omega* **2020,** *5*, 30502–30518.
37. Uemura, K.; Miyake, R., Paramagnetic One-Dimensional Chain Complex Consisting of Three Kinds of Metallic Species Showing Magnetic Interaction through Metal–Metal Bonds. *Inorg. Chem.* **2020,** *59*, 1692–1701.
38. Uemura, K.; Aoki, Y.; Takamori, A., Paramagnetic One-dimensional Chain Containing High-spin Manganese Atoms Showing Weak Antiferromagnetic Interaction Through –Pt–Rh–Rh–Pt– Bonds. *Dalton Trans.* **2022,** *51*, 946–957.
39. Chen, C.; Qiu, H.; Liu, F.; Chen, W., Synthesis and Crystal Structure of Pivalamidate-Bridged Trinuclear Platinum–Copper Complex with a Linear Pt–Cu–Pt Core. *J. Chem. Crystallogr.* **2007,** *37*, 619–622.
40. Chen, W.; Matsumoto, K., Pivalamidate-bridged dinuclear platinum and platinum–

palladium complexes: synthesis, NMR and X-ray structural characterization of *cis*-$[Pt(NH_3)_2(NHCO^tBu)_2]\cdot 2H_2O$, and *cis*-$[Pt(NH_3)_2(NHCO^tBu)_2MLL']X_n$ (M = Pt, LL' = cod; L = L' = dmso; L = Cl, L' = dmso; M = Pd, L = L' = NH_3; X = ClO_4^- , NO_3^-). *Inorg. Chim. Acta* **2003,** *342*, 88–96.

41. Cotton, F. A.; Matonic, J. H.; Murillo, C. A., Completion of the series of $Pt_2(ArNC(H)NAr)_4^n$, *n* = 0, +1, +2, compounds, with Pt–Pt sigma bend orders of 0, 1/2, 1, respectively. *Inorg. Chim. Acta* **1997,** *264*, 61–65.
42. Clérac, R.; Cotton, F. A.; Daniels, L. M.; Donahue, J. P.; Murillo, C. A.; Timmons, D. J., Completion of the Series of $M_2(hpp)_4Cl_2$ Compounds from W to Pt: The W, Os, and Pt Compounds. *Inorg. Chem.* **2000,** *39*, 2581–2584.
43. Muller, J.; Freisinger, E.; Miguel, P. J. S.; Lippert, B., Diplatinum(III) Complexes with Four Bridging 1-Methylcytosinato Nucleobases Derived from a Mononuclear *trans*-$(NH_3)_2Pt^{II}$ Complex and Cu^{II}. *Inorg. Chem.* **2003,** *42*, 5117–5125.
44. Bokach, N. A.; Tyan, M. R.; Aleksandrov, G. G.; Haukka, M.; Kukushkin, V. Y., Diplatinum(III) $[Pt_2^{III}Cl_2(\mu_2\text{-amidinate})_4]$ compound derived from air oxidation of mononuclear *cis*-$[Pt^{II}(NH_3)_2(\text{amidine-}\kappa^1)_2]^{2+}$ complex. *Inorg. Chem. Commun.* **2009,** *12*, 1061–1063.
45. Dolmella, A.; Intini, F. P.; Pacifico, C.; Padovano, G.; Natile, G., Structural characterization of the 'lantern-shaped' platinum(III) complex $[Pt_2Cl_2\{N(H)C(Bu^t)O\}_4]$. *Polyhedron* **2002,** *21*, 275–280.
46. Conder, H. L.; Cotton, F. A.; Falvello, L. R.; Han, S.; Walton, R. A., Dinuclear, Metal–Metal-Bonded Platinum(III) Compounds. 2. Synthesis and Properties of Complexes Containing the $[Pt_2(HPO_4)_4(B)_2]_2^-$ Anions (B = a Heterocyclic Tertiary Amine) or the $[Pt_2(H_2PO_4)(HPO_4)_3(py)_2]^-$ Ion. *Inorg. Chem.* **1983,** *22*, 1887–1891.
47. Alexander, K. A.; Bryan, S. A.; Fronczek, F. R.; Fultz, W. C.; Rheingold, A. L.; Roundhill, D. M.; Stein, P.; Watkins, S. F., Crystal and Molecular Structures of Dihalotetrakis(pyrophosphito)diplatinum(III) Complexes. Integrative Use of Structural and Vibrational Data To Assess Intermetallic Bonding and the Trans Influence of the Pt(III)–Pt(III) Bond. *Inorg. Chem.* **1985,** *24*, 2803–2808.
48. Chen, W.; Matsumoto, K., Synthesis and Structural Characterization of Trinuclear, Amidate-Bridged Heterobimetallic Complexes $[\{Pt(NH_3)_2(NHCOtBu)_2\}_2M]X_n$ (M = Mn, Fe, Co, Ni, Cu; X = BF_4^-, ClO_4^-; *n* = 2 or 3). *Eur. J. Inorg. Chem.* **2002,** *46*, 2664–2670.
49. Uemura, K.; Taoka, M., Isolation and characterization of a tetranuclear Pt–Fe···Fe–Pt intermediate *en route* to the trinuclear Pt–Fe–Pt cluster. *Dalton Trans.* **2017,** *46*, 14012–14020.
50. Matsumoto, K.; Sakai, K.; Nishio, K.; Tokisue, Y.; Ito, R.; Nishide, T.; Shichi, Y., Syntheses, Crystal Structures, and Electronic, ESR, and X-ray Photoelectron Spectra of Acetamidate- and 2-Fluoroacetamidate-Bridged Mixed-Valent Octanuclear Platinum Blues. *J. Am. Chem. Soc.* **1992,** *114*, 8110–8118.
51. Carver, J. C.; Schweitzer, G. K.; Carlson, T. A., Use of X-Ray Photoelectron

Spectroscopy to Study Bonding in Cr, Mn, Fe, and Co Compounds. *J. Chem. Phys.* **1972,** *57*, 973–982.

52. Strydom, C. A.; Strydom, H. J., X-ray photoelectron spectroscopy studies of some cobalt(II) nitrate complexes. *Inorg. Chim. Acta* **1989,** *159*, 191–195.
53. Klein, J. C.; Proctor, A.; Hercules, D. M., X-ray Excited Auger Intensity Ratios for Differentiating Copper Compounds. *Anal. Chem.* **1983,** *55*, 2055–2059.
54. Matienzo, L. J.; Yin, L. I.; Grim, S. O.; Swartz, W. E., X-ray photoelectron spectroscopy of nickel compounds. *Inorg. Chem.* **1973,** *12* (12), 2762–2769.
55. Dowsing, R. D.; Gibson, J. F.; Goodgame, D. M. L.; Goodgame, M.; Hayward, P. J., Determination of the Stereochemistry of Manganese(II) Complexes by Electron Spin Resonance. *Nature* **1968,** *219*, 1037–1038.
56. Wagnon, B. K.; Jackels, S. C., Synthesis, characterization, and aqueous proton relaxation enhancement of a manganese(II) heptaaza macrocyclic complex having pendant arms. *Inorg. Chem.* **1989,** *28* (10), 1923–1927.
57. Jiménez-Sandoval, O.; Ramírez-Rosales, D.; Rosales-Hoz, M. d. J.; Sosa-Torres, M. E.; Zamorano-Ulloa, R., Magnetostructural behaviour of the complex $[MnL(H_2O)_2]Cl_2{\cdot}4H_2O$ at variable temperature studied by electron spin resonance (L = 2,13-dimethyl-3,6,9,12,18-pentaazabicyclo[12.3.1]octadeca-1(18),2,12,14,16-pentaene). *J. Chem. Soc., Dalton Trans.* **1998**, 1551–1556.
58. Hansen, S.; Müller-Warmuth, W.; Pilbrow, J.R., *Transition Ion ElectronParamagnetic Resonance*, Clarendon Press, Oxford, 1990.
59. Cox, D. D.; Benkovic, S. J.; Bloom, L. M.; Bradley, F. C.; Nelson, M. J.; Que, L.; Wallick, D. E., Catecholate LMCT bands as probes for the active sites of nonheme iron oxygenases. *J. Am. Chem. Soc.* **1988,** *110* (7), 2026–2032.
60. Ohgo, Y.; Chiba, Y.; Hashizume, D.; Uekusa, H.; Ozekie, T.; Nakamura, M., Novel spin transition between S = 5/2 and S = 3/2 in highly saddled iron(iii) porphyrin complexes at extremely low temperatures. *Chem. Commun.* **2006**, 1935–1937.
61. Guisado-Barrios, G.; Zhang, Y.; Harkins, A. M.; Richens, D. T., Low temperature reaction of $[Fe(TPA)(CH_3CN)_2]^{2+}$ with excess 3-chloroperoxybenzoic acid in semi-frozen acetonitrile; EPR detection of an acylperoxo iron(III) adduct. *Inorg. Chem. Commun.* **2012,** *20*, 81–85.
62. Brown, D. G.; Weser, U., XPS Spectra of Spin-Triplet Cobalt(III) Complexes. *Z. Naturforsch., B: J. Chem. Sci.* **1979,** *34B*, 1468–1470.
63. Yokoi, H.; Isobe, T., On the Hyperfine Structure of the ESR Spectra of Copper(II) Complexes. *Bull. Chem. Soc. Jpn.* **1966,** *39*, 2054.
64. Antosik, S.; Brown, N. M. D.; McConnell, A. A.; Porte, A. L., The Effects of Axial Interactions on Electron Paramagnetic Resonance Spectra of Copper(II) Chelates : Weak Complexes of Copper(II) Chelates and Chloroform *J. Chem. Soc. A* **1969**, 545–550.
65. Adato, I.; Eliezer, I., Effect of the Solvent on the ESR Parameters of Copper Acetylacetonate. *J. Chem. Phys.* **1971,** *54*, 1472–1476.

66. Yokoi, H.; Kishi, T., THE CORRELATION OF THE ESR PARAMETERS OF VARIOUS *β*-DIKETONE CHELATES OF COPPER(II) WITH THE pK_a OF THE LIGANDS *Chem. Lett.* **1973**, 749–754.
67. Kivelson, D.; Neiman, R., ESR Studies on the Bonding in Copper Complexes. *J. Chem. Phys.* **1961,** *35*, 149–155.
68. Gaal, H. L. M. v.; Linden, J. G. M. v. d., Trends in Redox Potentials of Transition Metal Complexes *Coord. Chem. Rev.* **1982,** *47*, 41–54.
69. Uemura, K., Magnetic behavior in heterometallic one-dimensional chains or octanuclear complex regularly aligned with metal–metal bonds as –Rh–Rh–Pt–Cu–Pt. *J. Mol. Str.* **2018,** *1162*, 31–36.
70. Mabbs, F. E.; Machin, D. J., *Magnetism and Transition Metal Complexes*. 1973; Vol. Chapman And Hall.
71. Figgis, B. N.; Hitchman, M. A., *Ligand Field Theory and its Applications*. 2000; Vol. Wiley-VCH: New York.
72. Dey, S. K.; Hazra, M.; Thompson, L. K.; Patra, A., Manganese(II) coordination polymer having pyrazine and *μ*-phenolato bridging: Structure, magnetism and biological studies. *Inorg. Chim. Acta* **2016,** *443*, 224–229.
73. Dingle, R.; Lines, M. E.; Holt, S. L., Linear-Chain Antiferromagnetism in $[(CH_3)_4N][MnCl_3]$. *Phys. Rev.* **1969,** *187*, 643–648.
74. Liu, B.-L.; Xiao, H.-P.; Nfor, E. N.; Song, Y.; You, X.-Z., A new two-dimensional manganese(II) coordination polymer with alternating double end-on and single end-to-end azido bridges: Crystal structure and magnetic properties. *Inorg. Chem. Commun.* **2009,** *12*, 8–10.
75. McElearney, J. N.; Merchant, S.; Carlin, R. L., Isotropic Magnetic Exchange in Magnesium Dichloride Dihydrate, $MnCl_2 \cdot 2H_2O$, a Chemical Linear Chain. *Inorg. Chem.* **1973,** *12*, 906–908.
76. Wu, J.-Z.; Tanase, S.; Bouwman, E.; Reedijk, J.; Mills, A. M.; Spek, A. L., Synthesis, structure and magnetic properties of a linear-chain manganese(II) complex $[Mn(\mu\text{-}Cl)_2(mppma)]_n$, where mppma is *N*-(3-methoxypropyl)-*N*-(pyridin-2-ylmethyl)amine. *Inorg. Chim. Acta* **2003,** *351*, 278–282.
77. Yang, L.; Bian, F.; Yan, S.-p.; Liao, D.-z.; Cheng, P.; Jiang, Z.-h., Structure and magnetic properties of a one-dimensional chain complex $\{[Mn_2(TPA)_2(o\text{-phth})](ClO_4)_2\}_n$. *Inorg. Chem. Commun.* **2003,** *6*, 1188–1191.
78. Albela, B.; Corbella, M.; Ribas, J.; Castro, I.; Sletten, J.; Stoeckli-Evans, H., Synthesis, Structural Characterization (X-ray and EXAFS), and Magnetic Properties of Polynuclear Manganese(II) Complexes with Chlorobenzoato Bridges. *Inorg. Chem.* **1998,** *37*, 788–798.
79. Fernández, G.; Corbella, M.; Mahía, J.; Maestro, M. A., Polynuclear Mn^{II} Complexes with Chloroacetate Bridge – Syntheses, Structure, and Magnetic Properties. *Eur. J. Inorg. Chem.* **2002**, 2502–2510.

80. Simizu, S.; Chen, J.-Y.; Friedberg, S. A., Quasi-one-dimensional antiferromagnetism in $(CH_3NH_3)MnCl_3 \cdot 2H_2O$. *J. Appl. Phys.* **1984,** *55*, 2398–2400.
81. Cano, J.; Munno, G. D.; Sanz, J.; Ruiz, R.; Lloret, F.; Faus, J.; Julve, M., Significant antiferromagnetic coupling in a terephthalate (ta)-bridged manganese(II) compound: preparation, crystal structure and magnetic properties of the chain $[Mn_2(bipy)_4(ta)][ClO_4]_2$ (bipy = 2,2′-bipyridine). *J. Chem. Soc., Dalton Trans.* **1994**, 3465–3469.
82. Chen, W.; Yue, Q.; Chen, C.; Yuan, H.-M.; Xu, W.; Chen, J.-S.; Wang, S.-N., Assembly of a manganese(II) pyridine-3,4-dicarboxylate polymeric network based on infinite Mn–O–C chains. *Dalton Trans.* **2003**, 28–30.
83. Tan, X. S.; Xiang, D. F.; Tang, W. X.; Yu, K. B., Synthesis, crystal structure and magnetic properties of an isophthalate-bridged manganese(II) chain complex. *Polyhedron* **1997,** *16*, 1411–1415.
84. Cicha, W. V.; Haynes, J. S.; Oliver, K. W.; Rettig, S. J.; Thompson, R. C.; Trotter, J., Magnetic properties of anhydrous and hydrated dimethylphosphinates of manganese(II). The crystal and molecular structure of poly-bis(μ-dimethylphosphinato)diaquomanganese(II). *Can. J. Chem.* **1985,** *63*, 1055–1062.
85. Sun, Z.; Gantzel, P. K.; Hendrickson, D. N., One-dimensional polymeric bicinate manganese complex. *Polyhedron* **1997,** *16*, 3267–3271.
86. Dockum, B. W.; Eisman, G. A.; Witten, E. H.; Reiff, W. M., Thiocyanate-bridged transition-metal polymers. 4. A study of the structural, electronic, and magnetic properties of some mono(2,2'-bipyridyl) transition-metal thiocyanates: zigzag polymeric chains based on $Mn(bpy)(NCS)_2$ and $Co(bpy)(NCS)_2$. *Inorg. Chem.* **1983,** *22* (1), 150–156.
87. Borrás-Almenar, J. J.; Burriel, R.; Coronado, E.; Gatteschi, D.; Gómez-Garcia, C. J.; Zanchini, C., Magnetic Interactions and Single-Ion Zero-Field-Splitting Effects in the Two-Sublattice Manganese Chain $MnMn(EDTA) \cdot 9H_2O$: Magnetism and Single-Crystal EPR Spectra. *Inorg. Chem.* **1991,** *30*, 947–950.
88. Thétiot, F.; Triki, S.; Sala-Pala, J.; Golhen, S., The cyanocarbanion $(C[C(CN)_2]_3)^{2-}$ as monodentate ligand: Synthesis, structure and magnetic properties of $[Mn_2(bpym)_3(tcpd)_2(H_2O)_2]$ ($tcpd^{2-}$ = $(C[C(CN)_2]_3)^{2-}$ and bpym = 2,2'-bipyrimidine). *Inorg. Chim. Acta* **2005,** *358*, 3277–3282.
89. Du, J.-L.; Rettig, S. J.; Thompson, R. C.; Trotter, J.; Betz, P.; Bino, A., Structure and magnetic properties of monophenylphosphinate bridged chain polymers of manganese(II), $[MnL_2(HPhPO_2)_2]_x$ (where L = $HPhPO_2H$, CH_3CONH_2, H_2O, $HCONH(CH_3)$, and C_5H_5N). *Can. J. Chem.* **1992,** *70*, 732–741.
90. Paraschiv, C.; Sutter, J.-P.; Schmidtmann, M.; Müller, A.; Andruh, M., $[Mn(MAC)\{\mu_{1.5}\text{-}N(CN)_2\}](PF_6)$: a new one-dimensional coordination polymer with $\mu_{1.5}$-dicyanamido bridges (MAC = pentaaza macrocyclic ligand)–synthesis, crystal structure and magnetic properties. *Polyhedron* **2003,** *22*, 1611–1615.
91. Gutschke, S. O. H.; Price, D. J.; Powell, A. K.; Wood, P. T., Solvothermal

Construction of a Coordination Polymer around in Situ Generated Pyroglutamic Acid: Preparation, Crystal Structure, and Magnetic Behavior of $[Mn(C_5H_6NO_3)_2]_\infty$. *Inorg. Chem.* **2000,** *39*, 3705–3707.

92. Oshio, H.; Ino, E.; Mogi, I.; Ito, T., A weak antiferromagnetic interaction between manganese(2+) centers through a TCNQ column: crystal structures and magnetic properties of $[Mn^{II}(tpa)(TCNQ)(CH_3OH)](TCNQ)_2 \cdot CH_3CN$, $[Mn^{II}(tpa)(\mu\text{-}O_2CCH_3)]_2(TCNQ)_2 \cdot 2CH_3CN$, and $[Mn^{II}(tpa)(NCS)_2] \cdot CH_3CN$ (tpa = tris(2-pyridylmethyl)amine). *Inorg. Chem.* **1993,** *32*, 5697–5703.
93. Madalan, A. M.; Voronkova, V.; Galeev, R.; Korobchenko, L.; Magull, J.; Roesky, H. W.; Andruh, M., Exchange Interactions at the Supramolecular Level – Synthesis, Crystal Structure, Magnetic Properties, and EPR Spectra of $[Mn(MAC)(TCNQ)_2]$ (MAC = Pentaaza Macrocyclic Ligand; $TCNQ^{\cdot -}$ = Radical Anion of 7,7,8,8-Tetracyano-*p*-quinodimethane). *Eur. J. Inorg. Chem.* **2003**, 1995–1999.
94. Yu, L.-C.; Lee, G.-H.; Sigrist, M.; Lin, T.-S.; Peng, S.-M., Structure and Antiferromagnetism of Trinuclear Heterometallic Strings Containing Mn^{II}–M^{II}–Mn^{II} Frameworks (M = Ni, Pd, Pt). *Eur. J. Inorg. Chem.* **2016**, 4250–4256.
95. Pakula, R. J.; Berry, J. F., Cobalt complexes of the chelating dicarboxylate ligand "esp": a paddlewheel-type dimer and a heptanuclear coordination cluster. *Dalton Trans.* **2018,** *47*, 13887–13893.
96. Zhang, S.-Y.; Li, Y.; Li, W., Pyrazolato-bridged 1-D Co(II) coordination polymer and dinuclear Ni(II) and Cu(II) complexes: Syntheses, crystal structures and magnetic properties. *Inorg. Chim. Acta* **2009,** *362*, 2247–2252.
97. Wang, Y.-Q.; Gao, Y.-F.; Tan, Q.-H.; Liu, Z.-L.; Gao, E.-Q., A new cobalt coordination polymer based on Co(II)-azide chains and a tetrapyridyl ligand: Synthesis, unprecedented topology and magnetism. *Inorg. Chem. Commun.* **2014,** *45*, 101–104.
98. Olea, D.; García-Couceiro, U.; Castillo, O.; Gómez-Herrero, J.; Zamora, F., Nanoprocessability of a one-dimensional oxalato-bridged cobalt(II) complex with 1,2,4-triazole. *Inorg. Chim. Acta* **2007,** *360*, 48–54.
99. Kang, J.; Lee, Y.; Kim, S.; Yun, H.; Do, J., 1D and 2D Cobalt(II) Coordination Polymers, Co(ox)(en): Synthesis, Structures and Magnetic Properties. *Bull. Korean Chem. Soc.* **2014,** *35*, 3244–3248.
100. Rueff, J.-M.; Masciocchi, N.; Rabu, P.; Sironi, A.; Skoulios, A., Structure and Magnetism of a Polycrystalline Transition Metal Soap - $Co^{II}[OOC(CH_2)_{10}COO](H_2O)_2$. *Eur. J. Inorg. Chem.* **2001**, 2843–2848.
101. Rueff, J.-M.; Masciocchi, N.; Rabu, P.; Sironi, A.; Skoulios, A., Synthesis, Structure and Magnetism of Homologous Series of Polycrystalline Cobalt Alkane Mono- and Dicarboxylate Soaps. *Chem. −Eur. J.* **2002,** *8*, 1813–1820.
102. Holman, K. T.; Hammud, H. H.; Isber, S.; Tabbal, M., One-dimensional coordination polymer $[Co(H_2O)_4(pyz)](NO_3)_2 \cdot 2H_2O$ (pyz = pyrazine) with intra- and inter-chain H-bonds: structure, electronic spectral studies and magnetic properties. *Polyhedron* **2005,**

24, 221–228.

103. Ma, B.-Q.; Gao, S.; Yi, T.; Xu, G.-X., One-dimensional coordination polymers $[Co(acac)_2pz]_n$ and $[Co(acac)_2(4,4'\text{-bipy})]_n$ (acac = acetylacetone, pz = pyrazine, bipy = 4,4'-bipyridine): synthesis, structures and magnetic properties. *Polyhedron* **2001,** *20*, 1255–1261.
104. P. Alborés; Rentschler, E., Expanding the 2,2'-bipyrimidine bridged 1D homonuclear coordination polymers family: $[M^{II}(bpym)Cl_2]$ (M = Fe, Co) magnetic and structural characterization. *Dalton Trans.* **2013,** *42*, 9621–9627.
105. Munno, G. D.; Poerio, T.; Julve, M.; Lloret, F.; Viau, G., Synthesis, crystal structure and magnetic properties of the cobalt(II) chain $[Co(bipym)(H_2O)_2](NO_3)_2$ and the dinuclear compounds $[Co_2(bipym)_3(H_2O)_4](NO_3)_4{\cdot}2H_2O$ and $[Co_2(bipym)_3(H_2O)_2(SO_4)_2]{\cdot}12H_2O$. *New J. Chem.* **1998**, 299–305.
106. Roy, S.; Choubey, S.; Khan, S.; Bhar, K.; Ribas, J.; Ghosh, B. K., Synthesis, characterization and magnetic property of a succinate bridged 1D coordination polymer of cobalt(II) containing benzidine as end-capping ligand. *J. Mol. Str.* **2014,** *1061*, 54–60.
107. Majumder, A.; Gramlich, V.; Rosair, G. M.; Batten, S. R.; Masuda, J. D.; Fallah, M. S. E.; Ribas, J.; Sutter, J.-P.; Desplanches, C.; Mitra, S., Five New Cobalt(II) and Copper(II)-1,2,4,5-benzenetetracarboxylate Supramolecular Architectures: Syntheses, Structures, and Magnetic Properties. *Cryst. Growth Des.* **2006,** *6*, 2355–2368.
108. Rohmer, M.-M.; Liu, I. P.-C.; Lin, J.-C.; Chiu, M.-J.; Lee, C.-H.; Lee, G.-H.; Bénard, M.; López, X.; Peng, S.-M., Structural, Magnetic, and Theoretical Characterization of a Heterometallic Polypyridylamide Complex. *Angew. Chem., Int. Ed.* **2007,** *46*, 3533–3536.
109. Zhang, W.-L.; He, Z.-Z.; Xia, T.-L.; Luo, Z.-Z.; Zhang, H.; Lin, C.-S.; Cheng, W.-D., Syntheses and Magnetic Properties Study of Isostructural $BiM_2BP_2O_{10}$ (M = Co, Ni) Containing a Quasi-1D Linear Chain Structure. *Inorg. Chem.* **2012,** *51*, 8842–8847.
110. Ma, K.-R.; Xu, J.-N.; Ning, D.-K.; Shi, J.; Zhang, D.-J.; Fan, Y.; Song, T.-Y., Solvothermal syntheses, characterizations and properties of two new Ni^{II}-PMIDA phosphonates. *Inorg. Chem. Commun.* **2009,** *12*, 119–121.
111. Colacio, E.; Domínguez-Vera, J. M.; Ghazi, M.; Kivekäs, R.; Klinga, M.; Moreno, J. M., Singly anti-anti Carboxylate-Bridged Zig-Zag Chain Complexes from a Carboxylate-Containing Tridentate Schiff Base Ligand and $M(hfac)_2$ [M = Mn^{II}, Ni^{II}, and Cu^{II}]: Synthesis, Crystal Structure, and Magnetic Properties. *Eur. J. Inorg. Chem.* **1999**, 441–445.
112. Hoffman, A. E.; Marino, N.; Lloret, F.; Julve, M.; Doyle, R. P., Synthesis, structural, thermal, and magnetic investigations of Co(II), Ni(II), and Mn(II) pyrophosphate chains. *Inorg. Chim. Acta* **2012,** *389*, 151–158.
113. Zhang, C.-Z.; Mao, H.-Y.; Wang, J.; Zhang, H.-Y.; Tao, J.-C., Hydrothermal self-organization of two 2,2'-bipyridine-3,3'-dicarboxylate bridged polymers of Tb^{III} and Ni^{II} involving in situ ligand synthesis. *Inorg. Chim. Acta* **2007,** *360*, 448–454.

114. Choi, K.-Y.; Chun, K. M.; Suh, I.-H., Synthesis and characterization of one-dimensional nickel(II) macrocyclic complexes with bridging organic ligands. *Polyhedron* **2001,** *20*, 57–65.
115. Escuer, A.; Vicente, R.; Ribas, J.; Fallah, M. S. E.; Solans, X.; Font-Bardía, M., *trans*-[Ni(333-tet)(μ-N_3)]$_n$(ClO_4)$_n$ and *cis*-[Ni(333-tet)(μ-N_3)]$_n$(PF_6)$_n$: Two Novel Kinds of Structural Nickel(II) Chains with a Single Azido Bridge. Magnetic Behavior of an Alternating $S = 1$ chain with $\alpha = 0.46$. *Inorg. Chem.* **1994,** *33*, 1842–1847.
116. Vicente, R.; Escuer, A.; Ribas, J.; Fallah, M. S. E.; Solans, X.; Font-Bardia, M., X-ray Structure Determination and Magnetic Behavior of the New Uniform $S = 1$ Chain [{Ni(Me_2[14]-1,3-dieneN_4)(μ-N_3)}$_n$]($ClO4$)$_n$. Magneto–Structural Correlations. *Inorg. Chem.* **1995,** *34*, 1278–1281.
117. Ribas, J.; Monfort, M.; Diaz, C.; Bastos, C.; Mer, C.; Solans, X., Two New One-Dimensional Antiferromagnetic Nickel(II) Complexes Bridged by Azido Ligands in Cis Positions. Effect of the Counteranion on the Magnetic Properties. *Inorg. Chem.* **1995,** *34*, 4986–4990.
118. Kauffman, G. B.; Cowan, D. O.; Slusarczuk, G.; Kirschner, S., *cis- and trans-Dichlorodiammineplatinum(II)*. 1963; Vol. VII.
119. Lee, C. T.; Yang, W. T.; Parr, R. G., Development of the Colle-Salvetti correlation-energy formula into a functional of the electron density. *Phys. Rev. B* **1988,** *37*, 785–789.
120. Miehlich, B.; Savin, A.; Stoll, H.; Preuss, H., Results obtained with the correlation energy density functionals of becke and Lee, Yang and Parr. *Chem. Phys. Lett.* **1989,** *157*, 200–206.
121. Becke, A. D., Density-functional thermochemistry. III. The role of exact exchange. *J. Chem. Phys.* **1993,** *98*, 5648–5652.
122. Gaussian 16, Revision C.01, Frisch, M. J.; Trucks, G. W.; Schlegel, H. B.; Scuseria, G. E.; Robb, M. A.; Cheeseman, J. R.; Scalmani, G.; Barone, V.; Petersson, G. A.; Nakatsuji, H.; Li, X.; Caricato, M.; Marenich, A. V.; Bloino, J.; Janesko, B. G.; Gomperts, R.; Mennucci, B.; Hratchian, H. P.; Ortiz, J. V.; Izmaylov, A. F.; Sonnenberg, J. L.; Williams-Young, D.; Ding, F.; Lipparini, F.; Egidi, F.; Goings, J.; Peng, B.; Petrone, A.; Henderson, T.; Ranasinghe, D.; Zakrzewski, V. G.; Gao, J.; Rega, N.; Zheng, G.; Liang, W.; Hada, M.; Ehara, M.; Toyota, K.; Fukuda, R.; Hasegawa, J.; Ishida, M.; Nakajima, T.; Honda, Y.; Kitao, O.; Nakai, H.; Vreven, T.; Throssell, K.; Montgomery, J. A., Jr.; Peralta, J. E.; Ogliaro, F.; Bearpark, M. J.; Heyd, J. J.; Brothers, E. N.; Kudin, K. N.; Staroverov, V. N.; Keith, T. A.; Kobayashi, R.; Normand, J.; Raghavachari, K.; Rendell, A. P.; Burant, J. C.; Iyengar, S. S.; Tomasi, J.; Cossi, M.; Millam, J. M.; Klene, M.; Adamo, C.; Cammi, R.; Ochterski, J. W.; Martin, R. L.; Morokuma, K.; Farkas, O.; Foresman, J. B.; Fox, D. J. Gaussian, Inc., Wallingford CT, 2016.
123. Hay, P. J.; Wadt, W. R., Ab initio effective core potentials for molecular calculations. Potentials for K to Au including the outermost core orbitals. *J. Chem. Phys.* **1985,** *82*, 299–310.

124. Hariharan, P. C.; Pople, J. A., The influence of polarization functions on molecular orbital hydrogenation energies. *Theo. Chim. Acta* **1973,** *28*, 213–222.
125. Casida, M. E.; Jamorski, C.; Casida, K. C.; Salahub, D. R., Molecular excitation energies to high-lying bound states from time-dependent density-functional response theory: Characterization and correction of the time-dependent local density approximation ionization threshold. *J. Chem. Phys.* **1998,** *108*, 4439–4449.
126. Stratmann, R. E.; Scuseria, G. E.; Frisch, M. J., An efficient implementation of time-dependent density-functional theory for the calculation of excitation energies of large molecules. *J. Chem. Phys.* **1998,** *109*, 8218–8224.
127. CrysAlisPRO, Oxford Diffraction /Agilent Technologies UK Ltd, Yarnton, England.
128. SCALE3 ABSPACK, An Oxford Diffraction program, 2005 Oxford Diffraction Ltd.
129. Altomare, A.; Burla, M. C.; Camalli, M.; Cascarano, G. L.; Giacovazzo, C.; Guagliardi, A.; Moliterni, A. G. G.; Polidori, G.; Spagna, R., SIR97: a new tool for crystal structure determination and refinement. *J. Appl. Cryst.* **1999,** *32*, 115–119.
130. Sheldrick, G. M., A short history of SHELX. *Acta Cryst.* **2008,** *A64*, 112–122.
131. Kabuto, C.; Akine, S.; Nemoto, T.; Kwon, E., *J. Cryst. Soc. Jpn.* **2009,** *51*, 218–224.

Chapter 2

Paramagnetic One-Dimensional Chains Aligning First Transition Metals Showing Significant Magnetic Coupling through −Pt···Pt− Bonds

Abstract

Paramagnetic trinuclear complexes, *trans*-$[Pt_2M(acam)_4(NH_3)_4](ClO_4)_2$ (**1-M**; acam = acetamidate, M = Co, Ni, and Cu), aligned as Pt–M–Pt were successfully synthesized and characterized by single-crystal X-ray structure analyses and physical measurements. The trinuclear complexes extend infinitely one-dimensional chains formed ···Pt–M–Pt···Pt–M–Pt··· alignments with Pt···Pt interactions between the adjacent end Pt atoms in close contact with each other (approximately 3.5 Å). Several physical measurements revealed all three first-row transition metals in **1-M** have high-spin states, where unpaired electrons are localized on M atoms, which three (**1-Co**), two (**1-Ni**), and one (**1-Cu**) respectively. Magnetic susceptibility measurements for **1-Co** and **1-Ni** showed relatively strong antiferromagnetic interaction (**1-Co**: $2J = -17.9$ cm^{-1}, **1-Ni**: $2J = -27.9$ cm^{-1}) between the high-spin M centers through Pt···Pt bonds. In contrast, **1-Cu** showed ferromagnetic interaction (**1-Cu**: $2J = 0.28$ cm^{-1}) between the Cu centers through Pt···Pt bonds, probably due to dz^2-ground state from dx^2–y^2 state on some Cu atoms in the chain where the energy level of dz^2 orbital was increased by one-dimensional chain.

Introduction

Generally, in order to regulate various metals or metalcluster complexes alignment in the solid state, coordination bonds by organic ligands and halide ions are very useful. The coordination polymers[1] and metal–organic frameworks[2] had been observed to show characteristic interactions and physical property through metal d orbitals and organic ligands σ or π orbitals.[3-6] In contrast, one-dimensional metal chain complexes have attracted on attention due to their conductivities[7,8] and magnetisim[9] through direct metal d orbitals interactions. These one-dimensional metal chain complexes are classified into two types of compounds, finite and infinite chains. The finite type of one-dimensional metal chain complexes is called extended metal atom chains (EMACs) and heteronuclear metal string complexes (HMSCs), which well-known synthetic method is mixing and refluxing multidentate ligands and several metals.[10-15] To date, various kinds of one-dimensional chain complexes have been reported, based on the combinations of multidentate ligands of various lengths and metal species, while it is still difficult to achieve the placement of metal species in desired positions. Then, in order to regulate metal species in desired positions, Pt metalloligand complexes have been utilized to selectively obtain heteronuclear complexes due to the combination of Pt and desired metals.[16] For example, thioacetate-bridged paddlewheel heterometallic Pt–M complexes, which are dimerized as M–Pt···Pt–M, show strong magnetic interactions through metal–metal bonds.[17-19] In contrast, general infinite one-dimensional chain synthetic methods are available through the oxidation of d^8 square-planar metals connecting to other metals at the dz^2 orbital, as a result of partially oxidized dz^2 bands showing metal–metal chains. Since metal species in infinite one-dimensional metal complexes are very restricted to d^7 or d^8 metal species[20-29], new approaches are required to construct such complexes using various metal species.

Previously, we reported the *trans*-bridged trinuclear Pt–M–Pt complexes, *trans*-$[Pt_2M(piam)_4(NH_3)_4](ClO_4)_2$ (***t*-M**, piam = pivalamidate, M =Mn, Co, Ni, and Cu) dimerized to align in Pt–M–Pt···Pt–M–Pt.[30] Such *trans*-bridged trinuclear Pt–M–Pt complexes are expected to possibly to further extended interaction of the outer Pt atoms as well. We were successful in obtaining *trans*-$[Pt_2M(acam)_4(NH_3)_4](ClO_4)_2$ (**1-M**, acam = acetamidate), which is expected to be extended infinite one-dimensional metal chain complexes with –Pt···Pt– bonds (Scheme 1). This infinite one-dimensional metal chain shows a significant magnetic interaction in the intra chain through –Pt···Pt– bonds.

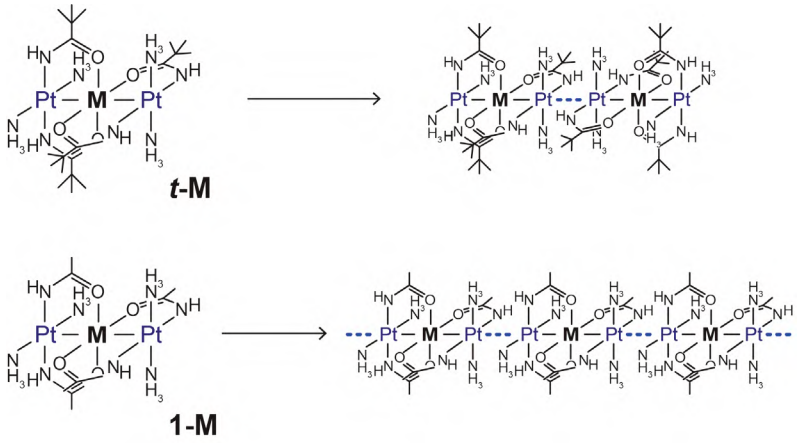

Scheme 1. Dimerized structure and infinite one-dimensional chain structure by –Pt···Pt– bonds of *trans*-bridged trinuclear Pt–M–Pt complexes containing paramagnetic species (M).

Result and Discussion

Synthetic Procedure.

The amidate-hanging Pt mononuclear complex, *trans*-$[Pt(piam)_2(NH_3)_2]$, is a useful precursor for heterometal multinuclear complexes, where the non-coordinated oxygen atoms are easily bound to second metals (M) in solution.[30] The previous amidate-hanging Pt mononuclear complex, *trans*-$[Pt(piam)_2(NH_3)_2]$, was obtained by the hydrolysis of nitrile in *trans*-$[Pt(NC^tBu)_2(NH_3)_2](ClO_4)_2$ under the basic conditions. Such direct ligand conversion of coordinated nitrile to amidate precludes the dimerization of platinum atoms bridged by amidate ligands, only giving mononuclear complexes as the precursor for further multinuclear complexes. As mentioned in the experimental section, preparing *trans*-$[Pt(NCMe)_2(NH_3)_2](ClO_4)_2$ from *trans*-$[PtCl_2(NH_3)_2]$ as the precursor of amidate-hanging Pt mononuclear complex, *trans*-$[Pt(acam)_2(NH_3)_2]$ (**1**) was successfully obtained by the hydrolysis of nitrile. Thereafter, mixing *trans*-$[Pt(acam)_2(NH_3)_2]$, MCl_2 (M = Co, Ni, and Cu), and Bu_4NClO_4 in MeOH afforded single-crystals of *trans*-$[Pt_2M(acam)_4(NH_3)_4](ClO_4)_2$ (**1-M**). The crystal dates and structure refinement results are summarized in Table 1. As shown in the crystal structures (Figure 1), all **1-M** have a Pt–M–Pt trinuclear structure where each metal is bridged by two acam ligands in a *trans* fashion.

Table 1. Crystallographic data and structure refinements for *trans*-[$Pt_2Co(acam)_4(NH_3)_4$](ClO_4)$_2$ (**1-Co**), *trans*-[$Pt_2Ni(acam)_4(NH_3)_4$](ClO_4)$_2$ (**1-Ni**), and *trans*-[$Pt_2Cu(acam)_4(NH_3)_4$](ClO_4)$_2$ (**1-Cu**).

	1-Co	**1-Ni**	**1-Cu**
Empirical formula	$C_8H_{28}Cl_2CoN_8O_{12}Pt_2$	$C_8H_{28}Cl_2NiN_8O_{12}Pt_2$	$C_8H_{28}Cl_2CuN_8O_{12}Pt_2$
Formula weight	948.39	948.17	953.00
Crystal system	Monoclinic	Monoclinic	Monoclinic
Space group	*P*2/*n*	*P*2/*n*	*P*2/*n*
a (Å)	17.6048(9)	17.6032(12)	17.5545(9)
b (Å)	8.8450(2)	8.6864(3)	8.7889(3)
c (Å)	18.0482(9)	18.1558(12)	18.1046(9)
α (°)	90	90	90
β (°)	118.379(7)	117.652(8)	117.721(7)
γ (°)	90	90	90
V (Å^3)	2472.6(2)	2459.1(3)	2472.7(2)
Z	4	4	4
Temperature (K)	293	293	293
*D*c (Mgm^{-3})	2.548	2.561	2.560
Absorption coefficient (mm^{-1})	12.234	12.392	12.423
F(000)	1780	1784	1788
Crystal size (mm^3)	0.10 × 0.20 × 0.28	0.02 × 0.10 × 0.18	0.05 × 0.12 × 0.30
Measured reflections	32731	31897	32243
Independent reflections	5679 [R_{int} = 0.0353]	5649 [R_{int} = 0.0589]	5691 [R_{int} = 0.0435]
Goodness-of fit on F^2	0.918	0.881	0.937
R [$I > 2\sigma(I)$]	R_1 = 0.0319, wR_2 = 0.1142	R_1 = 0.0407, wR_2 = 0.1193	R_1 = 0.0351, wR_2 = 0.1200
R (all data)	R_1 = 0.0447, wR_2 = 0.1254	R_1 = 0.0722, wR_2 = 0.1421	R_1 = 0.0531, wR_2 = 0.1339

Crystal Structures of *trans*-[$Pt_2M(acam)_4(NH_3)_4$](ClO_4)$_2$.

Figure 1 shows the crystal structure of *trans*-[$Pt_2Co(piam)_4(NH_3)_4$](ClO_4)$_2$ (**1-Co**). The Co atoms are sandwiched between two Pt atoms, where four acam ligands are bridged in a *trans* fashion, affording in a linear Pt–Co–Pt alignment (Figure 1a–b). There are four crystallographically independent Pt atoms and two crystallographically independent Co atoms, which form two crystallographically independent Pt–Co–Pt trinuclear complexes (Figure 1a–b). The Pt–Co distances are Pt(1)–Co(1) = 2.6188(12), Pt(2)–Co(1) = 2.6372(13), Pt(3)–Co(2) = 2.6106(11), and Pt(4)–Co(2) = 2.6211(11) Å. Compared with two crystallographically independent Pt–Co–Pt trinuclear complexes, the values of the torsional angle for acam and NH_3 ligand for both sides of the Pt atoms are 8.4° and 29.3°, respectively (Figure 1a–b: right side). The NH_3 ligands coordinated to Pt atoms are hydrogen bonded to the oxygen atoms of the acam ligands with a distance of 2.9 Å between the atoms. Considering the chemical formula **1-Co**, the sum of the metal oxidation states of Pt–Co–Pt is +6, where the formal oxidation states are Pt(+2)–Co(+2)–Pt(+2), because Pt(+3) complexes favor an axial coordination with anions, which the metal oxidation state for each metal is unchanged from the original compounds during the reaction. The most remarkable feature of **1-Co** is that each trinuclear complex are extended to be infinity one-dimensional chains ···Pt(1)–Co(1)–Pt(2)···Pt(1′)–Co(1′)–Pt(2′)··· or ···Pt(3)–Co(2)–Pt(4)···Pt(3′)–Co(2′)–Pt(4′)···, where ClO_4^- anions are bridged with hydrogen bonds to NH_3 and nitrogen atoms of acam ligand. The Pt···Pt distances are Pt(2)···Pt(1) = 3.5889 and Pt(4)···Pt(3) = 3.6133 Å, respectively. The Co---Co distances for the intra chain are 8.845 Å. Each chain runs along the *b* axis and is separated from the nearest chains with intermetallic distance of 8.8050 Å between the two Co center (Figure 1d–e).

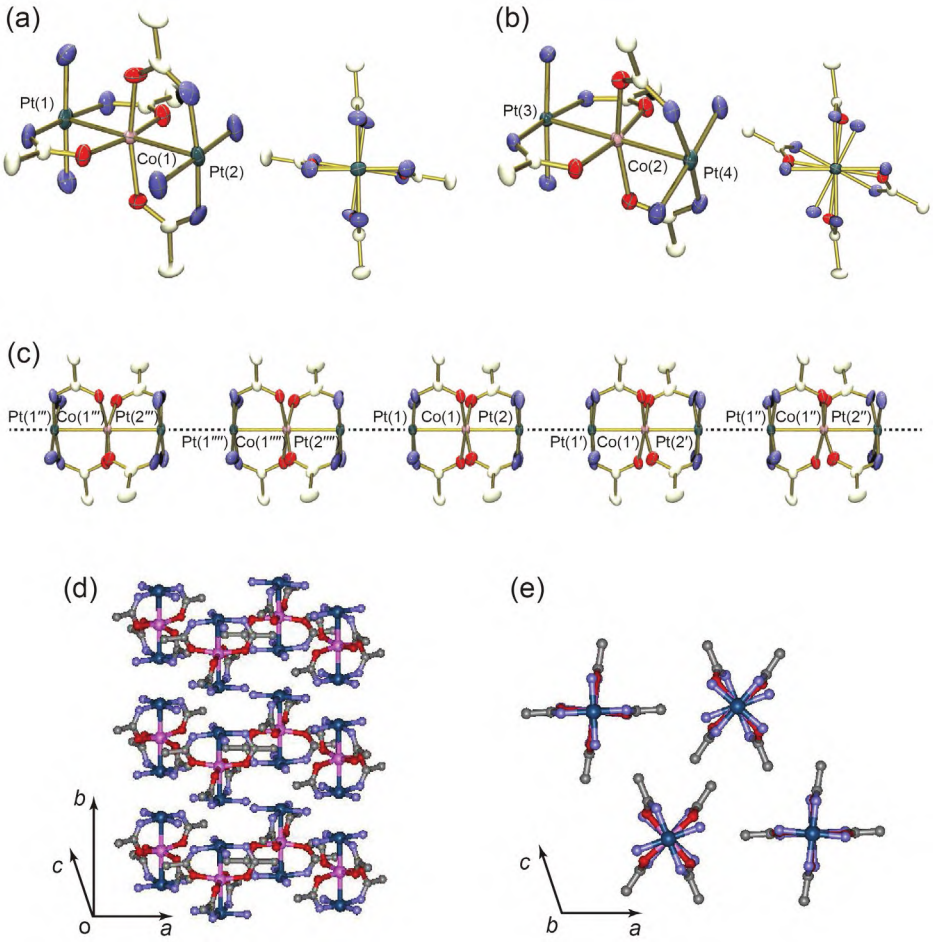

Figure 1. Molecular structure of (a) and (b) *trans*-$[Pt_2Co(piam)_4(NH_3)_4](ClO_4)_2$ (**1-Co**). The right sides are the views along the metal–metal bonds. (c) Pentamer structure of **1-Co**. (d) Packing view perpendicular with the metal–metal bonds. (e) Packing view along the metal–metal bonds. The hydrogen atoms and ClO_4^- ions are omitted for clarity.

As shown in Figures 2 and 3, *trans*-$[Pt_2Ni(piam)_4(NH_3)_4](ClO_4)_2$ (**1-Ni**) and *trans*-$[Pt_2Cu(piam)_4(NH_3)_4](ClO_4)_2$ (**1-Cu**) also formed trinuclear structures aligned with Pt–M–Pt. In **1-Ni** and **1-Cu**, there were four crystallographically independent Pt atoms and two crystallographically independent M atoms which form two crystallographically independent Pt–M–Pt trinuclear complexes (Figures 2a–b, 3a–b). The Pt–M distances are **1-Ni**: Pt(1)–Ni(1) = 2.5960(16), Pt(2)–Ni(1) = 2.5849(16), Pt(3)–Ni(2) = 2.5838(16), and Pt(4)–Ni(2) = 2.5739(16) Å, and **1-Cu**: Pt(1)–Cu(1) = 2.6574(14), Pt(2)–Cu(1) = 2.6551(14), Pt(3)–Cu(2) = 2.6398(13), and Pt(4)–Cu(2) = 2.6514(13) Å. As shown in Figures 2a–b and 3a–b, the values of the torsional angle for acam and NH_3 ligand for both sides of the Pt atoms are similar to those for **1-Co**. In **1-Ni** and **1-Cu**, the sum of the metal oxidation states of Pt–M–Pt is +6, respectively, the formal oxidation states are Pt(+2)–M(+2)–Pt(+2), which is unchanged from the original

compounds during the reaction. Similar to **1-Co**, each trinuclear complex is extended to have infinity one-dimensional chains, with Pt(2)···Pt(1) distances of 3.5056 Å (**1-Ni**) and 3.4764 Å (**1-Cu**), Pt(4)···Pt(3) distances of 3.5287 Å (**1-Ni**) and 3.4977 Å (**1-Cu**). The M---M distances for intra chain are **1-Ni**: Ni---Ni = 8.686 Å and **1-Cu**: Cu---Cu = 8.789 Å, respectively. Each chain runs along the *b* axis and is separated from the nearest chains with intermetallic distance of 8.8050 Å (**1-Ni**) and 8.7815 Å (**1-Cu**) between the two M center.

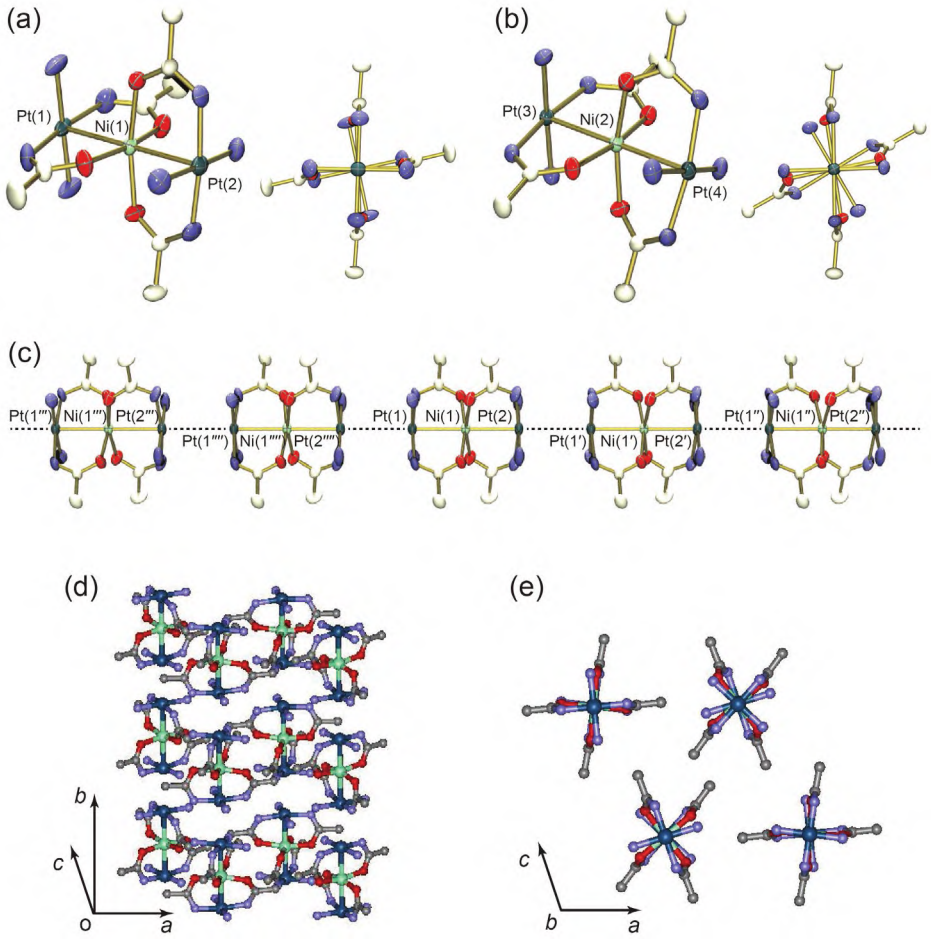

Figure 2. Molecular structure of (a) and (b) *trans*-$[Pt_2Co(piam)_4(NH_3)_4](ClO_4)_2$ (**1-Ni**). Right sides are views along the metal–metal bonds. (c) Pentamer structure of **1-Ni**. (c) Packing view perpendicular with the metal–metal bonds. (d) Packing view along the metal–metal bonds. The hydrogen atoms and ClO_4^- ions are omitted for clarity.

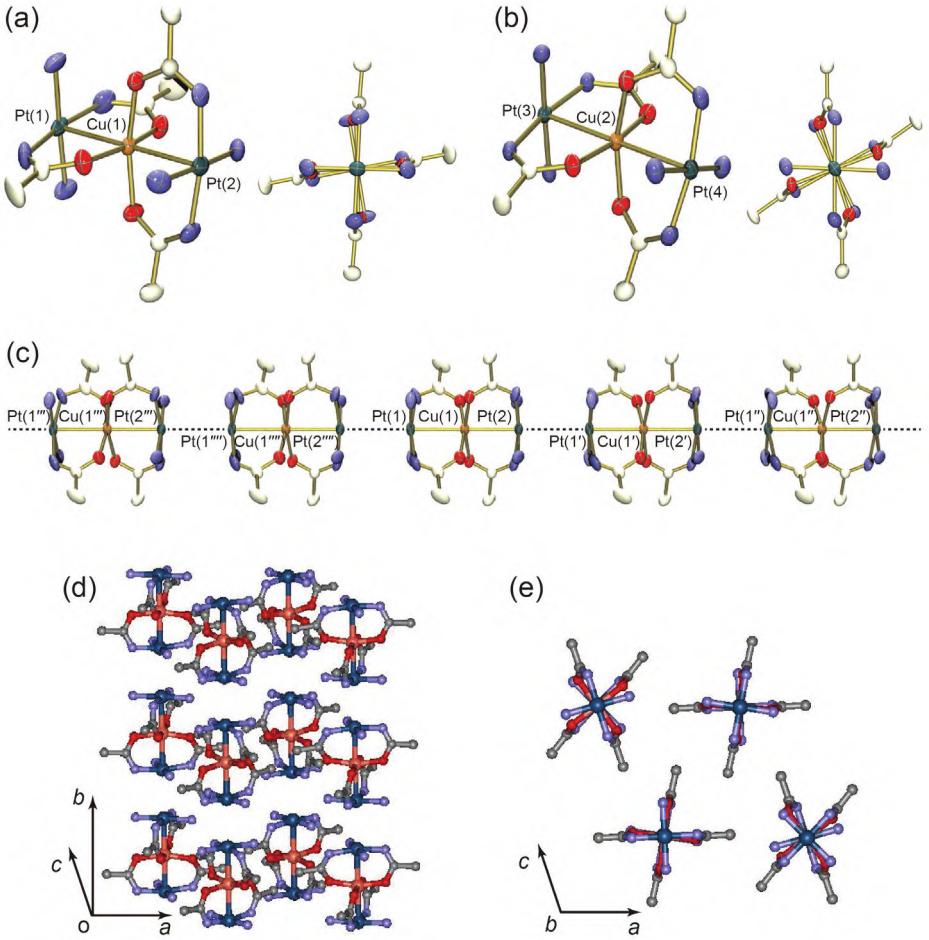

Figure 3. Molecular structure of (a) and (b) *trans*-$[Pt_2Cu(piam)_4(NH_3)_4](ClO_4)_2$ (**1-Cu**). Right sides are views along the metal–metal bonds. (c) Pentamer structure of **1-Cu**. (c) Packing view perpendicular with the metal–metal bonds. (d) Packing view along the metal–metal bonds. The hydrogen atoms and ClO_4^- ions are omitted for clarity.

Table 2 summarizes the metal–metal distances and angles between *trans*-$[Pt_2M(piam)_4(NH_3)_4](ClO_4)_2$ (***t*-M**) and **1-M**.[30] Among the series of trans coordinated compounds, the Pt−M distances tend to be in the same order as ***t*-Cu** > ***t*-Co** > ***t*-Ni** and **1-Cu** > **1-Co** > **1-Ni**. In ***t*-M** and **1-M**, the dihedral angles between the Pt and M coordination planes are approximately zero indicating that the planes are parallel, which is attributed to the *trans* bridging. Although the angles of Pt–M–Pt for ***t*-M** are approximately 177°, showing that it is slight bending from the 1D axis, while in the case of **1-M** it is 180° showing the straight stacking of metals. The angles of M–Pt···Pt for ***t*-M** are ***t*-Co**: ∠Co–Pt···Pt = 160.98(2)°, ***t*-Ni**: ∠Ni–Pt···Pt = 161.46(2)°, and ***t*-Cu**: ∠Cu–Pt···Pt = 161.08(2)° showing the stacking of each Pt–M–Pt complex is bent from the 1D axis, **1-M** are **1-Co**: ∠Co–Pt···Pt = 180.0°, **1-Ni**: ∠Ni–Pt···Pt = 180.0°, and **1-Cu**: ∠Cu–Pt···Pt = 180.0° showing the stacking of each Pt–M–Pt complex is

aligned along the 1D axis. Although the distance of Pt···Pt for ***t*-M** is approximately 3.9 Å, that for **1-M** is approximately 3.5 Å, showing short contact between Pt atoms. Furthermore, ***t*-M** only extends dimer structures, whereas **1-M** extends infinitely extended infinity one-dimensional chains. These are probably because the more proximity of the end Pt atoms due to the smaller bridging ligands helps the multimerization. The microcrystals of **1-M** were used for physical measurements, in which the X-ray powder diffraction coincided well with those calculated from single-crystal X-ray analyses (Figure S1).

Table 2. Comparison of selected distances and angles between *trans*-[$Pt_2Co(piam)_4(NH_3)_4](ClO_4)_2$ (***t*-Co**), *trans*-[$Pt_2Ni(piam)_4(NH_3)_4](ClO_4)_2$ (***t*-Ni**), and *trans*-[$Pt_2Cu(piam)_4(NH_3)_4](ClO_4)_2$ (***t*-Cu**) and *trans*-[$Pt_2Co(acam)_4(NH_3)_4](ClO_4)_2$ (**1-Co**), *trans*-[$Pt_2Ni(acam)_4(NH_3)_4](ClO_4)_2$ (**1-Ni**), and *trans*-[$Pt_2Cu(acam)_4(NH_3)_4](ClO_4)_2$ (**1-Cu**).

	Pt–M (Å)	Pt···Pt (Å)	Pt–M–Pt (°)	M–Pt···Pt (°)	Dihedral angles (°)	ref
***t*-Co**	2.6193(5), 2.6236(5)	3.8688(5)	177.66(2)	160.98(2)	0.6, 2.1	30
***t*-Ni**	2.5850(5), 2.5892(5)	3.9584(5)	177.84(2)	161.46(2)	0.3, 1.6	30
***t*-Cu**	2.6495(5), 2.6575(5)	3.8475(5)	177.72(2)	161.08(2)	0.6, 1.7	30
1-Co	2.6188(12), 2.6372(13),	3.5889	180.0	180.0	0.0	this work
	2.6106(11), 2.6211(11)	3.6133	180.0	180.0	0.0	
1-Ni	2.5849(16), 2.5960(16),	3.5056	180.0	180.0	0.0	this work
	2.5739(16), 2.5838(16)	3.5287	180.0	180.0	0.0	
1-Cu	2.6551(14), 2.6574(14),	3.4764	180.0	180.0	0.0	this work
	2.6398(13), 2.6514(13)	3.4977	180.0	180.0	2.5, 2.6	

Oxidation and Spin States of *trans*-$[Pt_2M(acam)_4(NH_3)_4](ClO_4)_2$.

XPS measurements were performed to determine the metal oxidation states in **1-M** (Figure 3). The Pt $4f_{7/2}$ binding energy for **1** is 72.8 eV, which is closer to the previous compounds of $[Pt_2^{II,II}(en)_2(\alpha\text{-pyridonato})_2](NO_3)_2$ (73.1 eV; en = ethylenediamine) than $[Pt_2^{III,III}(NH_3)_4(\alpha\text{-pyrrolidonato})_2(NO_3)_2](NO_3)_2$ (74.6 eV).[31] As summarized in Table 3, both the Pt $4f_{7/2}$ and $4f_{5/2}$ binding energies for **1-Co**, **1-Ni**, and **1-Cu** are close values for Pt(+2). The Co $2p_{3/2}$ binding energies for **1-Co** are 781.1 eV, which is closer to that for $Co^{II}(NO_3)_2$ (781.0 eV)[32] with high-spin state than $[Co^{III}(NH_3)_6]Cl_3$ (781.4 eV) with low-spin state.[33] Considering that high-spin Co(+2) normally exhibits a rather strong satellite at approximately 5 eV higher binding energy from the main peak, the Co $2p_{1/2}$ and $2p_{3/2}$ binding energies are 796.8 and 781.1 eV with broad satellite peaks at 802.9 and 784.9 eV, indicating high-spin Co(+2).[33] The Ni $2p_{3/2}$ binding energies for **1-Ni** are 855.3, which is closer to that for $Ni^{II}Cl_2$ (855.3 eV) with d^8 high-spin state than $[Ni^{II}(diars)_2Cl_2][ClO_4]_2$ (854.7 eV) with d^6 low-spin state.[34] The Ni $2p_{1/2}$ and $2p_{3/2}$ binding energies are 873.1 and 855.3 eV with satellite peaks at 880.3 and 860.1 eV, indicating high-spin Ni(+2) because high-spin Ni(+2) is normally observed as satellite peaks in only paramagnetic compounds.[34] The Cu $2p_{3/2}$ binding energies for **1-Cu** are 933.6 eV, which is closer to that for $Cu^{II}Cl_2$ (933.8 eV) than $Cu^{I}Cl$ (932.2 eV).[35] Consequently, based on the crystal structure and XPS measurement, the formal oxidation states for **1-M** are ⋯Pt(+2)–M(+2)–Pt(+2)⋯Pt(+2)–M(+2)–Pt(+2)⋯ with high-spin state, Co(+2), Ni(+2), and Cu(+2) have d^7, d^8, and d^9 configurations, respectively.

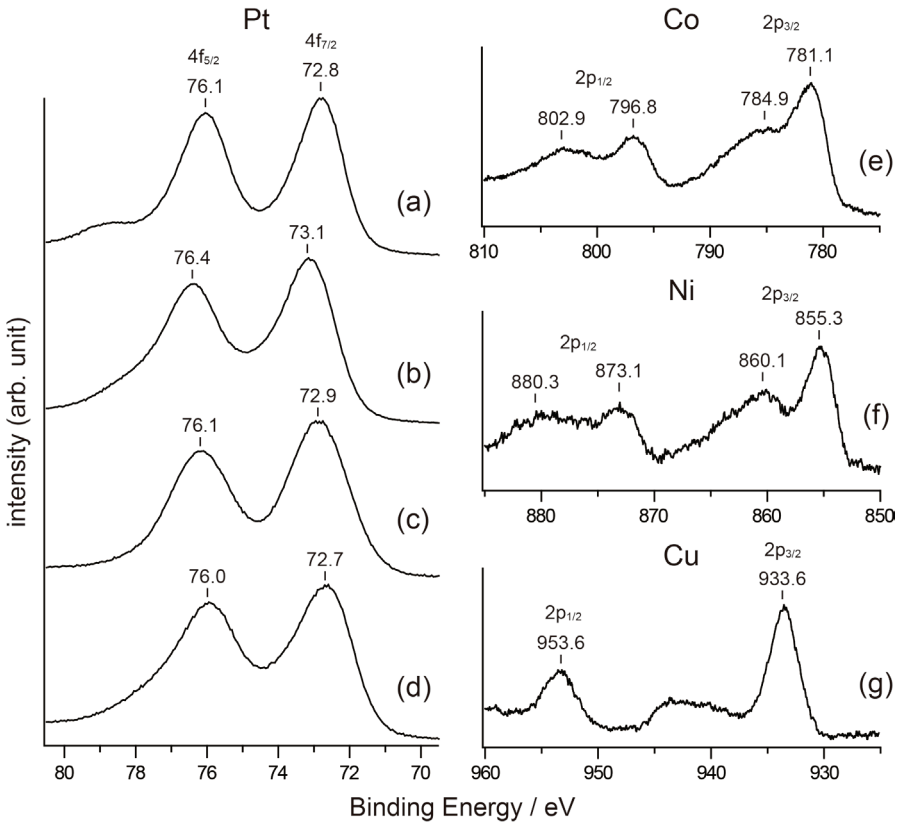

Figure 3. Pt $4f_{5/2}$ and $4f_{7/2}$ and M $2p_{1/2}$ and $2p_{3/2}$ core levels of XPS for (a) **1**, (b) **1-Co**, (c) **1-Ni**, (d) **1-Cu**, (e) **1-Co**, (f) **1-Ni**, and (g) **1-Cu**.

Table 3. The binding energies (eV) for 4f of Pt and 2p of M in **1** and **1-M**.

	Pt $4f_{5/2}$	Pt $4f_{7/2}$	M $2p_{1/2}$	M $2p_{3/2}$
1	76.1	72.8	-	-
1-Co	76.4	73.1	802.9, 796.8	784.9, 781.1
1-Ni	76.1	72.9	880.3, 873.1	860.1, 855.3
1-Cu	76.0	72.7	953.6	933.6

As shown in Figure 4, the EPR spectra for powdered ***t*-Cu** and **1-Cu** at 77 K show an axial-type signal with ***t*-Cu**, $g_{//} = 2.35$ and $g_{\perp} = 2.07$, and with **1-Cu**, $g_{//} = 2.36$ and $g_{\perp} = 2.06$, without hyperfine splitting. The observed profile at $g_{//} > g_{\perp}$ is characteristic of the Cu $dx^2–y^2$ spin.[36-42] Although the g values are similar for ***t*-Cu** and **1-Cu**, the $g_{//}$ absorption is clearly sharper at **1-Cu**, which is attributed to the exchange narrowing due to the strong interactions between Cu centers caused by short Pt···Pt contacts. The EPR spectra for both **1-Co** and **1-Ni**

are difficult to observe because the spin-lattice relaxation time is very short.

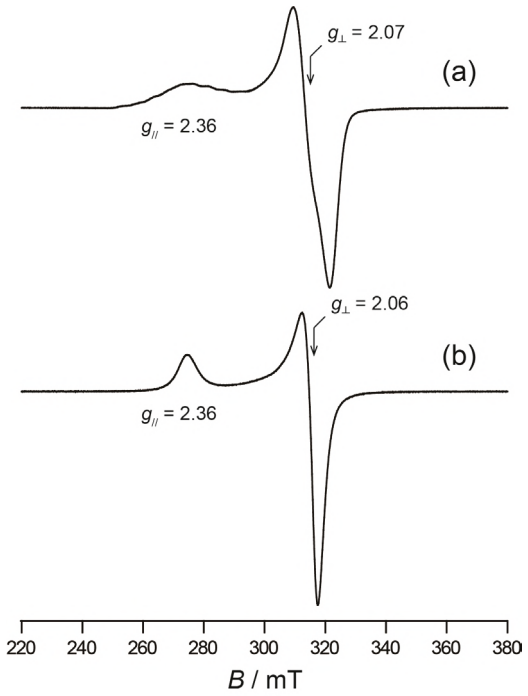

Figure 4. Continuous wave EPR spectra for powder samples of (a) ***t*-Cu** and (b) **1-Cu** at 77 K. Experimental settings: microwave frequency, (a) 9.0641 and (b) 9.0662 GHz; microwave power, 6 mW; and field modulation, 0.2 mT.

Magnetic Behaviors of *trans*-$[Pt_2M(acam)_4(NH_3)_4](ClO_4)_2$.

The temperature-dependent magnetic susceptibilities of powdered samples of **1-M** measured from 2 to 300 K are shown in Figure 5. The χT values in **1-M** at 300 K are 2.70 (**1-Co**), 0.89 (**1-Ni**), and 0.46 (**1-Cu**) cm^3 K mol^{-1} (Figure 4d–f), which are close to the theoretical values for high-spin Co(+2) (S = 3/2, 1.87 cm^3 K mol^{-1}), Ni(+2) (S = 1, 1.00 cm^3 K mol^{-1}), and Cu(+2) (S = 1/2, 0.37 cm^3 K mol^{-1}), respectively. The larger χT value of **1-Co** than the theoretical value is consistent with a significant orbital contribution to susceptibility, which is common for Co(+2) complexes.[43,44] The χT values in **1-Co** and **1-Ni** gradually decreased by lowering the temperature, reaching 0.05, and 0.01 cm^3 K mol^{-1} at 2 K, respectively. In contrast, the χT values in **1-Cu** plateaued until 12 K and increased to 0.50 cm^3 K mol^{-1} at 2 K. The data for **1-Co**, and **1-Ni** follow the Curie−Weiss law, with Weiss constants of θ = −49.0, −68.1 K, respectively (Table 4), where large negative θ values indicate the presence of strong antiferromagnetic coupling between the M(+2) ions. Furthermore, the plots of χ versus T for **1-Co**, and **1-Ni** show maxima at 24 K and 55 K, respectively (Figure 5a–b), supporting the

presence of antiferromagnetic coupling. In contrast, although **1-Cu** were inversely proportional to temperature, the data follow the Curie−Weiss law, with Weiss constants of $\theta = 0.14$ K, where positive θ values indicate the presence of ferromagnetic coupling between the Cu(+2) ions. In addition, the χT values in **1-Cu** increased with lowering the temperature, supporting the presence of ferromagnetic coupling. Considering the crystal structures, the magnetic interactions in **1-M** were probably present between the M atoms centers in the intra chain which arise through −Pt···Pt− bonds, although the intra chain M---M distance and inter chain distance ware similarly 8.8 Å because there are no interactions between inter chain due to separation.

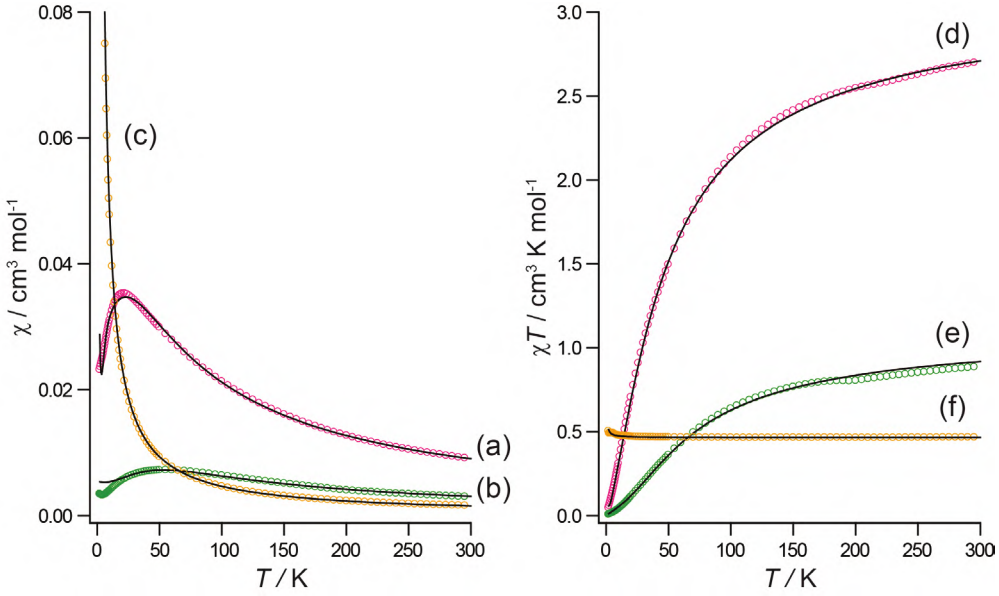

Figure 5. Temperature dependence of χ and χT in (a) **1-Co**, (b) **1-Ni**, (c) **1-Cu**, (d) **1-Co**, (e) **1-Ni**, and (f) **1-Cu** per M ion. The solid lines represent the theoretical fitting.

Table 4. Magnetic parameters estimated by theoretical fittings in ***t*-M** and **1-M**.

	C (cm^3 K mol^{-1})[a]	θ (K)[a]	D (cm^{-1})	zJ (cm^{-1})	$2J$ (cm^{-1})
***t*-Co**	2.73	−24.8	0.40	−9.1	−7.0
***t*-Ni**	1.13	−19.3	0.38	−19.6	−14.6
***t*-Cu**	0.43	0.15	-	-	0.0
1-Co	3.16	−49.0	0.40	−18.9	−17.9
1-Ni	1.09	−68.1	0.38	−69.7	−27.9
1-Cu	0.46	0.14	-	-	0.28

[a]Estimated from Curie–Weiss law $\chi = C/(T - \theta)$.

In order to extract an approximate value for the antiferromagnetic intrachain exchange strength, *J*, in **1-Co** and **1-Ni**, the data were fitted to the predictions made from the model of a molecular field-corrected susceptibility equation to obtain an estimate of *J*. Based on the assumption that *D* values between ***t*-M** and **1-M** are similar, *g* and *D* values were fixed according to that of ***t*-M**, and the susceptibility data[30] were fit to the theoretical prediction with zero single-ion anisotropy (Figures S2 and S3). The best fits were obtained for the values zJ = −18.9 (**1-Co**), and −69.7 cm^{-1} (**1-Ni**), where *z* represents the number of nearest paramagnetic atoms. These results indicated that the decreased χT values in lower temperature regions are not only attributed to ZFS but also to relatively strong antiferromagnetic couplings. However, as shown in Figures S2 and S3, these theoretical predictions were different from the experimental plots.

In order to estimate the strength of the antiferromagnetic exchange interaction in **1-Co**, simple phenomenological equation[45,46], the sum of A exp($-E_1/kT$) and B exp($-E_2/kT$), used to fit the data. The sum ($A + B$) equals the Curie constant, and E_1 and E_2 get the activation energies corresponding to the spin–orbit coupling and the antiferromagnetic exchange interaction, respectively. This equation fitted the data produced ($A + B$) = 3.03 cm^3 K mol^{-1}, E_1/k = 51 K, and $-E_2/k$ = 13 K. The value for ($A + B$) is similar to the obtained value (3.16 cm^3 K mol^{-1}) fitted to the Curie−Weiss law between 50 and 300 K. The value of E_1/k is consistent with the effect of spin–orbit coupling and site distortion (the order of +100 K).[43] The value of $-E_2/k$ is corresponds to J = −9.5 cm^{-1} in the Ising chain approximation, indicating relatively strong antiferromagnetic interaction. Similarly, to estimate the strength of the **1-Ni** antiferromagnetic exchange interaction, the data were fitted using previously reported equation[47] mentioned in the Experimental Section, that contains the following valuable parameters: ρ, a monomeric impurity and that the magnetic susceptibility follows the Curie-law. The theoretical fitting led to the following values: g = 2.11, J = −13.5 cm^{-1}, and ρ = 0.00, indicating strong antiferromagnetic interaction. The strong antiferromagnetic interactions observed in **1-M** are probably due to the short Pt···Pt distance in the chain, which results in a larger overlap between the d orbitals.

In order to estimate the strength of the ferromagnetic exchange interaction in **1-Cu**, the Heisenberg model[48] for a 1-D chain was applies to fit the data. The best fitting gives 0.14 cm^{-1} and 2.23 for J and g, exhibiting a weak ferromagnetic coupling through the metal−metal bonds. The ferromagnetic interaction is probably attributed to dz^2-ground state on some Cu

atoms in the chain due to the increase in the energy level of dz^2 orbital by one-dimensional chain.

Conclusion

In this study, trinuclear Pt–M–Pt (M = Co, Ni, and Cu) complexes bridged in a trans fashion were successfully synthesized from the acetamidate-hanging Pt mononuclear complex, *trans*-[Pt(acam)$_2$(NH$_3$)$_2$], and characterized. Each trinuclear complex are extended to be infinity one-dimensional chains in solid with Pt···Pt interactions aligned as ···Pt–M–Pt···Pt–M–Pt··· with high-spin M. The significant magnetic interactions were observed with a length of approximately 8.7 Å, which are attributed to electronic coupling through unbridged Pt···Pt bond (3.5 Å). The *trans*-[Pt$_2$M(acam)$_4$(NH$_3$)$_4$] is a new simple model for paramagnetic 1D chains with metal–metal bond, having the potential to provide new insights into magnetism.

Experimental Section

Materials. Potassium tetrachloroplatinate(II) was obtained from Tanaka Kikinzoku Co. Acetonitrile and $NaClO_4$ was obtained from Wako Co. $CoCl_2$ and $CuCl_2 \cdot 2H_2O$ were obtained from Nacalai Tesque Co. $NiCl_2 \cdot 6H_2O$ was obtained from Wako Co. Bu_4NClO_4 was obtained from Tokyo Chemical Industry Co. *trans*-$[PtCl_2(NH_3)_2]$ was synthesized according to a previously reported procedure.[49]

Synthesis of *trans*-$[Pt(acam)_2(NH_3)_2]$ (1)

An aqueous solution (45 mL) containing *trans*-$[PtCl_2(NH_3)_2]$ (2.4 g, 8.0 mmol) and $AgClO_4$ (3.3 g, 16.0 mmol) was stirred for 2 days at 50 ºC under dark conditions, and the resulting AgCl was removed by filtration. The filtrate with acetonitrile (3.6 mL, 69 mmol) was stirred for 12 h and $NaClO_4$ (2.0 g, 16 mmol) was mixed with the solution and stirred for 12 h at room temperature. The resulting white powder was collected by filtration, washed with water, and dried (3.5 g). The white powder was treated with 1 M aqueous NaOH solution (14 mL) and stirred for 1 days at room temperature. The resulting white powder of *trans*-$[Pt(acam)_2(NH_3)_2]$ was collected by filtration, washed with MeOH, and dried (1.2 g, 3.5 mmol). Yield: 43%. Elemental analysis calculated for $C_4H_{14}N_4O_2Pt$: C, 13.92; H, 4.09; N, 16.23%. Found: C, 13.93; H, 3.55; N, 16.07%.

Synthesis of *trans*-$[Pt_2Co(acam)_4(NH_3)_4](ClO_4)_2$ (1-Co)

The suspension of *trans*-$[Pt(acam)_2(NH_3)_2]$ (345 mg, 1.0 mmol) in MeOH (80 mL) was mixed with $CoCl_2$ (65 mg, 0.5 mmol) and stirred for 2 h at room temperature. After removing the unreacted *trans*-$[Pt(acam)_2(NH_3)_2]$ by filtration, MeOH solution (20 mL) of Bu_4NClO_4 (2.0 g, 6.0 mmol) was added and stirred for 2 h at room temperature. The solution was filtered and washed with MeOH to obtain the pale blue powdered product of *trans*-$[Pt_2Co(acam)_4(NH_3)_4](ClO_4)_2$ (304 mg, 3.2 mmol). Yield: 64%. Elemental analysis calculated for $C_8H_{28}Cl_2CoN_8O_{12}Pt_2$: C, 10.13; H, 2.98; N, 11.82%. Found: C, 10.20; H, 3.05; N, 11.93%.

Synthesis of *trans*-$[Pt_2Ni(acam)_4(NH_3)_4](ClO_4)_2$ (1-Ni)

The suspension of *trans*-$[Pt(acam)_2(NH_3)_2]$ (345 mg, 1.0 mmol) in MeOH (80 mL) was mixed with $NiCl_2 \cdot 6H_2O$ (120 mg, 0.5 mmol) and stirred for 2 h at room temperature. After

removing the unreacted *trans*-$[Pt(acam)_2(NH_3)_2]$ by filtration, MeOH solution (20 mL) of Bu_4NClO_4 (2.0 g, 6.0 mmol) was added and stirred for 15 h at room temperature. The solution was filtered and washed with MeOH to obtain the yellow powdered product of *trans*-$[Pt_2Ni(acam)_4(NH_3)_4](ClO_4)_2$ (330 mg, 3.5 mmol). Yield: 70%. Elemental analysis calculated for $C_8H_{28}Cl_2NiN_8O_{12}Pt_2$: C, 10.13; H, 2.98; N, 11.82%. Found: C, 10.10; H, 3.03; N, 11.91%.

Synthesis of *trans*-$[Pt_2Cu(acam)_4(NH_3)_4](ClO_4)_2$ (1-Cu)

The suspension of *trans*-$[Pt(acam)_2(NH_3)_2]$ (345 mg, 1.0 mmol) in MeOH (160 mL) was mixed with $CuCl_2 \cdot 2H_2O$ (85 mg, 0.5 mmol) and stirred for 3 h at room temperature. After removing the unreacted *trans*-$[Pt(acam)_2(NH_3)_2]$ by filtration, MeOH solution (20 mL) of Bu_4NClO_4 (2.0 g, 6.0 mmol) was added and stirred for 5 h at room temperature. The solution was filtered and washed with MeOH to obtain the orange powdered product of *trans*-$[Pt_2Cu(acam)_4(NH_3)_4](ClO_4)_2$ (337 mg, 3.5 mmol). Yield: 71%. Elemental analysis calculated for $C_8H_{28}Cl_2CuN_8O_{12}Pt_2$: C, 10.08; H, 2.96; N, 11.76%. Found: C, 10.06; H, 3.00; N, 11.71%.

Physical Measurements. X-ray photoelectron spectroscopy (XPS) measurements were performed using a Quantera-SXM spectrometer at room temperature. The binding energies were measured relative to the C 1s peak (284.8 eV) of the internal hydrocarbons. Electron paramagnetic resonance (EPR) spectra were recorded using a JEOL TE-200 spectrometer. Magnetic data were obtained in the 2–300 K range using a Quantum Design MPMS-XL SQUID susceptometer working at a 1.0 T field strength. Data were corrected for the sample holder, and the diamagnetism of the content was estimated from the Pascal constants.

X-ray Structure Determination. X-ray diffraction measurements were performed using a Rigaku Mercury diffractometer equipped with a normal-focus Mo-target X-ray tube (λ = 0.71070 Å) operated at 2 kW power (50 kW, 40 mA) and a Rigaku Mercury charge-coupled device (CCD) two-dimensional detector. A total of 1272 frames were collected with a scan width of 0.5º and exposure time of 15 s/frame (**1-Co**), 30 s/frame (**1-Ni**), and 15 s/frame (**1-Cu**), operated with CrysAlisPRO software package.[50] Empirical absorption correction using spherical harmonics was implemented in the SCALE3 ABSPACK scaling algorithm.[51] The structure was solved by applying the direct method[52] with subsequent difference Fourier

synthesis and refinement using SHELX-2017[53] controlled by a Yadokari-XG software package.[54] Non-hydrogen atoms were refined anisotropically and all the hydrogen atoms were treated as riding atoms.

Analyses of magnetic susceptibility measurements.

The data for **1-M** were fitted to the Curie–Weiss law $\chi = C/(T - \theta)$. The resulting least-squares fit between 50 K and 300 K yielded **1-Co**: $C = 3.16$ cm^3 K mol^{-1}, $\theta = -49.0$ K, between 80 K and 300 K yielded **1-Ni**: $C = 1.09$ cm^3 K mol^{-1}, $\theta = -68.1$ K, and between 10 K and 300 K yielded **1-Cu**: $C = 0.46$ cm^3 K mol^{-1}, $\theta = 0.14$ K. $C = N\beta^2g^2S(S + 1)/3k$, where N is Avogadro constant, β is the Bohr magneton, g is the Lande value, k is Boltzmann constant, θ is the Weiss constant, as the combination of constants $3k/N\beta^2$ is 7.991, gives **1-Co**: $g = 2.59$, **1-Ni**: $g = 2.08$, and **1-Cu**: $g = 2.22$.

The equations describing the temperature dependence of the molar magnetic susceptibility of a sextet state undergoing an axial ZFS are

$$\chi_{\parallel} = \frac{Ng^2\beta^2}{4kT}\frac{1 + 9\exp\left(\frac{-2D}{kT}\right)}{1 + \exp\left(\frac{-2D}{kT}\right)}$$

$$\chi_{\perp} = \frac{Ng^2\beta^2}{4kT}\frac{4 + \frac{3kT}{D}\left(1 - \exp\left(\frac{-2D}{kT}\right)\right)}{1 + \exp\left(\frac{-2D}{kT}\right)}$$

where D is axial zero-field splitting parameter, k is Boltzmann constant, T is temperature, N is Avogadro constant, g is g-factor, and β is the Bohr magneton. The average molar magnetic susceptibility of a powdered sample is given by

$$\chi' = \frac{\chi_{\parallel} + 2\chi_{\perp}}{3} + \text{TIP} \qquad (1)$$

where TIP is the temperature independent paramagnetism. In some cases, it was necessary to include the contribution of an impurity present in a proportion P and which was assumed to follow a Curie law with $S = 1/2$ and a g factor noted as g_{mo} (fixed as 2.00). The complete expression of the magnetic susceptibility used for the refinements was therefore

$$\chi = (1 - P)\chi' + P\frac{Ng_{mo}^2\beta^2}{4kT} \qquad (2)$$

For **1-Co**, in order to estimate the intermolecular interaction, the molecular field approximation may be used with the equation

$$\chi'' = \frac{\chi'}{1 - \left(\frac{2zJ}{Ng^2\beta^2}\right)\chi'} \qquad (3)$$

where zJ is the exchange energy (J multiplied by the number z of interacting neighbors), and χ' is the magnetic susceptibility of an isolated molecules, resulting from previous equation, where D = 0.40 cm^{-1} obtained by the simulation with EPR spectrum for ***t*-Co**. Similarly, the contribution of a paramagnetic impurity was included to yield the complete expression used for the refinements

$$\chi = (1 - P)\chi'' + P\frac{Ng_{\mathrm{mo}}^2\beta^2}{4kT} \qquad (4)$$

According to the above equation, the resulting least-squares fit of the data of **1-Co** between 2 K and 300 K yielded g = 2.24, zJ = −19.6 cm^{-1}, TIP = 0.00 cm^3 mol^{-1}, and P = 1.04 × 10^{-4}.

The equations describing the temperature dependence of the molar magnetic susceptibility of a triplet state undergoing an axial ZFS are

$$\chi_{\parallel} = \frac{Ng^2\beta^2}{kT}\frac{2\exp\left(\frac{-D}{kT}\right)}{1 + 2\exp\left(\frac{-D}{kT}\right)}$$

$$\chi_{\perp} = \frac{Ng^2\beta^2}{kT}\frac{\frac{2kT}{D}\left(1 - \exp\left(\frac{-D}{kT}\right)\right)}{1 + 2\exp\left(\frac{-D}{kT}\right)}$$

For **1-Ni**, in order to estimate the intermolecular interaction, the molecular field approximation may be used with the equation (3), where D = 0.38 cm^{-1} obtained by the simulation with EPR spectrum for ***t*-Ni**. According to the above equation (4) with the above equation, the resulting least-squares fit of the data of **1-Ni** between 2 K and 300 K yielded g = 2.32, zJ = −69.7 cm^{-1}, TIP = 0.00 cm^3 mol^{-1}, and P = 1.02 × 10^{-4}.

For **1-Co**, in order to estimate the strength of antiferromagnetic exchange interaction, the susceptibility data was fitted to the following simple phenomenological equation.

$$\chi T = A\exp\left(\frac{-E_1}{kT}\right) + B\exp\left(\frac{-E_2}{kT}\right)$$

Here, A + B equals the Curie constant (C), and E_1 and E_2 represent the activation energies corresponding to the spin-orbit coupling and the antiferromagnetic exchange interaction.

According to the above equation, the resulting least-squares fit of the data of **1-Co** between 2 K and 300 K yielded $A + B = 3.03$ cm^3 K mol^{-1}, $E_1/k = 51$ K, and $-E_2/k = 13$ K. The value of $-E_2/k = 13$ K is corresponds to $J = -9.0$ cm^{-1} in the Ising chain approximation.

The susceptibility data of **1-Ni** was fitted to the expression for the molar susceptibility derived.

$$\chi = \chi_{\text{chain}}(1 - \rho) + \frac{2Ng^2\beta^2}{3kT}\rho$$

$$\chi_{\text{chain}} = \frac{Ng^2\beta^2}{kT}\frac{2 + 0.0194X + 0.777X^2}{3 + 4.346X + 3.232X^2 + 5.834X^3}$$

$$X = |J|/kT$$

where J represents the antiferromagnetic coupling parameter, and ρ represents a monomeric impurity that the magnetic susceptibility follows the Curie-law. According to the above equation, the resulting least-squares fit of the data of **1-Ni** between 2 K and 300 K yielded $g = 2.11$, $J = -13.5$ cm^{-1}, and $\rho = 0.00$.

The susceptibility data of **1-Cu** was fitted to the expression for the molar susceptibility derived from the Heisenberg model for a 1-D chain.

$$\chi = \frac{Ng^2\beta^2}{4kT}\left\{\frac{1 + Ax + Bx^2 + Cx^3 + Dx^4 + Ex^5}{1 + Fx + Gx^2 + Hx^3 + Ix^4}\right\}^{2/3}$$

$$x = |J|/2kT$$

$$A = 5.7979916, B = 16.902653, C = 29.376885, D = 29.832959, E = 14.036918,$$

$$F = 2.7979916, G = 7.0086780, H = 8.6538644, I = 4.5743114$$

where J represents the ferromagnetic coupling parameter. According to the above equation, the resulting least-squares fit of the data of **1-Cu** between 2 K and 300 K yielded $g = 2.23$ and $J = 0.14$ cm^{-1}.

Supporting Figures

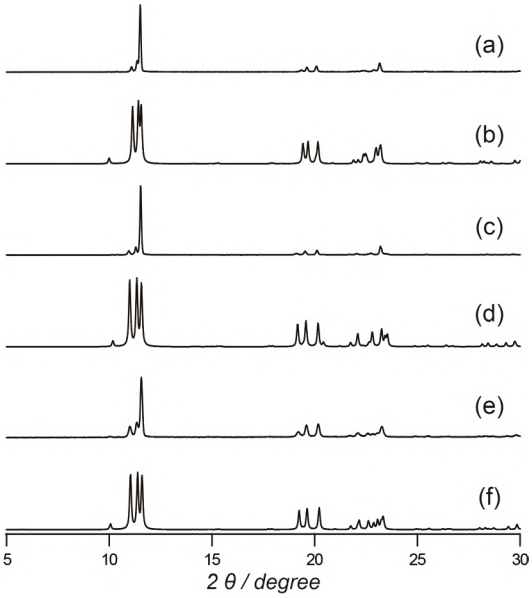

Figure S1. Powder X-ray diffraction for microcrystal samples for (a) **1-Co**, (b) simulation of **1-Co**, (c) **1-Ni**, (d) simulation of **1-Ni**, (e) **1-Cu**, and (f) simulation of **1-Cu**. Simulation were calculated based on the results of single-crystal X-ray analyses.

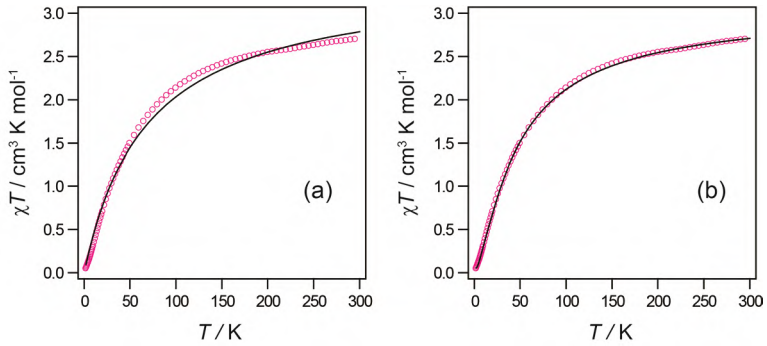

Figure S2. Temperature dependence of χT for *trans* -$[Pt_2Co(acam)_4(NH_3)_4](ClO_4)_2$ (**1-Co**) per Co ion. The solid lines represent the theoretical fitting to (a) the axial ZFS model and (b) the simple phenomenological equation.

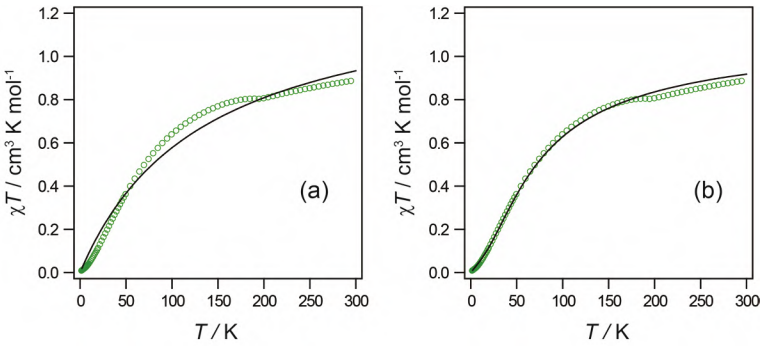

Figure S3. Temperature dependence of χT for *trans* -$[Pt_2Ni(acam)_4(NH_3)_4](ClO_4)_2$ (**1-Ni**) per Ni ion. The solid lines represent the theoretical fitting to (a) the axial ZFS model and (b) the Heisenberg model for 1-D chain.

References

1. Kitagawa, S.; Kitaura, R.; Noro, S.-i., Functional Porous Coordination Polymers. *Angew. Chem., Int. Ed.* **2004,** *43*, 2334–2375.
2. Yaghi, O. M.; O'Keeffe, M.; Ockwig, N. W.; Chae, H. K.; Eddaoudi, M.; Kim, J., Reticular synthesis and the design of new materials. *Nature* **2003,** *423*, 705–714.
3. Kitagawa, H.; Mitani, T., Valence transition with charge ordering in a conductive MMX-chain complex. *Coord. Chem. Rev.* **1999,** *190–192*, 1169–1184.
4. Yamashita, M.; Takaishi, S.; Kobayashi, A.; Kitagawa, H.; Matsuzaki, H.; Okamoto, H., Tuning of electronic structures of quasi one-dimensional iodide-bridged dinuclear platinum mixed-valence complexes. *Coord. Chem. Rev.* **2006,** *250*, 2335–2346.
5. Yamashita, M.; Takaishi, S., Tuning of Electronic Structures of Quasi-One-Dimensional Halogen-Bridged Ni–Pd Mixed-Metal Complexes, $[Ni_{1-x}Pd_x(chxn)_2X]X_2$ (X = Cl, Br) with Strong Electron Correlation. *Bull. Chem. Soc. Jpn.* **2006,** *79*, 1820–1833.
6. Miyasaka, H., Control of Charge Transfer in Donor/Acceptor Metal–Organic Frameworks. *Acc. Chem. Res.* **2013,** *46*, 248–257.
7. Bera, J. K.; Dunbar, K. R., Chain Compounds Based on Transition Metal Backbones: New Life for an Old Topic. *Angew. Chem. Int. Ed.* **2002,** *41*, 4453–4457.
8. Givaja, G.; Amo-Ochoa, P.; Gómez-García, C. J.; Zamora, F., Electrical conductive coordination polymers. *Chem. Soc. Rev.* **2012,** *41*, 115–147.
9. Chipman, J. A.; Berry, J. F., Paramagnetic Metal−Metal Bonded Heterometallic Complexes. *Chem. Rev.* **2020,** *120*, 2409–2447.
10. Murahashi, T.; Mochizuki, E.; Kai, Y.; Kurosawa, H., Organometallic Sandwich Chains Made of Conjugated Polyenes and Metal−Metal Chains. *J. Am. Chem. Soc.* **1999,** *121*, 10660–10661.
11. Goto, E.; Begum, R. A.; Zhan, S.; Tanase, T.; Tanigaki, K.; Sakai, K., Linear, Redox-Active Pt_6 and $Pt_2Pd_2Pt_2$ Clusters. *Angew. Chem., Int. Ed.* **2004,** *43*, 5029–5032.
12. Liu, I. P.-C.; Wang, W.-Z.; Peng, S.-M., New generation of metal string complexes: strengthening metal–metal interaction *via* naphthyridyl group modulated oligo-α-pyridylamido ligands. *Chem. Commun.* **2009**, 4323–4331.
13. Ismayilov, R. H.; Wang, W.-Z.; Lee, G.-H.; Yeh, C.-Y.; Hua, S.-A.; Song, Y.; Rohmer, M.-M.; Bénard, M.; Peng, S.-M., Two Linear Undecanickel Mixed-Valence Complexes: Increasing the Size and the Scope of the Electronic Properties of Nickel Metal Strings. *Angew. Chem., Int. Ed.* **2011,** *50*, 2045–2048.
14. Hua, S.-A.; Cheng, M.-C.; Chen, C.-h.; Peng, S.-M., From Homonuclear Metal String Complexes to Heteronuclear Metal String Complexes. *Eur. J. Inorg. Chem.* **2015**, 2510–2523.
15. Brogden, D. W.; Berry, J. F., Coordination Chemistry of 2,2'-Dipyridylamine: The Gift That Keeps on Giving. *Comments Inorg. Chem.* **2016,** *36*, 17–37.
16. Beach, S. A.; Doerrer, L. H., Heterobimetallic Lantern Complexes and Their Novel Structural and Magnetic Properties. *Acc. Chem. Res.* **2018,** *51*, 1063–1072.

17. Dahl, E. W.; Baddour, F. G.; Fiedler, S. R.; Hoffert, W. A.; Shores, M. P.; Yee, G. T.; Djukic, J.-P.; Bacon, J. W.; Rheingold, A. L.; Doerrer, L. H., Antiferromagnetic coupling across a tetrametallic unit through noncovalent interactions. *Chem. Sci.* **2012,** *3*, 602–609.
18. Baddour, F. G.; Fiedler, S. R.; Shores, M. P.; Bacon, J. W.; Golen, J. A.; Rheingold, A. L.; Doerrer, L. H., Pt···Pt vs Pt···S Contacts Between Pt-Containing Heterobimetallic Lantern Complexes. *Inorg. Chem.* **2013,** *52*, 13562–13575.
19. Baddour, F. G.; Fiedler, S. R.; Shores, M. P.; Golen, J. A.; Rheingold, A. L.; Doerrer, L. H., Heterobimetallic Lantern Complexes That Couple Antiferromagnetically through Noncovalent Pt···Pt Interactions. *Inorg. Chem.* **2013,** *52*, 4926–4933.
20. Atoji, M.; Richardson, J. W.; Rundle, R. E., On the Crystal Structures of the Magnus Salts, $Pt(NH_3)_4PtCl_4$. *J. Am. Chem. Soc.* **1957,** *79*, 3017–3020.
21. Krogmann, K.; Hausen, H. D. Z., Pt-Chain Structures. 1. Potassium Tetracyanoplatinate Violets $K_2[Pt(CN)_4]X_{0.3}\cdot 2.5H_2O$ (X = Cl, Br). *Z. Anorg. Allg. Chem.* **1968,** *358*, 67.
22. Krogmann, K.; Binder, W.; Hausen, H. D., Crystal Structure of "$Ir(CO)_3Cl$" = $Ir(CO)_{2.93}CI_{1.07}$. *Angew. Chem., Int. Ed.* **1968,** *7*, 812.
23. Finniss, G. M.; Canadell, E.; Campana, C.; Dunbar, K. R., Unprecedented Conversion of a Compound with Metal-Metal Bonding into a Solvated Molecular Wire. *Angew. Chem., Int. Ed.* **1996,** *35*, 2772–2774.
24. Prater, M. E.; Pence, L. E.; Clerac, R.; Finniss, G. M.; Campana, C.; Auban-Senzier, P.; Jerome, D.; Canadell, E.; Dunbar, K. R., A Remarkable Family of Rhodium Acetonitrile Compounds Spanning Three Oxidation States and with Nuclearities Ranging from Mononuclear and Dinuclear to One-Dimensional Chains. *J. Am. Chem. Soc.* **1999,** *121*, 8005–8016.
25. Sakai, K.; Ishigami, E.; Konno, Y.; Kajiwara, T.; Ito, T., New Partially Oxidized 1-D Platinum Chain Complexes Consisting of Carboxylate-Bridged *cis*-Diammineplatinum Dimer Cations. *J. Am. Chem. Soc.* **2002,** *124*, 12088–12089.
26. Mitsumi, M.; Ueda, H.; Furukawa, K.; Ozawa, Y.; Toriumi, K.; Kurmoo, M., Constructing Highly Conducting Metal–Metal Bonded Solids by Electrocrystallization of $[Pt^{II2}(RCS_2)_4]$ (RCS_2^-) Dithiocarboxylato, R = Methyl or Ethyl). *J. Am. Chem. Soc.* **2008,** *130*, 14102–14104.
27. Cotton, F. A.; Dikarev, E. V.; Petrukhina, M. A., *cis*-Di(μ-trifluoroacetate)dirhodium tetracarbonyl: structure and chemistry. *J. Chem. Soc., Dalton Trans.* **2000**, 4241–4243.
28. Pruchnik, F. P.; Jakimowicz, P.; Ciunik, Z.; Stanislawek, K.; Oro, L. A.; Tejel, C.; Ciriano, M. A., Rhodium wires based on binuclear acetate-bridged complexes. *Inorg. Chem. Commun.* **2001,** *4*, 19–22.
29. Campbell, M. G.; Powers, D. C.; Raynaud, J.; Graham, M. J.; Xie, P.; Lee, E.; Ritter, T., Synthesis and structure of solution-stable one-dimensional palladium wires. *Nature Chem.* **2011,** *3*, 949–953.
30. Takamori, A.; Uemura, K., Dimerization of paramagnetic trinuclear complexes by

coordination geometry changes showing mixed-valency and significant antiferromagnetic coupling through –Pt···Pt– bonds. *Inorg. Chem.* **2022,** *61*, 5762–5778.

31. Matsumoto, K.; Sakai, K.; Nishio, K.; Tokisue, Y.; Ito, R.; Nishide, T.; Shichi, Y., Syntheses, Crystal Structures, and Electronic, ESR, and X-ray Photoelectron Spectra of Acetamidate- and 2-Fluoroacetamidate-Bridged Mixed-Valent Octanuclear Platinum Blues. *J. Am. Chem. Soc.* **1992,** *114*, 8110–8118.
32. Strydom, C. A.; Strydom, H. J., X-ray photoelectron spectroscopy studies of some cobalt(II) nitrate complexes. *Inorg. Chim. Acta* **1989,** *159*, 191–195.
33. Brown, D. G.; Weser, U., XPS Spectra of Spin-Triplet Cobalt(III) Complexes. *Z. Naturforsch., B: J. Chem. Sci.* **1979,** *34B*, 1468–1470.
34. Matienzo, L. J.; Yin, L. I.; Grim, S. O.; Swartz, W. E., X-ray photoelectron spectroscopy of nickel compounds. *Inorg. Chem.* **1993,** *12* (12), 2762–2769.
35. Klein, J. C.; Proctor, A.; Hercules, D. M., X-ray Excited Auger Intensity Ratios for Differentiating Copper Compounds. *Anal. Chem.* **1983,** *55*, 2055–2059.
36. Lippert, B.; Thewalt, U.; Schöllhorn, H.; Goodgame, D. M. L.; Rollins, R. W., Formation, Crystal Structure, and EPR Spectroscopic Properties of a Heteronuclear (Pt_2, Cu) Mixed-Nucleobase (1-Methylcytosine, 1-Methyluracil) Complex: Bis[(μ-1-methyluracilato-N^3,O^4)(μ-1-methylcytosine-N^3,O^2)-*cis*-diammineplatinum(II)]-copper(II) Tetranitrate-6-Water. *Inorg. Chem.* **1984,** *23*, 2807–2813.
37. Schreiber, A.; Krizanovic, O.; Fusch, E. C.; Lippert, B.; Lianza, F.; Albinati, A.; Hill, S.; Goodgame, D. M. L.; Stratemeier, H.; Hitchman, M. A., Heteronuclear Complexes Derived from *trans*-a_2PtL_2 (a = NH_3 or CH_3NH_2, L = 2-Pyridonate). Distorted Coordination Geometries of All Three Metals in *trans*-$[a_2PtL_2CuL_2Pt(a_2)]^{2+}$ and an Extraordinary Short Hydrogen Bond in *trans*-$[a_2PtL(LH)]^+$. *Inorg. Chem.* **1994,** *33*, 6101–6110.
38. Erxleben, A.; Albinati, A.; Lippert, B., Heteronuclear Pt−Pd, Pt_2Cu and Pt_2Ni complexes with bridging acetamidate crystal structures and spectroscopic studies. *J. Chem. Soc., Dalton Trans.* **1996**, 1823–1828.
39. Yokoi, H.; Isobe, T., On the Hyperfine Structure of the ESR Spectra of Copper(II) Complexes. *Bull. Chem. Soc. Jpn.* **1966,** *39*, 2054.
40. Antosik, S.; Brown, N. M. D.; McConnell, A. A.; Porte, A. L., The Effects of Axial Interactions on Electron Paramagnetic Resonance Spectra of Copper(II) Chelates : Weak Complexes of Copper(II) Chelates and Chloroform *J. Chem. Soc. A* **1969**, 545–550.
41. Adato, I.; Eliezer, I., Effect of the Solvent on the ESR Parameters of Copper Acetylacetonate. *J. Chem. Phys.* **1971,** *54*, 1472–1476.
42. Yokoi, H.; Kishi, T., THE CORRELATION OF THE ESR PARAMETERS OF VARIOUS β-DIKETONE CHELATES OF COPPER(II) WITH THE pK_a OF THE LIGANDS *Chem. Lett.* **1973**, 749–754.
43. Mabbs, F. E.; Machin, D. J., *Magnetism and Transition Metal Complexes*. 1973; Vol. Chapman And Hall.

44. Figgis, B. N.; Hitchman, M. A., *Ligand Field Theory and its Applications*. 2000; Vol. Wiley-VCH: New York.
45. Rueff, J.-M.; Masciocchi, N.; Rabu, P.; Sironi, A.; Skoulios, A., Structure and Magnetism of a Polycrystalline Transition Metal Soap - $Co^{II}[OOC(CH_2)_{10}COO](H_2O)_2$. *Eur. J. Inorg. Chem.* **2001**, 2843–2848.
46. Rueff, J.-M.; Masciocchi, N.; Rabu, P.; Sironi, A.; Skoulios, A., Synthesis, Structure and Magnetism of Homologous Series of Polycrystalline Cobalt Alkane Mono- and Dicarboxylate Soaps. *Chem. −Eur. J.* **2002,** *8*, 1813–1820.
47. Meyer, A.; Gleizes, A.; Girerd, J. J.; Verdaguer, M.; Kahn, O., Crystal structures, magnetic anisotropy properties and orbital interactions in *catena*-(μ-nitrito)-bis(ethylenediamine)nickel(II) perchlorate and triiodide. *Inorg. Chem.* **1982,** *21*, 1729–1739.
48. G. A. Baker, J.; Rushbrooke, G. S.; Gilbert, H. E., High-Temperature Series Expansions for the Spin-1/2 Heisenberg Model by the Method of Irreducible Representations of the Symmetric Group. *Phys. Rev.* **1964,** *135*, 1272–1276.
49. Kauffman, G. B.; Cowan, D. O.; Slusarczuk, G.; Kirschner, S., *cis- and trans-Dichlorodiammineplatinum(II)*. 1963; Vol. VII.
50. CrysAlisPRO, Oxford Diffraction /Agilent Technologies UK Ltd, Yarnton, England.
51. SCALE3 ABSPACK, An Oxford Diffraction program, 2005 Oxford Diffraction Ltd.
52. Altomare, A.; Burla, M. C.; Camalli, M.; Cascarano, G. L.; Giacovazzo, C.; Guagliardi, A.; Moliterni, A. G. G.; Polidori, G.; Spagna, R., SIR97: a new tool for crystal structure determination and refinement. *J. Appl. Cryst.* **1999,** *32*, 115–119.
53. Sheldrick, G. M., A short history of SHELX. *Acta Cryst.* **2008,** *A64*, 112–122.
54. Kabuto, C.; Akine, S.; Nemoto, T.; Kwon, E., *J. Cryst. Soc. Jpn.* **2009,** *51*, 218–224.

Chapter 3

Syntheses, Crystal Structures, and Properties of Paramagnetic Copper One-Dimensional Chains with Heterometallic Bonds via Amidate Ligands

Abstract

Paramagnetic one-dimensional chain complexes $[PtCu(piam)_2(NH_3)_2Cl_2]\cdot H_2O$ (**2-Cu**; piam = pivalamidate) with aligned –Pt–Cu–Pt–Cu– were successfully synthesized and characterized by single-crystal X-ray structure analyses and physical measurements. The one-dimensional chain extends infinitely, where all the metals are bridged by amidate ligands, and by piam ligands the coordinated platinum atoms are hanged to the opposite direction to bind the copper atoms. Several physical measurements revealed that unpaired electrons in the one-dimensional chains are localized on the copper atoms, dx^2–y^2-ground state. Magnetic susceptibility measurements showed the presence of antiferromagnetic interaction (J = –0.91 cm^{-1}) between the copper atoms through metal–metal bonds.

Introduction

One-dimensional metal chain complexes have attracted much attention due to their conductivities[1,2] and magnetisim[3] through direct metal d orbitals interactions. Among these compounds, heteronuclear metal string complexes (HMSCs)[4,5], consisted of two or three kinds of metal with metal–metal bonds have interesting physical property which is not found homometals. The finite one-dimensional metal chain complexes have been reported in various kinds of compounds[4-9] where the synthesis strategy is a template method utilizing multidentate ligands. In contrast, the infinite one-dimensional metal complexes are restricted to d^7 or d^8 metal species[10-19] reported in few examples. Thus, a new approach is required to construct such one-dimensional metal complexes.

The amidate-hanging Pt mononuclear complex is an examples of metalloligands that are suitable for heterometallic complexes because the non-coordinated oxygen atoms are easily bound to the second metals (M).[20] To date, several dinuclear Pt–M[20,21] and trinuclear Pt–M–Pt[22-28] complexes utilize an amidate-hanging Pt mononuclear complex. In the process, it has been reported that infinite one-dimensional chain complexes have an alignment of –Pt–Ag–Pt–Ag–[22] and –Pt–Tl–Pt–Tl–[29] where all the metals are bridged by amidate ligands obtained accidentally (Scheme 1). These one-dimensional chain complexes consist of Pt atoms linked in *cis* fashion a to the two adjacent M ions via two amidate ligands. These crystal structures inspired synthetic research because one-dimensional chain complexes are spontaneously bridged all metals aligned in –Pt–M–Pt–M– by the combination of platinum and the second metal. Here, we present the synthesis and characterization of paramagnetic infinite one-dimensional chains aligned in –Pt–Cu–Pt–Cu– (**2-Cu**) where all metals are bridged by amidate ligands (Scheme 1).

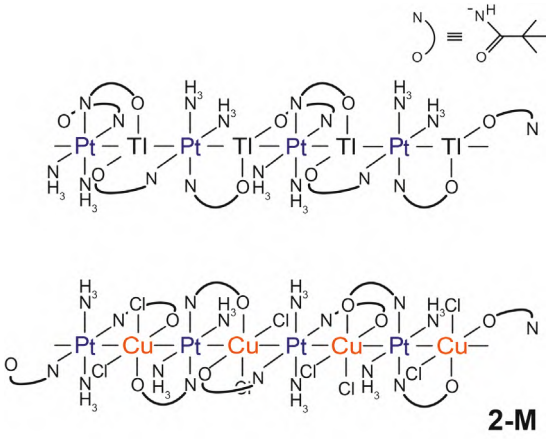

Scheme 1. Infinite one-dimensional chains where all metals are bridged by amidate ligands with alignment –Pt–Tl–Pt–Tl– and –Pt–Cu–Pt–Cu–, respectively.

Results and Discussion

Synthetic Procedure.

The amidate-hanging Pt mononuclear complex, *trans*-[Pt(piam)$_2$(NH$_3$)$_2$], is a useful precursor for heterometal multinuclear complexes, where non-coordinated oxygen atoms are easily bound to second metals (M).[30] Simply mixing *trans*-[Pt(piam)$_2$(NH$_3$)$_2$], $CuCl_2$ with the ratio of 2:1 in MeOH afforded single-crystals of [PtCu(piam)$_2$(NH$_3$)$_2$Cl$_2$]·H$_2$O (**2-Cu**). The crystal dates and structure refinement results are summarized in Table 1. As shown in the crystal structures (Figure 1), **2-Cu** has infinite one-dimensional chain structure where all the metals are bridged by amidate ligands.

Table 1. Crystallographic data and structure refinements for [PtCu(piam)$_2$(NH$_3$)$_2$Cl$_2$]·H$_2$O (**2-Cu**).

	2-Cu
Empirical formula	$C_{80}H_{208}Cl_{16}Cu_8N_{32}O_{24}Pt_8$
Formula weight	4639.01
Crystal system	Orthorhombic
Space group	*Fddd*
a (Å)	10.99520(10)
b (Å)	31.3503(5)
c (Å)	43.8353(6)
α (°)	90
β (°)	90
γ (°)	90
V (Å^3)	15110.2(3)
Z	4
Temperature (K)	123
*D*c (Mgm^{-3})	2.039
absorption coefficient (mm^{-1})	8.819
F(000)	8928
crystal size (mm^3)	0.11 × 0.18 × 0.28
measured reflections	28792
Independent reflections	4350 [R_{int} = 0.0269]
Goodness-of fit on F^2	0.805
R [$I > 2\sigma(I)$]	R_1 = 0.0208, wR_2 = 0.0871
R (all data)	R_1 = 0.0241, wR_2 = 0.0918

Crystal Structures of [PtCu(piam)$_2$(NH$_3$)$_2$Cl$_2$]·H$_2$O.

Figure 1 shows the crystal structure of [PtCu(piam)$_2$(NH$_3$)$_2$Cl$_2$]·H$_2$O (**2-Cu**). The most remarkable structural feature in **2-Cu** is that the Cu atoms are bridged by one of two piam ligands at the two adjacent Pt atoms, affording alternating alignment –Pt–Cu–Pt–Cu– in which all the metals are bridged by a piam ligand (Figure 1a). The one-dimensional chain extends infinitely, where piam ligands coordinated with Pt atoms are hanged to the opposite direction, to bind copper atoms. Although the Pt atoms were coordinated in a *trans* fashion which were unchanged from the original compounds, the Cu atoms were coordinated with two Cl atoms and two piam ligands in a *cis* fashion in the one-dimensional chain. There are two crystallographically independent Pt atoms. The Pt–Cu distances are Pt(1)–Cu(1) = 2.8914(4) and Pt(2)–Cu(1) = 2.8596(4) Å, which are relatively longer (2.63−2.98 Å) than the other Pt–Cu–Pt complexes.[22,23,30-38] The Cu---Cu distance between the nearest intra chain was 5.7 Å, while the nearest inter chain was 7.6 Å. The NH$_3$ ligands coordinated to Pt atoms are hydrogen bonded to the Cl atoms and oxygen atoms of the piam ligands on Cu atoms with a distance of 2.9 Å and 3.3 Å, respectively. The dihedral angles between the Pt and Cu coordination planes are 16–18°, which forms a zigzag structure. This is attributed to the geometric structure in the one-dimensional chain due to the differences in the *trans*- and *cis*- coordination environments of the Pt and Cu atoms. Each chain running along the *c* axis is separated from the nearest chains with an intermetallic distance between the two Cu center of 7.6 Å (Figure 1c). Considering the chemical formula of **2-Cu**, the sum of the metal oxidation states in the –Pt–Cu– unit is +4, where the formal oxidation states are –Pt(+2)–Cu(+2)–. The oxidation state for each metal is unchanged from the original compounds during the reaction.

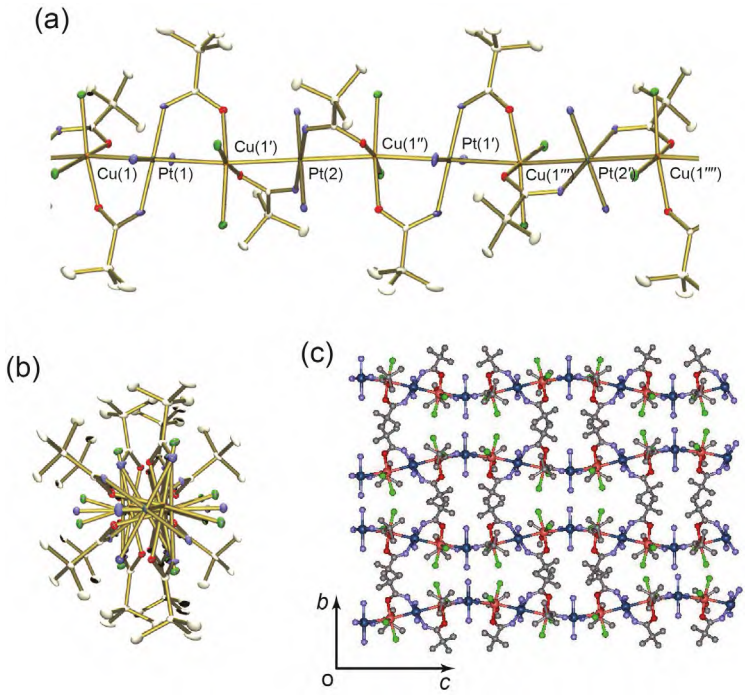

Figure 1. Molecular structure of (a) $[PtCu(piam)_2(NH_3)_2Cl_2]\cdot H_2O$ (**2-Cu**). (b) View along the metal–metal bonds. (c) Packing structure. The hydrogen atoms and water molecules are omitted for clarity.

Oxidation and Spin States of $[PtCu(piam)_2(NH_3)_2Cl_2]\cdot H_2O$.

XPS measurements were performed to determine the metal oxidation states of **2-Cu** (Figure 2). The Pt $4f_{7/2}$ binding energy for original compound of *trans*-$[Pt(piam)_2(NH_3)_2]$ is 72.6 eV, which is closer to the previous compounds of $[Pt_2^{II,II}(en)_2(\alpha\text{-pyridonato})_2](NO_3)_2$ (73.1 eV; en = ethylenediamine) than $[Pt_2^{III,III}(NH_3)_4(\alpha\text{-pyrrolidonato})_2(NO_3)_2](NO_3)_2$ (74.6 eV).[39] In **2-Cu**, the Pt $4f_{7/2}$ binding energy is 73.0 eV, which is a close value to Pt(+2). The Cu $2p_{3/2}$ binding energy for **2-Cu** is 932.7 eV. Considering the crystal structure, oxidation state and Pt binding energies for **2-Cu**, it is suggested that the formal oxidation state is –Pt(+2)–Cu(+2)–, which are unchanged from the starting compounds. However, the charge of the Cu atoms might fluctuate because the observed Cu $2p_{3/2}$ binding energy is closer to that for $Cu^{I}Cl$ (932.2 eV) than $Cu^{II}Cl_2$ (933.8 eV).[40]

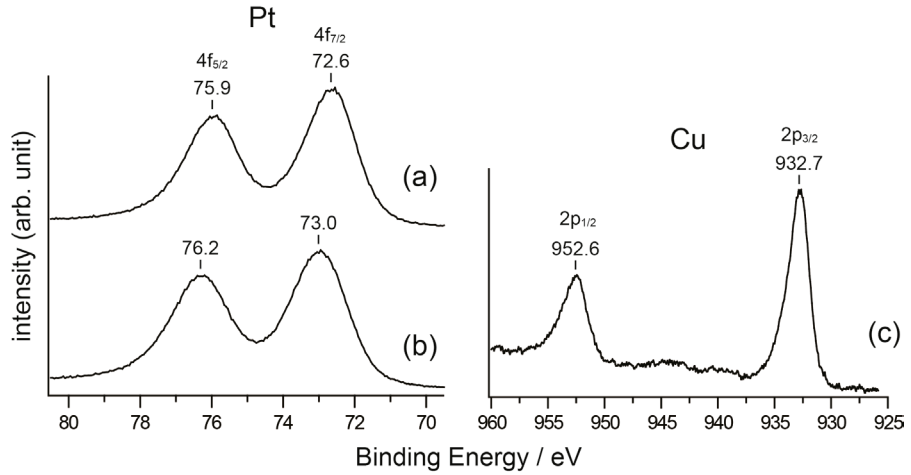

Figure 2. Pt $4f_{5/2}$ and $4f_{7/2}$ and Cu $2p_{1/2}$ and $2p_{3/2}$ core levels of XPS for (a) *trans*-$[Pt(piam)_2(NH_3)_2]$, (b) **2-Cu** and (c) **2-Cu**.

As shown in Figure 3, the EPR spectrum for powdered **2-Cu** at 77 K shows an axial-type signal with $g_{//} = 2.27$ and $g_{\perp} = 2.04$, without hyperfine splitting. The observed profile at $g_{//} > g_{\perp}$ is characteristic of the Cu $dx^2–y^2$ spin.[31,34,35,41-44] A sharp absorption at $g_{//}$ was observed, which is probably attributed to an exchange narrowing due to strong interactions between Cu centers caused by direct metal–metal bond.

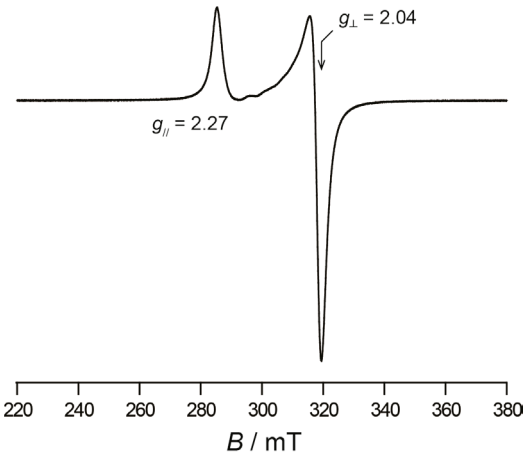

Figure 3. Continuous wave EPR spectra for powder samples of **2-Cu** at 77 K. Experimental settings: microwave frequency, 9.0657 GHz; microwave power, 6 mW; and field modulation, 0.2 mT.

Magnetic Behaviors of $[PtCu(piam)_2(NH_3)_2Cl_2]\cdot H_2O$.

The temperature-dependent magnetic susceptibilities of powdered samples of **2-Cu** measured from 2 to 300 K are shown in Figure 4. The χT value in **2-Cu** at 300 K is 0.48 cm^3 K mol^{-1}, which is close to the theoretical value for one Cu(+2) ions (S = 1/2, 0.37 cm^3 K mol^{-1}). The χT values in **2-Cu** maintained a plateau until 15 K and then steeply decreased to 0.30 cm^3 K mol^{-1} at 2 K. The data for **2-Cu** follow the Curie−Weiss law (Figure S4), with Weiss constant of θ = −0.27 K, where the negative θ value indicates an antiferromagnetic coupling between the Cu(+2) ions. The plots of χ versus T for **2-Cu** did not show a maximum point which is a characteristic of antiferromagnetic coupling, suggesting a weak magnetic interaction. Considering the crystal structures, the antiferromagnetic interaction found in **2-Cu** is attributed to the one-dimensional structure of –Pt–Cu–Pt–Cu– through the interaction via metal-metal bonds.

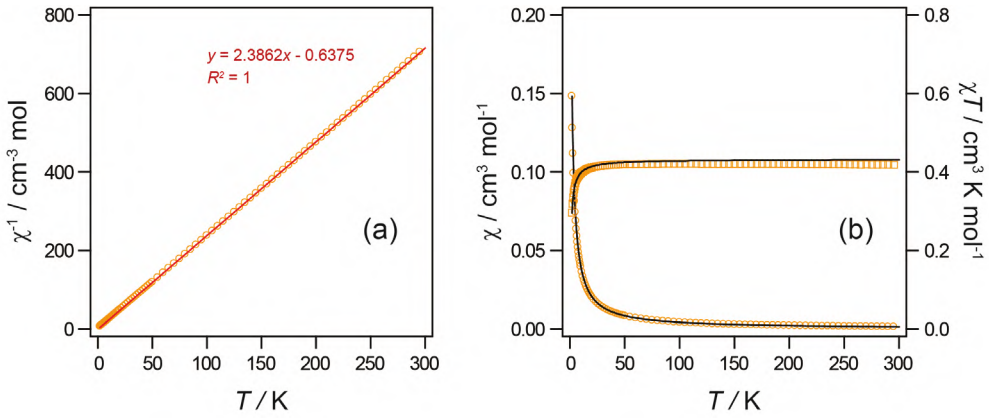

Figure 4. Temperature dependence of (a) χ^{-1}(circle), and (b) χ (circle) and χT (square) for **2-Cu**. The red solid line represents the result of least square fitting. The black solid lines represent the theoretical fitting.

In order to estimate the strength of the antiferromagnetic exchange interaction in **2-Cu**, the Heisenberg model for a 1-D chain[45] was applied to fit the data. The best fitting gives −0.91 cm^{-1} and 2.15 for J and g, exhibiting the presence of a weak antiferromagnetic coupling through the –Pt– bonds. This antiferromagnetic coupling was probably present between the Cu atoms centers in the intra chain, which arises through metal−metal bonds, as the intra chain Cu---Cu distance of 5.7 Å is shorter than the inter chain distance of 7.6 Å. The weak exchange interaction in **2-Cu** involves only one singly occupied $dx^2–y^2$ orbital, which is perpendicular to the chain direction, where the small overlapping of the d-orbitals resulted in a lower contribution to the

J value. In addition, **2-Cu** in a zigzag structure is also expected due to the small overlapping of the d-orbitals.

Conclusion

In this study, paramagnetic one-dimensional chain complexes, $[PtCu(piam)_2(NH_3)_2Cl_2]\cdot H_2O$ with an aligned –Pt–Cu–Pt–Cu– with direct metal–metal bonds, where all the metals are bridged by amidate ligands were successfully synthesized from the amidate-hanging Pt mononuclear complex, *trans*-$[Pt(piam)_2(NH_3)_2]$, and characterized. The geometric structure in the one-dimensional chain is in the *trans*- and *cis*- coordination environment of Pt and Cu atoms, where the amidate ligands coordinated with Pt atoms are hanged to the opposite direction to be bound to Cu atoms. Significant antiferromagnetic interactions were observed between Cu atoms in the intra chain with a length of 5.7 Å, which is attributed to an electronic coupling via –Pt– bonds. The findings of $[PtCu(piam)_2(NH_3)_2Cl_2]\cdot H_2O$ show a construction guideline for one-dimensional chains with direct metal–metal bonds where all metals are bridged by ligands, having a potential to provide a new synthesis method for one-dimensional chain complexes.

Experimental Section

Materials. Potassium tetrachloroplatinate(II) was obtained from Tanaka Kikinzoku Co. Pivalonitrile was obtained from the Tokyo Chemical Industry Co. $CuCl_2 \cdot 2H_2O$ were obtained from Nacalai Tesque Co. *trans*-$[Pt(piam)_2(NH_3)_2]$ was synthesized according to a previously reported procedure.[46]

Synthesis of $[PtCu(piam)_2(NH_3)_2Cl_2] \cdot H_2O$ (2-Cu)

A MeOH (12 mL) solution of $CuCl_2 \cdot 2H_2O$ (34 mg, 0.2 mmol) was mixed with *trans*-$[Pt(piam)_2(NH_3)_2]$ (172 mg, 0.4 mmol) and stirred for 16 h at room temperature. After removing the unreacted *trans*-$[Pt(piam)_2(NH_3)_2]$ by filtration, the solution was gently evaporated at room temperature until red microcrystals were obtained. Evaporation was then stopped and red block crystals (23.3 mg) were obtained after several days. Yield: 20.6%. Elemental analysis calculated for $C_{10}H_{28}Cl_2CuN_4O_3Pt$: C, 20.64; H, 4.85; N, 9.63%. Found: C, 20.55; H, 4.92; N, 9.70%.

Physical Measurements. X-ray photoelectron spectroscopy (XPS) measurements were performed using a Quantera-SXM spectrometer at room temperature. The binding energies were measured relative to the C 1s peak (284.8 eV) of the internal hydrocarbons. Electron paramagnetic resonance (EPR) spectra were recorded using a JEOL TE-200 spectrometer. Magnetic data were obtained in the 2–300 K range using a Quantum Design MPMS-7 SQUID susceptometer working at a 1.0 T field strength. Data were corrected for the sample holder, and the diamagnetism of the content was estimated from the Pascal constants.

X-ray Structure Determination. The measurements of single-crystal X-ray analysis were performed on a Rigaku Mercury CCD diffractometer equipped with a normal focus Mo-target X-ray tube (λ = 0.71073 Å) operated at 5 kW power (50 kV, 100 mA). The system was equipped with a CCD two-dimensional detector, and 744 frames were collected for exposure times of 5 s/frame. The system was operated with the CrysAlisPRO software package.[47] Empirical absorption correction using spherical harmonics was implemented in the SCALE3 ABSPACK scaling algorithm.[48] The structure was solved by applying the direct method[49] with subsequent difference Fourier synthesis and refinement using SHELX-2017[50] controlled by a Yadokari-XG

software package.[51] Non-hydrogen atoms were refined anisotropically and all the hydrogen atoms were treated as riding atoms. The oxygen atoms of the water molecules were refined without hydrogen atoms.

Analyses of magnetic susceptibility measurements.

The data for **2-Cu** were fitted to the Curie–Weiss law $\chi = C/(T - \theta)$. The resulting least-squares fit between 30 K and 300 K yielded $C = 0.42$ cm^3 K mol^{-1}, $\theta = -0.27$ K. $C = N\beta^2g^2S(S + 1)/3k$, where N is Avogadro constant, β is the Bohr magneton, g is the Lande value, k is Boltzmann constant, θ is the Weiss constant, as the combination of constants $3k/N\beta^2$ is 7.991, gives $g = 2.11$ (Figure 4a).

The susceptibility data of **2-Cu** was fitted to the expression for the molar susceptibility derived from the Heisenberg model for a 1-D chain.

$$\chi = \frac{Ng^2\beta^2}{kT}\frac{0.25 + 0.14995x + 0.30094x^2}{1 + 1.9862x + 0.68854x^2 + 6.0626x^3} + \frac{C_{\mathrm{imp}}}{T}$$

$$x = |J|/kT$$

where J represents the antiferromagnetic coupling parameter and C_{imp} represents a possible Curie spin impurity. According to the above equation, the resulting least-squares fit of the data of **2-Cu** between 2 K and 300 K yielded $g = 2.15$, and $J = -0.91$ cm^{-1}, and $C_{\mathrm{imp}} = 1.0 \times 10^{-4}$ cm^3 mol^{-1} (Figure 4b).

References

1. Bera, J. K.; Dunbar, K. R., Chain Compounds Based on Transition Metal Backbones: New Life for an Old Topic. *Angew. Chem., Int. Ed.* **2002,** *41*, 4453–4457.
2. Givaja, G.; Amo-Ochoa, P.; Gómez-García, C. J.; Zamora, F., Electrical conductive coordination polymers. *Chem. Soc. Rev.* **2012,** *41*, 115–147.
3. Chipman, J. A.; Berry, J. F., Paramagnetic Metal−Metal Bonded Heterometallic Complexes. *Chem. Rev.* **2020,** *120*, 2409–2447.
4. Hua, S.-A.; Cheng, M.-C.; Chen, C.-h.; Peng, S.-M., From Homonuclear Metal String Complexes to Heteronuclear Metal String Complexes. *Eur. J. Inorg. Chem.* **2015**, 2510–2523.
5. Brogden, D. W.; Berry, J. F., Coordination Chemistry of 2,2'-Dipyridylamine: The Gift That Keeps on Giving. *Comments Inorg. Chem.* **2016,** *36*, 17–37.
6. Murahashi, T.; Mochizuki, E.; Kai, Y.; Kurosawa, H., Organometallic Sandwich Chains Made of Conjugated Polyenes and Metal−Metal Chains. *J. Am. Chem. Soc.* **1999,** *121*, 10660–10661.
7. Goto, E.; Begum, R. A.; Zhan, S.; Tanase, T.; Tanigaki, K.; Sakai, K., Linear, Redox-Active Pt_6 and $Pt_2Pd_2Pt_2$ Clusters. *Angew. Chem., Int. Ed.* **2004,** *43*, 5029–5032.
8. Liu, I. P.-C.; Wang, W.-Z.; Peng, S.-M., New generation of metal string complexes: strengthening metal–metal interaction *via* naphthyridyl group modulated oligo-α-pyridylamido ligands. *Chem. Commun.* **2009**, 4323–4331.
9. Ismayilov, R. H.; Wang, W.-Z.; Lee, G.-H.; Yeh, C.-Y.; Hua, S.-A.; Song, Y.; Rohmer, M.-M.; Bénard, M.; Peng, S.-M., Two Linear Undecanickel Mixed-Valence Complexes: Increasing the Size and the Scope of the Electronic Properties of Nickel Metal Strings. *Angew. Chem., Int. Ed.* **2011,** *50*, 2045–2048.
10. Atoji, M.; Richardson, J. W.; Rundle, R. E., On the Crystal Structures of the Magnus Salts, $Pt(NH_3)_4PtCl_4$. *J. Am. Chem. Soc.* **1957,** *79*, 3017–3020.
11. Krogmann, K.; Hausen, H. D. Z., Pt-Chain Structures. 1. Potassium Tetracyanoplatinate Violets $K_2[Pt(CN)_4]X_{0.3}\cdot 2.5H_2O$ (X = Cl, Br). *Z. Anorg. Allg. Chem.* **1968,** *358*, 67.
12. Krogmann, K.; Binder, W.; Hausen, H. D., Crystal Structure of "$Ir(CO)_3Cl$" = $Ir(CO)_{2.93}CI_{1.07}$. *Angew. Chem., Int. Ed.* **1968,** *7*, 812.
13. Finniss, G. M.; Canadell, E.; Campana, C.; Dunbar, K. R., Unprecedented Conversion of a Compound with Metal-Metal Bonding into a Solvated Molecular Wire. *Angew. Chem., Int. Ed.* **1996,** *35*, 2772–2774.
14. Prater, M. E.; Pence, L. E.; Clerac, R.; Finniss, G. M.; Campana, C.; Auban-Senzier, P.; Jerome, D.; Canadell, E.; Dunbar, K. R., A Remarkable Family of Rhodium Acetonitrile Compounds Spanning Three Oxidation States and with Nuclearities Ranging from Mononuclear and Dinuclear to One-Dimensional Chains. *J. Am. Chem. Soc.* **1999,** *121*, 8005–8016.
15. Sakai, K.; Ishigami, E.; Konno, Y.; Kajiwara, T.; Ito, T., New Partially Oxidized 1-

D Platinum Chain Complexes Consisting of Carboxylate-Bridged *cis*-Diammineplatinum Dimer Cations. *J. Am. Chem. Soc.* **2002,** *124*, 12088–12089.

16. Mitsumi, M.; Ueda, H.; Furukawa, K.; Ozawa, Y.; Toriumi, K.; Kurmoo, M., Constructing Highly Conducting Metal–Metal Bonded Solids by Electrocrystallization of $[Pt^{II2}(RCS_2)_4]$ (RCS_2^-) Dithiocarboxylato, R = Methyl or Ethyl). *J. Am. Chem. Soc.* **2008,** *130*, 14102–14104.
17. Cotton, F. A.; Dikarev, E. V.; Petrukhina, M. A., *cis*-Di(μ-trifluoroacetate)dirhodium t etracarbonyl: structure and chemistry. *J. Chem. Soc., Dalton Trans.* **2000**, 4241–4243.
18. Pruchnik, F. P.; Jakimowicz, P.; Ciunik, Z.; Stanislawek, K.; Oro, L. A.; Tejel, C.; Ciriano, M. A., Rhodium wires based on binuclear acetate-bridged complexes. *Inorg. Chem. Commun.* **2001,** *4*, 19–22.
19. Campbell, M. G.; Powers, D. C.; Raynaud, J.; Graham, M. J.; Xie, P.; Lee, E.; Ritter, T., Synthesis and structure of solution-stable one-dimensional palladium wires. *Nature Chem.* **2011,** *3*, 949–953.
20. Chen, W.; Matsumoto, K., Pivalamidate-bridged dinuclear platinum and platinum–palladium complexes: synthesis, NMR and X-ray structural characterization of *cis*-$[Pt(NH_3)_2(NHCO^tBu)_2]\cdot 2H_2O$, and *cis*-$[Pt(NH_3)_2(NHCO^tBu)_2MLL']X_n$ (M = Pt, LL' = cod; L = L' = dmso; L = Cl, L' = dmso; M = Pd, L = L' = NH_3; X = ClO_4^- , NO_3^-). *Inorg. Chim. Acta* **2003,** *342*, 88–96.
21. Uemura, K.; Yamasaki, K.; Fukui, K.; Matsumoto, K., Synthesis, Crystal Structures, and Oxidation States of MM'X-Type Platinum–Rhodium Dinuclear Complexes Having Amidate Bridging Ligands. *Eur. J. Inorg. Chem.* **2007**, 809–815.
22. Chen, W.; Liu, F.; Nishioka, T.; Matsumoto, K., Heterotrimetallic Complexes $[\{Pt(RNH_2)_2(m\text{-}NHCO^tBu)_2\}_2M](ClO_4)_n$ (M = Mn, Co, Cu, Ni, Cd, and Zn, n = 2; M = In, n =3) $[\{Pt(NH_3)(m\text{-}DACHCO^tBu)(m\text{-}NHCO^tBu)\}_2Ni](ClO_4)_2$, and $[\{Pt(RNH_2)_2(NHCO^tBu)_2\}_3Ag_3](ClO_4)_3$ Bridged by Amidate Ligands: A Novel Amidate-Amine Interligand Reaction During the Pt–Ni Bond Formation. *Eur. J. Inorg. Chem.* **2003**, 4234–4243.
23. Uemura, K.; Ebihara, M., Paramagnetic One-Dimensional Chains Comprised of Trinuclear Pt−Cu−Pt and Paddlewheel Dirhodium Complexes with Metal−Metal Bonds. *Inorg. Chem.* **2013,** *52*, 5535–5550.
24. Uemura, K.; Sugiyama, Y.; Yasuda, E.; Ebihara, M., Syntheses, crystal structures and copper-binding capabilities of amidate-hanging platinum mononuclear complexes containing alkylamine moieties. *Polyhedron* **2014,** *67*, 513–519.
25. Uemura, K., One-dimensional complexes extended by unbridged metal–metal bonds based on a HOMO–LUMO interaction at the dz^2 orbital between platinum and heterometal atoms. *Dalton Trans.* **2017,** *46*, 5474–5492.
26. Uemura, K.; Taoka, M., Isolation and characterization of a tetranuclear Pt–Fe···Fe–Pt intermediate *en route* to the trinuclear Pt–Fe–Pt cluster. *Dalton Trans.* **2017,** *46*, 14012–14020.

27. Uemura, K.; Miyake, R., Paramagnetic One-Dimensional Chain Complex Consisting of Three Kinds of Metallic Species Showing Magnetic Interaction through Metal–Metal Bonds. *Inorg. Chem.* **2020,** *59*, 1692–1701.
28. Uemura, K.; Aoki, Y.; Takamori, A., Paramagnetic One-dimensional Chain Containing High-spin Manganese Atoms Showing Weak Antiferromagnetic Interaction Through –Pt–Rh–Rh–Pt– Bonds. *Dalton Trans.* **2022,** *51*, 946–957.
29. Chen, W.; Liu, F.; Xu, D.; Matsumoto, K.; Kishi, S.; Kato, M., Luminescent Amidate-Bridged One-Dimensional Platinum(II)-Thallium(I) Coordination Polymers Assembled via Metallophilic Attraction. *Inorg. Chem.* **2006,** *45*, 5552–5560.
30. Takamori, A.; Uemura, K., Dimerization of paramagnetic trinuclear complexes by coordination geometry changes showing mixed-valency and significant antiferromagnetic coupling through –Pt···Pt– bonds. *Inorg. Chem.* **2022,** *61*, 5762–5778.
31. Lippert, B.; Thewalt, U.; Schöllhorn, H.; Goodgame, D. M. L.; Rollins, R. W., Formation, Crystal Structure, and EPR Spectroscopic Properties of a Heteronuclear (Pt_2, Cu) Mixed-Nucleobase (1-Methylcytosine, 1-Methyluracil) Complex: Bis[(μ-1-methyluracilato-N^3,O^4)(μ-1-methylcytosine-N^3,O^2)-*cis*-diammineplatinum(II)]-copper(II) Tetranitrate-6-Water. *Inorg. Chem.* **1984,** *23*, 2807–2813.
32. Mutikainen, I.; Orama, O.; Pajunen, A.; Lippert, B., The crystal structure of a heteronuclear Pt_2CuL_4 complex of 1-methyluracil, $Cu[Pt(NH_3)_2(C_5H_5N_2O_2)_2]_2SO_4{\cdot}8H_2O$. *Inorg. Chim. Acta* **1987,** *137* (3), 189–193.
33. Frommer, G.; Lianza, F.; Albinati, A.; Lippert, B., Diplatinum and Heteronuclear Complexes Derived from (tmeda)Pt(1-MeU)$_2$ (tmeda = *N*,*N*,*N*′,*N*′-Tetramethylethylenediamine, 1-MeU = 1-methyluracilate-N^3). Steric Effect of the tmeda Ligand on the Orientation of the Second Metal. *Inorg. Chem.* **1992,** *31* (12), 2434–2439.
34. Schreiber, A.; Krizanovic, O.; Fusch, E. C.; Lippert, B.; Lianza, F.; Albinati, A.; Hill, S.; Goodgame, D. M. L.; Stratemeier, H.; Hitchman, M. A., Heteronuclear Complexes Derived from *trans*-a_2PtL_2 (a = NH_3 or CH_3NH_2, L = 2-Pyridonate). Distorted Coordination Geometries of All Three Metals in *trans*-$[a_2PtL_2CuL_2Pt(a_2)]^{2+}$ and an Extraordinary Short Hydrogen Bond in *trans*-$[a_2PtL(LH)]^+$. *Inorg. Chem.* **1994,** *33*, 6101–6110.
35. Erxleben, A.; Albinati, A.; Lippert, B., Heteronuclear Pt–Pd, Pt_2Cu and Pt_2Ni complexes with bridging acetamidate crystal structures and spectroscopic studies. *J. Chem. Soc., Dalton Trans.* **1996**, 1823–1828.
36. Chen, W.; Matsumoto, K., Synthesis and Structural Characterization of Trinuclear, Amidate-Bridged Heterobimetallic Complexes $[\{Pt(NH_3)_2(NHCOtBu)_2\}_2M]X_n$ (M = Mn, Fe, Co, Ni, Cu; X = BF_4^-, ClO_4^-; *n* = 2 or 3). *Eur. J. Inorg. Chem.* **2002,** *46*, 2664–2670.
37. Chen, C.; Qiu, H.; Liu, F.; Chen, W., Synthesis and Crystal Structure of Pivalamidate-Bridged Trinuclear Platinum–Copper Complex with a Linear Pt–Cu–Pt Core. *J. Chem. Crystallogr.* **2007,** *37*, 619–622.

38. Moret, M.-E.; Chen, P., Mononuclear Platinum(II) Complexes of a Bis(bidentate) Ligand Based on 1,3,4-Oxadiazole and Their Reactions with Copper(I) Salts. *Eur. J. Inorg. Chem.* **2010**, 438–446.
39. Matsumoto, K.; Sakai, K.; Nishio, K.; Tokisue, Y.; Ito, R.; Nishide, T.; Shichi, Y., Syntheses, Crystal Structures, and Electronic, ESR, and X-ray Photoelectron Spectra of Acetamidate- and 2-Fluoroacetamidate-Bridged Mixed-Valent Octanuclear Platinum Blues. *J. Am. Chem. Soc.* **1992,** *114*, 8110–8118.
40. Klein, J. C.; Proctor, A.; Hercules, D. M., X-ray Excited Auger Intensity Ratios for Differentiating Copper Compounds. *Anal. Chem.* **1983,** *55*, 2055–2059.
41. Yokoi, H.; Isobe, T., On the Hyperfine Structure of the ESR Spectra of Copper(II) Complexes. *Bull. Chem. Soc. Jpn.* **1966,** *39*, 2054.
42. Antosik, S.; Brown, N. M. D.; McConnell, A. A.; Porte, A. L., The Effects of Axial Interactions on Electron Paramagnetic Resonance Spectra of Copper(II) Chelates : Weak Complexes of Copper(II) Chelates and Chloroform *J. Chem. Soc. A* **1969**, 545–550.
43. Adato, I.; Eliezer, I., Effect of the Solvent on the ESR Parameters of Copper Acetylacetonate. *J. Chem. Phys.* **1971,** *54*, 1472–1476.
44. Yokoi, H.; Kishi, T., THE CORRELATION OF THE ESR PARAMETERS OF VARIOUS *β*-DIKETONE CHELATES OF COPPER(II) WITH THE pK_a OF THE LIGANDS *Chem. Lett.* **1973**, 749–754.
45. Bonner, J. C.; Fisher, M. E., Linear Magnetic Chains with Anisotropic Coupling. *Phys. Rev.* **1964,** *135*, 640–658.
46. Tisato, F.; Refosco, F.; Bandoli, G.; Pilloni, G.; Corain, B., Synthesis, Characterization, and Crystal Structure of the Water Soluble Copper(I) Complex with Trisulfonated Triphenylphosphine. *Inorg. Chem.* **2001,** *40*, 1394–1396.
47. CrysAlisPRO, Oxford Diffraction /Agilent Technologies UK Ltd, Yarnton, England.
48. SCALE3 ABSPACK, An Oxford Diffraction program, 2005 Oxford Diffraction Ltd.
49. Altomare, A.; Burla, M. C.; Camalli, M.; Cascarano, G. L.; Giacovazzo, C.; Guagliardi, A.; Moliterni, A. G. G.; Polidori, G.; Spagna, R., SIR97: a new tool for crystal structure determination and refinement. *J. Appl. Cryst.* **1999,** *32*, 115–119.
50. Sheldrick, G. M., A short history of SHELX. *Acta Cryst.* **2008,** *A64*, 112–122.
51. Kabuto, C.; Akine, S.; Nemoto, T.; Kwon, E., *J. Cryst. Soc. Jpn.* **2009,** *51*, 218–224.

Chapter 4

Paramagnetic One-Dimensional Chains Comprised of Trans-Bridged Pt–Cu–Pt Trinuclear Complexes and Paddlewheel Dirhodium Complexes with Metal–Metal Bonds

Abstract

Paramagnetic one-dimensional chain complexes with direct metal–metal bond containing three types of metal species aligned with ···Pt–Cu–Pt–Rh–Rh–Pt–Cu–Pt··· (**4-Cu**) and –Rh–Rh–Pt–Cu–Pt– (**5-Cu**) were successfully synthesized and characterized by single-crystal X-ray structure analyses and physical measurements. Several physical measurements revealed the oxidation states of the one-dimensional complexes are Rh(+2), Pt(+2), and Cu(+2), where the unpaired electrons lie on the Cu dx^2–y^2 orbitals. Magnetic susceptibility measurements in **4-Cu** showed an antiferromagnetic interaction (J = –0.28 cm^{-1}) between the copper atoms centers through –Pt···Pt– bonds. In contrast, **5-Cu** showed a weak ferromagnetic interaction (J = 0.01 cm^{-1}) between the copper centers through –Pt–Rh–Rh–Pt– bonds, probably due to the dz^2-ground state from dx^2–y^2 state on some copper atoms in the chain where the energy level of dz^2 orbital was increased by one-dimensional chain.

Introduction

One-dimensional metal chain complexes have attracted attention, due to their conductivities[1,2] and magnetism[3] through direct metal d orbital interactions. These one-dimensional metal chain complexes are classified into two types of compounds, finite and infinite chains. The finite type of one-dimensional metal chain complexes has been reported for various kinds of compound called extended metal atom chains (EMACs)[4,5] and heteronuclear metal string complexes (HMSCs)[6,7] because synthesis strategy is a template method utilizing multidentate ligands. In contrast, the infinite one-dimensional metal complexes are restricted to d^7 or d^8 metal species[8-17] where few examples were reported. Thus, a new approach is required due to construct such one-dimensional metal complexes.

We have tried to synthesize infinite heterometallic one-dimensional chains in which paramagnetic metal species are connected by direct metal–metal bonds with a second metal species.[18-25] The synthetic method for the infinite paramagnetic heterometallic one-dimensional chains uses the HOMO–LUMO interaction at the dz^2 orbital (σ*) between two kinds of complex. In this process mixing *cis*-$[Pt_2M(piam)_4(NH_3)_4]X_2$ (piam = pivalamidate, M = metal, X = anion) and $[Rh_2(O_2CCH_3)_4]$ that have filled and vacant σ*, respectively, afforded –Pt–M–Pt–Rh–Rh– alignments, showing antiferromagnetic interactions through –Pt–Rh–Rh–Pt– bonds.[19, 24, 25] However, the magnetic interaction of these one-dimensional chain was expected to be weak due to the small overlapping of the d-orbitals in the zigzag structure caused by the trinuclear Pt–M–Pt unit derived from the *cis* fashion (Scheme 1).[19,25] In contrast, *trans*-$[Pt_2M(piam)_4(NH_3)_4]^{2+}$ has recently been synthesized and characterized to reveal the metal stacking in a face-to-face fashion due to the *trans* geometrical structure. Therefore, a strong magnetic interaction has been expected to construct straight backbone one-dimensional complexes in the *trans* fashion due to a large overlapping of the d-orbitals (Scheme 1). Here, we will present the synthesis and characterization of paramagnetic one-dimensional chains with aligned –Rh–Rh–Pt–Cu–Pt– via Rh–Pt direct metal–metal bonds by HOMO–LUMO interactions.

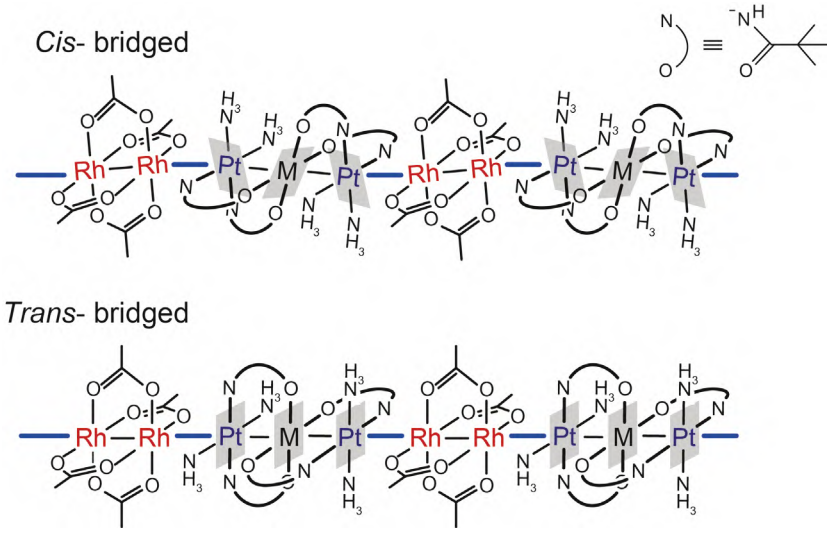

Scheme 1. *Cis*- bridged zigzag one-dimensional chain structure and *trans*- bridged face-to-face one-dimensional chain structure.

Results and Discussion

Synthetic Procedure.

$[Rh_2(O_2CCH_3)_4]$ having vacant σ* (dz^2) orbitals with two unpaired electrons which accepts the electrons from the filled dz^2 orbital. In contrast, *trans*-$[Pt_2Cu(piam)_4(NH_3)_4]^{2+}$ with filled σ* (dz^2) orbitals are expected to be possibly linked to $[Rh_2(O_2CCH_3)_4]$, which afforded a paramagnetic one-dimensional chain aligned as –Rh–Rh–Pt–Cu–Pt– with Rh–Pt direct metal–metal bonds by HOMO–LUMO interactions. Simply mixing $[Rh_2(O_2CCH_3)_4]$ and *trans*-$[Pt_2Cu(piam)_4(NH_3)_4](PF_6)_2\cdot 4H_2O$ (**3-Cu**) in solvent with an excess of $NaPF_6$ afforded single-crystals of $[\{Rh_2(O_2CCH_3)_4\}\{Pt_2Cu(piam)_4(NH_3)_4\}_2]_n(PF_6)_{4n}\cdot 4n$MeOH (**4-Cu**) and $[\{Rh_2(O_2CCH_3)_4\}\{Pt_2Cu(piam)_4(NH_3)_4\}]_n(PF_6)_{2n}\cdot 2n$THF (**5-Cu**), respectively. The crystal data and structure refinement results are summarized in Table 1. As shown in the crystal structures (Figure 1), **4-Cu** and **5-Cu** are infinitely one-dimensional chain structures with Rh–Pt direct metal–metal bonds.

Table 1. Crystallographic data and structure refinements for *trans*-$[Pt_2Cu(piam)_4(NH_3)_4](PF_6)_2\cdot 4H_2O$ (**3-Cu**), $[\{Rh_2(O_2CCH_3)_4\}\{Pt_2Cu(piam)_4(NH_3)_4\}_2]_n(PF_6)_{4n}\cdot 4n$MeOH (**4-Cu**), and $[\{Rh_2(O_2CCH_3)_4\}\{Pt_2Cu(piam)_4(NH_3)_4\}]_n(PF_6)_{2n}\cdot 2n$THF (**5-Cu**).

	3-Cu	**4-Cu**	**5-Cu**
Empirical formula	$C_{20}H_{52}CuF_{12}N_8O_8P_2Pt_2$	$C_{26}H_{64}CuF_{12}N_8O_{10}P_2Pt_2Rh$	$C_{36}H_{80}CuF_{12}N_8O_{14}P_2Pt_2Rh_2$
Formula weight	1276.35	1495.42	1798.56
Crystal system	Orthorhombic	Monoclinic	Monoclinic
Space group	*Pnnm*	$P2_1/n$	*Cc*
a (Å)	17.7767(3)	13.4114(2)	23.3157(4)
b (Å)	18.3469(3)	17.2449(3)	12.52690(10)
c (Å)	13.9816(3)	21.4020(3)	23.1871(4)
α (°)	90	90	90
β (°)	90	93.8630(10)	114.417(2)
γ (°)	90	90	90
V (Å^3)	4560.06	4938.57(13)	6166.62(18)
Z	4	4	4
Temperature (K)	293	123	123
*D*c (Mgm^{-3})	1.859	2.011	1.937
absorption coefficient (mm^{-1})	6.745	6.563	5.531
F(000)	2460	2896	3508
crystal size (mm^3)	0.35 × 0.35 × 0.35	0.17 × 0.60 × 0.65	0.11 × 0.18 × 0.24
measured reflections	72318	53751	34548
Independent reflections	5445 [R_{int} = 0.0453]	11348 [R_{int} = 0.0208]	12912 [R_{int} = 0.0237]
Goodness-of fit on F^2	1.156	1.430	1.002
R [$I > 2\sigma(I)$]	R_1 = 0.0386, wR_2 = 0.1335	R_1 = 0.0400, wR_2 = 0.1578	R_1 = 0.0348, wR_2 = 0.1148
R (all data)	R_1 = 0.0455, wR_2 = 0.1420	R_1 = 0.0436, wR_2 = 0.1612	R_1 = 0.0364, wR_2 = 0.1165

Synthesis and Crystal Structures of 3-Cu.

The amidate-hanging Pt mononuclear complex, *trans*-[Pt(piam)$_2$(NH$_3$)$_2$], is a useful precursor for heterometal multinuclear complexes, where non-coordinated oxygen atoms are easily bound to second metals (M) in solution. Simply mixing *trans*-[Pt(piam)$_2$(NH$_3$)$_2$], $CuCl_2 \cdot H_2O$ and $NaPF_6$ in solvent afforded single-crystals of *trans*-[Pt$_2$Cu(piam)$_4$(NH$_3$)$_4$](PF$_6$)$_2 \cdot 4H_2O$ (**3-Cu**). The crystal structure of **3-Cu** is presented in Figure 1. The Cu atoms are sandwiched between two Pt atoms, where four piam ligands are bridged in a *trans* fashion, resulting in a linear Pt–Cu–Pt alignment (Figure 1a). There were two crystallographically independent Pt atoms. The Pt–Cu distances are Pt(1)–Cu(1) = 2.6620(9) Å and Cu(1)–Pt(2) = 2.6537(8) Å, which is similar to the values (2.63–2.67 Å)[26-28] in other *trans* bridged Pt−Cu−Pt complexes. The dihedral angles between the Pt and Cu coordination planes are 0.19° and 0.23°, showing that they are approximately parallel. Each trinuclear complex in **3-Cu** is dimerized to Pt(1)–Cu(1)–Pt(2)···Pt(2′)–Cu(1′)–Pt(1′) with Pt(2)···Pt(2′) at a distance of 3.5567 Å. Considering the chemical formula **3-Cu**, the sum of the metal oxidation states of Pt–Cu–Pt is +6, the formal oxidation states are Pt(+2)–Cu(+2)–Pt(+2), because Pt(+3) complexes favor an axial coordination with anions, which the metal oxidation state for each metal is unchanged from the original compounds during the reaction.

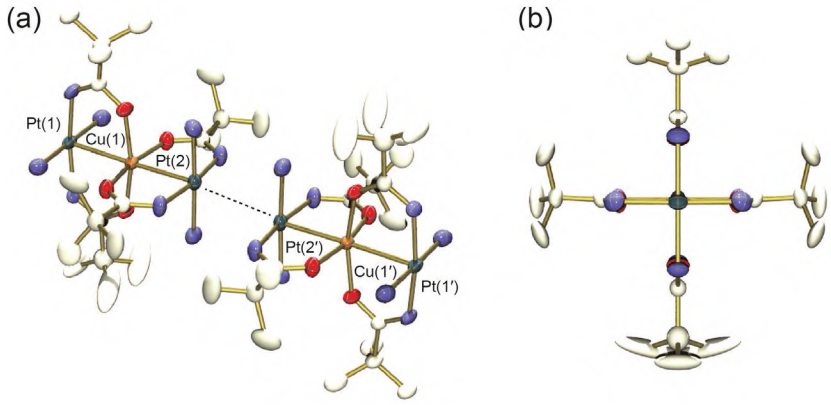

Figure 1. Molecular structure of (a) *trans*-[Pt$_2$Cu(piam)$_4$(NH$_3$)$_4$](PF$_6$)$_2$ (**3-Cu**). (b) View along the metal–metal bonds. The hydrogen atoms and water molecular are omitted for clarity.

Crystal Structures of 4-Cu and 5-Cu.

The crystal structure of [{Rh$_2$(O$_2$CCH$_3$)$_4$}{Pt$_2$Cu(piam)$_4$(NH$_3$)$_4$}$_2$]$_n$(PF$_6$)$_{4n} \cdot 4n$MeOH (**4-Cu**) is shown in Figure 2. As the most remarkable structural feature of **4-Cu**, paddlewheel

dinuclear complexes of $[Rh_2(O_2CCH_3)_4]$ are linked by *trans*-$[Pt_2Cu(piam)_4(NH_3)_4]$ units at both ends with metal–metal bonds to give an octanuclear complex which is aligned one-dimensionally as Pt(1)–Cu(1)–Pt(2)–Rh(1)–Rh(1′)–Pt(2′)–Cu(1′)–Pt(1′), where the crystallographic inversion center is positioned at the center of the Rh_2 complex. In addition, a significant feature of **4-Cu** is that each octanuclear complex is extended to be infinite one-dimensional chains ⋯Pt(1)–Cu(1)–Pt(2)–Rh(1)–Rh(1′)–Pt(2′)–Cu(1′)–Pt(1′)⋯Pt(1″)–Cu(1″)–Pt(2″)–Rh(1′)–Rh(1″)–Pt(2‴)–Cu(1‴)–Pt(1‴)⋯ with the end of Pt⋯Pt at a distance of 3.5467(5) Å, where PF_6^- anions are bridged with hydrogen bonds to NH_3 and nitrogen atoms of piam, which supports Pt⋯Pt close contact (Figure 2a and 2c). The Pt atoms are linked to Rh complex with a distance of Pt(2)–Rh(1) = 2.7619(4) Å, where quadruple hydrogen bonds between NH_3 and nitrogen atoms of piam coordinated Pt atoms and carbonyl O atoms in Rh complex with distances of 2.83–3.10 Å, which supports these unbridged metal–metal bonds. The Pt–Cu distances are Pt(1)–Cu(1) = 2.6189(6) Å and Cu(1)–Pt(2) = 2.6720(6) Å, in which the side of the Pt–Cu–Pt trinuclear complex linked at the end by Pt⋯Pt was the short distance. Although the dihedral angles between the PtN_4 and CuO_4 coordination plane are 0.12° and 1.43° showing that they are approximately parallel due to the *trans* fashion in the $[Pt_2Cu(piam)_4(NH_3)_4]$ unit, whereas the dihedral angles between unbridged the PtN_4 and RhO_4 coordination plane is a relatively large value of 7.2°. The torsion angles of about 25° between the $[Rh_2]$ and [Pt–Cu–Pt] complexes induces the bending angles of Rh–Pt–Cu (Figure 2b). Each chain in **4-Cu** was crossed to one another in the crystal (Figure 2d). Considering the chemical formula **4-Cu**, the sum of the metal oxidation states of Pt–Cu–Pt–Rh–Rh–Pt–Cu–Pt is +16, the formal oxidation states are Pt(+2)–Cu(+2)–Pt(+2)–Rh(+2)–Rh(+2)–Pt(+2)–Cu(+2)–Pt(+2), which is unchanged from the original compounds during the reaction.

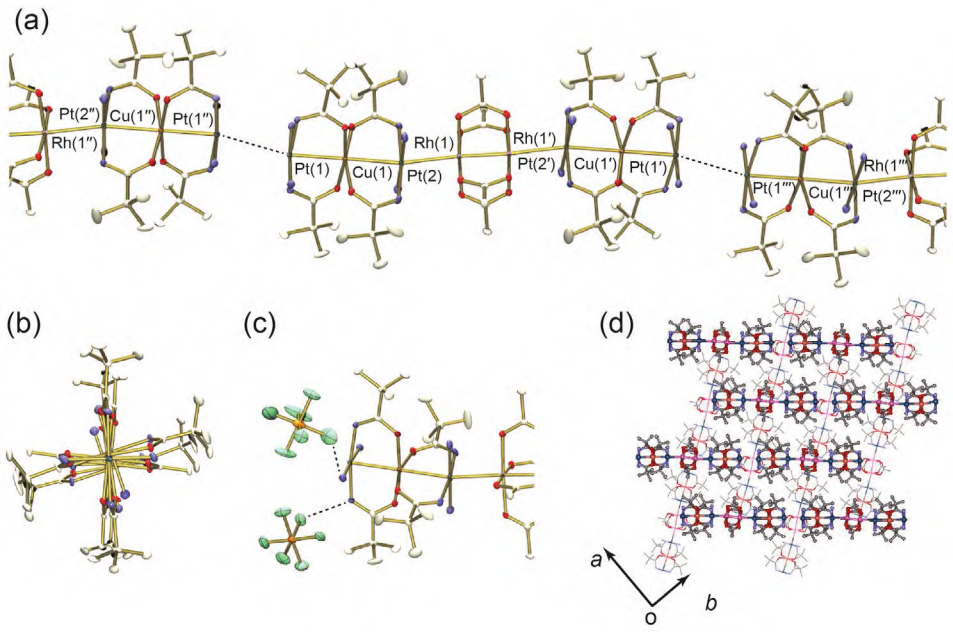

Figure 2. Molecular structure of (a) $[\{Rh_2(O_2CCH_3)_4\}\{Pt_2Cu(piam)_4(NH_3)_4\}_2]_n(PF_6)_{4n}\cdot 4n$MeOH (**4-Cu**). (b) View along the metal–metal bonds. (c) Hydrogen bonds between the chain and PF_6^- ions shown as dotted lines. (d) Packing view of octanuclear complexes. The thick and thin lines show the upper and lower chains, respectively. The hydrogen atoms, PF_6^- ions and MeOH molecular are omitted for clarity.

The crystal structure of $[\{Rh_2(O_2CCH_3)_4\}\{Pt_2Cu(piam)_4(NH_3)_4\}]_n(PF_6)_{2n}\cdot 2n$THF (**5-Cu**) is shown in Figure 3. As the most remarkable structural feature of **5-Cu**, paddlewheel dinuclear complexes of $[Rh_2(O_2CCH_3)_4]$ are linked by *trans*-$[Pt_2Cu(piam)_4(NH_3)_4]$ units at both ends with metal–metal bonds to give a one-dimensional chain complex aligned as –Rh–Rh–Pt–Cu–Pt– (Figure 3a). The Pt atoms are linked to the Rh complex with a distance of Rh(2)–Pt(1) = 2.7971(8) Å and Pt(2)–Rh(1) = 2.7927(8) Å, where quadruple hydrogen bonds between NH_3 and nitrogen atoms of piam coordinated with Pt atoms and carbonyl O atoms in Rh complex with distances of 2.87−2.96 Å, which supports these unbridged metal–metal bonds. The Pt–Cu distances are Pt(1)–Cu(1) = 2.6460(14) Å and Cu(1)–Pt(2) = 2.6445(14) Å, which are similar to that in **3-Cu**. The dihedral angles between the PtN_4 and CuO_4 coordination plane are 0.30° and 0.74° showing that they are approximately parallel due to the *trans* fashion in the $[Pt_2Cu(piam)_4(NH_3)_4]$ unit. In addition, the dihedral angles between unbridged the PtN_4 and RhO_4 coordination plane are 0.67° and 0.86°, indicating that the $[Rh_2]$ units and [Pt–Cu–Pt] units are arranged in a face-to-face fashion. The torsion angle of about 3° between the $[Rh_2]$

and [Pt–Cu–Pt] complexes showed straight backbone chains (Figure 3b). The PF_6^- anions are hydrogen bonds to NH_3 ligand on Pt atoms with a distance of about 3.0 Å (Figure 2c). Each chain in **5-Cu** was crossed to one another in the crystal (Figure 3d). Considering the chemical formula **5-Cu**, the sum of the metal oxidation states of Rh–Rh–Pt–Cu–Pt is +10, the formal oxidation states are –Rh(+2)–Rh(+2)–Pt(+2)–Cu(+2)–Pt(+2), which is unchanged from the original compounds during the reaction.

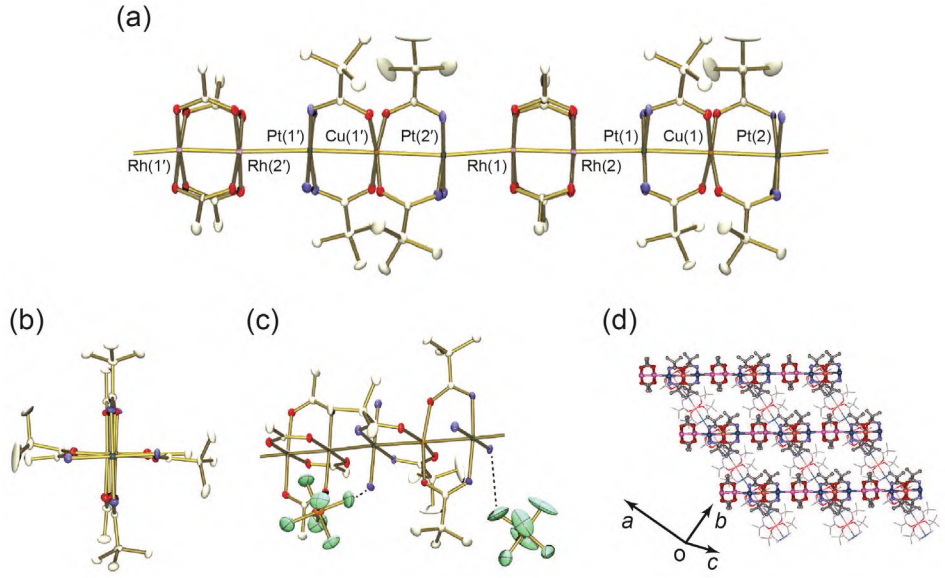

Figure 3. Molecular structure of (a) $[\{Rh_2(O_2CCH_3)_4\}\{Pt_2Cu(piam)_4(NH_3)_4\}]_n(PF_6)_{2n}\cdot 2n$THF (**5-Cu**). (b) View along the metal–metal bonds. (c) Hydrogen bonds between the chain and PF_6^- ions shown as dotted lines. (d) Packing view of one-dimensional chain complexes. The thick and thin lines show the upper and lower chains, respectively. The hydrogen atoms, PF_6^- ions and THF molecular are omitted for clarity.

Oxidation and Spin States of 4-Cu and 5-Cu.

XPS measurements were performed to determine the metal oxidation states (Figure 4). The Pt $4f_{7/2}$ binding energies for **3-Cu**, **4-Cu**, and **5-Cu** are 73.2 eV, 72.9 eV, and 73.2 eV, which are closer to the previous compounds of $[Pt_2^{II,II}(en)_2(\alpha\text{-pyridonato})_2](NO_3)_2$ (73.1 eV; en = ethylenediamine) than $[Pt_2^{III,III}(NH_3)_4(\alpha\text{-pyrrolidonato})_2(NO_3)_2](NO_3)_2$ (74.6 eV).[29] Considering the value of 72.6 eV for *trans*-$[Pt(piam)_2(NH_3)_2]$, which is the original compound, the higher energy shift might be caused by charge fluctuation in the Pt atoms. The Rh $3d_{5/2}$ binding energies for **4-Cu** and **5-Cu** are 308.8 eV, which are close to the value for original compound $[Rh_2^{II,II}(O_2CCH_3)_4]$ (308.9 eV). The Cu $2p_{3/2}$ binding energies for **3-Cu**, **4-Cu**, and

5-Cu are 932.7 eV, 932.4 eV, and 932.6 eV. Considering the crystal structure, oxidation state and the resulted of Pt binding energies and Rh binding energies for **3-Cu**, **4-Cu**, and **5-Cu**, it is suggested that the formal oxidation states are Pt(+2), Rh(+2), and Cu(+2), which are unchanged from the original compounds. However, the charge of the Cu atoms might fluctuate because the observed Cu $2p_{3/2}$ binding energies are closer to that for $Cu^{I}Cl$ (932.2 eV) than $Cu^{II}Cl_2$ (933.8 eV).[30]

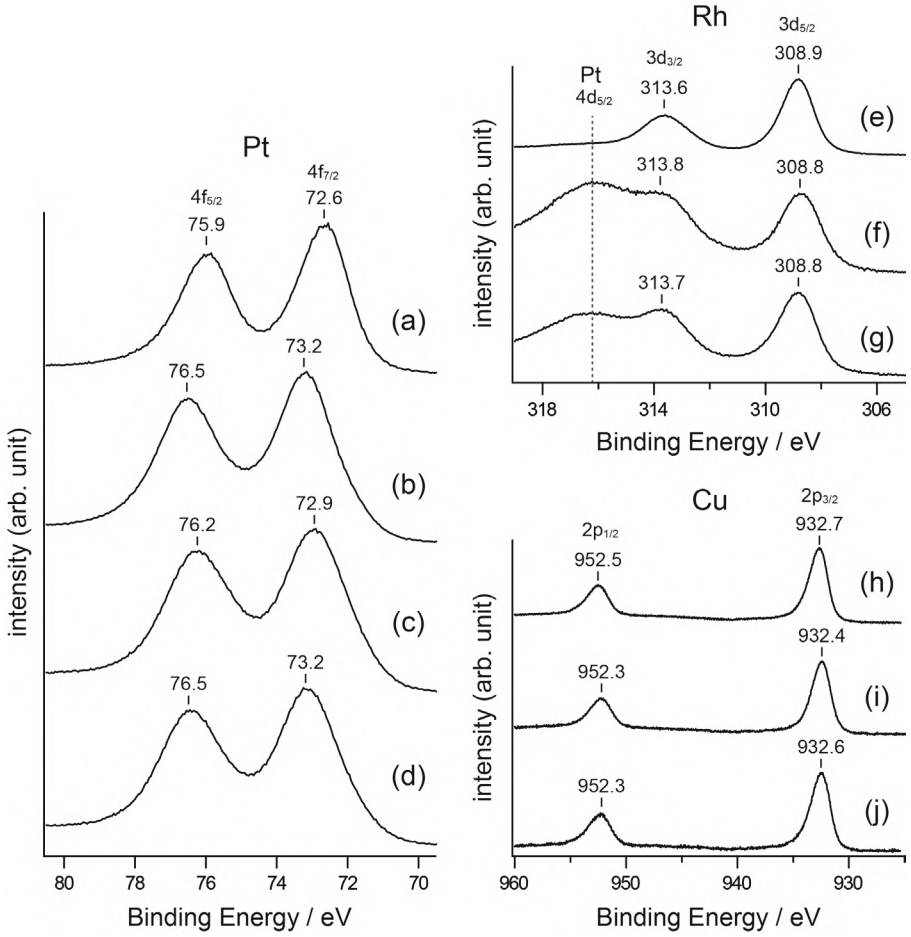

Figure 4. Pt $4f_{5/2}$ and $4f_{7/2}$, Rh $3d_{3/2}$ and $3d_{5/2}$, and Cu $2p_{1/2}$ and $2p_{3/2}$ core levels of XPS for (a) *trans*-$[Pt(piam)_2(NH_3)_2]$, (b) **3-Cu**, (c) **4-Cu**, (d) **5-Cu**, (e) $[Rh_2(O_2CCH_3)_4]$, (f) **4-Cu**, (g) **5-Cu**, (h) **3-Cu**, (i) **4-Cu**, and (j) **5-Cu**.

As shown in Figure 5, the EPR spectra for powdered **3-Cu**, **4-Cu**, and **5-Cu** at 77 K show an axial-type signal with **3-Cu**: $g_{//} = 2.27$, $g_{\perp} = 2.04$, an overlapping profile of two axial-type signals with **4-Cu**: $g_1 = 2.34$, $g_2 = 2.07$, and $g_3 = 2.06$ and with **4-Cu**: $g_1 = 2.35$, $g_2 = 2.05$, and $g_3 = 2.04$ without hyperfine splitting, respectively. In **3-Cu**, the observed profile at $g_{//} > g_{\perp}$ is characteristic of the Cu $dx^2–y^2$ spin.[26,31-36] In **4-Cu** and **5-Cu**, the both of g_1 absorption are

probably derived from the unpaired electron lies on the Cu atom, which observed at $g_1 > g_2$ (or g_3) is characterized of the Cu dx^2–y^2 spin. A relatively sharper absorption at g_1 of **4-Cu** and **5-Cu** than $g_{//}$ of **3-Cu** was observed, which is probably attributed to an exchange narrowing due to strong interactions between Cu centers caused by direct metal-metal bond or the shorter Pt···Pt distance.

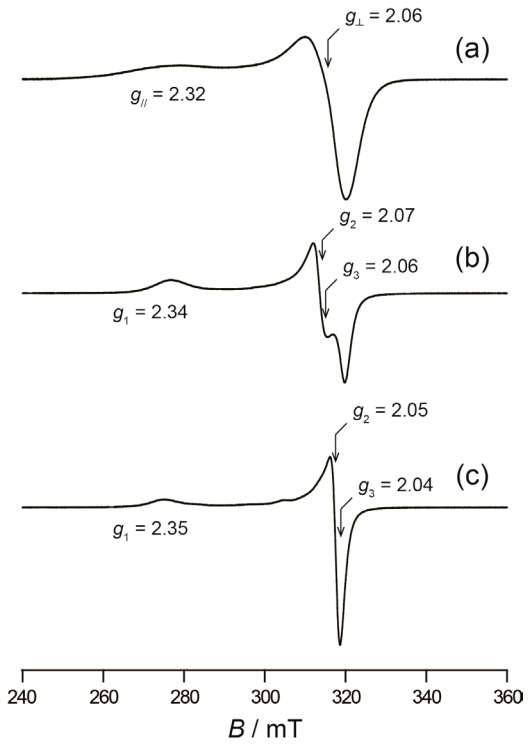

Figure 5. Continuous wave EPR spectra for powder samples of (a) **3-Cu**, (b) **4-Cu**, and (c) **5-Cu** at 77 K. Experimental settings: microwave frequency, (a) 9.0617, (b) 9.0650, and (c) 9.0637 GHz; microwave power, 6 mW; and field modulation, 0.2 mT.

Magnetic Behaviors of $[PtCu(piam)_2(NH_3)_2Cl_2]\cdot H_2O$.

The temperature-dependent magnetic susceptibilities of powdered samples of **3-Cu**, **4-Cu**, and **5-Cu** measured from 2 to 300 K are shown in Figures 6–8. The χT values in **3-Cu** plateau over the temperature range investigated and show 0.39 cm^3 K mol^{-1} at 300 K, which is close to the theoretical values for one Cu(+2) ion (S = 1/2, 0.37 cm^3 K mol^{-1}). The data for **3-Cu** follow the Curie−Weiss law (Figure 6a) with Weiss constant of θ = −0.02 K. The magnetic data of **3-Cu** coupled through an isotropic exchange interaction J (the Hamiltonian is written as: $H = -2JS_1 \cdot S_2$) gave the exchange parameter J = 0.0 cm^{-1} (**3-Cu**). The χT values in **4-Cu** and **5-Cu** are 0.43 and 0.40 cm^3 K mol^{-1} at 300 K, which are close to the theoretical values for one Cu(+2) ion (S = 1/2, 0.37 cm^3 K mol^{-1}). The χT values in **4-Cu** plateau until 5 K and decreased

to 0.38 cm^3 K mol^{-1} at 2 K, whereas in **5-Cu** the χT values showed a plateau over the temperature range investigated, reaching 0.39 cm^3 K mol^{-1} at 2 K. The data for **4-Cu** and **5-Cu** follow the Curie−Weiss law (Figure 7a–8a), with Weiss constants of $\theta = 3.00$ and 0.01 K, where the positive θ values indicate a ferromagnetic coupling between the Cu(+2) ions.

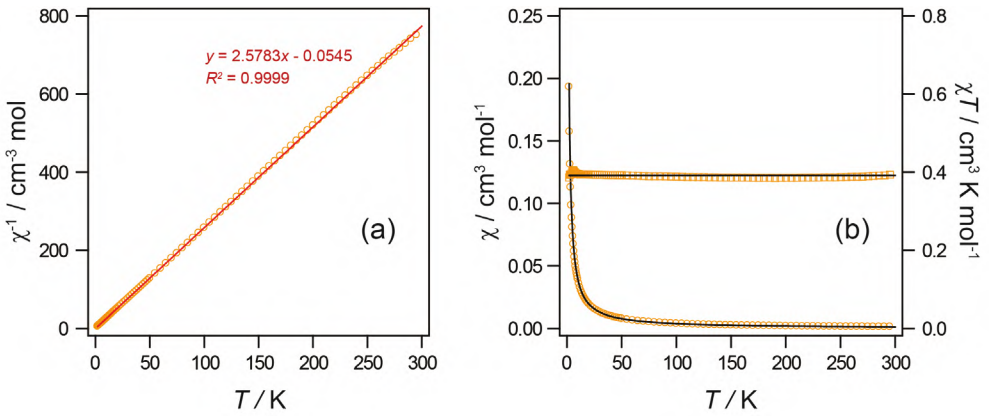

Figure 6. Temperature dependence of (a) χ^{-1}(circle), and (b) χ (circle) and χT (square) for **3-Cu**. The red solid line represents the result of least square fitting. The black solid line represents the theoretical fitting.

In order to estimate the strength of the magnetic exchange interaction in **4-Cu** and **5-Cu**, the Heisenberg model for a 1-D chain[37,38] was applied to fit the data. The best fitting gives **4-Cu**: −0.28 cm^{-1} and 2.13 and **5-Cu**: 0.01 cm^{-1} and 2.06 for J and g, respectively. Considering the crystal structures, the –Pt–Rh–Rh–Pt– direct metal–metal bonds are expected to be stronger than the –Pt···Pt– interaction. However, the antiferromagnetic interaction found in **4-Cu** was probably present between the Cu atoms centers in the intra chain through –Pt···Pt– because the intra chain via –Pt···Pt– between Cu---Cu distance of 8.740(1) Å is shorter than the inter chain via –Pt–Rh–Rh–Pt– metal–metal bonds between Cu---Cu distance of 13.182(1) Å. In contrast, the weak ferromagnetic interactions found in **5-Cu** was probably present between the Cu atoms in the intra chain through –Pt–Rh–Rh–Pt– metal–metal bonds. The ferromagnetic interaction in **5-Cu** is probably attributed to the dz^2-ground state on some Cu atoms in the chain due to raising the energy level of dz^2 orbital by one-dimensional chain. The very weak contribution of ferromagnetism to the J value is probably due to the long distance between the Cu ions (13.2 Å).

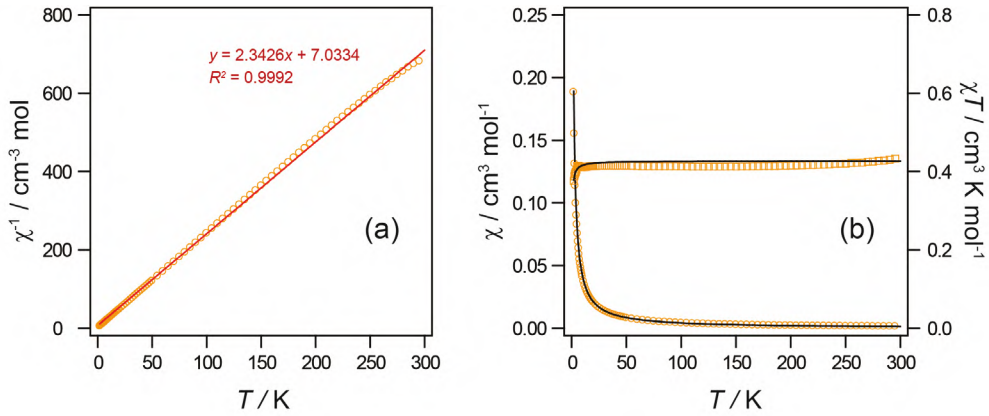

Figure 7. Temperature dependence of (a) χ^{-1}(circle), and (b) χ (circle) and χT (square) for **4-Cu**. The red solid line represents the result of least square fitting. The black solid line represents the theoretical fitting.

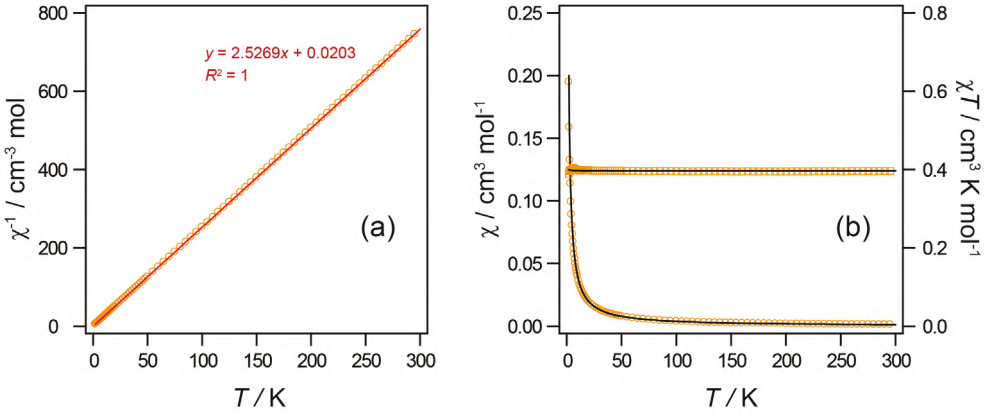

Figure 8. Temperature dependence of (a) χ^{-1}(circle), and (b) χ (circle) and χT (square) for **4-Cu**. The red solid line represents the result of least square fitting. The black solid line represents the theoretical fitting.

Conclusion

In this study, paramagnetic one-dimensional chain complexes with direct metal–metal bond by three metal species, Rh, Pt, and Cu were successfully synthesized and characterized. The paddlewheel dinuclear complexes of $[Rh_2(O_2CCH_3)_4]$ are linked by *trans*-$[Pt_2Cu(piam)_4(NH_3)_4]$ units at both ends with Rh–Pt metal–metal bonds to give octanuclear and one-dimensional chain complex. The XPS and EPR results showed that the oxidation states of each complex are Rh(+2), Pt(+2), and Cu(+2), where unpaired electrons lie on the Cu dx^2–y^2 orbitals. The significant antiferromagnetic interactions in octanuclear chains complex were observed with a length of 8.7 Å, which are attributed to an electronic coupling through

unbridged –Pt···Pt– bonds. In contrast, the significant ferromagnetic interactions in one-dimensional chain complex were observed with a length of 13.2 Å through –Pt–Rh–Rh–Pt– direct metal–metal bonds. It is anticipated that such an approach will be applicable to the construction of various novel paramagnetic one-dimensional chains with magnetic interactions by changing the transition metal in the trinuclear complex of *trans*-$[Pt_2M(piam)_4(NH_3)_4]$.

Experimental Section

Materials. Rhodium(III) chloride trihydrate and potassium tetrachloroplatinate(II) were obtained from Tanaka Kikinzoku Co. $CuCl_2 \cdot 2H_2O$ were obtained from Nacalai Tesque Co. $NaPF_6$ was obtained from the Tokyo Chemical Industry Co. *trans*-$[Pt(piam)_2(NH_3)_2]$ and $[Rh_2(O_2CCH_3)_4]$ were synthesized according to a previously reported procedure.[28,39]

Synthesis of *trans*-$[Pt_2Cu(piam)_4(NH_3)_4](PF_6)_4 \cdot 4H_2O$ (3-Cu)

The suspension of *trans*-$[Pt(piam)_2(NH_3)_2]$ (860 mg, 2.0 mmol) in a mixed solution of water and MeOH (180 mL, v/v = 2:1) was mixed with $CuCl_2 \cdot 2H_2O$ (340 mg, 2.0 mmol), and stirred for 1 h at room temperature. After removing the unreacted *trans*-$[Pt(piam)_2(NH_3)_2]$ by filtration, $NaPF_6$ (678 mg, 4.0 mmol) was added into the solution and stirred for 5 h at room temperature. The solution was filtered to obtain the orange powdered product of *trans*-$[Pt_2Cu(piam)_4(NH_3)_4](PF_6)_2$ (1.1 g). Yield: 90%. Elemental analysis calculated for $C_{20}H_{52}CuF_{12}N_8O_4F_2Pt_2$: C, 19.81; H, 4.32; N, 9.24%. Found: C, 19.74; H, 4.55; N, 8.80%.

Synthesis of $[\{Rh_2(O_2CCH_3)_4\}\{Pt_2Cu(piam)_4(NH_3)_4\}_2]_n(PF_6)_{4n} \cdot 4n$MeOH (4-Cu)

$[Rh_2(O_2CCH_3)_4]$ (30 mg, 68 μmol) was added to MeOH solution (45 mL) of **3-Cu** (164 mg, 135 μmol) and stirred at 50 ºC for 30 minutes. After removing the unreacted compounds by filtration, the resulting solution was slowly evaporated in a glass tube (10 mm internal diameter) at room temperature to obtain red crystals after 1 month. For the elemental analysis, the samples were dried (59 mg). Yield: 28%. Elemental analysis calculated for $C_{48}H_{116}Cu_2F_{24}N_{16}O_{16}P_4Pt_4Rh_2$: C, 20.11; H, 4.08; N, 7.82%. Found: C, 19.98; H, 3.87; N, 7.68%.

Synthesis of $[\{Rh_2(O_2CCH_3)_4\}\{Pt_2Cu(piam)_4(NH_3)_4\}]_n(PF_6)_{2n} \cdot 2n$THF (5-Cu)

$[Rh_2(O_2CCH_3)_4]$ (40 mg, 90 μmol) was added to THF solution (30 mL) of **3-Cu** (110 mg, 90 μmol) with $NaPF_6$ (30 mg, 180 μmol) and stirred at 50 ºC for 30 minutes. After removing the unreacted compounds by filtration, the resulting solution was slowly evaporated in a glass tube (10 mm internal diameter) at room temperature to obtain dark brown crystals after 2 weeks. For the elemental analysis, the samples were dried (24 mg). Yield: 15%. Elemental analysis calculated for $C_{28}H_{64}CuF_{12}N_8O_{12}P_2Pt_2Rh_2$: C, 20.33; H, 3.90; N, 6.77%. Found: C, 20.12; H,

3.75; N, 6.64%.

Physical Measurements. X-ray photoelectron spectroscopy (XPS) measurements were performed using a Quantera-SXM spectrometer at room temperature. The binding energies were measured relative to the C 1s peak (284.8 eV) of the internal hydrocarbons. Electron paramagnetic resonance (EPR) spectra were recorded using a JEOL TE-200 spectrometer. Magnetic data were obtained in the 2–300 K range using a Quantum Design MPMS-7 superconducting SQUID susceptometer working at a 1.0 T field strength. Data were corrected for the sample holder, and the diamagnetism of the content was estimated from the Pascal constants.

X-ray Structure Determination. The measurements of single-crystal X-ray analysis were performed on a Rigaku Mercury CCD diffractometer equipped with a normal focus Mo-target X-ray tube (λ = 0.71073 Å) operated for X at 2 kW power (50 kW, 40 mA) and for **4-Cu** and **5-Cu** at 5 kW power (50 kV, 100 mA). The system was equipped with a CCD two-dimensional detector, 1536 frames were collected for exposure time of 15 s/frame (**3-Cu**), 744 frames were collected for exposure times of 3 s/frame (**4-Cu**) and 4 s/frame (**5-Cu**). The system was operated with the CrysAlisPRO software package.[40] Empirical absorption correction using spherical harmonics was implemented in the SCALE3 ABSPACK scaling algorithm.[41] The structure was solved by applying the direct method[42] with subsequent difference Fourier synthesis and refinement using SHELX-2017[43] controlled by a Yadokari-XG software package.[44] Non-hydrogen atoms were refined anisotropically and all the hydrogen atoms were treated as riding atoms. In **3-Cu**, the oxygen atoms of the water molecules were refined without hydrogen atoms.

Analyses of magnetic susceptibility measurements.

The data for **3-Cu**, **4-Cu**, and **5-Cu** were fitted to the Curie–Weiss law $\chi = C/(T - \theta)$. The resulting least-squares fit between 30 K and 300 K yielded **3-Cu**: C = 0.39 cm^3 K mol^{-1}, θ = −0.02 K, **4-Cu**: C = 0.43 cm^3 K mol^{-1}, θ = 3.00 K, and **5-Cu**: C = 0.40 cm^3 K mol^{-1}, θ = 0.01 K. $C = N\beta^2g^2S(S + 1)/3k$, where N is Avogadro constant, β is the Bohr magneton, g is the Lande value, k is Boltzmann constant, θ is the Weiss constant, as the combination of constants $3k/N\beta^2$ is 7.991, gives **3-Cu**:g = 2.03, **4-Cu**: g = 2.13, and **5-Cu**: g = 2.05.

The susceptibility data of **3-Cu** was fitted to the expression for the molar susceptibility derived from $H = -2JS_1 \cdot S_2$.

$$\chi = \frac{Ng^2\beta^2}{kT}\frac{1}{3+x^2} + \text{TIP}$$

$$x = \exp\left(\frac{-J}{kT}\right)$$

where J represents the exchange interactions between two adjacent Cu(+2) centers. According to the above equation, the resulting least-squares fit of the data of **3-Cu** between 2 K and 300 K yielded $g = 2.04$ and $J = 0.0$ cm^{-1}.

The susceptibility data of **4-Cu** was fitted to the expression for the molar susceptibility derived from the Heisenberg model for a 1-D chain.

$$\chi = \frac{Ng^2\beta^2}{kT}\frac{0.25 + 0.14995x + 0.30094x^2}{1 + 1.9862x + 0.68854x^2 + 6.0626x^3} + \frac{C_{\text{imp}}}{T}$$

$$x = |J|/kT$$

where J represents the antiferromagnetic coupling parameter and C_{imp} represents a possible Curie spin impurity. According to the above equation, the resulting least-squares fit of the data of **4-Cu** between 2 K and 300 K yielded $g = 2.13$, $J = -0.28$ cm^{-1}, and $C_{\text{imp}} = 1.0 \times 10^{-4}$ cm^3 mol^{-1}.

The susceptibility data of **5-Cu** was fitted to the expression for the molar susceptibility derived from the Heisenberg model for a 1-D chain.

$$\chi = \frac{Ng^2\beta^2}{4kT}\left\{\frac{1 + Ax + Bx^2 + Cx^3 + Dx^4 + Ex^5}{1 + Fx + Gx^2 + Hx^3 + Ix^4}\right\}^{2/3}$$

$$x = |J|/2kT$$

$$A = 5.7979916, B = 16.902653, C = 29.376885, D = 29.832959, E = 14.036918,$$

$$F = 2.7979916, G = 7.0086780, H = 8.6538644, I = 4.5743114$$

where J represents the ferromagnetic coupling parameter. According to the above equation, the resulting least-squares fit of the data of **5-Cu** between 2 K and 300 K yielded $g = 2.06$ and $J = 0.01$ cm^{-1}.

References

1. Bera, J. K.; Dunbar, K. R., Chain Compounds Based on Transition Metal Backbones: New Life for an Old Topic. *Angew. Chem., Int. Ed.* **2002,** *41*, 4453–4457.
2. Givaja, G.; Amo-Ochoa, P.; Gómez-García, C. J.; Zamora, F., Electrical conductive coordination polymers. *Chem. Soc. Rev.* **2012,** *41*, 115–147.
3. Chipman, J. A.; Berry, J. F., Paramagnetic Metal−Metal Bonded Heterometallic Complexes. *Chem. Rev.* **2020,** *120*, 2409–2447.
4. Liu, I. P.-C.; Wang, W.-Z.; Peng, S.-M., New generation of metal string complexes: strengthening metal–metal interaction *via* naphthyridyl group modulated oligo-α-pyridylamido ligands. *Chem. Commun.* **2009**, 4323–4331.
5. Ismayilov, R. H.; Wang, W.-Z.; Lee, G.-H.; Yeh, C.-Y.; Hua, S.-A.; Song, Y.; Rohmer, M.-M.; Bénard, M.; Peng, S.-M., Two Linear Undecanickel Mixed-Valence Complexes: Increasing the Size and the Scope of the Electronic Properties of Nickel Metal Strings. *Angew. Chem., Int. Ed.* **2011,** *50*, 2045–2048.
6. Hua, S.-A.; Cheng, M.-C.; Chen, C.-h.; Peng, S.-M., From Homonuclear Metal String Complexes to Heteronuclear Metal String Complexes. *Eur. J. Inorg. Chem.* **2015**, 2510–2523.
7. Brogden, D. W.; Berry, J. F., Coordination Chemistry of 2,2'-Dipyridylamine: The Gift That Keeps on Giving. *Comments Inorg. Chem.* **2016,** *36*, 17–37.
8. Atoji, M.; Richardson, J. W.; Rundle, R. E., On the Crystal Structures of the Magnus Salts, $Pt(NH_3)_4PtCl_4$. *J. Am. Chem. Soc.* **1957,** *79*, 3017–3020.
9. Krogmann, K.; Hausen, H. D. Z., Pt-Chain Structures. 1. Potassium Tetracyanoplatinate Violets $K_2[Pt(CN)_4]X_{0.3}\cdot 2.5H_2O$ (X = Cl, Br). *Z. Anorg. Allg. Chem.* **1968,** *358*, 67.
10. Krogmann, K.; Binder, W.; Hausen, H. D., Crystal Structure of "$Ir(CO)_3Cl$" = $Ir(CO)_{2.93}CI_{1.07}$. *Angew. Chem., Int. Ed.* **1968,** *7*, 812.
11. Finniss, G. M.; Canadell, E.; Campana, C.; Dunbar, K. R., Unprecedented Conversion of a Compound with Metal-Metal Bonding into a Solvated Molecular Wire. *Angew. Chem., Int. Ed.* **1996,** *35*, 2772–2774.
12. Prater, M. E.; Pence, L. E.; Clerac, R.; Finniss, G. M.; Campana, C.; Auban-Senzier, P.; Jerome, D.; Canadell, E.; Dunbar, K. R., A Remarkable Family of Rhodium Acetonitrile Compounds Spanning Three Oxidation States and with Nuclearities Ranging from Mononuclear and Dinuclear to One-Dimensional Chains. *J. Am. Chem. Soc.* **1999,** *121*, 8005–8016.
13. Sakai, K.; Ishigami, E.; Konno, Y.; Kajiwara, T.; Ito, T., New Partially Oxidized 1-D Platinum Chain Complexes Consisting of Carboxylate-Bridged *cis*-Diammineplatinum Dimer Cations. *J. Am. Chem. Soc.* **2002,** *124*, 12088–12089.
14. Mitsumi, M.; Ueda, H.; Furukawa, K.; Ozawa, Y.; Toriumi, K.; Kurmoo, M., Constructing Highly Conducting Metal–Metal Bonded Solids by Electrocrystallization of $[Pt^{II2}(RCS_2)_4]$ (RCS_2^-) Dithiocarboxylato, R = Methyl or Ethyl). *J. Am. Chem. Soc.*

2008, *130*, 14102–14104.

15. Cotton, F. A.; Dikarev, E. V.; Petrukhina, M. A., *cis*-Di(*μ*-trifluoroacetate)dirhodium tetracarbonyl: structure and chemistry. *J. Chem. Soc., Dalton Trans.* **2000**, 4241–4243.
16. Pruchnik, F. P.; Jakimowicz, P.; Ciunik, Z.; Stanislawek, K.; Oro, L. A.; Tejel, C.; Ciriano, M. A., Rhodium wires based on binuclear acetate-bridged complexes. *Inorg. Chem. Commun.* **2001,** *4*, 19–22.
17. Campbell, M. G.; Powers, D. C.; Raynaud, J.; Graham, M. J.; Xie, P.; Lee, E.; Ritter, T., Synthesis and structure of solution-stable one-dimensional palladium wires. *Nature Chem.* **2011,** *3*, 949–953.
18. Uemura, K.; Ebihara, M., One-Dimensionally Extended Paddlewheel Dirhodium Complexes from Metal–Metal Bonds with Diplatinum Complexes. *Inorg. Chem.* **2011,** *50*, 7919–7921.
19. Uemura, K.; Ebihara, M., Paramagnetic One-Dimensional Chains Comprised of Trinuclear Pt−Cu−Pt and Paddlewheel Dirhodium Complexes with Metal−Metal Bonds. *Inorg. Chem.* **2013,** *52*, 5535–5550.
20. Uemura, K.; Kanbara, T.; Ebihara, M., Two Types of Heterometallic One-Dimensional Alignment Composed of Acetamidate-Bridged Dirhodium and Pivalamidate-Bridged Diplatinum Complexes. *Inorg. Chem.* **2014,** *53*, 4621–4628.
21. Uemura, K.; Uesugi, N.; Matsuyama, A.; Ebihara, M.; Yoshikawa, H.; Awaga, K., Integration of Paramagnetic Diruthenium Complexes into an Extended Chain by Heterometallic Metal−Metal Bonds with Diplatinum Complexes. *Inorg. Chem.* **2016,** *55*, 7003–7011.
22. Uemura, K., One-dimensional complexes extended by unbridged metal–metal bonds based on a HOMO–LUMO interaction at the dz^2 orbital between platinum and heterometal atoms. *Dalton Trans.* **2017,** *46*, 5474–5492.
23. Uemura, K.; Ito, D.; Pirillo, J.; Hijikata, Y.; Saeki, A., Modulation of Band Gaps toward Varying Conductivities in Heterometallic One-Dimensional Chains by Ligand Alteration and Third Metal Insertion. *ACS Omega* **2020,** *5*, 30502–30518.
24. Uemura, K.; Miyake, R., Paramagnetic One-Dimensional Chain Complex Consisting of Three Kinds of Metallic Species Showing Magnetic Interaction through Metal–Metal Bonds. *Inorg. Chem.* **2020,** *59*, 1692–1701.
25. Uemura, K.; Aoki, Y.; Takamori, A., Paramagnetic One-dimensional Chain Containing High-spin Manganese Atoms Showing Weak Antiferromagnetic Interaction Through –Pt–Rh–Rh–Pt– Bonds. *Dalton Trans.* **2022,** *51*, 946–957.
26. Schreiber, A.; Krizanovic, O.; Fusch, E. C.; Lippert, B.; Lianza, F.; Albinati, A.; Hill, S.; Goodgame, D. M. L.; Stratemeier, H.; Hitchman, M. A., Heteronuclear Complexes Derived from *trans*-a_2PtL_2 (a = NH_3 or CH_3NH_2, L = 2-Pyridonate). Distorted Coordination Geometries of All Three Metals in *trans*-$[a_2PtL_2CuL_2Pt(a_2)]^{2+}$ and an Extraordinary Short Hydrogen Bond in *trans*-$[a_2PtL(LH)]^{+}$. *Inorg. Chem.* **1994,** *33*, 6101–6110.

27. Chen, C.; Qiu, H.; Liu, F.; Chen, W., Synthesis and Crystal Structure of Pivalamidate-Bridged Trinuclear Platinum–Copper Complex with a Linear Pt–Cu–Pt Core. *J. Chem. Crystallogr.* **2007,** *37*, 619–622.
28. Takamori, A.; Uemura, K., Dimerization of paramagnetic trinuclear complexes by coordination geometry changes showing mixed-valency and significant antiferromagnetic coupling through –Pt···Pt– bonds. *Inorg. Chem.* **2022,** *61*, 5762–5778.
29. Matsumoto, K.; Sakai, K.; Nishio, K.; Tokisue, Y.; Ito, R.; Nishide, T.; Shichi, Y., Syntheses, Crystal Structures, and Electronic, ESR, and X-ray Photoelectron Spectra of Acetamidate- and 2-Fluoroacetamidate-Bridged Mixed-Valent Octanuclear Platinum Blues. *J. Am. Chem. Soc.* **1992,** *114*, 8110–8118.
30. Klein, J. C.; Proctor, A.; Hercules, D. M., X-ray Excited Auger Intensity Ratios for Differentiating Copper Compounds. *Anal. Chem.* **1983,** *55*, 2055–2059.
31. Lippert, B.; Thewalt, U.; Schöllhorn, H.; Goodgame, D. M. L.; Rollins, R. W., Formation, Crystal Structure, and EPR Spectroscopic Properties of a Heteronuclear (Pt_2, Cu) Mixed-Nucleobase (1-Methylcytosine, 1-Methyluracil) Complex: Bis[(μ-1-methyluracilato-N^3,O^4)(μ-1-methylcytosine-N^3,O^2)-*cis*-diammineplatinum(II)]-copper(II) Tetranitrate-6-Water. *Inorg. Chem.* **1984,** *23*, 2807–2813.
32. Erxleben, A.; Albinati, A.; Lippert, B., Heteronuclear Pt−Pd, Pt_2Cu and Pt_2Ni complexes with bridging acetamidate crystal structures and spectroscopic studies. *J. Chem. Soc., Dalton Trans.* **1996**, 1823–1828.
33. Yokoi, H.; Isobe, T., On the Hyperfine Structure of the ESR Spectra of Copper(II) Complexes. *Bull. Chem. Soc. Jpn.* **1966,** *39*, 2054.
34. Antosik, S.; Brown, N. M. D.; McConnell, A. A.; Porte, A. L., The Effects of Axial Interactions on Electron Paramagnetic Resonance Spectra of Copper(II) Chelates : Weak Complexes of Copper(II) Chelates and Chloroform *J. Chem. Soc. A* **1969**, 545–550.
35. Adato, I.; Eliezer, I., Effect of the Solvent on the ESR Parameters of Copper Acetylacetonate. *J. Chem. Phys.* **1971,** *54*, 1472–1476.
36. Yokoi, H.; Kishi, T., THE CORRELATION OF THE ESR PARAMETERS OF VARIOUS β-DIKETONE CHELATES OF COPPER(II) WITH THE pK_a OF THE LIGANDS *Chem. Lett.* **1973**, 749–754.
37. Bonner, J. C.; Fisher, M. E., Linear Magnetic Chains with Anisotropic Coupling. *Phys. Rev.* **1964,** *135*, 640–658.
38. G. A. Baker, J.; Rushbrooke, G. S.; Gilbert, H. E., High-Temperature Series Expansions for the Spin-1/2 Heisenberg Model by the Method of Irreducible Representations of the Symmetric Group. *Phys. Rev.* **1964,** *135*, 1272–1276.
39. Rempel, G. A.; Legzdins, P.; Smith, H.; Wilkinson, G., Tetrakis(acetato)dirhodium(II) and Similar Carboxylato Compounds. *Inorg. Syn.* **1972,** *13*, 90–91.
40. CrysAlisPRO, Oxford Diffraction /Agilent Technologies UK Ltd, Yarnton, England.
41. SCALE3 ABSPACK, An Oxford Diffraction program, 2005 Oxford Diffraction Ltd.
42. Altomare, A.; Burla, M. C.; Camalli, M.; Cascarano, G. L.; Giacovazzo, C.;

Guagliardi, A.; Moliterni, A. G. G.; Polidori, G.; Spagna, R., SIR97: a new tool for crystal structure determination and refinement. *J. Appl. Cryst.* **1999,** *32*, 115–119.
43. Sheldrick, G. M., A short history of SHELX. *Acta Cryst.* **2008,** *A64*, 112–122.
44. Kabuto, C.; Akine, S.; Nemoto, T.; Kwon, E., *J. Cryst. Soc. Jpn.* **2009,** *51*, 218–224.

Chapter 5

Structure and Magnetic Behavior of a Two-Dimensional Honeycomb Sheet Containing Trans-Bridged Platinum and Iron Trinuclear Complex Linked using Rhodium Acetate with Chloride Coordination

Abstract

The paramagnetic trinuclear complex *trans*-$[Pt_2Fe(piam)_4(NH_3)_4](ClO_4)_3 \cdot H_2O$ (***t*-Fe**) has a half-filled σ-type orbital over Pt–Fe–Pt, making it an excellent option for magnetic assemblies. It was successfully used in synthesizing $[\{Rh_2(O_2CCH_3)_4Cl_2\}\{Pt_2Fe(piam)_4(NH_3)_4\}_2]_n(ClO_4)_{4n}$ (**6**) from ***t*-Fe** and $[Rh_2(O_2CCH_3)_4Cl_2]$, where each trinuclear complex was bridged by Cl^- ions aligned as –Pt–Fe–Pt–Cl–Pt–Fe–Pt– with Fe···Fe distance of 10.1 Å. The zigzag chains were further linked by –Rh–Rh– to form a two-dimensional honeycomb sheet. The X-ray photoelectron spectroscopy, electron paramagnetic resonance, and magnetic susceptibilities measurements revealed that the formal metal oxidation states in **6** were Pt(+2), Fe(+3), and Rh(+2), where five unpaired electrons were located on the Fe(+3) atoms. A significant decrease in χT below 40 K was observed, where the theoretical fitting affords the axial zero-field splitting parameter $D = 5.23\ cm^{-1}$ and $zJ = -0.12\ cm^{-1}$.

Introduction

Until now, networked complexes containing paramagnetic species, such as first transition metals, have been rationally aligned with designed bridging ligands toward significant magnetic interaction through s or p orbitals in organic ligands.[1-13] Nevertheless, to explore magnetic properties, we attemped to synthesize heterometallic one-dimensional chains in which paramagnetic metal species are connected by direct metal–metal bonds with a second metal species instead of an organic ligand.[14-20] The synthetic method for the paramagnetic heterometallic one-dimensional chains uses the HOMO–LUMO interaction at the dz^2 orbital (σ*) between two kinds of complex, where mixing *cis*-$[Pt_2M(piam)_4(NH_3)_4]X_2$ (piam = pivalamidate, M = metal, X = anion) and $[Rh_2(O_2CCH_3)_4]$ that have filled and vacant σ*, respectively, afforded –Pt–M–Pt–Rh–Rh– alignments, showing antiferromagnetic interactions through –Pt–Rh–Rh–Pt– bonds.[15,18-20] Furthermore, *trans*-$[Pt_2M(piam)_4(NH_3)_4]^{x+}$ (x = 2 or 3)[21] has recently been synthesized and characterized that exhibits different electronic structures attributed to metal stacking motif with face-to-face fashion, despite having a similar formula as *cis*-$[Pt_2M(piam)_4(NH_3)_4]^{x+}$ (Scheme 1). Due to this face-to-face fashion, *trans*-$[Pt_2M(piam)_4(NH_3)_4]^{2+}$ is dimerized with the HOMO–LUMO interaction to form hexanuclear Pt–M–Pt···Pt–M–Pt, showing significant antiferromagnetic interaction between two paramagnetic M through –Pt···Pt–.[21]

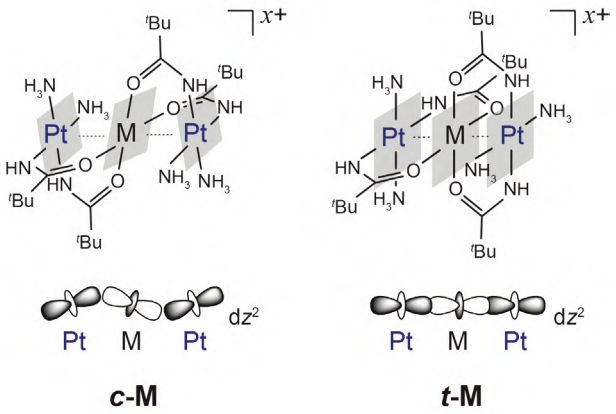

Scheme 1. Structures and schematic dz^2 orbitals for *cis*- or *trans*-bridged trinuclear complexes aligned as Pt–M–Pt.

Considering that *trans*-$[Pt_2M(piam)_4(NH_3)_4]^{x+}$ acts as both electron donors and acceptors due to the half-filled σ-type orbitals, three types of components, namely, *trans*-$[Pt_2Fe(piam)_4(NH_3)_4]^{3+}$, $[Rh_2(O_2CCH_3)_4]$, and Cl^-, were mixed in this study. Various aggregates

are possible, such as heterometallic one-dimensional chains aligned as –Pt–M–Pt–Rh–Rh–, or one-dimensional or two-dimensional aggregates aligned as –Pt–M–Pt–Cl–Rh–Rh–, with the linkages by Cl^- ions inducing mixed-valence states in Fe(+2/+3), Pt(+2/+3/+4), and Rh(+1/+2/+3) ions. Here, we isolated a paramagnetic two-dimensional honeycomb sheet, $[\{Rh_2(O_2CCH_3)_4Cl_2\}\{Pt_2Fe(piam)_4(NH_3)_4\}_2]_n(ClO_4)_{4n}$ (**6**), from the above three components, showing the oxidation and spin states, alongside magnetic behaviors.

Results and Discussion

Synthetic Procedure of $[\{Rh_2(O_2CCH_3)_4Cl_2\}\{Pt_2Fe(piam)_4(NH_3)_4\}_2]_n(ClO_4)_{4n}$ (6)

As reported previously,[21] *trans*-$[Pt_2M(piam)_4(NH_3)_4](ClO_4)_2$ (M = Mn, Co, Ni, Cu,) can be dimerized in both solid and solution states to form hexanuclear Pt–M–Pt···Pt–M–Pt. However, *trans*-$[Pt_2Fe(piam)_4(NH_3)_4](ClO_4)_3\cdot H_2O$ (***t*-Fe**) cannot be dimerized because trinculear complexes have a +3 charge, causing more surrounding ClO_4^- ions as well as coulomb repulsions to prevent dimerization. Although it is possible to obtain $[Pt_2Fe(piam)_4(NH_3)_4]^{2+}$ with the oxidation state of Pt(+2)–Fe(+2)–Pt(+2) by reducing compound ***t*-Fe**,[21] the obtained red powder synthesized from *trans*-$[Pt(piam)_2(NH_3)_2]$ and $Fe(ClO_4)_2$ was *trans*-$[Pt_2Fe(piam)_4(NH_3)_4](ClO_4)_3\cdot H_2O$ with the oxidation state of Pt(+2)–Fe(+3)–Pt(+2). As mentioned in the experimental section, simply mixing ***t*-Fe**, $[Rh_2(O_2CCH_3)_4]$, and Bu_4NCl in MeOH afforded black single crystals for $[\{Rh_2(O_2CCH_3)_4Cl_2\}\{Pt_2Fe(piam)_4(NH_3)_4\}_2]_n(ClO_4)_{4n}$ (**1**). According to single-crystal X-ray analysis, one of the crystal independent ClO_4^- ions was highly disordered; thus, after PLATON/SQUEEZE without this ion, analysis for $[\{Rh_2(O_2CCH_3)_4Cl_2\}\{Pt_2Fe(piam)_4(NH_3)_4\}_2]_n(ClO_4)_{2n}$ was performed. Table 1 shows the crystal data and structure refinement.

Table 1. Crystallographic data and structure refinements for $[\{Rh_2(O_2CCH_3)_4Cl_2\}\{Pt_2Fe(piam)_4(NH_3)_4\}_2]_n(ClO_4)_{4n}$ (**6**).

	6
Empirical formula	$C_{48}H_{116}Cl_4Fe_2N_{16}O_{24}Pt_4Rh_2$
Formula weight	2541.24
Crystal system	Monoclinic
Space group	*C*2/*c*
a (Å)	27.3708(8)
b (Å)	20.0833(4)
c (Å)	22.7806(7)
α (°)	90
β (°)	126.289(2)
γ (°)	90
V (Å^3)	10093.6(5)
Z	4
Temperature (K)	123
*D*c (Mgm^{-3})	1.672
Absorption coefficient (mm^{-1})	6.285
F(000)	4920
Crystal size (mm^3)	0.20 × 0.20 × 0.05
Measured reflections	11550
Independent reflections	11550 [R_{int} = 0.0403]
Data/restraints/parameters	8860/12/469
Goodness-of fit on F^2	1.060
R [$I > 2\sigma(I)$]	0.0408
R (all data)	0.0591

Crystal Structure of $[\{Rh_2(O_2CCH_3)_4Cl_2\}\{Pt_2Fe(piam)_4(NH_3)_4\}_2]_n(ClO_4)_{4n}$ (6)

Figure 1 shows the crystal structure of **6**. The crystal structure of **6** contains $[Rh_2(O_2CCH_3)_4]$ and $[Pt_2Fe(piam)_4(NH_3)_4]$ in the ratio of 1:2, where Cl^- ions were axially coordinated to both Rh atoms at a distance of 2.5657(14) Å. The *trans*-$[Pt_2Fe(piam)_4(NH_3)_4]$ were bridged by these Cl^- ions with distances of Pt(1)–Cl(1) = 2.8121(14) Å and Cl(1)–Pt(2′) = 2.926(1) Å to induce zigzag chains attributed to the bending angle of ∠Pt(1)–Cl(1)–Pt(2′) = 128.04(6)°. These zigzag chains were further linked by $[Rh_2(O_2CCH_3)_4Cl_2]$ to form a two-dimensional honeycomb sheet. The metal–metal distances in **6** were Pt(1)–Fe(1) = 2.5704(8) Å, Pt(2)–Fe(1) = 2.5985(8) Å, and Rh(1)–Rh(1′) = 2.4036(8) Å, resembling those in parent compounds, *trans*-$[Pt_2Fe(piam)_4(NH_3)_4]$ (2.5909(9), 2.5983(9) Å)[21] and $[Rh_2(O_2CCH_3)_4]$

(2.3855(5) Å)[22]. Honeycomb sheets were stacked in a slightly slipped fashion, forming the channel along the *c* axis fulfilled with ClO_4^- ions (Figure 1b).

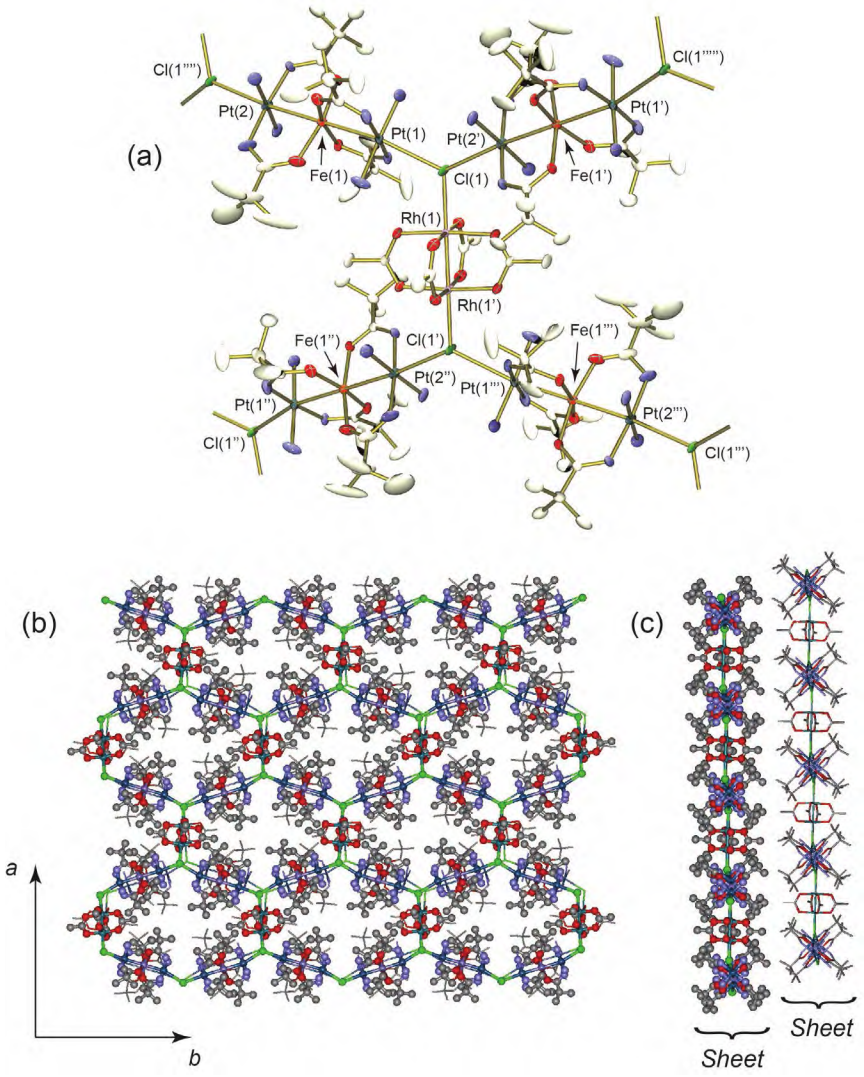

Figure 1. (a) Crystal structure of $[\{Rh_2(O_2CCH_3)_4Cl_2\}\{Pt_2Fe(piam)_4(NH_3)_4\}_2]_n(ClO_4)_{4n}$ (**6**). (b)(c) Stacking fashion of two honeycomb sheets along the *c* axis. The thick and thin lines show the upper and lower sheets, respectively. The hydrogen atoms and ClO_4^- anions are omitted for clarity.

The channel contained two types of crystallographically independent ClO_4^- ion, one of which was assigned (Figure S1) following the static position with hydrogen bonding to NH_3 in *trans*-$[Pt_2Fe(piam)_4(NH_3)_4]$ and the other of which is difficult to position due to the high disorder. Accordingly, the PLATON/SQUEEZE for analysis was conducted to obtain the structure for $[\{Rh_2(O_2CCH_3)_4Cl_2\}\{Pt_2Fe(piam)_4(NH_3)_4\}_2]_n(ClO_4)_{2n}$ with excellent accuracy. Since the volume of the open channel for $[\{Rh_2(O_2CCH_3)_4Cl_2\}\{Pt_2Fe(piam)_4(NH_3)_4\}_2]_n$

calculated by PLATON[23] was 782 Å^3, four ClO_4^- (346.2 Å^3)[24] ions can be accommodated. Thus, the true formula for the obtained single crystals is $[\{Rh_2(O_2CCH_3)_4Cl_2\}\{Pt_2Fe(piam)_4(NH_3)_4\}_2]_n(ClO_4)_{4n}$ (**6**), which was also confirmed with elemental analysis.

Oxidation and Spin State for 6

Given the chemical formula for **6**, the sum of Rh–Rh and two Pt–Fe–Pt was +18. For Fe ions, estimation using the bond valence sum method is possible[25,26]. Using the Fe–O and Fe–Pt distances in **6**, the oxidation state *z* in Fe(1) was 2.21, whereas it was 2.27 in parent ***t*-Fe**.[21]

XPS measurements were performed to determine the metal oxidation states in **6** (Figure 2). The Pt $4f_{7/2}$ binding energy for parent ***t*-Fe** and **6** were 74.2 and 73.5 eV, respectively, with the former being closer to $[Pt_2^{III,III}(NH_3)_4(\alpha\text{-pyrrolidonato})_2(NO_3)_2](NO_3)_2$ (74.6 eV),[27] and the latter being closer to $[Pt_2^{II,II}(en)_2(\alpha\text{-pyridonato})_2](NO_3)_2$ (73.1 eV; en = ethylenediamine)[27]. The Fe $2p_{1/2}$ and $2p_{3/2}$ binding energies were 725.2 and 711.6 eV for ***t*-Fe**, and 724.9 and 711.2 eV for **6**, respectively, which were characteristic values for Fe(+3) as found in $Fe^{III}Cl_3$ ($2p_{3/2}$: 711.3 eV)[28]. Considering the crystal structure, the oxidation state of ***t*-Fe** was Pt(+2)−Fe(+3)−Pt(+2),[21] where the higher energy shift of the Pt binding energies of ***t*-Fe** might be caused by electronic donating in the Pt atoms to Fe atoms originating from the close Pt−Fe(+3) contact. Consequently, considering the chemical formula, the formal oxidation state of the trinuclear part in **6** was Pt(+2)−Fe(+3)−Pt(+2), making the sum of oxidation states for Rh–Rh to be +4. Rh $3d_{3/2}$ and $3d_{5/2}$ binding energies for $[Rh_2^{II,II}(O_2CCH_3)_4]$ and **6** resembled, resulting in the formal oxidation state of Rh(+2)–Rh(+2) in **6** (Figures 2a and 2b).

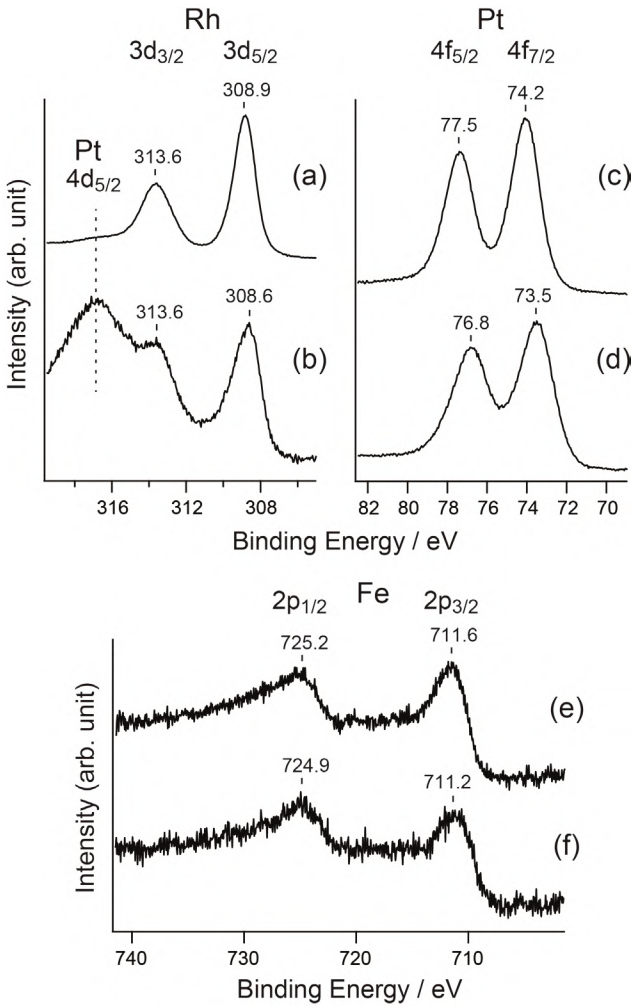

Figure 2. Rh $3d_{3/2}$ and $3d_{5/2}$, Pt $4f_{5/2}$ and $4f_{7/2}$, Fe $2p_{1/2}$ and $2p_{3/2}$ core levels of XPS for (a) $[Rh_2(O_2CCH_3)_4]$, (b) **6**, (c) *trans*-$[Pt_2Fe(piam)_4(NH_3)_4](ClO_4)_3$, (d) **6**, (e) *trans*-$[Pt_2Fe(piam)_4(NH_3)_4](ClO_4)_3$, and (f) **6**.

The results of the crystal structures and XPS measurements indicated that the iron atoms in **6** were Fe(+3). EPR measurements can be used to determine the oxidation state of Fe(+3), which can have a three-electron configuration: high-spin (S = 5/2), intermediate-spin (S = 3/2), and low-spin (S = 1/2).[29] Figure 3 shows the EPR spectra for powdered ***t*-Fe** and **6** at 77 K. The spectrum for ***t*-Fe** showed axial-type signals with $g_{\perp} = 5.51$ and $g_{//} = 1.96$, where an apparent g peak around 6 was due to high-spin (S = 5/2) with zero-field splitting (ZFS).[30-32] For the systems with large axial crystal fields, $D > 0.25$ cm^{-1} and $\lambda = 0$, where D and E are axial and rhombic ZFS parameters, respectively, where $\lambda = E/D$, an intense feature at $g = 6$ and a small feature at $g = 2$ were observed.[30-32] As reported previously,[21] the EPR simulation with several D and λ values was performed, yielding $D = 5.23$ cm^{-1} and $\lambda = 0$ (Figure 3a). Powder **6**

also exhibited a larger apparent *g* value of 5.13, indicating a high-spin Fe(+3) environment distortion in the crystal structure of **6** (Figure 3b). Compared with the spectrum for ***t*-Fe**, that for **6** was broader because of the magnetic interaction with neighboring high-spin Fe(+3). Consequently, five unpaired electrons were localized on Fe atoms in **6**, where each metal was bound with the overlapping of σ-type orbitals (see Scheme 2).

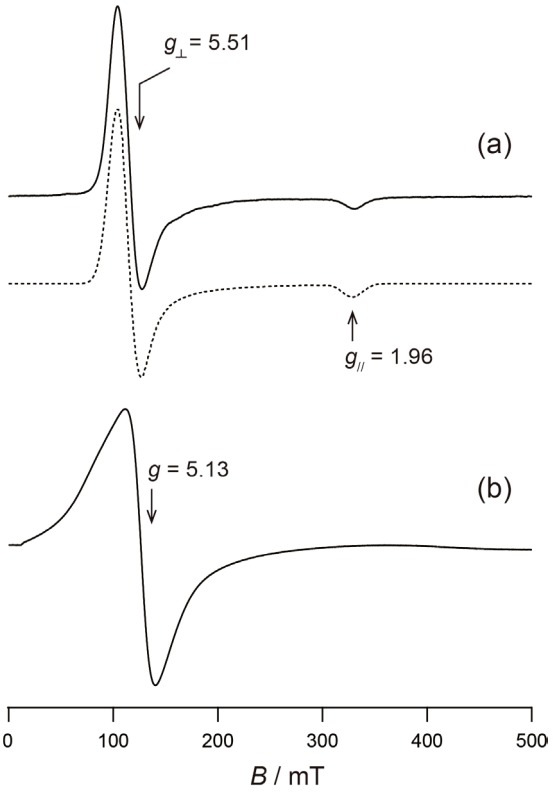

Figure 3. Continuous wave EPR spectra for powder samples of (a) ***t*-Fe** and (b) **6** at 77 K. Experimental settings: microwave frequency, (a) 9.0573 and (b) 9.0598; microwave power, 6 mW; field modulation, 0.2 mT. Dotted lines are simulation calculated using EasySpin software.

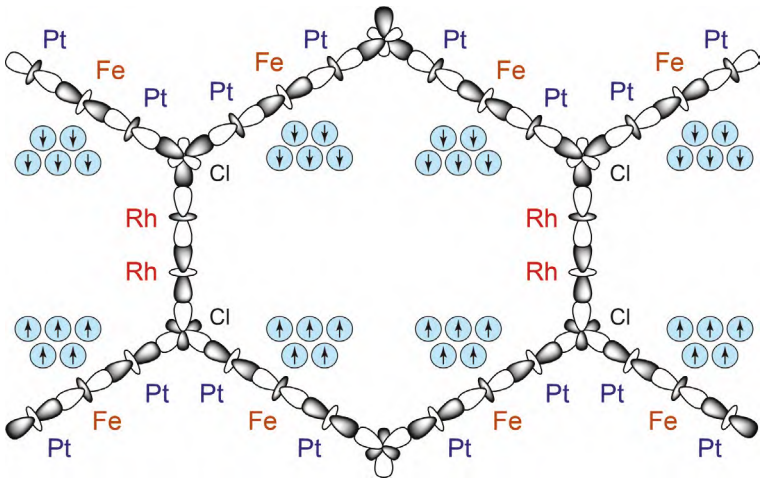

Scheme 2. Schematic view for the overlapping of σ-type orbitals in **6**.

Absorption Spectrum of 1

Figure 4 shows diffuse reflectance spectra for **6** and parent compounds, ***t*-Fe** and $[Rh_2(O_2CCH_3)_4]$. In ***t*-Fe**, an intense absorption peak at 2.88 eV with a shoulder around 2.44 eV was observed because of the transition between filled and vacant σ-type orbitals and that for δ-type orbitals, respectively.[21] However, in $[Rh_2(O_2CCH_3)_4]$, two absorption peaks at 2.06 and 2.73 eV were observed owing to the transitions from π* (Rh_2) to σ* (Rh_2) and from π* (Rh_2) to σ* (Rh−O), respectively.[33] Meanwhile, in **6**, two absorption peaks at 3.59 and 2.54 eV were observed. Considering the assignments for ***t*-Fe** and $[Rh_2(O_2CCH_3)_4]$, the transition between σ-type conduction and valence bands necessitated intense and broad absorption peaks at approximately 2.54 eV. This spectrum profile was over 1.5−3.0 eV, corresponding to 413−827 nm to cover the visible region, resulting in the black color for compound **6**.

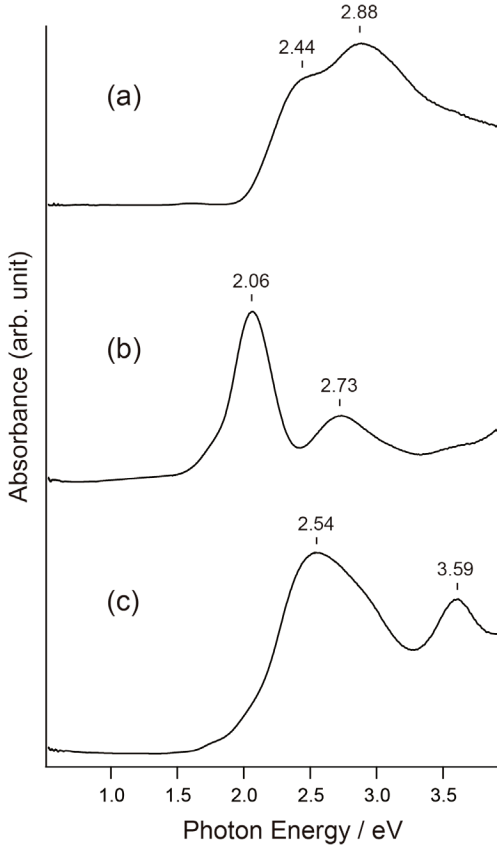

Figure 4. Diffuse reflectance spectra of (a) ***t*-Fe**, (b) $[Rh_2(O_2CCH_3)_4]$, and (c) **6** with MgO at room temperature.

Magnetic Behavior of 6

Figure 5 shows the temperature-dependent magnetic susceptibility of the powdered samples of ***t*-Fe** and **6** under 0.1 T in the temperature range of 2–300 K. The χT value for ***t*-Fe**

at 300 K was 4.30 cm^3 K mol^{-1}, which agrees well with that expected for the spin-only moment of a single $S = 5/2$ (4.38 cm^3 K mol^{-1}) species. This value remained constant up to 15 K. Below 15 K, χT decreased sharply, reaching 2.81 cm^3 K mol^{-1} at 2 K due to ZFS.[34] For molar susceptibility with D, the experimental data were fitted using the following expression:[34]

$$\chi_{\parallel} = \frac{Ng^2\beta^2}{4kT}\frac{1 + 9exp\left(\frac{-2D}{kT}\right) + 25exp\left(\frac{-6D}{kT}\right)}{1 + exp\left(\frac{-2D}{kT}\right) + exp\left(\frac{-6D}{kT}\right)}$$

$$\chi_{\perp} = \frac{Ng^2\beta^2}{8kT}\frac{18 + \frac{kT}{D}\left(16 - 11exp\left(\frac{-2D}{kT}\right) - 5exp\left(\frac{-6D}{kT}\right)\right)}{1 + exp\left(\frac{-2D}{kT}\right) + exp\left(\frac{-6D}{kT}\right)}$$

where k is the Boltzmann constant, T is the temperature, N is the Avogadro constant, g is the g-factor, and β is the Bohr magneton. The average molar magnetic susceptibility of a powdered sample is given by

$$\chi' = \frac{\chi_{\parallel} + 2\chi_{\perp}}{3} + \text{TIP}$$

where TIP is the temperature independent of paramagnetism. In some cases, including the contribution of impurity present in a proportion P was necessary, which was assumed to follow the Curie law with $S = 1/2$ and a g factor noted as g_{mo} (fixed as 2.00). The complete expression of the magnetic susceptibility used for the refinements is as follows:

$$\chi = (1 - P)\chi' + P\frac{Ng_{\text{mo}}^2\beta^2}{4kT}$$

According to the above equation, the resulting least-squares fit of the data of ***t*-Fe** between 2 and 300 K yielded $g = 1.98$, $D = 5.23$ cm^{-1}, TIP = 1.58×10^{-5} cm^3 mol^{-1}, and $P = 1.00 \times 10^{-4}$ (Figure 5a). The ZFS for the Fe(+3) ion is usually very small due to the electronic configuration ($^6A_1$) of the ion, and the ground state is well isolated from the high energy level.[35] However, the estimated D value was relatively large, which paralleled the results of the EPR analysis (Figure 3a).

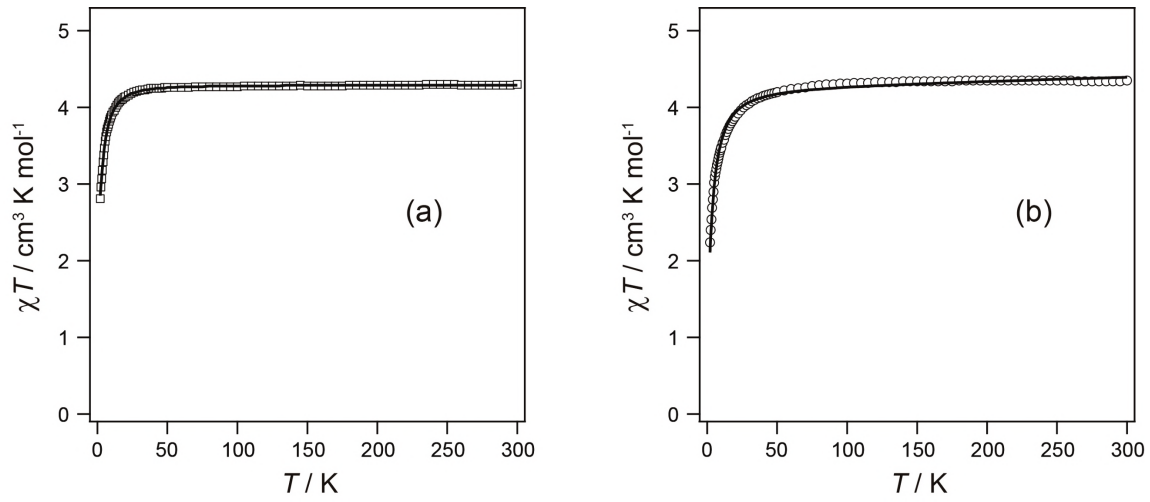

Figure 5. Temperature dependence of χT in (a) ***t*-Fe** and (b) **6** per Fe ion. The solid line represents the theoretical fitting to (a) the axial ZFS model and (b) the molecular field approximation with D and zJ.

However, the value of χT for **6** at 300 K was 4.35 cm^3 K mol^{-1}. Upon cooling, the value of χT gradually decreased at 40 K, and decreasing to 2.24 cm^3 K mol^{-1} at 2 K. The data followed the Curie–Weiss law (Figure S1), with a Curie constant of C = 4.38 cm^3 K mol^{-1} and a Weiss constant of θ = −1.86 K. The negative θ value indicated antiferromagnetic coupling between the Fe(+3) ions. From the crystal structure of **6**, the shortest pathway of interaction was along Fe–Pt–Cl–Pt–Fe in the 1D chain, where the shortest intrachain Fe···Fe distance was 10.1 Å. The shortest Fe···Fe distance between the chains was 11.5 Å, and those between the sheets were 10.9 Å and 12.0 Å. Because each Fe atoms is surrounded by six neighboring Fe atoms with the distances of 10.1 Å, 10.1 Å, 11.5 Å, 11.5 Å, 10.9 Å, and 12.0 Å, it is difficult to apply the model with dipolar interaction. Hence, for **6**, the molecular field approximation can be used with the following analytical expression to estimate the intermolecular interaction:

$$\chi'' = \frac{\chi'}{1 - \left(\frac{2zJ}{Ng^2\beta^2}\right)\chi'}$$

where zJ is the exchange energy (J multiplied by the number z of interacting neighbors) and χ' is the magnetic susceptibility of isolated molecules, resulting from the previous equation, where D = 5.23 cm^{-1} obtained by the result for parent compound ***t*-Fe**. Similarly, the contribution of a

paramagnetic impurity was included to yield the complete expression used for the refinements.

$$\chi = (1 - P)\chi'' + P\frac{Ng_{\mathrm{mo}}^2\beta^2}{4kT}$$

According to the above equation, the resulting least-squares fit of the data of **6** between 2 and 300 K yielded g = 1.98, zJ = −0.12 cm^{-1}, TIP = 4.70 × 10^{-4} cm^3 mol^{-1}, and P = 1.02 × 10^{-4} (Figure 5b).

Conclusion

This study demonstrated the synthesis and characterization of paramagnetic honeycomb sheets made from two types of metal complex, trinculear ***t*-Fe** and dinuclear rhodium acetate, where five unpaired electrons were located on Fe(+3) atoms, showing antiferromagnetic interaction with zJ = −0.12 cm^{-1}. Since the terminal Pt atoms of *trans*-[$Pt_2Fe(piam)_4(NH_3)_4$] in **6** were coordinated by Cl^- ions, the crystal structure found in this work also probed the electronic structure for ***t*-Fe**, a half-filled σ-type orbital over Pt–Fe–Pt. Hence, *trans*-[$Pt_2M(piam)_4(NH_3)_4]^{x+}$ are good candidates for novel magnetic assemblies, and further synthetic studies are now in progress.

Experimental Section

Materials. Tanaka Kikinzoku Co. supplied rhodium(III) chloride trihydrate and potassium tetrachloroplatinate(II). *trans*-$[Pt_2Fe(piam)_4(NH_3)_4](ClO_4)_3 \cdot H_2O$ (***t*-Fe**) and $[Rh_2(O_2CCH_3)_4]$ were synthesized following previous procedures.[21,36]

Synthesis of $[\{Rh_2(O_2CCH_3)_4Cl_2\}\{Pt_2Fe(piam)_4(NH_3)_4\}_2]_n(ClO_4)_{4n}$ (6)

A MeOH solution (3 mL) of $[Pt_2Fe(piam)_4(NH_3)_4](ClO_4)_3$ (11 mg, 9.0 μmol) was mixed with $[Rh_2(O_2CCH_3)_4]$ (2.0 mg, 4.5 μmol) and Bu_4NCl (2.5 mg, 9.0 μmol) and stirred for 5 h at room temperature. The resulting solution was slowly evaporated in a glass tube (10 mm internal diameter) at room temperature to obtain black crystals (1.2 mg) after 1 month. Yield 9.5%. Elemental analysis calcd for $C_{48}H_{124}Cl_6Fe_2N_{16}O_{36}Pt_4Rh_2$: C, 20.50; H, 4.44; N, 7.97%, found: C, 20.23; H, 4.56; N, 7.93%.

Physical Measurements. X-ray photoelectron spectroscopy (XPS) measurements were conducted on a Quantera-SXM spectrometer at room temperature. Binding energies were measured relative to the C 1s peak (284.8 eV) of an internal hydrocarbon. The diffuse reflectance spectra were recorded on a JASCO V-770 spectrophotometer over the range of 200–1500 nm at room temperature. The IR spectra were recorded on a JASCO FT/IR-4600AC over the range of 400–4000 cm^{-1} at room temperature. Electron paramagnetic resonance (EPR) spectra were measured on a JEOL TE-200 spectrometer. Magnetic data were obtained in the 2–300 K range using a Quantum Design MPMS superconducting SQUID susceptometer working at a 0.1 T field strength. The data were corrected for the sample holder, and the content diamagnetism was estimated from the Pascal constants.

Single-crystal X-ray analysis. The measurements of single-crystal X-ray analysis were performed on a Rigaku Mercury CCD diffractometer equipped with a normal focus Mo-target X-ray tube (λ = 0.71073 Å) operated at 5 kW power (50 kV, 100 mA). The system was equipped with a CCD two-dimensional detector, and 744 frames were collected for exposure times of 10 s/frame. The system was operated with the CrysAlisPRO software package.[37] Empirical absorption correction using spherical harmonics was implemented in the SCALE3 ABSPACK scaling algorithm.[38] The structure of **6** was solved by direct methods[39] with a subsequent

difference Fourier synthesis and refinement using SHELX-2017[40], controlled by the Yadokari-XG software package[41]. Nonhydrogen atoms were refined anisotropically, and all hydrogen atoms were treated as riding atoms. Because of the highly disordered ClO_4^-, after removing one of the ClO_4^- ions, PLATON and SQUEEZE[23] were used to apply data to assign as $[\{Rh_2(O_2CCH_3)_4Cl_2\}\{Pt_2Fe(piam)_4(NH_3)_4\}_2]_n(ClO_4)_{2n}$.

Analyses of magnetic susceptibility measurements.

The data for ***t*-Fe** and **6** were fitted to the Curie–Weiss law $\chi = C/(T - \theta)$. The resulting least-squares fit between 30 K and 300 K yielded ***t*-Fe**: C = 4.30 cm^3 K mol^{-1}, θ = −0.59 K, **6**: C = 4.38 cm^3 K mol^{-1}, θ = −1.86 K (Figure S). $C = N\beta^2g^2S(S + 1)/3k$, where N is Avogadro constant, β is the Bohr magneton, g is the Lande value, k is Boltzmann constant, θ is the Weiss constant, as the combination of constants $3k/N\beta^2$ is 7.991, gives ***t*-Fe**: g = 1.98, **6**: g = 2.00.

Supporting Figure

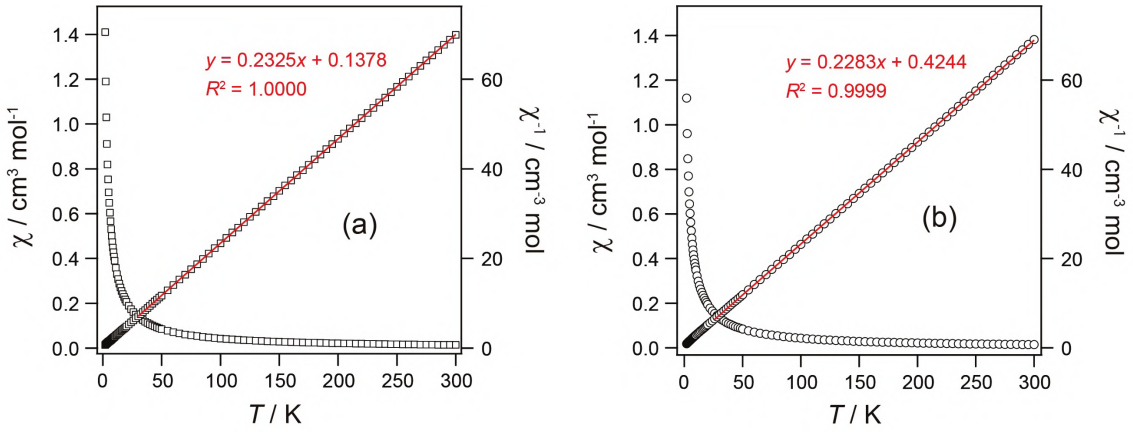

Figure S1. Temperature dependence of χ and χ^{-1} for (a) *trans*-$[Pt_2Fe(piam)_4(NH_3)_4](ClO_4)_3\cdot H_2O$ (***t*-Fe**) and (b) $[\{Rh_2(O_2CCH_3)_4Cl_2\}\{Pt_2Fe(piam)_4(NH_3)_4\}_2]_n(ClO_4)_{4n}$ (**6**). The red solid line represents the result of least square fitting.

References

1. Ito, A.; Suenaga, M.; Ôno, K., Mössbauer Study of Soluble Prussian Blue, Insoluble Prussian Blue, and Turnbull's Blue. *J. Chem. Phys.* **1968,** *48*, 3597–3599.
2. Miller, J. S.; Calabrese, J. C.; Rommelmann, H.; Chittipeddi, S. R.; Zhang, J. H.; Reiff, W. M.; Epstein, A. J., Ferromagnetic Behavior of $[Fe(C_5Me_5)_2]^{\cdot+}[TCNE]^{\cdot-}$. Structural and Magnetic Characterization of Decamethylferrocenium Tetracyanoethenide, $[Fe(C_5Me_5)_2]^{\cdot+}[TCNE]^{\cdot+}\cdot MeCN$, and Decamethylferrocenium Pentacyanopropenide, $[Fe(C_5Me_5)_2]^{\cdot+}[C_3(CN)_5]^{-}$. *J. Am. Chem. Soc.* **1987,** *109*, 769–781.
3. Kahn, O.; Pei, Y.; Verdaguer, M.; Renard, J. P.; Sletten, J., Magnetic Ordering of $Mn^{II}Cu^{II}$ Bimetallic Chains; Design of a Molecular-Based Ferromagnet. *J. Am. Chem. Soc.* **1988,** *110*, 782–789.
4. Caneschi, A.; Gatteschi, D.; Renard, J. P.; Rey, P.; Sessoli, R., Magnetic Phase Transitions in Manganese(II) Pentafluorobenzoate Adducts with Nitronyl Nitroxides. *J. Am. Chem. Soc.* **1989,** *111*, 785–786.
5. Tamaki, H.; Zhong, Z. J.; Matsumoto, N.; Kida, S.; Koikawa, M.; Achiwa, N.; Hashimoto, Y.; Okawa, H., Design of Metal–Complex Magnets. Syntheses and Magnetic Properties of Mixed-Mmetal Assemblies $\{NBu_4[MCr(ox)_3]\}_x$ (NBu_4^+ = tetra(*n*-butyl)ammonium ion; ox_2^- = oxalate ion; M = Mn^{2+}, Fe^{2+}, Co^{2+}, Ni^{2+}, Cu^{2+}, Zn^{2+}). *J. Am. Chem. Soc.* **1992,** *114*, 6974–6979.
6. Ferlay, S.; Mallah, T.; Ouahès, R.; Veillet, P.; Verdaguer, M., A room-temperature organometallic magnet based on Prussian blue. *Nature* **1995,** *378*, 701–703.
7. Ohba, M.; Ōkawa, H., Synthesis and magnetism of multi-dimensional cyanide-bridged bimetallic assemblies. *Coord. Chem. Rev.* **2000,** *198*, 313–328.
8. Caneschi, A.; Gatteschi, D.; Lalioti, N.; Sangregorio, C.; Sessoli, R.; Venturi, G.; Vindigni, A.; Rettori, A.; Pini, M. G.; Novak, M. A., Cobalt(II)-Nitronyl Nitroxide Chains as Molecular Magnetic Nanowires. *Angew. Chem., Int. Ed.* **2001,** *40*, 1760–1763.
9. Clérac, R.; Miyasaka, H.; Yamashita, M.; Coulon, C., Evidence for Single-Chain Magnet Behavior in a Mn^{III}–Ni^{II} Chain Designed with High Spin Magnetic Units: A Route to High Temperature Metastable Magnets. *J. Am. Chem. Soc.* **2002,** *124*, 12837–12844.
10. Yanai, N.; Kaneko, W.; Yoneda, K.; Ohba, M.; Kitagawa, S., Reversible Water-Induced Magnetic and Structural Conversion of a Flexible Microporous Ni(II)Fe(III) Ferromagnet. *J. Am. Chem. Soc.* **2007,** *129*, 3496–3497.
11. Nowicka, B.; Rams, M.; Stadnicka, K.; Sieklucka, B., Reversible Guest-Induced Magnetic and Structural Single-Crystal-to-Single-Crystal Transformation in Microporous Coordination Network $\{[Ni(cyclam)]_3[W(CN)_8]_2\}_n$. *Inorg. Chem.* **2007,** *46*, 8123–8125.
12. Liu, T.; Zhang, Y.-J.; Kanegawa, S.; Sato, O., Photoinduced Metal-to-Metal Charge

Transfer toward Single-Chain Magnet. *J. Am. Chem. Soc.* **2010,** *132*, 8250–8251.

13. Guillet, J. L.; Bhowmick, I.; Shores, M. P.; Daley, C. J. A.; Gembicky, M.; Golen, J. A.; Rheingold, A. L.; Doerrer, L. H., Thiocyanate-Ligated Heterobimetallic {PtM} Lantern Complexes Including a Ferromagnetically Coupled 1D Coordination Polymer. *Inorg. Chem.* **2016,** *55*, 8099–8109.
14. Uemura, K.; Ebihara, M., One-Dimensionally Extended Paddlewheel Dirhodium Complexes from Metal–Metal Bonds with Diplatinum Complexes. *Inorg. Chem.* **2011,** *50*, 7919–7921.
15. Uemura, K.; Ebihara, M., Paramagnetic One-Dimensional Chains Comprised of Trinuclear Pt−Cu−Pt and Paddlewheel Dirhodium Complexes with Metal−Metal Bonds. *Inorg. Chem.* **2013,** *52*, 5535–5550.
16. Uemura, K.; Uesugi, N.; Matsuyama, A.; Ebihara, M.; Yoshikawa, H.; Awaga, K., Integration of Paramagnetic Diruthenium Complexes into an Extended Chain by Heterometallic Metal−Metal Bonds with Diplatinum Complexes. *Inorg. Chem.* **2016,** *55*, 7003–7011.
17. Uemura, K., One-dimensional complexes extended by unbridged metal–metal bonds based on a HOMO–LUMO interaction at the dz^2 orbital between platinum and heterometal atoms. *Dalton Trans.* **2017,** *46*, 5474–5492.
18. Uemura, K., Magnetic behavior in heterometallic one-dimensional chains or octanuclear complex regularly aligned with metal–metal bonds as –Rh–Rh–Pt–Cu–Pt. *J. Mol. Str.* **2018,** *1162*, 31–36.
19. Uemura, K.; Miyake, R., Paramagnetic One-Dimensional Chain Complex Consisting of Three Kinds of Metallic Species Showing Magnetic Interaction through Metal–Metal Bonds. *Inorg. Chem.* **2020,** *59*, 1692–1701.
20. Uemura, K.; Aoki, Y.; Takamori, A., Paramagnetic One-dimensional Chain Containing High-spin Manganese Atoms Showing Weak Antiferromagnetic Interaction Through –Pt–Rh–Rh–Pt– Bonds. *Dalton Trans.* **2022,** *51*, 946–957.
21. Takamori, A.; Uemura, K., Dimerization of paramagnetic trinuclear complexes by coordination geometry changes showing mixed-valency and significant antiferromagnetic coupling through –Pt···Pt– bonds. *Inorg. Chem.* **2022,** *61*, 5762–5778.
22. Cotton, F. A.; DeBoer, B. G.; LaPrade, M. D.; Pipal, J. R.; Ucko, D. A., The Crystal and Molecular Structures of Dichromium Tetra-Acetate Dihydrate and Dirhodium Tetra-Acetate Dihydrate. *Acta Cryst.* **1971,** *B27*, 1664–1671.
23. Spek, A. L., PLATON SQUEEZE: a tool for the calculation of the disordered solvent contribution to the calculated structure factors. *Acta Cryst.* **2015,** *C71*, 9–18.
24. Jung, O.-S.; Kim, Y. J.; Lee, Y.-A.; Park, J. K.; Chae, H. K., Smart Molecular Helical Springs as Tunable Receptors. *J. Am. Chem. Soc.* **2000,** *122*, 9921–9925.
25. Kanowitz, S. M.; Palenik, G. J., Bond Valence Sums in Coordination Chemistry Using Oxidation-State-Independent R0 Values. A Simple Method for Calculating the Oxidation State of Iron in Fe–O Complexes. *Inorg. Chem.* **1998,** *37*, 2086–2088.

26. Oxidation state z = Σexp((1.745 – r)/0.37), where r (Å) is the observed bond length.
27. Matsumoto, K.; Sakai, K.; Nishio, K.; Tokisue, Y.; Ito, R.; Nishide, T.; Shichi, Y., Syntheses, Crystal Structures, and Electronic, ESR, and X-ray Photoelectron Spectra of Acetamidate- and 2-Fluoroacetamidate-Bridged Mixed-Valent Octanuclear Platinum Blues. *J. Am. Chem. Soc.* **1992,** *114*, 8110–8118.
28. Carver, J. C.; Schweitzer, G. K.; Carlson, T. A., Use of X-Ray Photoelectron Spectroscopy to Study Bonding in Cr, Mn, Fe, and Co Compounds. *J. Chem. Phys.* **1972,** *57*, 973–982.
29. Tisato, F.; Refosco, F.; Bandoli, G.; Pilloni, G.; Corain, B., Synthesis, Characterization, and Crystal Structure of the Water Soluble Copper(I) Complex with Trisulfonated Triphenylphosphine. *Inorg. Chem.* **2001,** *40*, 1394–1396.
30. Dowsing, R. D.; Gibson, J. F.; Goodgame, D. M. L.; Goodgame, M.; Hayward, P. J., Determination of the Stereochemistry of Manganese(II) Complexes by Electron Spin Resonance. *Nature* **1968,** *219*, 1037–1038.
31. Wagnon, B. K.; Jackels, S. C., Synthesis, characterization, and aqueous proton relaxation enhancement of a manganese(II) heptaaza macrocyclic complex having pendant arms. *Inorg. Chem.* **1989,** *28* (10), 1923–1927.
32. Jiménez-Sandoval, O.; Ramírez-Rosales, D.; Rosales-Hoz, M. d. J.; Sosa-Torres, M. E.; Zamorano-Ulloa, R., Magnetostructural behaviour of the complex $[MnL(H_2O)_2]Cl_2 \cdot 4H_2O$ at variable temperature studied by electron spin resonance (L = 2,13-dimethyl-3,6,9,12,18-pentaazabicyclo[12.3.1]octadeca-1(18),2,12,14,16-pentaene). *J. Chem. Soc., Dalton Trans.* **1998**, 1551–1556.
33. Cotton, F. A.; Murillo, C. A.; Walton, R. A., *Multiple Bonds Between Metal Atoms*. Springer Science and Business Media, Inc., New York: 2005; Vol. 3rd ed.
34. Kahn, O., *Molecular Magnetism*. VCH Publishers Inc., New York: 1993.
35. Figgis, B. N.; Lewis, J., The Magnetic Properties of Transition Metal Complexes. *Prog. Inorg. Chem.* **1964,** *6* (37).
36. Rempel, G. A.; Legzdins, P.; Smith, H.; Wilkinson, G., Tetrakis(acetato)dirhodium(II) and Similar Carboxylato Compounds. *Inorg. Syn.* **1972,** *13*, 90–91.
37. CrysAlisPRO, Oxford Diffraction /Agilent Technologies UK Ltd, Yarnton, England.
38. SCALE3 ABSPACK, An Oxford Diffraction program, 2005 Oxford Diffraction Ltd.
39. Altomare, A.; Burla, M. C.; Camalli, M.; Cascarano, G. L.; Giacovazzo, C.; Guagliardi, A.; Moliterni, A. G. G.; Polidori, G.; Spagna, R., SIR97: a new tool for crystal structure determination and refinement. *J. Appl. Cryst.* **1999,** *32*, 115–119.
40. Sheldrick, G. M., A short history of SHELX. *Acta Cryst.* **2008,** *A64*, 112–122.
41. Kabuto, C.; Akine, S.; Nemoto, T.; Kwon, E., *J. Cryst. Soc. Jpn.* **2009,** *51*, 218–224.

General Conclusion

The author investigated the synthesis based on new construction strategy and characterization of the paramagnetic multinuclear assembles with heterometallic bonds and to elucidate the crystal structure, spin state, and magnetic properties of paramagnetic multinuclear assembles. In order to obtain paramagnetic multinuclear assembles, the author mainly tried to construct with *trans* bridged multinuclear units containing paramagnetic species. The author has been synthesized and characterized 11 paramagnetic multinuclear assembles with heterometallic bonds, and studied on the relationship between the crystal structure and magnetic properties.

Chapter 1, the author synthesized and characterized novel trinuclear Pt–M–Pt (M = Mn, Fe, Co, Ni, and Cu) complexes bridged in a trans fashion from the amidate-hanging Pt mononuclear complex, *trans*-[Pt(piam)$_2$(NH$_3$)$_2$]. Each trinuclear complex is dimerized in both solvents and solid with Pt···Pt interactions aligned as hexanuclear Pt–M–Pt···Pt–M–Pt with high-spin M. Thereby, the spin density was modified, which allowed for mixed valencies. Although relatively longer distances of unbridged Pt···Pt (3.9 Å) were observed, significant antiferromagnetic interactions with lengths of approximately 9.0 Å were observed, which are caused by electronic coupling through –Pt···Pt– bonds.

Chapter 2, the author synthesized and characterized trinuclear Pt–M–Pt (M = Co, Ni, and Cu) complexes bridged in a trans fashion from the acetamidate-hanging Pt mononuclear complex, *trans*-[Pt(acam)$_2$(NH$_3$)$_2$]. Each trinuclear complex are extended to be infinity one-dimensional chains in solid with Pt···Pt interactions aligned as ···Pt–M–Pt···Pt–M–Pt··· with high-spin M. The significant magnetic interactions were observed with a length of approximately 8.7 Å, which are attributed to electronic coupling through unbridged Pt···Pt bond (3.5 Å).

Chapter 3, the author synthesized and characterized novel paramagnetic one-dimensional chain complexes, [PtCu(piam)$_2$(NH$_3$)$_2$Cl$_2$]·H$_2$O, aligned –Pt–Cu–Pt–Cu– with direct metal–metal bonds, where all metals are bridged by amidate ligand. The geometric structure in the one-dimensional chain is in the *trans*- and *cis*- coordination environment of Pt and Cu atoms, where the amidate ligands coordinated with Pt atoms are hanged to the opposite direction to be bound to Cu

atoms. Significant antiferromagnetic interactions were observed between Cu atoms in the intra chain with a length of 5.7 Å, which is attributed to an electronic coupling via –Pt– bonds.

Chapter 4, the author synthesized and characterized paramagnetic one-dimensional chain complexes with direct metal–metal bond by three metal species, Rh, Pt, and Cu. The paddlewheel dinuclear complexes of $[Rh_2(O_2CCH_3)_4]$ are linked by *trans*-$[Pt_2Cu(piam)_4(NH_3)_4]$ units at both ends with Rh–Pt metal–metal bonds to give octanuclear and one-dimensional chain complex. The oxidation states of each complex are Rh(+2), Pt(+2), and Cu(+2), where unpaired electrons lie on the Cu $dx^2–y^2$ orbitals. The significant antiferromagnetic interactions in octanuclear chains complex were observed with a length of 8.7 Å, which are attributed to an electronic coupling through unbridged –Pt···Pt– bonds. In contrast, the ferromagnetic interactions in one-dimensional chain complex were observed with a length of 13.2 Å through –Pt–Rh–Rh–Pt– direct metal–metal bonds.

Chapter 5, the author synthesized and characterized paramagnetic honeycomb sheets made from two types of metal complex, trinculear Pt–Fe–Pt and dinuclear rhodium acetate, where five unpaired electrons were located on Fe(+3) atoms, showing antiferromagnetic interaction with $zJ = -0.12\ cm^{-1}$.

The author mainly showed the two topics, (1) synthesis of *trans* bridged multinuclear units and paramagnetic multinuclear assembles containing paramagnetic metal species, (2) magnetic properties of paramagnetic multinuclear assembles with metal–metal bonds.

(1) Although it was difficult to construct one-dimensional metal chain complexes with metal–metal bonds containing paramagnetic species, *trans* bridged type multinuclear units are useful because *trans* bridged type multinuclear units are self-assembled one-dimensionally and also construct heterometallic bonds with other metal complexes (Chapter 1–2, 4–5). In addition, utilizing for *trans* coordinated geometrical structures, novel one-dimensional metal chain complexes are possible to be construct with direct metal–metal bonds, where all metals are bridged by bridging ligand (Chapter 3).

(2) The author investigated magnetic properties various one-dimensionally metal chain complexes with metal–metal bonds containing various paramagnetic metal species. Among the few reported cases of magnetic interactions through direct metal bond, the systematic studies obtained in this theses are considered to be significant. Especially, trinuclear Pt–M–Pt complexes are new simple models for paramagnetic one-dimensionally chains with metal–metal bond, having the potential to provide new insights into magnetism.

Publications List

[1] Takamori, A.; Uemura, K., Dimerization of Paramagnetic Trinuclear Complexes by Coordination Geometry Changes Showing Mixed Valency and Significant Antiferromagnetic Coupling through –Pt···Pt– Bonds, *Inorg. Chem.* **2022**, *61*, 5762–5778.

[2] Takamori, A.; Uemura, K., Structure and magnetic behavior of a two-dimensional honeycomb sheet containing trans-bridged platinum and iron trinuclear complex linked using rhodium acetate with chloride coordination, *Polyhedron*, **2022**, *224*, 116017.

[3] Uemura, K.; Takamori, A., Recent studies on the magnetic properties of paramagnetic metals linked by diamagnetic second metals, *Coord. Chem. Rev.*, **2022**, *471*, 214736.

Following publications are not included in this thesis.

[4] Uemura, K.; Aoki, Y.; Takamori, A., Paramagnetic One-dimensional Chain Containing High-spin Manganese Atoms Showing Weak Antiferromagnetic Interaction Through –Pt–Rh–Rh–Pt– Bonds. *Dalton Trans.* **2022**, *51*, 946–957.

[5] Uemura, K.; Ikeda, Y.; Takamori, A.; Takeyama, T.; Iwatsuki, S., Asymmetrical Platinum and Rhodium Dinuclear Complex Strongly Bound to Filled dz^2 Complexes by Unbridged Pt–metal Bonds Toward Heterometallic-Extended Metal Atom Chains. *Chem. Eur. J.* **2023**, in press.

Presentations List

[1] Syntheses, Structures and Properties of Paramagnetic Trans-Bridged Heterometallic One-dimensional Chains Incorporating First Transition Metals
Takamori, A.; Uemura, K.,
70th Symposium on Coordination Chemistry of Japan, Online, September 2020
(Poster Presentation)

[2] Syntheses, Crystal Structures, and Electronic Structures of Paramagnetic Multinuclear Assembles with Trans Pt–M–Pt Trinuclear Complexes
Takamori, A.; Uemura, K.
Young Electrochemist's and Photoelectrochemist's Association, Online, December 2020

[3] Syntheses, Crystal Structures, and Properties of Paramagnetic Multinuclear Assembles with Trans Pt–M–Pt Trinuclear Complexes
Takamori, A.; Uemura, K.
101th Annual Meeting of Chemical Society of Japan, Online, March 2021

[4] Syntheses and magnetic properties containing paramagnetic one-dimensional chains of first transition metals bridged by platinum atoms with metal-metal bonds
Takamori, A.; Uemura, K.
71th Symposium on Coordination Chemistry of Japan, Online, September 2021

[5] Syntheses, Crystal Structures, and Properties of Paramagnetic Copper One-dimensional Chains with Heterometallic Bonds
Takamori, A.; Uemura, K.
102th Annual Meeting of Chemical Society of Japan, Online, March 2022

[6] Syntheses, Crystal Structures, and Properties of Paramagnetic Multinuclear Assembles with Trans Pt–M–Pt Trinuclear Complexes
Takamori, A.; Uemura, K.

8th Asian Conference on Coordination Chemistry, Taipei and Online, August 2022
(Poster Presentation)

[7] Syntheses and properties containing paramagnetic one-dimensional chains comprised of trans-bridged Pt–Cu–Pt trinuclear complexes and paddlewheel dirhodium complexes with metal–metal bonds
Takamori, A.; Uemura, K.
72th Symposium on Coordination Chemistry of Japan, Kyushu, September 2022
(Poster Presentation)

[8] Syntheses and magnetic properties paramagnetic one-dimensional chains aligning first transition metals by metal–metal bonds with platinum atoms
Takamori, A.; Uemura, K.
72th Symposium on Coordination Chemistry of Japan, Kyushu, September 2022

[9] Syntheses and properties containing paramagnetic one-dimensional chains comprised of trans-bridged Pt–Cu–Pt trinuclear complexes and paddlewheel dirhodium complexes with metal–metal bonds
Takamori, A.; Uemura, K.
53th Annual Meeting of Union of Chemistry–Related Societies in Chubu Area, Japan, Online, October 2022

[10] Magnetic properties of paramagnetic one-dimensional chains where first transition metals are infinitely aligned with metal–metal bonds
Takamori, A.; Uemura, K.
103th Annual Meeting of Chemical Society of Japan, Chiba, March 2023